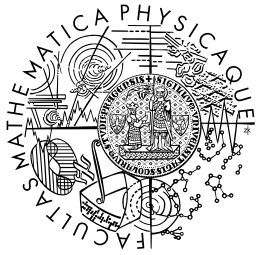

FACULTY
OF MATHEMATICS
AND PHYSICS
Charles University

DOCTORAL THESIS

Jan Dvořák

Contribution to theory of low-energy electron-molecule collisions

Institute of Theoretical Physics

Supervisor of the doctoral thesis: doc. RNDr. Martin Čížek, PhD.

Study programme: Physics

Study branch: Theoretical Physics, Astronomy and Astrophysics

Prague 2022

I declare that I carried out this doctoral thesis independently, and only with the cited sources, literature and other professional sources. It has not been used to obtain another or the same degree.

I understand that my work relates to the rights and obligations under the Act No. 121/2000 Sb., the Copyright Act, as amended, in particular the fact that the Charles University has the right to conclude a license agreement on the use of this work as a school work pursuant to Section 60 subsection 1 of the Copyright Act.

In Prague, September 30, 2022 Jan Dvořák

I thank my supervisor Martin Čížek for his friendly guidance and all the help during my studies at the Charles University. My gratitude belongs to Karel Houfek and Zdeněk Mašín as well, not only for the implementation of the FEM DVR ECS method and fixed-nuclei data but also for advice and many fruitful discussions we had over the years.

The financial support provided by the Charles University Grant Agency under Project No. 552120 is also gratefully acknowledged.

Title: Contribution to theory of low-energy electron-molecule collisions

Author: Jan Dvořák

Institute: Institute of Theoretical Physics

Supervisor: doc. RNDr. Martin Čížek, PhD., Institute of Theoretical Physics

Abstract: Collisions of low-energy electrons with molecules lead to excitation of vibrational degrees of freedom or even to bond dissociation. Such phenomena are not fully understood in the case of polyatomic targets since the theoretical treatment is complicated by the multidimensionality of the vibrational dynamics and the interaction of multiple short-lived electronic states. In this thesis, we extend the nonlocal theory of these processes by considering the vibronic coupling through the electron continuum. In particular, we study vibrational excitation of carbon dioxide and dissociation of the N-H bond of pyrrole. For carbon dioxide, the dynamics includes all vibrational modes and three electronic states. The model explains the long-time puzzling shape of the observed energy-loss spectra as well as the origin of a fine structure revealed in a recent experiment. In the case of pyrrole, we study the effect of the motion of distant parts of the molecule on the dissociation.

Keywords: quantum scattering theory, resonances, nonlocal dynamics, carbon dioxide, pyrrole

Contents

List of abbreviations

DEA	dissociative electron attachment
DVR	discrete variable representation
ECS	exterior complex scaling
FEM	finite element method
LCP	local complex potential
PES	potential energy surface
VE	vibrational excitation

Introduction

Excitation of molecules, their ionization or bond dissociation induced by collisions with low-energy electrons (< 20 eV) play an important role in nature, ranging from interstellar media and planetary atmospheres to living cells and cancer treatment [1–3]. During the collisions, temporary states of the molecular anion are formed by the electron capture, which mediate the processes and manifest themselves by sharp structures in the cross sections [4]. The existence of these *compound states* or *resonances* was experimentally proven by Schulz in elastic scattering in helium [5]. The compound states may interact upon the vibrational motion of the nuclei, known as *vibronic coupling*, which often leads to interesting phenomena observed in the cross sections. The dynamics of the temporary molecular anion in the case of inelastic electron scattering can be well probed by the two-dimensional (2D) energy-loss spectroscopy developed by Reddish *et al.* [6] and improved by Allan [7].

In this thesis, we focus on the description of vibrational excitation (VE) and dissociative electron attachment (DEA) with polyatomic molecules in the nonlocal theory. Using the projection formalism, the many-electron problem is effectively transformed to a potential scattering problem with energy-dependent and nonlocal potentials [8]. However, the theory has to include not only the electron interaction but also the motion of the nuclei, which renders the treatment challenging even in the case of small molecules. The VE and DEA processes are generally well understood in the case of diatomic molecules but the construction of the nonlocal models is still no routine task even for one nuclear degree of freedom. Therefore, to study polyatomic systems, a simpler local approximation has been preferentially used and typically no more than three vibrational modes have been considered.

In 1986, Estrada, Cederbaum and Domcke [9] extended the vibronic coupling model originally developed for bound states [10] to short-lived anionic states. This nonlocal model is ideal for studying multidimensional effects of the nuclear dynamics in the presence of interacting electronic states at least on a qualitative level, but its full potential has not yet been exploited. We were about to conduct such a qualitative study of the 2D dynamics when Juraj Fedor and his collaborators from the Heyrovský Institute of the Czech Academy of Sciences asked us for a help in interpreting their experimental 2D spectrum of the CO_2 molecule. Although this system received a lot of attention from experimentalists as well as theoreticians in the past, its behavior in the highly inelastic regime was not understood. Motivated by the new observations, we have further extended the model of Estrada *et al.* [9] in order to study the $e + CO_2$ system by taking into account all four vibrational modes, together with the $^2\Sigma_g^+$ virtual state and both Renner-Teller components of the $^2\Pi_u$ shape resonance. Most of this thesis is devoted to these nonlocal calculations that qualitatively reproduce the 2D spectrum, explain the origin of various observed structures, and reveal the importance of the vibronic coupling in this system. The presentation is based on three papers. Two of these papers [11, 12], which focus on our primary results and the model construction, have been

published in *Physical Review Letters* and *Physical Review A* and even selected as *Editors' Suggestions*. The third paper [13] recently submitted to *Physical Review A* concludes the work on CO_2 by a detailed discussion of the results and their comparison with experiments.

Due to the vibronic coupling, cleavage of a molecular bond can be affected by a movement of distant parts of the molecule. Recently, Kumar *et al.* [14] have observed that such an effect plays a significant role in the DEA to pyrrole (C_4H_4NH). The original model of Estrada *et al.* [9] and our treatment of CO_2 do not include dissociation of the molecular anion. Therefore, we introduce a simple two-dimensional model where the anion can dissociate in one coordinate. This approach is applied to the e + pyrrole system to study the direct and indirect mechanisms of the N-H dissociation. Apart from the N-H stretching, we include the out-of-plane movement of carbon-bonded hydrogens that couples a σ^* virtual-like state with a π^* resonance. The N-H bond can dissociate via both mechanisms but the results suggest that the out-of-plane movement of the detaching hydrogen, which is missing in the current model, needs to be considered to fully explain the observations.

The thesis is organized as follows. In Chapter 1, we briefly review the theoretical description of the VE and DEA processes including the most important applications to polyatomic systems. The original model of Estrada *et al.* [9] is also discussed in more detail there. Chapter 2 presents our calculations of the VE of CO_2. We incorporate 1D dissociation into 2D nuclear dynamics in Chapter 3. Finally, we employ this simple model to study the e + pyrrole system in Chapter 4.

If not stated otherwise, we use the atomic units ($\hbar = e = m_e = 1$) throughout this thesis.

Chapter 1

Electron-molecule collisions

1.1 Theory of VE and DEA processes

When a low-energy electron (< 20 eV) collides with a molecule, the electron is often captured to one or a few unoccupied molecular orbitals [2, 4]. The formed molecular anion has typically a finite lifetime (10^{-12}–10^{-15} s) because the electron can autodetach back to the continuum at least for some nuclear configurations. The electron capture can lead to the vibrational excitation (VE) process

$$e + M(\nu_i) \rightarrow e + M(\nu_f), \tag{1.1}$$

where energy is transferred between the electron and molecule M changing the initial molecular vibrational state ν_i to a final state ν_f. In some cases, when the molecular anion lives long enough, the anion can split into fragments A^- and B known as the dissociative electron attachment (DEA) process

$$e + M(\nu_i) \rightarrow A^- + B. \tag{1.2}$$

Both these processes have received a lot of scientific attention in the last hundred years because of their fundamental role in many areas of physics and chemistry including astrophysical and atmospheric applications or radiation chemistry used in medicine [2]. For example, Boudaïffa *et al.* [15] reported in 2000 that secondary low-energy electrons that are produced in living cells exposed to ionizing radiation cause a significant amount of single- and double-strand breaks in plasmid DNA via the DEA process. These observations sparked an intensive, mostly experimental, research of the DEA to biologically relevant molecules such as DNA bases or so-called radiosensitizers, molecules that enhance the effect of radiation therapy in tumor treatment [3, 16]. In the following text we limit ourselves to a brief overview of the achieved theoretical results in the description of the VE and DEA collisions. For more details we recommend excellent reviews by Hotop *et al.* [17], Bald *et al.* [3], and Fabrikant *et al.* [2], the book [18] edited by Čársky and Čurík, and references therein.

To model the VE and DEA processes, both electronic and nuclear degrees of freedom have to be considered. The description is usually divided into two steps. The electronic problem is solved first using the approximation of fixed nuclei to provide data for an effective parametrization of the electronic Hamiltonian in the subsequent treatment of the nuclear dynamics. Because the electron can leave to the continuum, standard quantum chemistry methods are not sufficient in the first step and the information about the quasistable states of the molecular anion has to be obtained from fixed-nuclei electron scattering calculations. There are

many well-established *ab initio* methods for treating the electron scattering off molecules with fixed nuclei, such as the R-matrix method [19], the complex Cohn method [20, 21] or the Schwinger variational principle [22]. For other methods and more details see, e.g., the overview in Ref. [18, ch. 2] and references therein.

The electron-molecule complex formed during the collision can be represented by one or a few so-called discrete states that characterize bound states, resonances or virtual states. As a result, the nuclear dynamics is described as an effective motion of the nuclei on one or a few coupled complex potential energy surfaces (PESs), where the imaginary part is related to the decay of the temporary anion by the autodetachment. There are also several methods with various complexity developed for the treatment of the nuclear motion. Probably the most straightforwardly applicable approach is the boomerang model also known as the local complex potential (LCP) approximation [23], where the anionic potential is only a function of the nuclear geometry. The energy dependence of the electron-molecule interaction is not considered, which restricts the LCP model mostly for narrow resonances and electron energies somewhat above the threshold [24].

Effective nonlocal and energy-dependent potentials have to be taken into account for treating especially broad resonances, virtual states and their analogs in dipolar systems [25]. The effective-range potential model was developed by Gauyacq and Herzenberg [26] for virtual states and extended by Vanroose *et al.* [27] to be more suitable for polyatomic systems. Fabrikant [28–30] utilized the R-matrix approach with a single-pole expansion, the resonance R-matrix method, for the nuclear motion. In this thesis, we use and extend the nonlocal resonance model also known as the model of discrete state in continuum, which was developed by works of Chen [31], O'Malley [32], Bardsley [33], and Nakamura [34] and thoroughly reviewed by Domcke [8].

The mentioned methods have been used to study various molecular systems. Overall, the VE and DEA processes that involve diatomic molecules, e.g., H_2, N_2, O_2, NO, CO, HX (X = F, Cl, Br, I), are well understood and the theory is in a very good agreement with experimental observations [2, 17]. Halogen halides HX were of a particular interest because of their rich threshold structures (Wigner cusps and vibrational Feshbach resonances) related to the long-range dipolar and polarization interactions between the electron and molecule [17]. In such systems the nonlocal approach proved to be essential.

The extension of the nuclear dynamics to polyatomic systems presents a significant challenge even in the LCP approximation, and for this reason, the nonlocal methods have been mostly restricted to systems that are dominated by one-dimensional (1D) dynamics. The production of X^- anions in the DEA to methyl halides CH_3X (X = F, Cl, Br, I), which behave similarly to the halogen halides, can be well described by the C–X stretching motion [2, 35]. Similarly, the dissociation of HNCO to H and NCO^- fragments takes place dominantly in the N–H stretching [36, 37]. Multimode effects in CF_3Cl were studied within the LCP model by Tarana *et al.* [38, 39], who considered two vibrational modes: the C–Cl stretching and the "umbrella" mode. Using the resonance R-matrix method, Ambalampitiya and Fabrikant [40] extended the 2D local dynamics into the 2D nonlocal variant for molecules of the type CY_3X (Y = H, F and X = F, Cl, Br, I). Vanroose *et al.* [41] employed the effective-range model to study the 2D dynamics for near threshold energies in the VE of CO_2.

The description of polyatomic systems is further complicated by the interaction of multiple electronic states of the temporary molecular anion, which leads to conical intersections of the PESs in the continuum. The time-dependent variant of the LCP model [42] in combination with the multiconfiguration time-dependent Hartree (MCTDH) method [43, 44] for the wave packet propagation was successfully employed for several such systems. McCurdy *et al.* [45] performed calculations of the VE process of CO_2, where they included symmetric stretching and bending as well as the Renner-Teller coupling of $^2A_1$ and $^2B_1$ states of CO_2^-. An impressive work was done on the VE and DEA processes with the H_2O molecule by Haxton *et al.* [46–52], who took into account the full vibrational dimensionality and the rich topology of the potentials including the Renner-Teller coupling of $^2B_1$ and $^2A_1$ states and the conical intersection of $^2A_1$ and $^2B_2$ states. The dissociation is naturally multidimensional because it does not proceed along one vibrational mode. Chourou and Orel studied 3D dynamics on the lowest adiabatic PES of acetylene (C_2H_2) [53, 54], HCN and HNC [55, 56] including the isotopic effect. Lowering of the molecular symmetry by distorting the geometry is necessary either to bypass a potential barrier on the path to dissociation or because the symmetry of the temporary anionic state is not in correspondence with the products. It can be viewed as a result of the interaction of two anionic states. The incoming electron is captured into a π^* resonant state but the dissociation proceeds via a σ^* state that is coupled to the π^* resonance upon appropriate distortion of the molecular symmetry.

The nature of the DEA process in formic acid (HCOOH) and the importance of the π^*/σ^* coupling received a lot of attention because this molecule can be used as a simplified model of amino acids. Based on fixed-nuclei calculations, Rescigno *et al.* [57] argued that the O-H dissociation is dominantly affected by the π^* resonance localized on the C=O bond in combination with the symmetry breaking caused by the out-of-plane movement of the hydrogen attached to the carbon atom. On the other hand, the 1D nonlocal calculations of Gallup *et al.* [58], who considered a reaction path close to the O-H stretching, reproduced well the experimental cross section without the need of the π^*/σ^* coupling. The further discussion [59, 60] was settled by measurements of the DEA cross sections for H/D isotopomers of HCOOH by Janečková *et al.* [61], who showed that the direct σ^* mechanism dominates. Gallup and Fabrikant [62] reported that the σ^* mechanism leads to a qualitative agreement with experimental observations in the DEA to uracil but they concluded that for a quantitative agreement the π^* state should be included as well. Recent observations by Kumar *et al.* [14] have shown that the movement of hydrogens attached to carbons is heavily involved in the dissociation of the N-H bond of pyrrole (C_4H_4NH).

Estrada *et al.* [9] generalized the discrete-state-in-continuum model and studied nonlocal 2D dynamics of a model system with *p*- and *d*-wave shape resonances coupled through a nontotally symmetric vibrational mode. Feuerbacher *et al.* [63, 64] further studied the topology of the complex PESs for this model and its generalization and showed that the model can reproduce *ab initio* PESs for σ^* and π^* states of the chloroethane anion. Šarmanová *et al.* [65–67] have recently investigated the effective numerical solution of the dynamics using Krylov subspace iterative methods.

As far as we know, the model of Estrada *et al.* [9] has not been applied to the

dynamics of any realistic system nor further utilized in qualitative studies of the dynamics in the presence of interacting anionic states. In the next chapters, we make use of this approach for the VE of CO_2 and our first attempt to tackle the DEA to pyrrole with the π^*/σ^* coupling. In the remaining part of this chapter, we introduce the equations for the nuclear dynamics within a general discrete-states-in-continuum model and discuss the insight that two-dimensional electron energy-loss spectra provides to the dynamics of the temporary anion.

1.2 Model of discrete states in continuum

Let us consider a temporary molecular anion that can be described by N_d discrete states labeled by $d = 1, \ldots, N_\mathrm{d}$. These diabatic discrete states belong to the electronic Hilbert space of the electron-molecule system and can represent bound states, resonances or virtual states. The Feshbach projection operators [68] are used to split the Hilbert space into the background scattering continuum and the discrete-state subspace. Consequently, effective equations for the motion of the nuclei are derived only within the small discrete-state subspace. The incoming electron with energy ϵ_i is represented by partial waves $\mu \equiv (l, m)$. Then, for each incoming partial wave μ_i and total energy E, the nuclear dynamics is described by the scattered wave function $|\Psi^{\mu_i}\rangle$ that satisfies the time-independent and inhomogenous Schrödinger equation

$$(E - H)|\Psi^{\mu_i}\rangle = |\Phi^{\mu_i}\rangle, \tag{1.3}$$

where H is the effective Hamiltonian and $|\Phi^{\mu_i}\rangle$ is the initial state. More details about the derivation is given in Sec. 2 II or Ref. [9] and the full derivation for the case of one discrete state can be found, e.g., in Refs. [8, 18].

The initial state of the anion $|\Phi^{\mu_i}\rangle$ is given by the vertical attachment of the incoming partial wave to the molecule that is in an initial vibrational state $|\nu_i\rangle$:

$$|\Phi^{\mu_i}\rangle = \begin{pmatrix} V^{\mu_i}_{1\epsilon_i}|\nu_i\rangle \\ V^{\mu_i}_{2\epsilon_i}|\nu_i\rangle \\ \vdots \\ V^{\mu_i}_{N_\mathrm{d}\epsilon_i}|\nu_i\rangle \end{pmatrix}, \tag{1.4}$$

where the energy-dependent coupling amplitudes $V^{\mu}_{d\epsilon}$ control the electron capture to the discrete states. The wave functions $|\Phi^{\mu_i}\rangle$ and $|\Psi^{\mu_i}\rangle$ thus have N_d vibrational components corresponding to the N_d discrete states. The $|\nu_i\rangle$ state is an eigenstate of the neutral vibrational Hamiltonian $H_0 = T_N + V_0$:

$$H_0|\nu\rangle = E_\nu|\nu\rangle, \tag{1.5}$$

where T_N is the kinetic energy operator of the nuclei and V_0 is typically the PES of the ground electronic state of the molecule. We consider only one neutral electronic state, that is, we do not describe electronic excitation of the molecule by electron impact.

The effective Hamiltonian H of the anion expressed in the basis of the discrete states is a $N_\mathrm{d} \times N_\mathrm{d}$ matrix

$$H = H_0 I + U + F(E - H_0), \tag{1.6}$$

where I is the unit operator in the discrete-state subspace, U and $F(E-H_0)$ are two additional potential terms that couples the discrete states. Note that we work in the diabatic representation where the kinetic energy operator is diagonal [10]. Diagonal elements of the matrix U describe diabatic discrete-state potential energies measured with respect to the threshold given by V_0, while off-diagonal elements characterize the so-called direct vibronic coupling, that is, the direct interaction of the electronic states through vibrational degrees of freedom.

The $F(E-H_0)$ potential matrix describes the interaction of the discrete states with the electron continuum. Its elements are complex, energy-dependent, and nonlocal operators given by

$$F_{dd'}(E-H_0) = \sum_{\mu} \int_0^{\infty} \mathrm{d}\epsilon \, V^{\mu}_{d\epsilon}(E-H_0-\epsilon+i\eta)^{-1} V^{\mu *}_{d'\epsilon}, \tag{1.7}$$

where the sum runs over all electron partial waves included in the model and η is a positive infinitesimal. The real part of F modifies the discrete-state PESs and the imaginary part effectively describes the decay of the anion by the electron autodetachment to the continuum.

The structure of the integral above helps us imagining the action of the F term. The nuclei move on the anionic potentials but an electron with energy ϵ can be released as a partial wave μ from a discrete state d' into the continuum [$V^{\mu *}_{d'\epsilon}$ term in Eq. (1.7)]. Then, the system evolves for some time as the free electron and neutral molecule (Green's function in the middle of the integral) but before the electron can leave sufficiently far away from the molecule, it can be recaptured in a different nuclear geometry to a discrete state d controlled by $V^{\mu}_{d\epsilon}$. Therefore, this interaction also indirectly couples the discrete states. Due to the neutral Hamiltonian H_0 in Eq. (1.7), the anion "feels" the vibrational structure of the molecule, which results in Wigner cusps at openings of vibrational channels in the cross sections for the VE and DEA processes.

The integral cross sections for the VE process $\nu_i \to \nu_f$ can be calculated from T matrix $T^{\mathrm{VE}}_{\nu_f\mu_f\leftarrow\nu_i\mu_i}$:

$$\sigma_{\nu_f\leftarrow\nu_i}(\epsilon_i) = \frac{2\pi^3}{\epsilon_i} \sum_{\mu_i,\mu_f} |T^{\mathrm{VE}}_{\nu_f\mu_f\leftarrow\nu_i\mu_i}|^2, \tag{1.8}$$

$$T^{\mathrm{VE}}_{\nu_f\mu_f\leftarrow\nu_i\mu_i} = \sum_{d,d'} \langle \nu_f | V^{\mu_f *}_{d'\epsilon_f} (E-H)^{-1}_{d'd} V^{\mu_i}_{d\epsilon_i} | \nu_i \rangle, \tag{1.9}$$

where ν_f and μ_f denote the final vibrational state and partial wave of the outgoing electron, respectively. The total energy E, which is conserved during the process, is given by

$$E = \epsilon_i + E_{\nu_i} = \epsilon_f + E_{\nu_f}, \tag{1.10}$$

where ϵ_f is final (residual) electron energy. In the study of the $e + \mathrm{CO_2}$ system, we also consider the differential cross sections, see Sec. 2 VI. A formula for the integral cross section of the DEA process is derived for 2D dynamics with one dissociative coordinate in Sec. 3.4.

To summarize, the model of the nuclear dynamics is defined by the neutral potential V_0, the $N_\mathrm{d} \times N_\mathrm{d}$ matrix U, and the $N_\mathrm{d} \times N_\mathrm{p}$ matrix V_ϵ, where N_p is the number of included electron partial waves. Their dependence on the molecular geometry cannot be arbitrary but is restricted by the molecular symmetry [9,

69]. To fix the unknown functions, fixed-nuclei quantities obtained within the model are typically compared with the same quantities from *ab initio* fixed-nuclei scattering calculations. We discuss the model construction in detail for the cases of CO_2 and pyrrole in Chapters 2 and 4.

The effective Hamiltonian H is expressed in the diabatic representation, where the potential term in not diagonal [10]. To obtain adiabatic PESs, which can be compared to *ab initio* calculations and also easily visualized in contrast to the nonlocal potential, we first have to diagonalize the fixed-nuclei variant of H where $T_N = 0$. Then, the dependence on energy has to be self-consistently replaced by a coordinate-dependent function typically defined in terms of K-matrix or S-matrix poles [8]. As a result, we get N_d adiabatic PESs, each of form

$$W_d = V^d_\mathrm{loc} - \frac{i}{2}\Gamma^d_\mathrm{loc}, \tag{1.11}$$

where the real part V^d_loc and the resonance width Γ^d_loc are functions only of the vibrational coordinates. More details is also given in Sec. 2 III C.

1.3 Two-dimensional energy-loss spectra

Two-dimensional electron energy-loss spectra provide a great insight into the nuclear dynamics of temporary molecular anions [7]. The 2D spectroscopy was developed by Reddish *et al.* [6] to study the $e + N_2$ system and later apply to CO_2 by Currell and Comer [70, 71]. Thanks to Michael Allan and the spectrometer he constructed in Fribourg (see, e.g., Ref. [72] and references therein), the 2D technique has been further utilized for studying larger molecules, such as acrylonitrile and methacrylonitrile [73, 74], pyrazine [7], $Fe(CO)_5$ [75], methyl formate [76], butadiene [77], nitrobenzene [78], C_3F_7CN [79], and pyrrole [14]. Note that 2D spectra for many benzene-like compounds have been presented by Allan on conferences but not yet published.

The signal measured by the electron spectrometer is plotted as a function of electron energy loss $\Delta\epsilon$ (horizontal axis) and incident electron energy (vertical axis), which may reveal many aspects that are not apparent from one-dimensional information: either 1D energy-loss spectra (for fixed incident ϵ_i or residual ϵ_f electron energies) or the VE cross sections (dependence on incident energy for a fixed energy loss).[1]

The conservation of the total energy [Eq. (1.10)] implies that features in the spectra along vertical lines (fixed $\Delta\epsilon$) correspond to individual final vibrational states of the molecule since $\Delta\epsilon = \epsilon_i - \epsilon_f = E_{\nu_f} - E_{\nu_i}$. The residual electron energy has to be positive resulting in the threshold line $\epsilon_i = \Delta\epsilon$. On the other hand, the energy loss can be negative when the molecule is initially in an excited vibrational state and the final state is energetically below the initial one, that is, the outgoing electron gains energy from the vibrations of the molecule. In contrast, horizontal structures are related to the initial vibrational states of the anion populated by the electron capture. Diagonal patterns are harder to interpret. They can correspond to boomerang oscillations (see below) or to de-excitation of particular vibrations,

[1] The 2D spectra are sometimes plotted with respect to the residual electron energy instead of the energy loss.

Table 1.1: Parameters of harmonic model for nuclear dynamics of diatomic systems inspired by H_2, N_2, O_2, and HF molecules.

		V_0	V_d			$\Gamma(\epsilon)$		
molecule	anion	ω_0 (eV)	k (eV)	h	c (eV)	a (eV)	l	β (eV^{-1})
H_2 $^1\Sigma_g^+$	H_2^- $^2\Sigma_u^+$	0.548	0.0736	6.77	3.77	10.3	1	0.246
N_2 $^1\Sigma_g^+$	N_2^- $^2\Pi_g$	0.292	0.183	2.09	2.17	0.812	2	0.562
O_2 $^3\Sigma_g^-$	O_2^- $^2\Pi_g$	0.201	0.0856	5.14	1.18	9.83	2	0.164
HF $^1\Sigma^+$	HF^- $^2\Sigma^+$	0.513	0.167	5.24	7.98	31.6	0	0.008

see Ref. [7], where the multidimensional dynamics is also illustrated using the Fribourg countryside representing the PES.

We are not aware of any calculated 2D spectra of polyatomic molecules that have been published except the spectrum for the model of Estrada *et al.* [9] and its generalization showed by Šarmanová *et al.* [65–67]. To further motivate the work presented in the following chapters, we next show and briefly discuss 2D spectra for four diatomic molecules calculated within a simple harmonic model and also the spectrum for the original model of Estrada *et al.* [9] with two vibrational degrees of freedom and two resonances.

1.3.1 Diatomic molecules

In the case of diatomic molecules (or for 1D nuclear dynamics), the 2D spectrum is not as revealing because we have only one vibrational quantum number and the same information can be easily plotted as a series of the VE cross sections. Nevertheless, it can be interesting to see how diatomic systems vary.

Let us consider one discrete state and the harmonic approximation for the neutral potential and the diabatic discrete-state potential:

$$H_0 = T_N + V_0 = -\frac{1}{2}\omega_0 \frac{\partial^2}{\partial Q^2} + \frac{1}{2}\omega_0 Q^2, \tag{1.12}$$

$$V_\mathrm{d} \equiv V_0 + U = \frac{1}{2}k(Q-h)^2 + c, \tag{1.13}$$

where the dimensionless coordinate Q describes the displacement of the nuclei from the neutral equilibrium position and ω_0, k, h, and c are model parameters. Furthermore, we consider one electron partial wave with angular momentum l and the discrete-state-continuum coupling $V_{d\epsilon}^{\mu}$ given by

$$\Gamma(\epsilon) \equiv 2\pi |V_{\mathrm{d}\epsilon}^{\mu}|^2 = a(b\epsilon)^{(2l+1)/2} e^{-b\epsilon}, \tag{1.14}$$

where $\Gamma(\epsilon)$ is the energy-dependent resonance width and its parameters a and b are kept constant, that is, the width is geometry independent.

We discuss four cases inspired by H_2, N_2, O_2, and HF molecules, for which the potentials behave rather differently. Values of the model parameters listed in Table 1.1 were chosen to approximate realistic nonlocal models constructed for these systems by Horáček *et al.* [80, 81], Berman *et al.* [82], Alt and Houfek [83], and Čížek *et al.* [84], respectively. We solved the Schrödinger equation Eq. (1.3)

using the iterative matrix method described in Sec. 2 VI and we considered only the ground neutral vibrational state as the initial state $|\nu_i\rangle$. To calculate the 2D spectrum, the obtained integral cross sections for VE $\nu_i \to \nu_f$ are placed along vertical lines with energy loss $\Delta\epsilon = E_{\nu_f} - E_{\nu_i}$ and convolved with a Gaussian distribution with the full width at half maximum of 20 meV to take into account a finite experimental resolution.

Figure 1.1 shows the resulting potentials and 2D spectra. For the H_2-like case, we have a broad p-wave resonance that leads to the broad resonance peak in the cross sections superimposed with boomerang oscillations. These oscillations result from interference of two contributions [80, 81]. First, the electron can autodetach very quickly after the attachment and so the nuclei have no time to perform almost any vibrational motion. Second, the anion survives long enough in order for the nuclei to perform at least one vibration and then it decays. The oscillations are even more pronounced for N_2 because the anion possesses a moderately wide resonance resulting in a longer lifetime [82].

In contrast, the structures in the spectra for O_2 and HF do not originate from the boomerang mechanism. The O_2^- anion has a very narrow d-wave resonance and the cross sections are comprised of narrow peaks at the positions of vibrational levels of O_2^- [83]. Finally, Wigner cusps and vibrational Feshbach resonances significantly affect the cross sections for HF [84]. In our simple model, the structures are not as sharp because we omitted the dipole interaction between the electron and the molecule and took into account only the pure s-wave behavior [85].

1.3.2 Model of Estrada, Cederbaum, and Domcke

The 2D energy-loss spectra from multidimensional dynamics are far more interesting but also harder to interpret. Here, we discuss the vibronic coupling model of Estrada, Cederbaum, and Domcke [9], who were the first to solve 2D nonlocal dynamics. They considered a model system with two vibrational modes: a totally symmetric *gerade* mode and a nontotally symmetric *ungerade* mode described by dimensionless coordinates Q_g and Q_u, respectively. The neutral PES is described within the harmonic approximation:

$$H_0 = T_N + V_0 = -\frac{1}{2}\omega_g \frac{\partial^2}{\partial Q_g^2} - \frac{1}{2}\omega_u \frac{\partial^2}{\partial Q_u^2} + \frac{1}{2}\omega_g Q_g^2 + \frac{1}{2}\omega_u Q_u^2, \tag{1.15}$$

where ω_g and ω_u are the corresponding vibrational frequencies.

Furthermore, they took into consideration two shape resonances of different symmetries (d- and p-waves) that are coupled through the *ungerade* mode. In order for the Hamiltonian H given by Eq. (1.6) to be invariant with respect to the molecular symmetry group, the diagonal elements can contain only even powers of Q_u whereas the off-diagonal elements can dependent only on odd powers of Q_u. We discuss this approach in detail in Chapter 2. For simplicity, they expanded elements of the matrix U around the equilibrium geometry to the first order:

$$U = \begin{pmatrix} E_1 + \kappa_1 Q_g & \lambda Q_u \\ \lambda Q_u & E_2 + \kappa_2 Q_g \end{pmatrix}, \tag{1.16}$$

where E_1, E_2, κ_1, κ_2, and λ are constant. Moreover, they considered the resonance

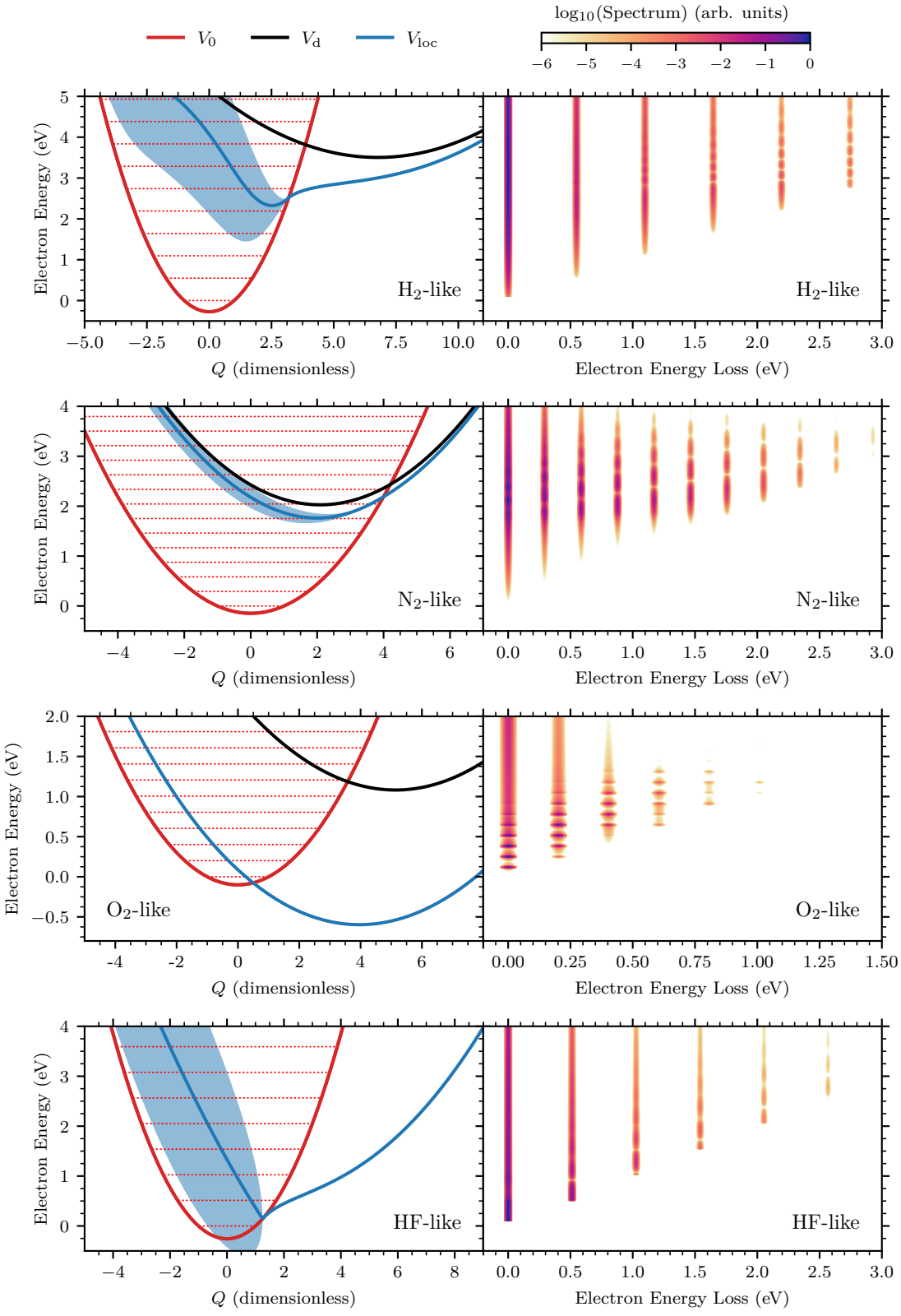

Figure 1.1: Potential energy curves (left column, legend on the top) and two-dimensional electron energy-loss spectra (right column) for diatomic systems inspired by H_2, N_2, O_2, and HF molecules. The shaded areas represent the local resonance widths and dotted horizontal lines indicate positions of neutral vibrational levels. The spectra are independently normalized to unity.

widths to be geometry independent, which results in a diagonal matrix V_ϵ

$$V_\epsilon = \begin{pmatrix} V_{1\epsilon}^{l=2} & 0 \\ 0 & V_{2\epsilon}^{l=1} \end{pmatrix}, \tag{1.17}$$

where $V_{1\epsilon}^{l=2}$ and $V_{2\epsilon}^{l=1}$ are parametrized analogically to Eq. (1.14). Actually, their form of $\Gamma(\epsilon)$ does not contain the parameter b in the threshold term, and thus, the parameter a does not have the dimension of energy. We prefer the parametrization given by Eq. (1.14) and we list the parameter values in Table 1.2 for completeness.[2]

Table 1.2: Parameters of model constructed by Estrada *et al.* [9].

Parameters					
ω_g	0.258 eV	κ_1	-0.212 eV	a_1	0.136 eV
ω_u	0.091 eV	κ_2	0.254 eV	b_1	0.833 eV^{-1}
E_1	2.45 eV	l_1	2	a_2	0.810 eV
E_2	2.85 eV	l_2	1	b_2	0.375 eV^{-1}

Cuts through the 2D PESs along coordinates Q_g and Q_u are shown in Fig. 1.2. For $Q_u \neq 0$, the resonances are vibronically coupled, which results in the double-well shape of the lower adiabatic potential W_-, and moreover, the adiabatic surfaces W_- and W_+ conically intersect for $Q_g = -0.68$, see Fig. 1.3. Because of the conical intersection, it is problematic to label the adiabatic surfaces in the left part of Fig. 1.2. Dividing the cut through the 2D manifold into the upper (W_+) and lower (W_-) parts result in a non-smooth transition of the potentials at $Q_g = -0.68$. However, this non-smoothness is artificial since the resonances are not coupled at all for $Q_u = 0$. Therefore, we prefer to show the smooth adiabatic curves labeled by $\tilde{W}_-$ and $\tilde{W}_+$ because they respect the topology of the intersection, which should be apparent from Fig. 1.3 (the widths are given by the color).

The imaginary part of the adiabatic surfaces causes that the PESs do not intersect at only one point as for bound states but the complex energies are degenerate at two points $(Q_g, Q_u) = (-0.68, \pm 0.14)$. These points are connected by a straight line where the real parts coincide but the widths differ, which is partially visible in Fig. 1.3. Such topology was further investigated by Feuerbacher *et al.* [63, 64] including the effect of geometry-dependent widths.

To calculate the VE cross sections, we again used the iterative approach that will be explained in Chapter 2. In contrast to the diatomic systems discussed above, the 2D spectrum for the 2D dynamics is much more filled-in because there are many more final vibrational states available, see Fig. 1.4. The number of vibrational states grows quadratically with energy loss. For higher energy losses the states form a vibrational pseudocontinuum, see vertical lines in Fig. 1.4 that indicate the positions of the states given by $\Delta\epsilon = E_{\nu_f} - E_{\nu_i} = \nu_g\omega_g + \nu_u\omega_u$, $\nu_g, \nu_u = 0, 1, \ldots$ for final states $\nu_f \equiv (\nu_g, \nu_u)$. We again consider only the ground state as the initial vibrational state. Note that Estrada *et al.* [9] limited their analysis only up to one excited quantum in each mode.

[2] Note that Estrada *et al.* [9] discuss the dynamics for several sets of parameter values. Here, we focus on their most complex model whose results are shown in their Fig. 7.

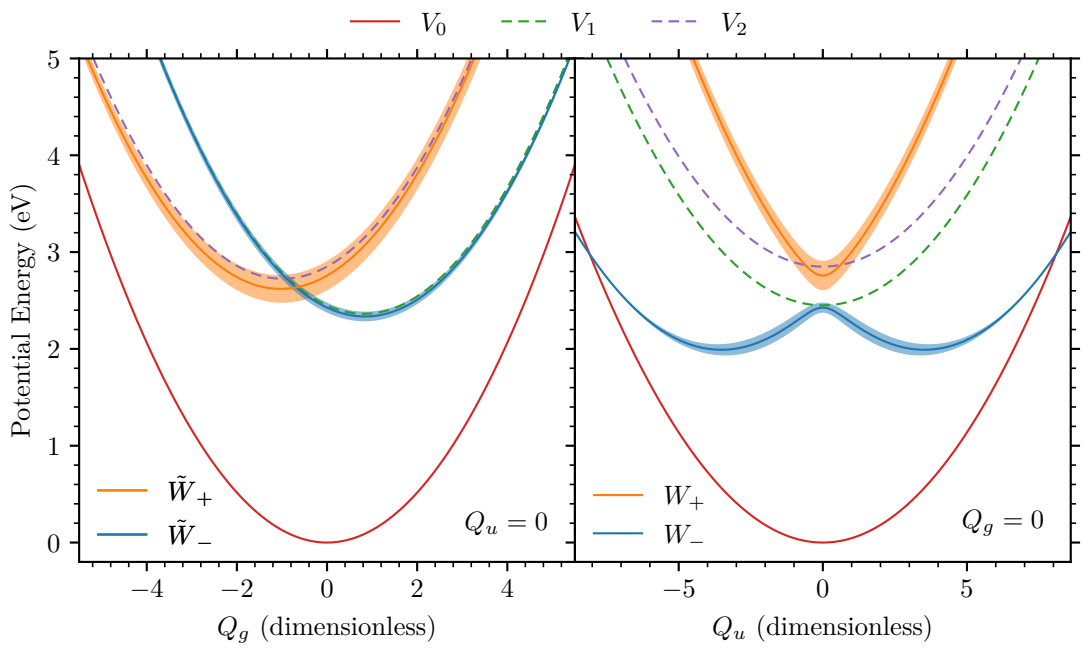

Figure 1.2: Potential energy surfaces for the model of Estrada *et al.* [9]. We show the neutral potential V_0, diabatic discrete-state potentials V_1 and V_2, and adiabatic (local) potentials W_- and W_+, see the text, with resonance widths represented by shaded areas. **Left panel**: cut along Q_g coordinate for $Q_u = 0$. **Right panel**: cut along Q_u coordinate for $Q_g = 0$.

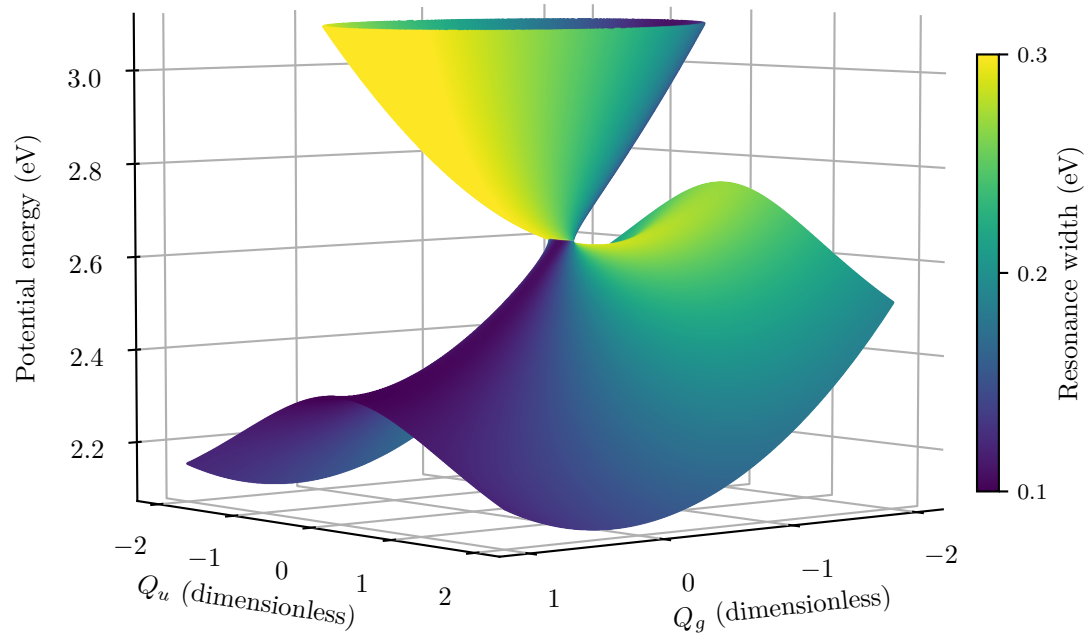

Figure 1.3: Adiabatic complex potential energy surfaces for the model of Estrada *et al.* [9] in the vicinity of the conical intersection. The real part is directly shown and the resonance width is represented by the color.

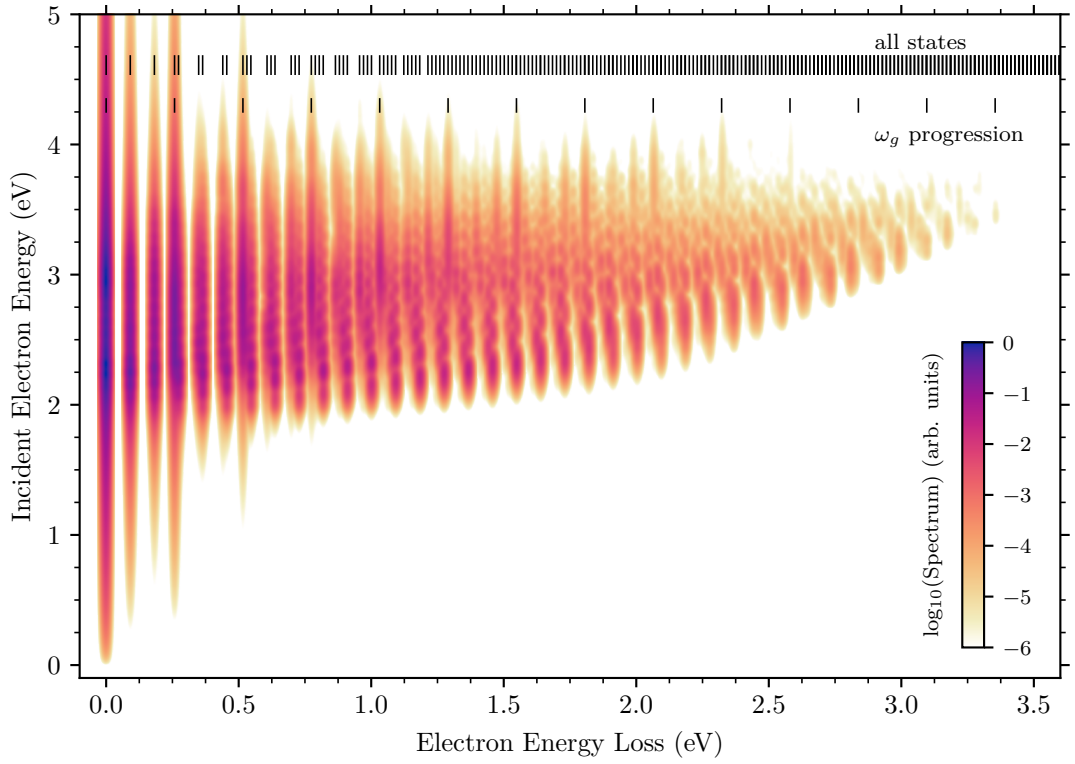

Figure 1.4: Two-dimensional electron energy-loss spectrum for the vibronic coupling model of Estrada *et al.* [9] with two vibrational modes. Vertical lines indicate positions of all neutral vibrational levels and vibrational levels only in the ω_g progression.

We can observe two peaks corresponding to the positions of the two resonances for low-lying states ($\Delta\epsilon < 0.4$ eV) in the spectrum. For higher energy losses there is a qualitative difference in the shape of the cross sections for excitation of the pure *gerade* mode, that is, excitation of final states $\nu_f = (\nu_g, 0)$, whose positions are also shown in Fig. 1.4. These excitation profiles have one peak at the position of the higher resonance. They are excited by the process where the electron attaches to the upper adiabatic surface. Then, the nuclei can substantially move only in the Q_g direction because the upper potential is repulsive in the Q_u mode. If the wave packet does not move pass the conical intersection, only the Q_g mode can be excited. On the other hand, if the wave packet starts on the lower surface or it goes through the intersection from the upper to the lower surface, it can easily move along the Q_u direction because it initially moves along the potential ridge, and as a result, significantly excites the Q_u mode. Moreover, the width of the lower surface is rather narrow and the wave packet can survive for a substantial amount of time leading to the distinct boomerang oscillations.

Even though this model is limited only to two vibrational modes, we have observed that it can reproduce features of 2D spectra of larger polyatomic molecules measured by Allan and others (see above), especially when one discrete state couples to an s wave. Therefore, this model is well suited for a qualitative study of the multidimensional dynamics to provide a better insight into systems where the vibronic coupling seems to play an important role. To focus on such a systematic study of the 2D dynamics was our original plan, but as we explained

in Introduction, we devote most of this thesis to the $e + CO_2$ system, which we look into in the next chapter. In Chapter 3, we generalize the model of Estrada *et al.* [9] to allow dissociation of the molecular anion in one vibrational coordinate, which is applied to the $e +$ pyrrole system in Chapter 4.

Chapter 2

Vibrational excitation of CO_2

In this chapter, we study the vibrational excitation of the CO_2 molecule by electron impact. We performed extensive calculations of the nuclear dynamics taking into account three interacting electronic states and all four vibrational modes. The presentation of our work is based on three papers. We start on page 25 by summarizing our primary results given in Ref. [11] published by *Physical Review Letters*. Next, we describe in detail the mathematical model, its construction from *ab initio* fixed-nuclei data, and the method for solving the dynamics using Ref. [12] published by *Physical Review A* and presented here starting on page 31. Finally, our theoretical results and their comparison with experimental observations are thoroughly analyzed and discussed in Ref. [13] submitted to *Physical Review A* (page 59). In all three cases authors' versions of the papers are presented.

Vibronic coupling through the continuum in the $e + CO_2$ system

Jan Dvořák,[1] Miloš Ranković,[2] Karel Houfek,[1] Pamir Nag,[2] Roman Čurík,[2] Juraj Fedor,[2,*] and Martin Čížek[1,†]

[1] *Charles University, Faculty of Mathematics and Physics, Institute of Theoretical Physics, V Holešovičkách 2, 180 00 Prague 8, Czech Republic*

[2] *J. Heyrovský Institute of Physical Chemistry, Czech Academy of Sciences, Dolejškova 2155/3, 182 23 Prague 8, Czech Republic*

We report two-dimensional electron energy-loss spectra of CO_2. The high-resolution experiment reveals a counterintuitive fine structure at energy losses where CO_2 states form a vibrational pseudocontinuum. Guided by the symmetry of the system, we constructed a four-dimensional nonlocal model for the vibronic dynamics involving two shape resonances (forming a Renner-Teller Π_u doublet at the equilibrium geometry) coupled to a virtual Σ_g^+ state. The model elucidates the extremely non-Born-Oppenheimer dynamics of the coupled nuclear motion and explains the origin of the observed structures. It is a prototype of the vibronic coupling of metastable states in continuum.

The most striking phenomena in the electron-molecule scattering are often related to the formation of compound anionic states [1, 2]. These states can have a mixed character combining bound states with resonances or virtual states [3]. The vibrational dynamics of such states can be represented by the familiar motion of nuclei on a potential energy surface (PES). The resonant PESs have, however, an imaginary component due to the embedding in the continuum and become nonlocal and energy dependent in the full form. This approach is well established for the theoretical treatment of the electron scattering from diatomic molecules including the understanding of the importance of the nonlocality for reproduction of many features observed in the cross sections [2, 3]. In polyatomic molecules a local complex potential approximation has almost exclusively been applied [4–7]. The intersection of multiple electronic states in the continuum has a specific topology due to the presence of the imaginary part [8–11]. Unlike in the case of bound states [12], the vibronic interaction of short-lived states is relatively unexplored. Estrada *et al.* [13] performed a full nonlocal dynamical calculation for a model system with two vibrational degrees of freedom and two states vibronically coupled (pseudo-Jahn-Teller effect). Their model assumes discrete-state-continuum amplitudes independent of vibrational coordinates, which prohibits an indirect coupling of electronic states of different symmetries through the continuum. We extend this approach by considering the indirect coupling in a model for multiple discrete states and up to four vibrational degrees of freedom, which opens the possibility to treat the nonlocal dynamics of metastable states for a larger class of polyatomic molecular anions.

The $e + CO_2$ system is well suited to test the theoretical approach. First, the neutral molecule has an intriguing vibrational-level structure. Those $(\nu_1, \nu_2^\ell, \nu_3)$ harmonic levels that are nearly degenerate and have the same symmetry are strongly Fermi-coupled and distributed in polyads [14]. Second, there are many experimental data available [15]. Several aspects of the system are already well understood including the boomerang oscillations [16], threshold peaks in vibrational excitation [17], and sharing of excitation between members of the Fermi dyad [4, 18]. On the other hand, some experimental data are still puzzling, especially those related to high vibrational excitation. Allan [19] reported a reappearance of structure in the spectra (with $\sim$ 160 meV spacing) at nearly complete energy losses where Fermi-coupled polyads overlap and should form a dense structureless continuum (he termed it 'spectroscopic order out of spectroscopic chaos'). Currell and Comer explained their data [14, 20, 21] as a result of excitation of very high bending modes and hypothesized that it is a signature of the quantum friction [22] in the CO_2^- nuclear motion. Up to this point, there have been no calculations that would provide an insight into the highly inelastic region. The Fermi coupling requires the inclusion of at least symmetric stretching and bending modes [23] and the most advanced treatment by McCurdy *et al.* [4] focused on excitation of low-lying vibrational states. In addition, theory has not addressed the sharing of excitation energies among nontotally symmetric vibrational states, such as odd quanta of bending or asymmetric stretching, which are clearly observed in experiments [15, 24]. In this Letter, we interpret our new and also previously unexplained experimental observations of the e+CO_2 system based on nonlocal calculations of the nuclear dynamics, demonstrating the predictive power of our theoretical approach and at the same time the feasibility of the calculations.

We have experimentally probed the CO_2 vibrational excitation using the 2D electron energy-loss spectroscopy (EELS) [25, 26] [Fig. 1a]. The incident electron energy (vertical axis) covers the region of the $^2\Pi_u$ resonance. The spectrum agrees well with previous reports, both classical 1D EELS studies [16, 19, 27–29] and early variants of 2D EELS [14, 20, 21]. However, the improved characteristics of the current experiment (energy resolution of 18 meV, sensitivity to electrons with residual energies down to 20 meV, high dynamic range) reveal new aspects. First, the "reappearing order" in 1D EELS spectra [19] corresponds to the lowest diagonal ray, which extends to complete energy losses. Second, the broad

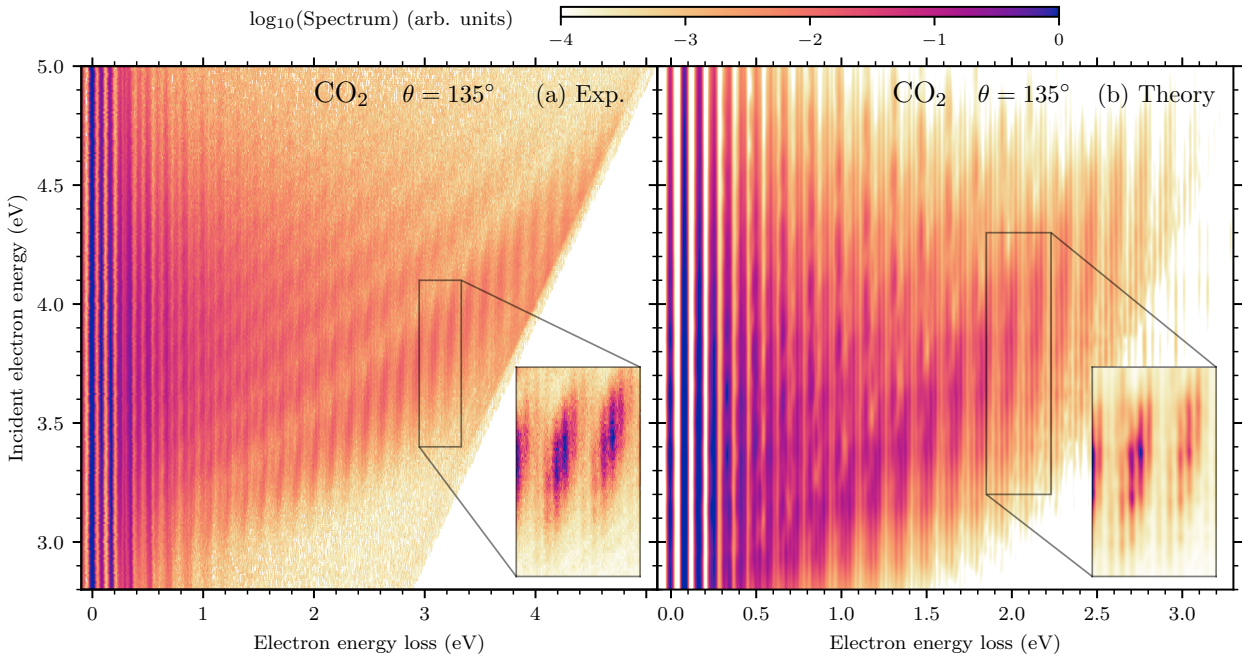

FIG. 1. (a) Experimental and (b) calculated 2D electron energy-loss spectra of CO_2 at a scattering angle of 135°. The main plots have the same logarithmic color scale shown at the top. The insets are in a linear scale from 0 to 1.

peaks in the high energy-loss region show a previously unreported fine structure (inset in Fig. 1a). The spacing of this progression empirically determined from 1D EELS spectrum, Fig. 2a is ~ 29 meV. Such a progression is surprising since first it is very different from the fundamental vibrational frequencies [30] (168 meV, 83 meV, and 297 meV for symmetric stretching, bending, and asymmetric stretching, respectively), and second, it appears in the region with a high vibrational level density. Therefore, there has to be some kind of selective mechanism. These results create an additional need for a proper multidimensional model of the vibrational excitation.

Our model is described in the companion paper [31]. Briefly, we consider three electronic states of CO_2^-: the $^2\Sigma_g^+$ virtual state and the $^2\Pi_u$ shape resonance, which splits due to the Renner-Teller effect into $2\,^2A_1$ and $^2B_1$ states as the molecule bends [32]. The $^2\Sigma_g^+$ and $^2\Pi_u$ states were previously treated separately [4, 18] and the topology of the PESs was unclear [33, 34]. Sommerfeld *et al.* [34] argued that the virtual state and the $2\,^2A_1$ Renner-Teller component mix upon bending, which couples all the three states together. We represent them by three diabatic discrete states $|d\rangle$ that are coupled directly through a potential matrix $V_{d_1 d_2} = \langle d_1|H_{\rm el}|d_2\rangle$, where $H_{\rm el}$ is the electronic Hamiltonian, and indirectly through the continuum by matrix elements $V^{\mu}_{d\epsilon} = \langle d|H_{\rm el}|\epsilon\mu\rangle$, which depend on electron energy ϵ. We consider the coupling to four electron partial waves $\mu \equiv (l, m)$ with $l = 0, 1$ for s, p waves, respectively. The coupling elements are functions of vibrational normal coordinates Q of all the modes but their form is restricted by the molecular symmetry [13, 35]. To determine the model parameters we performed *ab initio* fixed-nuclei R-matrix calculations of eigenphase sums and PESs for thousands of molecular geometries using the UKRmol+ [36] suite of codes. The cuts of adiabatic PESs obtained within our model are shown in Fig. 3. All the anionic states come close together and become bound as the molecule symmetrically stretches. The $^2B_1$ component is not much affected by the bending whereas the $2\,^2A_1$ component rapidly moves to the threshold and its width significantly increases due to a strong coupling to the s wave. On top of that, this s-wave coupling gives rise to the local minimum in the $1\,^2A_1$ potential but the minimum is connected with the $^2\Sigma_g^+$ virtual state while the $2\,^2A_1$ state remains unbound.

The dynamics of CO_2^- for total energy E is described by the inhomogeneous Schrödinger equation $[E - T - V - F(E)]|\Psi\rangle = V^{\mu_i}_{\epsilon_i}|\nu_i\rangle$, where T is the kinetic energy of the vibrations, V is the potential matrix $V_{d_1 d_2}$, and the nonlocal level-shift operator matrix $F(E)$ is calculated by an integral transformation from $V^{\mu}_{d\epsilon}$ [3]. The scattering wave function $|\Psi\rangle$ has three vibrational components $\Psi_d(Q)$, which are expressed in a four-dimensional oscillator basis. This transforms the Schrödinger equation into a (large) system of linear equations, which we solved by the iterative COCG method [37] based on Krylov subspaces. Finally, the vibrational excita-

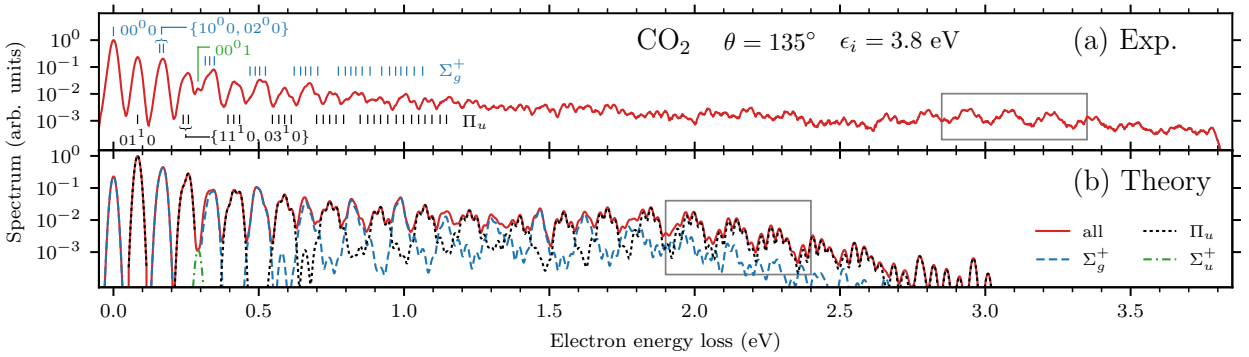

FIG. 2. (a) Experimental and (b) calculated 1D electron energy-loss spectra at a scattering angle of 135° and incident electron energy of 3.8 eV. We show the positions of the Σ_u^+ asymmetric stretching peak $(0, 0^0, 1)$ and vibrational states within Σ_g^+ polyads $(n, 2m^0, 0)$ and Π_u polyads $[n, (2m+1)^1, 0]$ for $n+m = 0, 1, \ldots, 6$. Panel (b) also shows calculated total contributions of Σ_g^+ and Π_u symmetries and the $(0, 0^0, 1)$ peak.

tion cross sections are calculated from T-matrix elements $T_{\nu_f \mu_f \leftarrow \nu_i \mu_i} = \sum_d \langle \nu_f | V_{d\epsilon_f}^{\mu_f \dagger} | \Psi_d \rangle$, where ϵ_i and ϵ_f are the initial and final electron energies, μ_i and μ_f the incoming and outgoing electron partial waves, and ν_i and ν_f the initial and final vibrational states, respectively.

Although anharmonic terms are included for the dynamics of the anion, the neutral molecule is only approximated by harmonic vibrations in order to keep the multidimensional calculations feasible. Thus, the dynamics does not include the Fermi resonance effect. Employing the anharmonic potential of Chedin [38], we calculated the expansion $|\nu_{\rm FR}\rangle = \sum_\nu c_\nu |\nu\rangle$ of the Fermi-coupled vibrational states $|\nu_{\rm FR}\rangle$ into harmonic states $|\nu\rangle$. By mixing the calculated harmonic T matrices using the coefficients c_ν, we partially incorporated this (crucial) effect.

To calculate the 2D spectrum shown in Fig. 1b, we convoluted the cross sections with a Gaussian distribution to simulate the finite experimental resolution. First, we should explain a well-understood drawback of our model that influences the direct comparison with the experiment: the shrinking of the calculated energy-loss spectra towards lower energies. The used R-matrix model produces the vibrational frequencies about 30% larger than the experimental ones. Therefore, when we project the calculated population of the harmonic states after the collision to more precise Fermi-coupled levels (with lower energies), the spectrum shrinks towards lower energy losses. Apart from this quantitative difference, the model qualitatively reproduces the observed features and allows for their interpretation:

(i) Boomerang rays. Perhaps the most visually dominant features in the 2D spectrum are the diagonal rays. These are the boomerang oscillations [27] that originate from interference due to the back and forth motion of the nuclei in symmetric stretching [16]. They are known to be somewhat weakened but not destroyed by the bending motion [23]. Calculated positions of boomerang peaks are also influenced by the above mentioned distortion and they do not directly correspond to the experimental data but the general character is reproduced.

(ii) Excitation of all modes. The dependence of the continuum coupling $V_{d\epsilon}^{\mu}$ on the vibrational coordinates allows excitation of nontotally symmetric vibrational states [39], which was not possible in previous calculations [4, 18]. The excitation of the fundamental bending mode $(0, 1^1, 0)$ (marked in Fig. 2), which is of the Π_u symmetry, requires an electron that changes its angular momentum projection on the molecular axis. In our model, the electron has to come in as the p_x or p_y waves and leave as the s wave or vice versa, which is controlled by $V_{d\epsilon}^{\mu}$ proportional to the bending coordinate. Similarly, the excitation of the asymmetric stretching $(0, 0^0, 1)$ (also marked in Fig. 2) of the Σ_u^+ symmetry requires a change from p_z wave to s or from s to p_z.

(iii) "Spectroscopic order out of spectroscopic chaos". Allan [19] pointed out that the experimental 1D EELS spectrum (such as the one in Fig. 2a) shows a very regular character at low energy losses (here up to some 1.3 eV), then the spectrum is seemingly structureless (1.3–2.5 eV), and above 2.5 eV a new regular peak progression appears (the resolution in [19] was insufficient to resolve the fine structure). Our model explains this behavior by selectivity of different polyads (Fig. 2b). Overall, the dominantly populated vibrational states $|\nu_{\rm FR}\rangle$ are even polyads composed of harmonic basis states $\nu = (n, 2m^0, 0)$ of the Σ_g^+ symmetry and odd polyads composed of $[n, (2m+1)^1, 0]$ of the Π_u symmetry, where $n + m = N =$ constant identifies individual polyads. For example, states within the Π_u polyad with $N = 12$ are linear combinations of $\nu = (12, 1^1, 0)$, $(11, 3^1, 0), \ldots, (0, 25^1, 0)$ and the corresponding amplitudes c_ν are typically non-negligible for all the states. At first, Σ_g^+ and Π_u peaks are well distinguishable since the Π_u peaks are shifted by one bending quantum. At

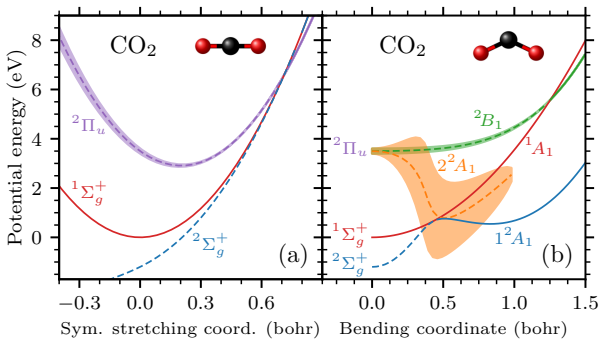

FIG. 3. Adiabatic potential energy curves of CO_2 (the ground state $^1\Sigma_g^+$) and CO_2^- ($^2\Sigma_g^+$, $^2\Pi_u$) within our model upon (a) symmetric stretching and (b) bending described by normal coordinates. The shaded areas represent the resonance widths.

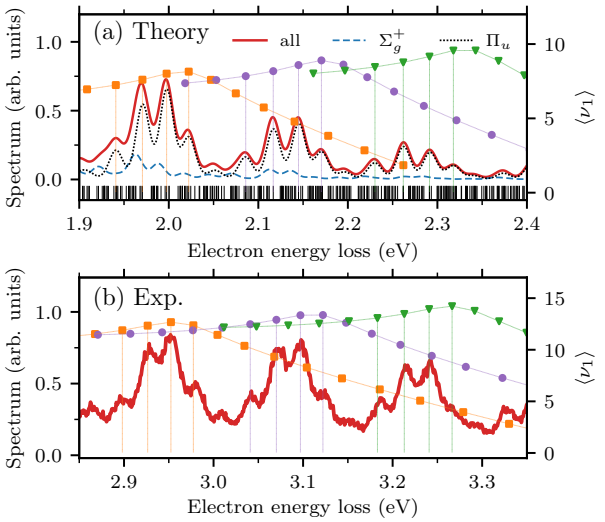

FIG. 4. (a) Theoretical and (b) experimental fine structures at high energy losses. The symbols represent the mean value of number of symmetric stretching quanta $\langle\nu_1\rangle$, see the text, for members of Π_u polyads $[n,(2m+1)^1,0]$ with $n+m=12,13,14$ for the theoretical spectrum and $n+m=18,19,20$ for the experimental result. Panel (a) also shows contributions of Σ_g^+ and Π_u vibrational states and the vertical lines at the bottom indicate energies of all relevant vibrational states included in our model.

intermediate energy losses, energy ranges of the polyads start to overlap and create seemingly chaotic patterns because of the similar magnitude of the excitation. In the high energy-loss region, the Π_u excitation dominates and the order is partially restored. This behavior is related to a change of the electron angular momentum from p to s discussed above. The incoming electron is dominantly of the p-wave character due to the existence of the 3.8 eV resonance. At high electron losses, the outgoing p-wave contribution with a small residual energy is suppressed due to the threshold law of Wigner [40]. The electron thus preferably leaves as an s wave forcing the change of angular momentum in the vibrational state leading dominantly to Π_u states.

(iv) Fine structure at high energy losses. Figure 4 depicts a detail of the 1D EELS spectra in the region dominated by the Π_u contribution as indicated by frames in Fig. 2. From the calculation we know which individual state is responsible for each peak in the theoretical spectrum. To understand it more, we characterize the Fermi-coupled states $|\nu_{\rm FR}\rangle$ by the mean value of number of symmetric stretching quanta $\langle\nu_1\rangle = \sum_\nu \nu_1 |c_\nu|^2$. In Fig. 4a, the horizontal positions of the symbols show the theoretical energies of the states within the Π_u polyads with $N=12,13,14$ and vertical positions represent the $\langle\nu_1\rangle$ values. Even though the polyads significantly overlap, only one polyad is responsible for each broad peak and the fine structure is given by the excitation of consecutive states somewhat below the maximum of $\langle\nu_1\rangle$. These fairly linear states are dominantly localized in the vibrational space along the symmetric stretching axis. Highly bent states, which are located at both ends of the polyads, are not significantly populated because the rapid broadening of the $2\,^2A_1$ state causes a fast decay of the anion in highly bent nuclear configurations, see Fig. 3b. To verify this mechanism, we plot the same quantity $\langle\nu_1\rangle$ for Π_u polyads with $N=18,19,20$ to the experimental spectrum in Fig. 4b. We found out that the positions of the predicted peaks follow very well the experimental peaks not only in the showed energy-loss interval but also in the spectra for other incident electron energies.

(v) Alternating excitation pattern in diagonal rays. Currell and Comer [14, 21] observed two types of excitation, which they labeled by A and B, alternating in the diagonal rays of the 2D spectrum for intermediate energy losses at a small scattering angle. We also observe the same patterns in our spectra at 135°. They correctly assigned the type A excitation to excitation of linear vibrational states of the Σ_g^+ polyads $(n,2m^0,0)$. However, they argued that the type B excitation is caused by decay to highly bent states of the same polyads via the quantum friction effect [22]. Our calculations show that this is not the case and that fairly linear states of the Π_u symmetry are responsible for the type B excitation.

In conclusion, the present nonlocal model qualitatively explains the observed features of the $e + CO_2$ system. The high energy-loss region is primarily influenced by the change of the incoming resonant p wave into the outgoing s wave, which leads to excitation of vibrational states of the Π_u symmetry. The model also singles out the states that are responsible for the emergence of the fine structure from the pseudocontinuum of available states. The theoretical approach, presented here on the example of the CO_2 molecule, can provide the explanation of the behavior of other polyatomic systems as well since the

change of the electron symmetry and the consequential excitation of nontotally symmetric vibrational modes appear to be an important phenomenon [39, 41–46].

We thank Michael Allan for inspiring discussions. This work was supported by the Czech Science Foundation Projects No. 19-20524S (M.Č., K.H., J.D.), 20-11460S (J.F.) and 21-12598S (R.Č.) and by the Charles University Grant Agency, Project No. 552120 (J.D., M.Č.).

* Corresponding author (experiment): juraj.fedor@jh-inst.cas.cz
† Corresponding author (theory): martin.cizek@mff.cuni.cz

[1] H. Hotop, M.-W. Ruf, M. Allan, and I. Fabrikant, Resonance and Threshold Phenomena in Low-Energy Electron Collisions with Molecules and Clusters (Academic Press, 2003) pp. 85–216.
[2] I. I. Fabrikant, S. Eden, N. J. Mason, and J. Fedor, Chapter Nine - Recent Progress in Dissociative Electron Attachment: From Diatomics to Biomolecules (Academic Press, 2017) pp. 545–657.
[3] W. Domcke, Theory of resonance and threshold effects in electron-molecule collisions: The projection-operator approach, Phys. Rep. **208**, 97 (1991).
[4] C. W. McCurdy, W. A. Isaacs, H.-D. Meyer, and T. N. Rescigno, Resonant vibrational excitation of CO_2 by electron impact: Nuclear dynamics on the coupled components of the $^2\Pi_u$ resonance, Phys. Rev. A **67**, 042708 (2003).
[5] D. J. Haxton, T. N. Rescigno, and C. W. McCurdy, Dissociative electron attachment to the H_2O molecule. II. Nuclear dynamics on coupled electronic surfaces within the local complex potential model, Phys. Rev. A **75**, 012711 (2007).
[6] S. T. Chourou and A. E. Orel, Dissociative electron attachment to HCN and HNC, Phys. Rev. A **80**, 032709 (2009).
[7] H. B. Ambalampitiya and I. I. Fabrikant, Nonlocal complex potential theory of dissociative electron attachment: Inclusion of two vibrational modes, Phys. Rev. A **102**, 022802 (2020).
[8] S. Feuerbacher, T. Sommerfeld, and L. S. Cederbaum, Intersections of potential energy surfaces of short-lived states: The complex analogue of conical intersections, J. Chem. Phys. **120**, 3201 (2004).
[9] S. Feuerbacher and L. S. Cederbaum, Jahn-Teller effect for short-lived states: Study of the complex potential energy surfaces, J. Chem. Phys. **121**, 5 (2004).
[10] D. J. Haxton, T. N. Rescigno, and C. W. McCurdy, Topology of the adiabatic potential enegy surfaces for the resonance states of the water anion, Phys. Rev. A **72**, 022705 (2005).
[11] D. J. Haxton, C. W. McCurdy, and T. N. Rescigno, Dissociative electron attachment to the H_2O molecule I. Complex-valued potential-energy surfaces for the $^2B_1$, $^2A_1$, and $^2B_2$ metastable states of the water anion, Phys. Rev. A **75**, 012710 (2007).
[12] H. Köppel, W. Domcke, and L. S. Cederbaum, Multimode Molecular Dynamics Beyond the Born-Oppenheimer Approximation, in *Adv. Chem. Phys.* (John Wiley & Sons, Ltd, 1984) pp. 59–246.
[13] H. Estrada, L. S. Cederbaum, and W. Domcke, Vibronic coupling of short-lived electronic states, J. Chem. Phys. **84**, 152 (1986).
[14] F. Currell, Friction effects in excitation to high vibrational states of the electronic ground state of carbon dioxide via the 4 eV shape resonance, J. Phys. B: At., Mol. Opt. Phys. **29**, 3855 (1996).
[15] M. Allan, Vibrational structures in electron-CO_2 scattering below the $^2\Pi_u$ shape resonance, J. Phys. B: At., Mol. Opt. Phys. **35**, L387 (2002).
[16] I. Čadež, F. Gresteau, M. Tronc, and R. I. Hall, Resonant electron impact excitation of CO_2 in the 4 eV region, J. Phys. B: At. Mol. Phys. **10**, 3821 (1977).
[17] H. Estrada and W. Domcke, On the virtual-state effect in low-energy electron-CO_2 scattering, J. Phys. B **18**, 4469 (1985).
[18] W. Vanroose, Z. Zhang, C. W. McCurdy, and T. N. Rescigno, Threshold vibrational excitation of CO_2 by slow electrons, Phys. Rev. Lett. **92**, 053201 (2004).
[19] M. Allan, Study of triplet states and short-lived negative ions by means of electron impact spectroscopy, J. Electron Spectrosc. Relat. Phenom. **48**, 219 (1989).
[20] F. Currell and J. Comer, Polyatomic excitation effects observed in an electron impact study of the 4 eV shape resonance of carbon dioxide, J. Phys. B: At., Mol. Opt. Phys. **26**, 2463 (1993).
[21] F. Currell and J. Comer, Observation of Friction in the Nuclear Dynamics of CO_2^- near the Equilibrium Geometry of the Negative Ion, Phys. Rev. Lett. **74**, 1319 (1995).
[22] W. Domcke and H. Estrada, Friction and memory effects in the dynamics of short-lived negative ions, J. Phys. B: At., Mol. Opt. Phys. **21**, L205 (1988).
[23] T. N. Rescigno, W. A. Isaacs, A. E. Orel, H.-D. Meyer, and C. W. McCurdy, Theoretical study of resonant vibrational excitation of CO_2 by electron impact, Phys. Rev. A **65**, 032716 (2002).
[24] M. Allan, Selectivity in the Excitation of Fermi-Coupled Vibrations in CO_2 by Impact of Slow Electrons, Phys. Rev. Lett. **87**, 033201 (2001).
[25] K. Regeta and M. Allan, Autodetachment Dynamics of Acrylonitrile Anion Revealed by Two-Dimensional Electron Impact Spectra, Phys. Rev. Lett. **110**, 203201 (2013).
[26] C. S. Anstöter, G. Mensa-Bonsu, P. Nag, M. Ranković, T. P. R. Kumar, A. N. Boichenko, A. V. Bochenkova, J. Fedor, and J. R. R. Verlet, Mode-Specific Vibrational Autodetachment Following Excitation of Electronic Resonances by Electrons and Photons, Phys. Rev. Lett. **124**, 203401 (2020).
[27] M. J. W. Boness and G. J. Schulz, Vibrational excitation in CO_2 via the 3.8-eV resonance, Phys. Rev. A **9**, 1969 (1974).
[28] S. Cvejanovic, J. Jureta, and D. Cvejanovic, Threshold Spectrum of CO_2, J. Phys. B: At. Mol. Opt. Phys. **18**, 2541 (1985).
[29] D. F. Register, H. Nishimura, and S. Trajmar, Elastic scattering and vibrational excitation of CO_2 by 4, 10, 20 and 50 eV electrons, J. Phys. B: At. Mol. Phys. **13**, 1651 (1980).
[30] D. M. Dennison, The Infra-Red Spectra of Polyatomic Molecules. Part II, Rev. Mod. Phys. **12**, 175 (1940).
[31] J. Dvořák, K. Houfek, and M. Čížek, Vibrational exci-

tation in the $e + co_2$ system: Nonlocal model of $\Sigma\Pi$ vibronic coupling through the continuum, Phys. Rev. A **105**, 062821 (2022).
[32] L. A. Morgan, Virtual States and Resonances in Electron Scattering by CO_2, Phys. Rev. Lett. **80**, 1873 (1998).
[33] W. Vanroose, C. W. McCurdy, and T. N. Rescigno, Interpretation of low-energy electron-CO_2 scattering, Phys. Rev. A **66**, 032720 (2002).
[34] T. Sommerfeld, H.-D. Meyer, and L. S. Cederbaum, Potential energy surface of the CO_2^- anion, Phys. Chem. Chem. Phys. **6**, 42 (2004).
[35] H. Köppel, W. Domcke, and L. S. Cederbaum, Theory of vibronic coupling in linear molecules, J. Chem. Phys. **74**, 2945 (1981).
[36] Z. Mašín, J. Benda, J. D. Gorfinkiel, A. G. Harvey, and J. Tennyson, UKRmol+: A suite for modelling electronic processes in molecules interacting with electrons, positrons and photons using the R-matrix method, Comput. Phys. Commun. **249**, 107092 (2020).
[37] H. van der Vorst and J. Melissen, A Petrov-Galerkin type method for solving Axk=b, where A is symmetric complex, IEEE Trans. Magn. **26**, 706 (1990).
[38] A. Chedin, The carbon dioxide molecule: Potential, spectroscopic, and molecular constants from its infrared spectrum, J. Mol. Spectrosc. **76**, 430 (1979).
[39] G. A. Gallup, Symmetry selection rules for vibrational excitation by resonant electron impact and a unified treatment of vibronic coupling between resonances and to the continuum: A complete symmetry analysis of vibrational excitation in benzene, J. Chem. Phys. **99**, 827 (1993).
[40] E. P. Wigner, On the Behavior of Cross Sections Near Thresholds, Phys. Rev. **73**, 1002 (1948).
[41] S. F. Wong and G. J. Schulz, Vibrational excitation in benzene by electron impact via resonances: Selection rules, Phys. Rev. Lett. **35**, 1429 (1975).
[42] G. A. Gallup, Selection rules for vibrational energy loss by resonant electron impact in polyatomic molecules, Phys. Rev. A **34**, 2746 (1986).
[43] R. Čurík, I. Paidarová, M. Allan, and P. Čársky, Joint experimental and theoretical study on vibrational excitation cross sections for electron collisions with diacetylene, J. Phys. Chem. A **118**, 9734 (2014).
[44] R. Čurík, P. Čársky, and M. Allan, Electron-impact vibrational excitation of cyclopropane, J. Chem. Phys. **142**, 144312 (2015).
[45] C. H. Yuen, N. Douguet, S. Fonseca dos Santos, A. E. Orel, and V. Kokoouline, Simplified model to treat the electron attachment of complex molecules: Application to H_2CN and the quest for the CN^- formation mechanism, Phys. Rev. A **99**, 032701 (2019).
[46] P. Nag, R. Čurík, M. Tarana, M. Polášek, M. Ehara, T. Sommerfeld, and J. Fedor, Resonant states in cyanogen NCCN, Phys. Chem. Chem. Phys. **22**, 23141 (2020).

Vibrational excitation in the $e + CO_2$ system: Nonlocal model of ΣΠ vibronic coupling through the continuum

Jan Dvořák,* Karel Houfek,† and Martin Čížek‡
Charles University, Faculty of Mathematics and Physics,
Institute of Theoretical Physics, V Holešovičkách 2, 180 00 Prague 8, Czech Republic

We present our model of the e+CO_2 system that has been used to calculate the two-dimensional electron energy-loss spectrum of CO_2 for incoming electron energies up to 5 eV reported in our Letter [Phys. Rev. Lett. **129**, 013401 (2022)]. We derive the effective Hamiltonian that describes the nonlocal dynamics of CO_2^- within the full vibrational space and in the presence of the $^2\Sigma_g^+$ virtual state and the Renner-Teller coupled $^2\Pi_u$ shape resonance. The electronic states are represented by three discrete states that interact directly with each other and also indirectly through the electronic continuum that consists of s and p partial waves. Based on our *ab initio* fixed-nuclei R-matrix calculations, parameters of the model are determined using a fitting procedure that utilizes the high symmetry of the system. The topology of the resulting complex potential energy surfaces is discussed. The model is constructed in such a way that the Hamiltonian expressed in a harmonic vibrational basis of the neutral molecule is a sparse matrix which enabled us to solve the multidimensional dynamics of vibrational excitation using iterative methods based on Krylov subspaces.

I. INTRODUCTION

The model of the discrete state in continuum has been used for the description of inelastic electron-molecule collisions for a long time [1]. The most natural application of the model is to narrow resonances where the finite lifetime of a compound electron-molecule state is directly related to the negative imaginary part of the potential [2]. In such cases, the model is known as the local-complex-potential (LCP) approximation or the boomerang model [3]. However, a more elaborate form of the theory with a nonlocal and energy-dependent effective potential is necessary in systems where a bound anionic state disappears in the continuum when the molecular geometry is deformed without becoming a clear resonance [4]. The importance of nonlocal effects has been recognized by Cederbaum and Domcke [5], who were also the first to solve the full nonlocal version of the dynamics for harmonic molecular potentials using the continuous fraction method [6]. Later, the nonlocal dynamics was numerically solved also for realistic *ab initio* potentials of diatomic molecules leading to a good correspondence with experimental data; see, for example, Ref. [7] and references therein.

In the application of the nonlocal approach to polyatomic molecules, we face numerous challenges including the presence of much more parameters for the construction of such models and a more difficult treatment of the dynamics. The interaction of multiple anionic states is also more often involved in polyatomics. Triatomic molecules already represent a very challenging problem, for which, however, a nearly complete solution of the dynamics may be hoped for. A large step in this direction within the LCP approximation has been done for the electron scattering from CO_2 [8, 9], H_2O (see Haxton *et al.* [10, 11] and references therein), and HCN [12, 13]. In the case of water and carbon dioxide molecules, authors even treated the nonadiabatic coupling of multiple metastable states. Although the LCP approximation correctly captures many features, its limitations in the case of the H_2O molecule have been pointed out in Ref. [11]. To the best of our knowledge only two works extend the calculations for polyatomic molecules beyond the LCP approximation and take into account more than one vibrational degree of freedom. Recently, Abalampitiya and Fabrikant [14] treated the dissociative attachment to the CF_3Cl molecule through a single discrete anionic state within the nonlocal theory with two relevant vibrational degrees of freedom. The full nonlocal vibronic dynamics of two discrete states and two vibrational modes was discussed for a model Hamiltonian by Estrada *et al.* [15]. Further generalization of this model with examples for specific molecules were discussed by Feuerbacher *et al.* [16, 17], but they focused only on static aspects of the potential energy surfaces and made no attempts to solve the dynamics.

We extend the approach of Estrada *et al.* [15] to the case of three electronic states of a linear triatomic molecule and four vibrational coordinates. We apply it to vibrational excitation of the CO_2 molecule by slow electrons. Since our work is rather extensive, we discuss it in three papers. Main results of our calculations together with new experimental data measured by our colleagues are presented in Ref. [18], where we propose our interpretation of the two-dimensional electron energy-loss spectrum of CO_2. Here, we describe the theoretical model, its construction from *ab initio* data, and a procedure how to solve the dynamics. The third paper (a follow-up to of this one) will focus on a detailed comparison and discussion of the theoretical and experimental results.

There is an extensive literature on theoretical descrip-

* Jan.Dvorak@utf.mff.cuni.cz
† Karel.Houfek@mff.cuni.cz
‡ Martin.Cizek@mff.cuni.cz

tion of vibrational excitation of the CO_2 molecule. We will review the previous works in more detail in a follow-up to this paper. Here, we would like to mention few works that affected our choice of the particular form of the model. The electron scattering off CO_2 up to about 2 eV is dominated by the $^2\Sigma_g^+$ virtual state [19–21]. For energies around 4 eV Boness and Schulz [22] observed a boomerang structure in their vibrational excitation cross sections, which they attributed to a $^2\Pi_u$ shape resonance.

The near threshold region was studied by Whitten and Lane [23] and Mazevet *et al.* [24]. Estrada and Domcke [25] performed one-dimensional (1D) calculations in symmetric stretching using the discrete-state-in-continuum model to study the effect of the virtual state. The most advanced treatment of the near threshold region so far has been the effective-range-potential model of combined excitation of symmetric stretching and bending by Vanroose *et al.* [26]. The theoretical treatment of the $^2\Pi_u$ shape resonance also involves works of different complexity. We would like to mention the 1D description of the origin of boomerang oscillations by Čadež *et al.* [27] and 2D LCP studies by Kazansky and Sergeeva [28, 29] and Rescigno *et al.* [8] who included both the symmetric stretching and bending, even based on *ab initio* fixed-nuclei data in the latter case. Finally, McCurdy *et al.* [9] improved the description even further by considering the Renner-Teller splitting of the $^2\Pi_u$ resonance.

The $^2\Sigma_g^+$ and $^2\Pi_u$ states have been treated separately in all previous theoretical works. It is well known that the potential of the ground state of CO_2^- possesses a minimum in C_{2v} geometry [30, 31] and *ab initio* calculations of Resigno *et al.* [32] indicated that the minimum is connected to the $^2\Pi_u$ shape resonance through the lower Renner-Teller component. On the other hand, R-matrix calculations of Morgan *et al.* [21, 33] showed that the virtual state becomes bound upon bending too, see also the discussion in the introduction of Vanroose *et al.* [34], who tried to provide an insight into this problem using an analytically solvable scattering model. Sommerfeld [35] reported that when a very diffuse basis is used, the potential energy of the ground state of CO_2^- behaves qualitatively differently than the earlier calculations [30, 31] had shown. The potential does not monotonically rise along the trajectory from the minimum to the autodetachment region but it drops before reaching the crossing point with the neutral potential, and then, it crosses or rather merges with the neutral potential. On top of that, Sommerfeld *et al.* [36] argued that the minimum is connected to the virtual state which mixes with the lower Renner-Teller component as the molecule bends [37]. Hence, they suggested that the low-energy scattering off CO_2 should be treated as a coupled nonlocal problem of the $^2\Sigma_g^+$ and $^2\Pi_u$ states. In this paper we present our attempt to construct such a model.

The paper is organized as follows. In Sec. II, we review basic ideas of the nonlocal model for the description of vibrational excitation by electron impact in the case of multiple interacting discrete states and several vibrational degrees of freedom. Then, we apply the approach to the $^2\Sigma_g^+$ and $^2\Pi_u$ states of CO_2^- taking into account all vibrational modes. We show how the $D_{\infty h}$ symmetry of the system restricts the model structure. Section III represents a preparation stage for the model construction from *ab initio* data. We describe there the relation of diabatic and adiabatic representations within the model and the effect of gradual lowering of the molecular symmetry on fixed-nuclei scattering quantities. In Sec. IV, we first describe our *ab initio* fixed-nuclei R-matrix calculations and then we focus on obtaining model parameters from these data using a least-squares fitting procedure. The quality and interpretation of the resulting model is discussed in Sec. V. Finally, Sec. VI is devoted to numerical details considering the evaluation of the nonlocal Hamiltonian and solution of the dynamics. We conclude in Sec. VII by summarizing the results and discussing possible future improvements of the present concept for the application to other molecular systems.

II. VIBRONIC COUPLING MODEL

The model is based on work by Estrada *et al.* [15] who generalized the original vibronic coupling model for bound states [38] to the case of short-lived states. They described a polyatomic system with two anionic discrete states of different symmetries and two vibrational degrees of freedom. The discrete states were coupled only directly through a nontotally symmetric vibrational mode since the coupling with the electronic continuum was considered independent of vibrational coordinates. Here, we extend their approach in two ways. The general vibronic coupling scheme in linear molecules as discussed by Köppel *et al.* [37] is used for the direct coupling of three discrete electronic states considering all vibrational modes of a linear triatomic molecule. Moreover, we apply the same scheme to the vibronic coupling of the discrete states with the continuum.

A. General discrete-states-in-continuum model

The key assumption of the model is that vibrational excitation of a molecule is mediated by a small number of metastable anionic discrete states that are formed by the attachment of an incoming electron to the neutral molecule. The effective Hamiltonian for the dynamics within the discrete-state space is then derived using the projection-operator formalism of Feshbach [39].

The electronic Hilbert space of the electron-molecule system is separated into a discrete-state (or resonant)[1]

[1] Since the discrete states involved in the context of electron-molecule collisions are not limited to resonances, this term caused some confusion in the past. We will mostly use the term discrete state instead of resonance.

subspace and a background continuum subspace. We define the projection operator on the discrete-state subspace by

$$\mathcal{Q} = \sum_d |d\rangle\langle d|, \tag{1}$$

where d runs over all included discrete states. The complementary operator

$$\mathcal{P} = \mathcal{I} - \mathcal{Q}, \tag{2}$$

where $\mathcal{I}$ is the identity operator, then projects on the background continuum part. The discrete states $|d\rangle$ thus form a basis in the discrete-state part of the electronic Hilbert space. The basis $|\epsilon\mu\rangle$ of the continuum part is chosen to diagonalize the fixed-nuclei electronic Hamiltonian $\mathscr{H}_{\rm el}$ projected on the background space

$$\mathcal{P}\mathscr{H}_{\rm el}\mathcal{P}|\epsilon\mu\rangle = [V_0 + \epsilon]|\epsilon\mu\rangle, \tag{3}$$

where ϵ and μ denote energy and additional quantum numbers identifying the electronic states in the continuum. As a result, $\mathscr{H}_{\rm el}$ can be formally written as the following infinite matrix

$$\mathscr{H}_{\rm el} = V_0\,\mathcal{I} + \left(\begin{array}{c|ccc} U & \multicolumn{3}{c}{V_\epsilon} \\ \hline & \ddots & & \\ V_\epsilon^\dagger & & \epsilon & \\ & & & \ddots \end{array}\right), \tag{4}$$

where V_0 is the potential energy surface of the neutral molecule, $U = \mathcal{Q}(\mathscr{H}_{\rm el} - V_0\mathcal{I})\mathcal{Q}$ is a matrix describing the discrete-state energies relative to the threshold V_0 (diagonal elements) and also the direct interaction among the discrete states (off-diagonal elements), and $V_\epsilon = \mathcal{Q}\mathscr{H}_{\rm el}\mathcal{P}$ represents the interaction of the discrete states with the electronic continuum states.

The potential energy $V_0(\vec{q}\,)$ and all matrix elements $U_{dd'}(\vec{q}\,) = \langle d|U|d'\rangle$, $V^\mu_{d\epsilon}(\vec{q}\,) = \langle d|V_\epsilon|\epsilon\mu\rangle$ depend on nuclear coordinates $\vec{q}$. The vibrational motion is included into the dynamics by adding the kinetic energy operator T_N for nuclei to $\mathscr{H}_{\rm el}$. The electronic continuum is eliminated by the projection-operator formalism of Feshbach [39], which assumes the diabaticity of the full basis $|d\rangle$, $|\epsilon\mu\rangle$. It means that all sharp features in the dependence on the molecular geometry $\vec{q}$ such as resonances or virtual states have to be eliminated from the continuum $|\epsilon\mu\rangle$ by the choice of the discrete states. As a consequence of the diabaticity, the projection operators $\mathcal{Q}$ and $\mathcal{P}$ commute with the kinetic energy operator T_N. Then, the vibrational dynamics of the electron-molecule collision process is reduced to the electronic discrete-state subspace $\mathcal{Q}$ only. For details we refer the reader to reviews [40, 41] which treat the system with only one discrete state but the generalization to more states is straightforward.

The effective Hamiltonian for the vibrational motion of the molecular anion reads

$$H = H_0\mathbb{1} + U + F(E - H_0), \tag{5}$$

where $H_0 = T_N + V_0$ is the vibrational Hamiltonian of the neutral molecule, $\mathbb{1}$ is the unit operator in the discrete-state subspace, U is the same matrix as in Eq. (4), $F(E - H_0)$ is the level-shift operator resulting from the interaction with the continuum, and E denotes total energy of the system that is conserved during the process. Throughout this paper, we reserve the symbol E only for the total energy. Electron energy will be denoted by ϵ. The elements of the level-shift operator matrix are defined by the integrals

$$F_{dd'}(E - H_0) = \sum_\mu \int V^\mu_{d\epsilon}(E - H_0 - \epsilon + i\eta)^{-1} V^{\mu^*}_{d'\epsilon}\,{\rm d}\epsilon, \tag{6}$$

where η is a positive infinitesimal. This operator is a matrix in the discrete-state indices d, d' and is also a nonlocal operator in the nuclear coordinates $\vec{q}$.

The discrete-state (resonant) contribution to the T matrix for vibrational excitation from the initial vibrational state ν_i to the final state ν_f is given by

$$T_{\nu_f\mu_f\leftarrow\nu_i\mu_i} = \langle\nu_f|V^{\mu_f\,\dagger}_{\epsilon_f}(E\mathbb{1} - H)^{-1}V^{\mu_i}_{\epsilon_i}|\nu_i\rangle, \tag{7}$$

where μ_i and μ_f denote the initial and final electron partial waves. The initial ϵ_i and final ϵ_f electron energies satisfy the conservation law

$$E = E_{\nu_i} + \epsilon_i = E_{\nu_f} + \epsilon_f \tag{8}$$

with internal vibrational energies E_{ν_i}, E_{ν_f} of the neutral molecule given by $H_0|\nu\rangle = E_\nu|\nu\rangle$. By solving the vibrational dynamics of the collision we mean the application of the matrix inversion $(E\mathbb{1} - H)^{-1}$ on the initial state. Details are given in Sec. VI, where the integral and differential cross sections obtained from the T matrix are also discussed.

B. Coordinates and states for $e + CO_2$ model

The discussion of the dynamics of the electron-molecule collision within the framework of the nonlocal model has been completely general so far. At this point we introduce details specific for the low-energy e+CO_2 collisions.

1. *Normal vibrational coordinates*

We describe nuclear configurations $\vec{q}$ of the molecule in terms of normal vibrational coordinates $\vec{q} = \{Q_i\}$. The CO_2 molecule is linear and symmetric in its equilibrium geometry. Thus, it has four vibrational modes: symmetric stretching, antisymmetric stretching and two-dimensional bending. We denote the corresponding dimensionless normal coordinates by Q_g, Q_u, Q_x and Q_y, respectively, which are defined in accordance with Witteman [42] in Appendix A. It is convenient to describe bending in terms of complex coordinates $Q_\pm = Q_x \pm iQ_y$.

Moreover, it also becomes useful to use polar bending coordinates (ρ, φ) defined by

$$Q_x = \rho\cos\varphi,\ Q_y = \rho\sin\varphi, \tag{9}$$

so that $Q_\pm = \rho e^{\pm i\varphi}$ and $\rho^2 = Q_x^2 + Q_y^2 = Q_+Q_-$.

We prefer to use normal coordinates measured in bohrs when we compare *ab initio* data with fixed-nuclei quantities obtained within the model. These coordinates are denoted by S_g, S_u, S_x, and S_y and are also defined in Appendix A. Finally, we denote the magnitude of bending by S_b which is defined by $S_b^2 = S_x^2 + S_y^2$.

2. Discrete electronic states

As discussed in the introduction, to capture the phenomena in the low-energy electron scattering with CO_2 we include both Renner-Teller components of the $^2\Pi_u$ shape resonance and the $^2\Sigma_g^+$ virtual state of CO_2^- in our discrete-state space. In the following discussion we simplify the notation and use $d \in \{\Pi_+, \Sigma, \Pi_-\}$ to identify the individual discrete states. These states are eigenstates of the projection of the electronic angular momentum operator on the molecular axis corresponding to eigenvalues $\hbar, 0, -\hbar$, respectively. Sometimes it is useful to work with real Cartesian components Π_x, Π_y, which are given by the relations $\Pi_\pm = (\Pi_x \pm i\Pi_y)/\sqrt{2}$.

Note that there is one more state of $^2\Pi_g$ symmetry in the energy window of interest, which connects to the O^- + CO dissociative attachment channel [43]. We do not consider this state for two reasons. First, it would be very difficult to include the dissociative channel in our calculation with four vibrational degrees of freedom. Second, this channel is connected through a conical intersection that is not much permeable since the magnitude of the dissociative attachment cross section [44] is at least one order of magnitude smaller then the vibrational excitation cross section even at high-energy loss [22].

3. Continuum electronic states

In general, the projection operators $\mathcal{Q}$ and $\mathcal{P}$ defined by Eqs. (1) and (2) are totally symmetric. The background scattering problem (3) is therefore solved in the same symmetry as the original neutral molecule and we can label the background continuum states according to the irreducible representations of the $D_{\infty h}$ point group.

In order to describe primary features of the e+CO_2 dynamics, we have to include at least all four components of s and p electron partial waves. The $^2\Sigma_g^+$ virtual state at the equilibrium molecular geometry is observed in fixed-nuclei eigenphases of the Σ_g^+ symmetry. This includes partial waves (l, m) for even values of l and $m = 0$. We consider only the lowest partial wave of this symmetry, $(l, m) = (0, 0)$, in our model and we denote the respective continuum states by $|\epsilon\mu\rangle$ with $\mu = s$. Similarly, the $^2\Pi_u$ shape resonance at the equilibrium geometry is observed in the Π_u symmetry, which corresponds to partial waves with odd l and $m = \pm 1$. We again limit the model to the lowest allowed l, that is $l = 1$, and the continuum states are denoted by $|\epsilon\mu\rangle$ with $\mu = p+$ and $\mu = p-$. Finally, we want to describe excitation of one quantum of asymmetric stretching, which is of the Σ_u^+ symmetry. Since the molecule is originally in the totally symmetric state, the product of representations of the incoming and outgoing electrons have to contain the Σ_u representation. The lowest partial waves allowing for this possibility is the combination of an s-wave and p_z-wave electron, i.e. $(l, m) = (1, 0)$. Therefore, we include continuum states $|\epsilon\mu\rangle$ with $\mu = p_z$ of the Σ_u^+ symmetry. To summarize, the continuum coupling matrix $V_\epsilon = \{V_{d\epsilon}^\mu\}$ is a 3×4 matrix in our model for three values of $d \in \{\Pi_+, \Sigma, \Pi_-\}$ and four values of $\mu \in \{s, p_z, p_+, p_-\}$. Once again, we also sometimes use Cartesian components p_x, p_y defined by the relations $p_\pm = (p_x \pm ip_y)/\sqrt{2}$.

C. Symmetry restrictions on U and V_ϵ matrices

Up to now, we have considered an arbitrary dependence of the U and V_ϵ matrices on the normal coordinates. At the equilibrium geometry, the CO_2 molecule has the symmetry given by the $D_{\infty h}$ point group, and therefore, the full Hamiltonian (4) and consequently also the effective Hamiltonian (5) and the matrices U and V_ϵ have to be invariant with respect to symmetry operations of the $D_{\infty h}$ group. This imposes strong restrictions on the possible dependence of individual matrix elements on the vibrational coordinates.

The discrete state Σ, symmetric stretching coordinate Q_g, and $|\epsilon s\rangle$ continuum states transform according to the Σ_g^+ representation of $D_{\infty h}$, the antisymmetric stretching coordinate Q_u and $|\epsilon p_z\rangle$ continuum states transform as Σ_u^+, and the discrete states $\Pi_\pm$, bending coordinates $Q_\pm$ and $|\epsilon p_\pm\rangle$ continuum states as Π_u. Let us denote either states or coordinates that transform according to the Σ_g^+, Σ_u^+, and Π_u representations by σ_g, σ_u, and $\pi_\pm$, respectively. The rotation C_α by an angle α around the molecular axis then gives [45]

$$C_\alpha\,\sigma_g = \sigma_g,\ \ C_\alpha\,\sigma_u = \sigma_u,\ \ C_\alpha\,\pi_\pm = e^{\pm i\alpha}\pi_\pm. \tag{10}$$

Similarly, the reflection $\sigma_{v\alpha}$ through the plane that contains the molecular axis (z axis) and is inclined by angle α with respect to the x axis acts as

$$\sigma_{v\alpha}\,\sigma_g = \sigma_g,\ \ \sigma_{v\alpha}\,\sigma_u = \sigma_u,\ \ \sigma_{v\alpha}\,\pi_\pm = e^{\pm 2i\alpha}\pi_\mp, \tag{11}$$

and finally, under the inversion i the states transform in the following way

$$\mathrm{i}\,\sigma_g = \sigma_g,\ \ \mathrm{i}\,\sigma_u = -\sigma_u,\ \ \mathrm{i}\,\pi_\pm = -\pi_\pm. \tag{12}$$

On top of that, the $D_{\infty h}$ group also contains rotations by 180° about lines that are perpendicular to the molecular

axis and improper rotations around the molecular axis, but we do not need these operations to derive the form of the U and V_ϵ matrices.

We explicitly derive the dependence of the $U_{\Pi_+\Sigma} = \langle\Pi_+|U|\Sigma\rangle$ element on the normal coordinates. Under the rotation we get

$$\mathrm{C}_\alpha(|\Pi_+\rangle U_{\Pi_+\Sigma}\langle\Sigma|) = e^{i\alpha}|\Pi_+\rangle(\mathrm{C}_\alpha\, U_{\Pi_+\Sigma})\langle\Sigma|. \quad (13)$$

To compensate the factor $\exp(i\alpha)$, the $U_{\Pi_+\Sigma}$ element has to transform as the Q_- bending coordinate, that is $U_{\Pi_+\Sigma} = \lambda_1 Q_-$ where λ_1 can be a function of Q_g, Q_u, and totally symmetric combination $Q_+Q_- = \rho^2$. Similarly, we find out that $U_{\Pi_-\Sigma} = \langle\Pi_-|U|\Sigma\rangle = \lambda_2 Q_+$. Under the reflection we have

$$\sigma_{\mathrm{v}\alpha}(|\Pi_+\rangle U_{\Pi_+\Sigma}\langle\Sigma|) = e^{-2i\alpha}|\Pi_-\rangle(\sigma_{\mathrm{v}\alpha}\, U_{\Pi_+\Sigma})\langle\Sigma|, \quad (14)$$

which leads to the following condition

$$e^{-2i\alpha}(\sigma_{\mathrm{v}\alpha}\, U_{\Pi_+\Sigma}) = U_{\Pi_-\Sigma}, \quad (15)$$

which implies $\lambda_1 = \lambda_2 \equiv \lambda$. Finally, the Q_- coordinate also compensates the sign change under the inversion

$$\mathrm{i}(|\Pi_+\rangle U_{\Pi_+\Sigma}\langle\Sigma|) = -|\Pi_+\rangle(\mathrm{i}\, U_{\Pi_+\Sigma})\langle\Sigma|, \quad (16)$$

hence, the function λ can not depend on odd powers of Q_u. In the end, we have $U_{\Pi_+\Sigma} = \lambda Q_-$ and $U_{\Pi_-\Sigma} = \lambda Q_+$, where λ is an arbitrary function of totally symmetric combinations of the normal coordinates, that is, a function of Q_g, Q_u^2, and Q_+Q_-.

By performing the symmetry analysis for the remaining elements of U, we get

$$U = \begin{array}{c} \\ \Pi_+ \\ \Sigma \\ \Pi_- \end{array} \begin{array}{c} \begin{array}{ccc} \Pi_+ & \Sigma & \Pi_- \end{array} \\ \begin{pmatrix} E_\Pi & \lambda Q_- & \xi Q_-^2 \\ \lambda Q_+ & E_\Sigma & \lambda Q_- \\ \xi Q_+^2 & \lambda Q_+ & E_\Pi \end{pmatrix} \end{array}, \quad (17)$$

where E_Π, E_Σ, λ, and ξ are in general arbitrary functions of Q_g, Q_u^2, and ρ^2. We are going to discuss a different basis for the discrete-state subspace in the next section, thus for clarity, we label the matrix rows and columns by the corresponding discrete states in Eq. (17) and in similar expressions that will follow.

The continuum coupling matrix V_ϵ depends not only on the vibrational coordinates but also on electron energy ϵ. However, the energy dependence does not change the symmetry properties and we can derive the V_ϵ elements in the same way as for U. We obtain

$$V_\epsilon = \begin{array}{c} \\ \Pi_+ \\ \Sigma \\ \Pi_- \end{array} \begin{array}{c} \begin{array}{cccc} s & p_z & p_+ & p_- \end{array} \\ \begin{pmatrix} v_{\Pi s}Q_- & v_{\Pi z}Q_-Q_\mathrm{u} & v_{\Pi p} & w_{\Pi p}Q_-^2 \\ v_{\Sigma s} & v_{\Sigma z}Q_\mathrm{u} & v_{\Sigma p}Q_+ & v_{\Sigma p}Q_- \\ v_{\Pi s}Q_+ & v_{\Pi z}Q_+Q_\mathrm{u} & w_{\Pi p}Q_+^2 & v_{\Pi p} \end{pmatrix} \end{array}, \quad (18)$$

where $v_{\Pi s}$, $v_{\Sigma s}$, $v_{\Pi z}$, $v_{\Sigma z}$, $v_{\Pi p}$, $v_{\Sigma p}$, and $w_{\Pi p}$ are again arbitrary functions of totally symmetric coordinates Q_g, Q_u^2, ρ^2 and of the energy ϵ.

The nonlocal potential matrix $F(\epsilon)$ can be obtained directly from Eq. (6). Note that when the $E - H_0$ operator is substituted for the argument of $F(\epsilon)$, a special attention has to be paid to the evaluation of the operator since the normal coordinates do not commute with H_0. We return to this problem in Sec. VI but for the discussion here and in the next section it is sufficient to consider only $F(\epsilon)$ with ϵ being a positive real number (electron energy). This level-shift potential matrix $F(\epsilon)$ enters the description of the electron scattering from the molecule with fixed positions of nuclei. Now, we can split the integral in Eq. (6) into Hermitian and anti-Hermitian components using the well-known formula $(x + i\eta)^{-1} = \mathrm{v.p.}\, x^{-1} - i\pi\delta(x)$ from theory of distributions, where v.p. is the Cauchy principal value and $\delta(x)$ is the Dirac δ distribution, and we get

$$F_{dd'}(\epsilon) = \Delta_{dd'}(\epsilon) - (i/2)\Gamma_{dd'}(\epsilon), \quad (19a)$$

$$\Gamma_{dd'}(\epsilon) = 2\pi \sum_\mu V_{d\epsilon}^\mu V_{d'\epsilon}^{\mu *}, \quad (19b)$$

$$\Delta_{dd'}(\epsilon) = \frac{\mathrm{v.p.}}{2\pi} \int \mathrm{d}x \frac{\Gamma_{dd'}(x)}{\epsilon - x}. \quad (19c)$$

Then, the nonlocal matrix F is as follows

$$F(\epsilon) = \begin{array}{c} \\ \Pi_+ \\ \Sigma \\ \Pi_- \end{array} \begin{array}{c} \begin{array}{ccc} \Pi_+ & \Sigma & \Pi_- \end{array} \\ \begin{pmatrix} F_\Pi(\epsilon) & f_{\Sigma\Pi}(\epsilon)Q_- & f_\Pi(\epsilon)Q_-^2 \\ f_{\Sigma\Pi}(\epsilon)Q_+ & F_\Sigma(\epsilon) & f_{\Sigma\Pi}(\epsilon)Q_- \\ f_\Pi(\epsilon)Q_+^2 & f_{\Sigma\Pi}(\epsilon)Q_+ & F_\Pi(\epsilon) \end{pmatrix} \end{array}, \quad (20a)$$

where imaginary parts multiplied by -2 (the widths) of the F_Π, F_Σ, $f_{\Sigma\Pi}$, and f_Π terms are given from Eq. (19b) by

$$\Gamma_\Pi = 2\pi(v_{\Pi s}^2\rho^2 + v_{\Pi z}^2\rho^2 Q_u^2 + v_{\Pi p}^2 + w_{\Pi p}^2\rho^4), \quad (20b)$$

$$\Gamma_\Sigma = 2\pi(v_{\Sigma s}^2 + v_{\Sigma z}^2 Q_u^2 + 2v_{\Sigma p}^2\rho^2), \quad (20c)$$

$$\gamma_{\Sigma\Pi} = 2\pi[v_{\Sigma s}v_{\Pi s} + v_{\Sigma z}v_{\Pi z}Q_u^2 + v_{\Sigma p}(v_{\Pi p} + w_{\Pi p}\rho^2)], \quad (20d)$$

$$\gamma_\Pi = 2\pi(v_{\Pi s}^2 + v_{\Pi z}^2 Q_u^2 + 2v_{\Pi p}w_{\Pi p}), \quad (20e)$$

and real parts are given by the Hilbert transform (19c). In formulas above we for simplicity assumed that functions $v_{d\mu}$, $w_{\Pi p}$ are real.

Before we continue to the fixed-nuclei approximation and static properties of our model, the derived Hamiltonian deserves a few comments. Potential energy surfaces of the Σ and $\Pi_\pm$ discrete states in the diabatic representation are given by $V_0 + E_\Sigma$ and $V_0 + E_\Pi$, respectively. The discrete states are shifted and broadened by the electronic continuum via the $F_\Sigma(\epsilon)$ and $F_\Pi(\epsilon)$ terms, and in addition, they directly interact with each other via off-diagonal elements of the matrix U and also indirectly

through the continuum via off-diagonal elements of $F(\epsilon)$. The mutual interaction of the discrete states vanishes not only at the equilibrium geometry, which is the consequence of the definition of the diabatic basis we work in, but also for any linear geometry because the asymmetric stretching can not change the angular momentum of the electronic states. The ξ and $f_{\Pi}(\epsilon)$ terms are responsible for the Renner-Teller splitting of the shape resonance upon bending. The λ and $f_{\Sigma\Pi}(\epsilon)$ terms cause the interaction of one Renner-Teller component with the virtual state as discussed by Sommerfeld *et al.* [36]. We also see that the continuum coupling V_ϵ (18) is consistent with our initial discussion in Sec. II B 3, that is, at the equilibrium the virtual state is coupled only to the s wave and the Π_u resonance to the p_+ and p_- (or equivalently to p_x and p_y) waves (p orbitals perpendicular to the molecular axis). However, when the molecule is bent, the Π states can interact with the s wave through the $v_{\Pi s}$ term, which as we will see is important in understanding of a rather peculiar behavior of the lower Renner-Teller state [8]. A deformation of the geometry in Q_u is necessary for the interaction with the p_z wave. The mentioned effects will become more apparent in the fixed-nuclei approximation discussed in the next section and in the discussion of the constructed model in Sec V.

III. FIXED-NUCLEI PROBLEM

We obtain the fixed-nuclei Hamiltonian $H_{\rm FN}$ by omitting the kinetic-energy operator T_N from Eq. (5)

$$H_{\rm FN} = V_0\mathbb{1} + U + F(\epsilon), \tag{21}$$

where the argument $\epsilon = E - V_0$ (electron energy) of the level-shift function F is no longer an operator. It is important to discuss the electron scattering and eigenenergies of this operator since they will be compared to *ab initio* data to fix the unknown functions E_d, λ, ξ, $v_{d\mu}$, $w_{\Pi p}$ in the model. While the whole vibronic dynamics of our problem respects the full $D_{\infty h}$ symmetry, the symmetry of the fixed-nuclei problem is lowered by deformations of the geometry. The full symmetry is preserved for deformations by pure symmetric stretch $\vec{q} = (Q_g, 0, 0, 0)$. The addition of the asymmetric stretch $\vec{q} = (Q_g, Q_u, 0, 0)$ removes the symmetry plane perpendicular to the molecular z axis and reduces the symmetry to $C_{\infty v}$, while pure bending deformations $\vec{q} = (Q_g, 0, Q_x, Q_y)$ remove the rotational axis and restricts the symmetry to C_{2v}. The molecule deformed in all directions $\vec{q} = (Q_g, Q_u, Q_x, Q_y)$ still has one nontrivial symmetry element (reflection through the molecular plane), i.e. C_s symmetry group. Depending on the geometry the matrix of the fixed-nuclei Hamiltonian (21) changes its form. As discussed above the matrix is diagonal in the linear $D_{\infty h}$ and $C_{\infty v}$ cases. The structure of the matrix is not completely general even if the molecule is bent. To see this we have to transform the discrete states to obtain a symmetry-adapted basis, which is the same for both the C_{2v} and C_s cases.

A. Transformation to symmetry-adapted basis for deformed geometries

In bent geometries the molecular plane is given by the z axis and the line pointing in the direction of the bending vector $(Q_x, Q_y, 0) \sim (\cos\varphi, \sin\varphi, 0)$. The symmetry-adapted components $\Pi_\parallel$ and $\Pi_\perp$ of the $^2\Pi_u$ resonance are obtained by rotating the Cartesian components Π_x, Π_y around the z axis by angle φ:

$$\Pi_\parallel = \cos\varphi\,\Pi_x + \sin\varphi\,\Pi_y, \tag{22a}$$

$$\Pi_\perp = -\sin\varphi\,\Pi_x + \cos\varphi\,\Pi_y. \tag{22b}$$

By expressing $\Pi_\parallel$ and $\Pi_\perp$ in terms of $\Pi_\pm$, we get

$$\Pi_\parallel = (e^{-i\varphi}\Pi_+ + e^{i\varphi}\Pi_-)/\sqrt{2}, \tag{23a}$$

$$\Pi_\perp = (e^{-i\varphi}\Pi_+ - e^{i\varphi}\Pi_-)/\sqrt{2}. \tag{23b}$$

Similarly, $(e^{-i\varphi}|\epsilon p_+\rangle \pm e^{i\varphi}|\epsilon p_-\rangle)/\sqrt{2}$ give the continuum electron partial waves $|\epsilon p_\parallel\rangle$ and $|\epsilon p_\perp\rangle$ adapted to the C_{2v} and C_s symmetries.

When $Q_u = 0$, the in-plane component $\Pi_\parallel$ transforms according to the same A_1 representation of the C_{2v} group as the Σ virtual state. On the other hand, the $\Pi_\perp$ state, which is perpendicular to the molecular plane, transforms according to the B_1 representation. Using these new basis states the Hamiltonian $H_{\rm FN}$ (21) splits into two blocks. A 2×2 block that consists of the Σ and $\Pi_\parallel$ states and a 1×1 block for the $\Pi_\perp$ state. The same structure is obtained in the general C_s case. The Σ and $\Pi_\parallel$ states transform according to the same A' representation and lead to a 2×2 block in $H_{\rm FN}$, while $\Pi_\perp$ transforms according to the A'' representation giving a 1×1 block. We performed all *ab initio* calculations discussed later in the C_s group, therefore, we use the nomenclature of the C_s group for the decoupled problems even in the C_{2v} case. The same reasoning can be applied to the 3×4 discrete-state-continuum coupling matrix V_ϵ. It splits into a 1×1 component $V_\epsilon^{A''}$ that couples the $\Pi_\perp$ state to the $p_\perp$ partial wave and a 2×3 block $V_\epsilon^{A'}$ that couples the Σ, $\Pi_\parallel$ discrete states to the s, p_z and $p_\parallel$ partial waves.

For the A'' block describing the upper Renner-Teller component we have

$$H_{A''} = V_0 + U_{A''} + F_{A''}(\epsilon) \tag{24a}$$

with

$$U_{A''} = E_\Pi - \xi\rho^2, \tag{24b}$$

$$F_{A''}(\epsilon) = F_\Pi(\epsilon) - f_\Pi(\epsilon)\rho^2. \tag{24c}$$

Alternatively, we can calculate the nonlocal potential $F_{A''}(\epsilon)$ using Eq. (19) with the coupling amplitude

$$V_\epsilon^{A''} = v_{\Pi p} - w_{\Pi p}\rho^2. \tag{25}$$

For the A' problem comprising of the virtual state interacting with the lower Renner-Teller component the Hamiltonian reads

$$H_{A'} = V_0 \mathbb{1}_2 + U_{A'} + F_{A'}(\epsilon), \tag{26a}$$

where $\mathbb{1}_2$ is the 2×2 unit matrix and

$$U_{A'} = \begin{matrix} \\ \Sigma \\ \Pi_\parallel \end{matrix} \begin{matrix} \begin{matrix} \Sigma & \Pi_\parallel \end{matrix} \\ \begin{pmatrix} E_\Sigma & \sqrt{2}\lambda\rho \\ \sqrt{2}\lambda\rho & E_\Pi + \xi\rho^2 \end{pmatrix} \end{matrix}, \tag{26b}$$

$$F_{A'}(\epsilon) = \begin{matrix} \\ \Sigma \\ \Pi_\parallel \end{matrix} \begin{matrix} \begin{matrix} \Sigma & \Pi_\parallel \end{matrix} \\ \begin{pmatrix} F_\Sigma(\epsilon) & \sqrt{2}f_{\Sigma\Pi}(\epsilon)\rho \\ \sqrt{2}f_{\Sigma\Pi}(\epsilon)\rho & F_\Pi(\epsilon) + f_\Pi(\epsilon)\rho^2 \end{pmatrix} \end{matrix}, \tag{26c}$$

In this case, the coupling amplitudes are given by

$$V_\epsilon^{A'} = \begin{matrix} \\ \Sigma \\ \Pi_\parallel \end{matrix} \begin{matrix} \begin{matrix} s & p_z & p_\parallel \end{matrix} \\ \begin{pmatrix} v_{\Sigma s} & v_{\Sigma z}Q_u & \sqrt{2}v_{\Sigma p}\rho \\ \sqrt{2}v_{\Pi s}\rho & \sqrt{2}v_{\Pi z}\rho\, Q_u & v_{\Pi p} + w_{\Pi p}\rho^2 \end{pmatrix} \end{matrix}. \tag{27}$$

The results of this section are important for the understanding of a very different behavior of the two Renner-Teller components upon bending of the CO_2 molecule [9]. Let us repeat that the originally degenerate $^2\Pi_u$ resonance splits into $^2A_1$ and $^2B_1$ states (in the nomenclature of the C_{2v} group) as the molecule bends, which are described within our model by the diabatic discrete states $\Pi_\parallel$ and $\Pi_\perp$, respectively. The $^2A_1$ state ($\Pi_\parallel$) is totally symmetric which has two consequences. First, it couples to the electronic s-wave continuum through the $v_{\Pi s}$ term in the nonlocal potential $F_\Pi(\epsilon) + f_\Pi(\epsilon)\rho^2$, see Eqs. (26c), (20b), and (20e). Second, it can also interact with the virtual state Σ either directly through λ, see Eq. (26b), or indirectly through the electronic continuum via the $f_{\Sigma\Pi}(\epsilon)$ nonlocal potential, see Eqs. (26c) and (20d). On the other hand, the $^2B_1$ ($\Pi_\perp$) state is not totally symmetric, and thus, it interacts only with the $p_\perp$ continuum in the nonlocal potential $F_\Pi(\epsilon) - f_\Pi(\epsilon)\rho^2$, see Eqs. (24c), (20b) and (20e). The low-energy dependence of the resonance width for s and p waves is fundamentally different [46] but we return to this problem in Sec. V.

In the end, we should emphasize that the splitting of the Hamiltonian into the 1×1 and 2×2 blocks occurs only in the fixed-nuclei limit. In the vibronic dynamics the change of the symmetry of the electronic states is compensated by the respective change of the symmetry of the vibrational wave function. The dynamics is truly a three-state problem. Similarly, the fixed-nuclei problem depends only on ρ and not on φ, which is hidden in the basis definition, but the dynamics takes place in the full four-dimensional vibrational space.

B. Eigenphase sums

The fixed-nuclei eigenphase sums for each irreducible representation of the symmetry group are decomposed to background and discrete-state (resonant) contributions

$$\delta(\epsilon) = \delta_{\rm bg}(\epsilon) + \delta_{\rm disc}(\epsilon). \tag{28}$$

The background is assumed to be a slowly varying function in both electron energy and nuclear coordinates.

The discrete-state term in the case of one discrete state, as we have in the A'' symmetry, is given by the generalized Breit-Wigner formula [41]

$$\delta^\mu_{\rm disc}(\epsilon) = -\arctan\left(\frac{\Gamma_\mu(\epsilon)/2}{\epsilon - U_\mu - \Delta_\mu(\epsilon)}\right) \tag{29a}$$

with

$$\Delta_\mu(\epsilon) = \mathrm{Re}[F_\mu(\epsilon)], \tag{29b}$$

$$\Gamma_\mu(\epsilon) = -2\ \mathrm{Im}[F_\mu(\epsilon)], \tag{29c}$$

where for the irreducible representation $\mu = A''$ the $U_{A''}$ and $F_{A''}$ terms are given by Eqs. (24b) and (24c). The same formula can be used for linear geometries (both $D_{\infty h}$ and $C_{\infty v}$ cases) where the operator $H_{\rm FN}$ consists only of the diagonal 1×1 blocks corresponding to Σ_g^+ and Π_u irreducible representations. In these cases we substitute $U_\mu = E_\Sigma$ and $F_\mu = F_\Sigma$ for $\mu = \Sigma_g^+$ and $U_\mu = E_\Pi$ and $F_\mu = F_\Pi$ for $\mu = \Pi_u$, see Eqs. (17) and (20).

In the case of the A' symmetry, there are two nontrivial discrete-state eigenphases. Their sum $\delta^{A'}_{\rm disc}$ can be computed using the following formula derived in Appendix B:

$$\exp[2i\delta^{A'}_{\rm disc}(\epsilon)] = \frac{(\epsilon - a^*)(\epsilon - b^*) - c^{2*}}{(\epsilon - a)(\epsilon - b) - c^2}, \tag{30}$$

where $a = \langle\Sigma|U_{A'} + F_{A'}(\epsilon)|\Sigma\rangle$, $b = \langle\Pi_\parallel|U_{A'} + F_{A'}(\epsilon)|\Pi_\parallel\rangle$, $c = \langle\Sigma|U_{A'} + F_{A'}(\epsilon)|\Pi_\parallel\rangle$.

C. Adiabatic potential energy surfaces

Up to this point we have worked in the diabatic representation. To obtain adiabatic potential energy surfaces we need to diagonalize the fixed-nuclei Hamiltonian $H_{\rm FN}$ (21). We have already partially diagonalized $H_{\rm FN}$ by transforming it to the symmetry-adapted basis, and thus, the adiabatic surface of the A'' state is directly given by Eq. (24). However, this quantity still parametrically depends on the electron energy ϵ, which has to be replaced by a function in the vibrational coordinates $\epsilon_{\rm disc}(\vec{q}\,)$. For a narrow resonance, the position of the anionic state can be determined from K-matrix poles [41, 47], however, as far as broad resonances or virtual states are concerned, the position should be defined via S-matrix poles [41], that is, by finding $\epsilon_{\rm disc} = E_R - (i/2)\Gamma_R$ as a complex selfconsistent solution of

$$\epsilon_{\rm disc} - U_\mu - \Delta_\mu(\epsilon_{\rm disc}) + (i/2)\Gamma_\mu(\epsilon_{\rm disc}) = 0 \tag{31}$$

for each geometry. Then, the adiabatic surface is

$$V^{\mu}_{\rm adiab} = V_0 + E_R - (i/2)\Gamma_R. \tag{32}$$

Not only for the A'' problem but also in linear geometries we can use the approach just described. In the case of the A' adiabatic surfaces, we have to first diagonalize the 2×2 Hamiltonian $H_{A'}$ (26). Its eigenvalues are

$$V_{\pm}(\epsilon) = V_0 + [\tilde{E}_\Sigma(\epsilon) + \tilde{E}_\Pi(\epsilon)]/2 \pm (1/2)\sqrt{[\tilde{E}_\Sigma(\epsilon) - \tilde{E}_\Pi(\epsilon)]^2 + 4\tilde{\lambda}(\epsilon)^2} \tag{33a}$$

with

$$\tilde{E}_\Sigma(\epsilon) = E_\Sigma + F_\Sigma(\epsilon), \tag{33b}$$

$$\tilde{E}_\Pi(\epsilon) = E_\Pi + F_\Pi(\epsilon) + [\xi + f_\Pi(\epsilon)]\rho^2, \tag{33c}$$

$$\tilde{\lambda}(\epsilon) = \sqrt{2}[\lambda + f_{\Sigma\Pi}(\epsilon)]\rho. \tag{33d}$$

Note that $\tilde{E}_\Sigma$, $\tilde{E}_\Pi$, and $\tilde{\lambda}$ defined above are identical with the constants a, b and c in Eq. (30). Complex solutions ϵ of $V_\pm(\epsilon) = \epsilon$ give the position of S-matrix poles since they correspond to zeros of the denominator of Eq. (30) in the complex plane.

Locating the S-matrix poles requires to analytically continue the nonlocal potential for complex-valued momenta, see Appendix B of Berman *et al.* [48]. To solve the implicit equations we used Python package CXROOTS [49] that implements methods for finding roots of complex analytical functions described by Kravanja and Barel [50]. The calculation can be simplified when we are interested only in the position of the bound anionic states. Then, the imaginary parts in formulas above vanish and we can solve the equations for real (and negative) values of $\epsilon_{\rm disc}$ by the bisection method.

IV. MODEL CONSTRUCTION FROM *AB INITIO* DATA

In this section, we determine the model parameters from *ab initio* data. Up to now, we have considered the functions that define the matrix elements of the effective Hamiltonian (5) to be arbitrary functions of totally symmetric combinations of the normal coordinates. Because computational demands of solving the four-dimensional and nonlocal vibronic dynamics are high, we had to make several simplifications which influenced the parametrization of the model functions. As we discuss in Sec. VI, by expressing the vibrational part of the anionic wave function in a suitable basis, we can rewrite the Schrödinger equation as a system of linear equations. If the Hamiltonian is represented by a sparse matrix, then the linear system can be effectively solved by iterative methods based on Krylov subspaces. By limiting the description of the neutral molecule only to the harmonic approximation, we can effectively evaluate the nonlocal potential $F(E - H_0)$ in a four-dimensional oscillator basis. Note that the evaluation of $F(E - H_0)$ is the most time-consuming step of the calculation. In addition, by restricting the model functions to low-order polynomials in the vibrational coordinates, the Hamiltonian matrix is sparse in the oscillator basis.

The harmonic approximation for the neutral molecule is rather limiting. First, it does not allow for the description of the Fermi resonance which couples nearly degenerate vibrational states of CO_2 [45]. Second, we will see that it is not sufficient for a good quantitative description of the potentials in symmetric stretching. Therefore, our goal is to study qualitative features of the multidimensional and nonlocal vibronic dynamics of the e+CO_2 system. We start the model construction by discussing our *ab initio* calculations.

A. *Ab initio* data

With the above mentioned goal of our work in mind, we approximated the ground electronic state of CO_2 only within the Hartree-Fock approximation with the cc-pVTZ basis [51]. This target description was used as a starting point for fixed-nuclei scattering calculations which were performed using the R-matrix method [52] implemented in the UKRmol+ suite of codes [53]. As a scattering model we chose a static-exchange plus polarization (SEP) model [52] in which one of target valence electrons and an incoming electron are allowed to occupy several lowest unoccupied orbitals above the highest-occupied molecular orbital which are called virtual orbitals. The number of used virtual orbitals in the final scattering SEP calculations was chosen in such a way to reproduce approximately the autodetachment region for symmetric stretch as was obtained by Sommerfeld *et al.* [36].

We tried several models with 10–20 virtual orbitals and optimal results for symmetric stretch were obtained for 18 virtual orbitals. The L^2 configurations [52] used in the final SEP model were of the type

$$({\rm core})^6({\rm valence})^{16}({\rm virtual})^1 \tag{34}$$

and

$$({\rm core})^6({\rm valence})^{15}({\rm virtual})^2. \tag{35}$$

Thus, 3 lowest (core) molecular orbitals were kept frozen and one of valence electrons from other 8 occupied orbitals was allowed to excite to one of 18 virtual orbitals to take into account polarization of the target. The R-matrix sphere radius was set to 13 bohrs which was sufficient for the SEP scattering calculations (all used target orbitals were well-contained in the R-matrix sphere). The same model was also used to calculated energies of the anionic states in the regions where these states are bound to have additional information for construction of

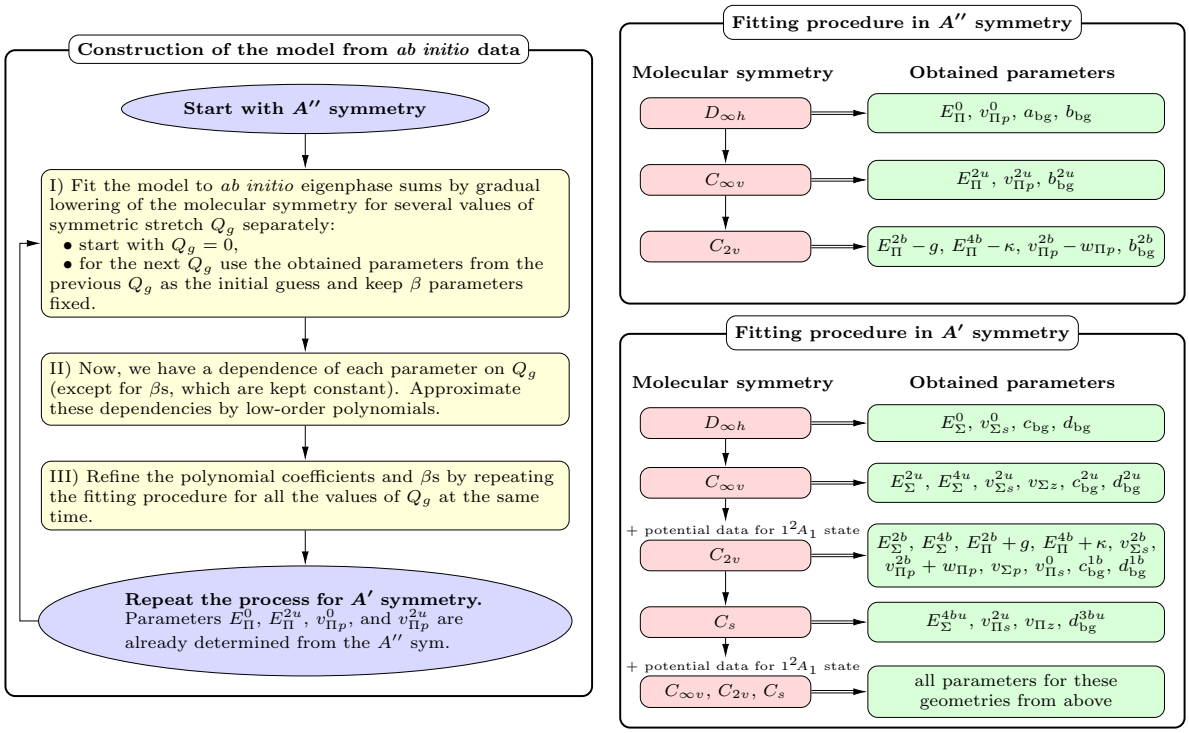

FIG. 1. Illustration of the construction of the model from *ab initio* R-matrix eigenphase sums and potential energies.

the model for the nuclear dynamics. We performed the above described fixed-nuclei calculations for more than 2000 nuclear configurations around the equilibrium geometry of CO_2 varying all three normal coordinates.

B. Parametrization of the model functions

Our model is determined if we know twelve functions V_0, E_d, λ, ξ, $v_{d\mu}$, $w_{\Pi p}$ of totally symmetric combinations of the normal coordinates, i.e. the potential energy surface of the neutral molecule and the functions entering the matrices U and V_ϵ. Considering the simplifications discussed at the beginning of this section, we use

$$V_0 = \frac{1}{2}\omega_g Q_g^2 + \frac{1}{2}\omega_b \rho^2 + \frac{1}{2}\omega_u Q_u^2, \tag{36}$$

where ω_g, ω_b, and ω_u are vibrational angular frequencies of symmetric stretching, bending and asymmetric stretching of CO_2, respectively. We specify their numerical values based on our quantum chemical calculations later. The other model functions were chosen as low-order polynomials in Q_g, Q_u^2, and ρ^2 and the number of terms in each polynomial was carefully chosen to get a reasonable agreement with the *ab initio* data. We explicitly show only the expansion of the functions into Q_u^2 and ρ^2. The remaining parameters are polynomials in Q_g up to the fourth order.

The parameters E_Π and E_Σ on the diagonal of the matrix U, see Eq. (17), are the most important. They describe the energy of the discrete states relative to the threshold V_0. Thus, we included more terms than in other cases and we have

$$E_\Pi = E^0_\Pi + E^{2b}_\Pi \rho^2 + E^{2u}_\Pi Q_u^2 + E^{4b}_\Pi \rho^4, \tag{37}$$

$$E_\Sigma = E^0_\Sigma + E^{2b}_\Sigma \rho^2 + E^{2u}_\Sigma Q_u^2 + E^{4b}_\Sigma \rho^4 + E^{4u}_\Sigma Q_u^4 + E^{4bu}_\Sigma \rho^2 Q_u^2. \tag{38}$$

In the case of the Renner-Teller coupling ξ, which is multiplied by $Q_\pm^2$ in the matrix U, we added one extra term in bending

$$\xi = g + \kappa \rho^2. \tag{39}$$

The $\Sigma\Pi$ coupling λ is assumed to be only a polynomial in Q_g.

In the case of the continuum coupling V_ϵ given by Eq. (18), we parametrized the coupling between the $\Pi_\pm$ discrete states and the $p_\pm$ partial waves in the following way

$$v_{\Pi p} = v^0_{\Pi p} + v^{2b}_{\Pi p} \rho^2 + v^{2u}_{\Pi p} Q_u^2 \tag{40}$$

and similarly for the coupling of the Σ discrete state to the s wave

$$v_{\Sigma s} = v^0_{\Sigma s} + v^{2b}_{\Sigma s} \rho^2 + v^{2u}_{\Sigma s} Q_u^2. \tag{41}$$

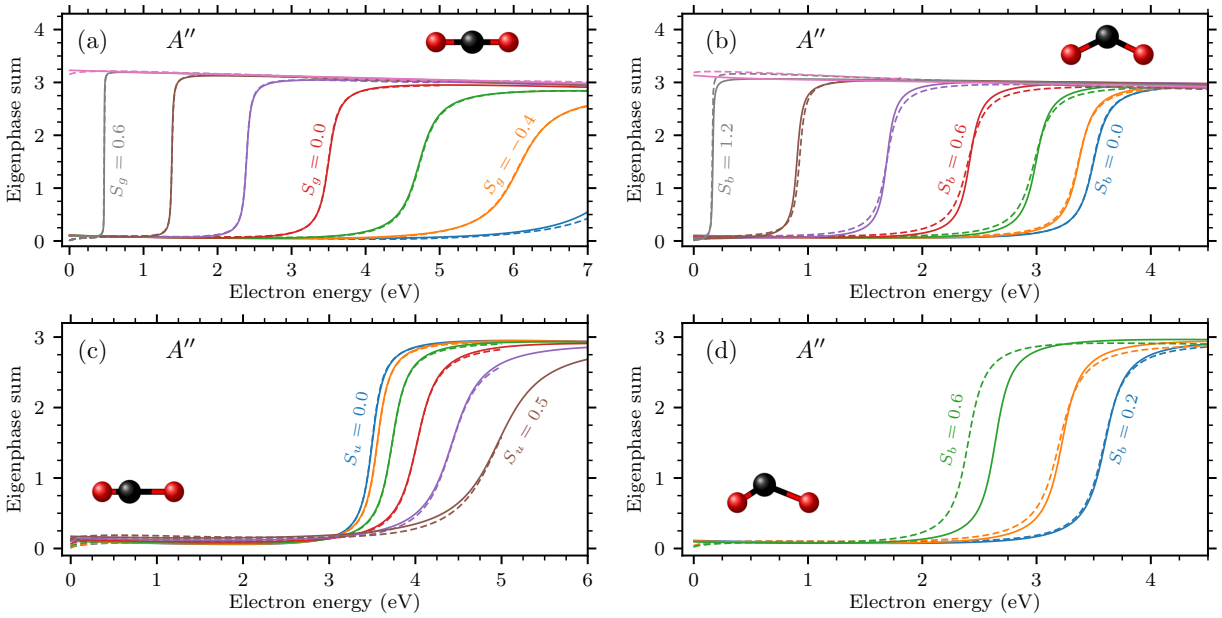

FIG. 2. Eigenphase sums in the A'' symmetry; solid lines, model; dashed lines, R-matrix data. Panel (a): symmetrically stretched geometries for $S_b = 0$, $S_u = 0$, and $S_g = -0.6$, -0.4, -0.2, 0.0, 0.2, 0.4, 0.6, and 0.8 bohrs (from right to left). Panel (b): bent geometries for $S_g = 0$, $S_u = 0$, and $S_b = 0.0$, 0.2, 0.4, 0.6, 0.8, 1.0, and 1.2 bohrs (from right to left). Panel (c): asymmetrically stretched geometries for $S_g = 0$, $S_b = 0$, and $S_u = 0.0$, 0.1, 0.2, 0.3, 0.4, and 0.5 bohrs (from left to right). Panel (d): bent and asymmetrically stretched geometries for $S_g = 0$, $S_u = 0.2$, and $S_b = 0.2$, 0.4, and 0.6 bohrs (from right to left).

We can expect that these terms are going to be the most important since only these couplings are non-zero at the equilibrium geometry and the incoming electron is captured to the CO_2 molecule in its ground vibrational state. For the coupling of the $\Pi_\pm$ states to the s wave, we used

$$v_{\Pi s} = v^0_{\Pi s} + v^{2u}_{\Pi s} Q_u^2. \tag{42}$$

The remaining terms

$$v_{\Sigma z},\ v_{\Sigma p},\ v_{\Pi z}, w_{\Pi p} \tag{43}$$

are assumed to be only polynomials in Q_g.

The continuum coupling terms depend not only on the normal coordinates but primarily on electron energy. Each coefficient in Eqs. (40)–(43) is independently parametrized by the Wigner threshold law [46] multiplied by an exponential cut-off function [41]

$$v(\epsilon) = a(\beta\epsilon)^{(2l+1)/4} e^{-\beta\epsilon}, \tag{44}$$

where $l = 0$ for the s-wave coupling, $l = 1$ for p_z or $p_\pm$ waves, a is a polynomial in Q_g, and β is a constant. Using the parametrization above, we can calculate the integral that appears in the shift operator $\Delta_{dd'}(\epsilon)$ (19c) in terms of the incomplete Gamma function and confluent hypergeometric function, see Eq. (24) in Ref. [54]. By considering the threshold exponent $(2l+1)/4$ and the β parameter constant, $v(\epsilon)$ is separable in the energy and normal coordinates which simplifies the evaluation of $F(E - H_0)$. However, a constant threshold exponent prevents the description of a geometry-dependent dipole moment [55]. The CO_2 molecule does not possess any dipole moment in its equilibrium geometry but it acquires one in bent or asymmetrically stretched geometries. This deficiency of our model may be important especially in the threshold region.

Finally, we used the following parametrization of the background eigenphase sums

$$\delta^{A''}_{\rm bg}(\epsilon) = a_{\rm bg}\epsilon + b_{\rm bg} + b^{2b}_{\rm bg}\rho^2 + b^{2u}_{\rm bg} Q_u^2, \tag{45}$$

$$\delta^{A'}_{\rm bg}(\epsilon) = (c_{\rm bg} + c^{1b}_{\rm bg}\rho + c^{2u}_{\rm bg} Q_u^2)\epsilon + d_{\rm bg} + d^{1b}_{\rm bg}\rho + d^{2u}_{\rm bg} Q_u^2 + d^{3bu}_{\rm bg}\rho\, Q_u^2 \tag{46}$$

in fitting the *ab initio* fixed nuclei data.

C. Fitting procedure

In the case of the neutral potential V_0, our original idea was to use experimental values of the vibrational frequencies, which are [56] $\omega_b^{\rm exp} = 83.3$ meV, $\omega_g^{\rm exp} = 167.5$ meV, and $\omega_u^{\rm exp} = 297.1$ meV. However, we found that the description of the neutral molecule within our R-matrix model is not ideal in comparison with the spectroscopic

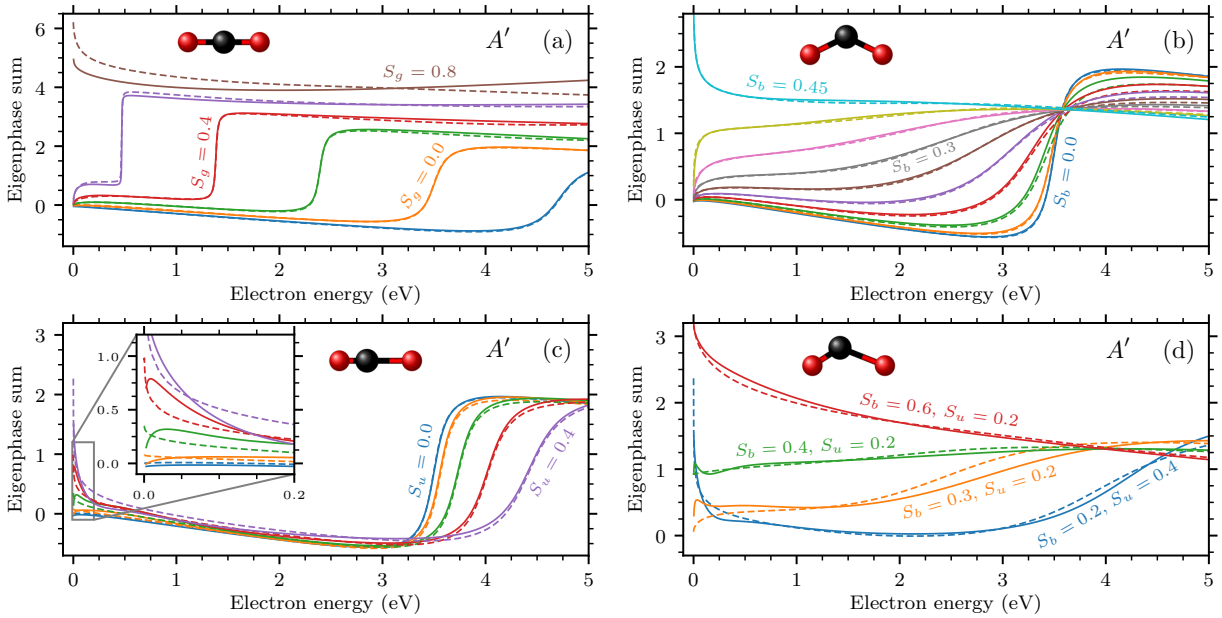

FIG. 3. Eigenphase sums in the A' symmetry; solid lines, model; dashed lines, R-matrix data. Panel (a): symmetrically stretched geometries for $S_b = 0$, $S_u = 0$, and $S_g = -0.2$, 0.0, 0.2, 0.4, 0.6, and 0.8 bohrs (from right to left). Panel (b): bent geometries for $S_g = 0$, $S_u = 0$, and for S_b from 0.0 to 0.45 bohrs with step 0.05 bohrs (from right to left). Panel (c): asymmetrically stretched geometries for $S_g = 0$, $S_b = 0$, and $S_u = 0.0$, 0.1, 0.2, 0.3, and 0.4 bohrs (from left to right). The inset shows a detail of the threshold region. Panel (d): bent and asymmetrically stretched geometries for $S_g = 0$, values of S_b and S_u are in the figure.

data. In order to have the consistent description of the potentials and eigenphase sums, we decided to determine the vibrational frequencies by fitting the quadratic form to the potential energies of the CO_2 target obtained within the R-matrix scattering calculations, see Sec. IV A. The fit of the data close to the equilibrium geometry provided $\omega_b = 110$ meV and $\omega_u = 308$ meV. The agreement on the asymmetric stretching is reasonable but the bending frequency in our model is about 30 % higher than the experimental value. In the case of the symmetric stretching we obtained 196 meV from the fit but we decided to use $\omega_g = 2\,\omega_b = 220$ meV instead to preserve the $\omega_b^{\rm exp}/\omega_g^{\rm exp}$ ratio important for the Fermi resonance [45].

We determined numerical values of the model functions E_d, λ, ξ, $v_{d\mu}$, $w_{\Pi p}$ by a least-squares fit to the *ab initio* eigenphase sums and potential energy surfaces for electron energies up to about 5 eV relative to the minimum of the neutral potential. Although the number of parameters is large, the splitting into the A' and A'' symmetries and gradual lowering of the molecular symmetry make the fitting feasible because only subsets of parameters contribute at different molecular symmetries.

The construction process illustrated in Fig. 1 has three main steps. In step I, we performed separate fits to the R-matrix eigenphase sums in the A'' symmetry for symmetric stretches $S_g \in \{0.0, \pm 0.2, \pm 0.4, 0.6\}$ bohrs. The fitting was divided into the $D_{\infty h}$, $C_{\infty v}$, and C_{2v} symmetries as it is indicated in the top right-hand part of Fig. 1, where the sequence in which the parameters are obtained is also shown. We did not consider C_s geometries in the A'' case since there are no parameters appearing exclusively in this symmetry and the prediction of the model constructed in other symmetries was good enough. For each symmetry we included the eigenphase sums for several geometries at the same time. The A'' results depend on $E^{2b}_{\Pi} - g$, that is we can not obtain values for the individual terms E^{2b}_{Π} and g. On the other hand, the A' results depend on their sum, therefore, we can obtain values of E^{2b}_{Π} and g afterwards. We dealt with E^{4b}_{Π}, κ, $v^{2b}_{\Pi p}$, and $w_{\Pi p}$ in the same way.

The result of step I is the S_g-dependence of the parameters given by series of six values. We approximated them by polynomials up to the fourth order in step II. We performed the fitting procedure from step I once again to improve the polynomial coefficients and the β parameters in step III, but this time we included data for all the values of S_g at the same moment. We did not include the position of the $^2B_1$ state where it is bound since its energy in this region is too high.

We repeated the three steps for the A' symmetry. The fitting procedure is more elaborate, see bottom right-hand part of Fig. 1, because there are two A' states. We included the R-matrix position of the $1\,^2A_1$ bound state in the fitting of the C_{2v} symmetry. We also performed a fit of C_s geometries since there are parameters that ap-

pear exclusively for these configurations in this case. The model constructed from these fits did not reproduce the eigenphase sums sufficiently well. To improve the agreement further, we performed one more fit where we varied all parameters that depend either on bending or asymmetric stretch for the $C_{\infty v}$, C_{2v}, and C_s geometries used in the previous fits.

We list the resulting values of all parameters in Appendix C. A comparison of the *ab initio* eigenphase sums of the A'' symmetry with their reproduction by our model is shown in Fig. 2 for a selected set of geometries. The moderately wide resonance corresponds to the $^2A''$ Renner-Teller component of the $^2\Pi_u$ shape resonance ($^2B_1$ in the C_{2v} nomenclature). It moves closer to the threshold and its width decreases as the molecule symmetrically stretches and it eventually becomes bound, see Fig. 2a. Although the eigenphase sums for $S_g = -0.6$ and 0.8 bohrs were not included into the fitting process, the agreement with the R-matrix data is very good even for these geometries. The resonance also becomes bound upon bending, see Fig. 2b. Note that upon change of S_b, the angle changes simultaneously with the bond length. This does not allow for the direct comparison with eigenphase sums of Morgan [21]. However, our results are in agreement with hers when recalculated for varying only the bending angle. Our model reproduces the resonance position well but there is some disagreement in its width. The width is described by the $v^{2b}_{\Pi p} - w_{\Pi p}$ parameter, which depends on ρ^2. Adding another term of the fourth order in ρ did not significantly improved the agreement and we were reluctant to increase the complexity of the model even more with regard to the feasibility of the dynamics. For asymmetric stretches the resonance moves further from the threshold, see Fig. 2c, and finally, Fig. 2d shows the data for general, both bent and asymmetrically stretched, geometries. The results shown in Fig. 2d are solely predictions of the model since the C_s geometries were not included to the fitting process.

Figure 3 shows the A' model eigenphase sums in comparison with the R-matrix data. The Renner-Teller states are degenerate for symmetrically stretched geometries, thus, the eigenphase sums exhibit the same resonance behavior as in the A'' symmetry, compare Fig. 3a with Fig. 2a. The virtual state manifests itself in the behavior near the threshold and it also becomes bound for S_g between 0.6 and 0.8 bohrs. The data for $S_g = 0.8$ bohrs were not included into the fitting procedure again, but the agreement is still reasonable. A dramatically different behavior of the A' Renner-Teller component in contrast to the A'' component is observed upon bending, see Fig. 3b. The A' state moves towards the threshold and its width is substantially increased, which agrees with Morgan [21]. For $S_b > 0.35$ bohrs the state becomes so wide that it is not observable in the eigenphases any more. Moreover, the threshold region and the resonance are not separated as for pure symmetric stretches since the states interact with each other.

For asymmetric stretches the model is not able to reproduce the low-energy behavior well, see Fig. 3c. The CO_2 molecule acquires a dipole moment which becomes supercritical for $S_u > 0.22$ bohrs. As a result, the eigenphase sums logarithmically diverge at the threshold for these geometries [57]. The threshold behavior is controlled by the threshold exponent that becomes geometry dependent [55] and vanishes at the critical value of the dipole moment. Such behavior is not reflected in our model where the threshold exponent is given by the pure s and p-wave behavior, see Eq. (44). In addition, the fact that the exponential parameters β in Eq. (44) are kept independent of the vibrational coordinates reduces the flexibility of the model as well. We expect that this model limitation will influence the low-energy behavior of the cross sections. The CO_2 molecule also acquires a dipole moment upon bending but it becomes critical for very large deviations ($S_b = 1.0$ bohrs) from the equilibrium geometries. Finally, the agreement for geometries that are simultaneously bent and asymmetrically stretched is reasonable, see Fig. 3d.

We showed only the comparison of the R-matrix and model eigenphase sums for a relatively small subset of calculated geometries. In total, R-matrix data for about 400 geometries were used to construct the model, which overall reproduces the data well.

V. DISCUSSION OF THE RESULTING MODEL

The fitting process described above is ambiguous in determination of the parameters. Since the model construction involves nonlinear least-squares fits with many parameters, we have no guarantee that the resulting parameters correspond to the global minimum of the least-squares cost function. Furthermore, the cost function itself is sensitive to the exact data set (energy and geometry ranges) included in the fitting procedure and the relative importance of different subsets of data (different symmetries, eigenphase sums versus potentials) is not clearly given. We therefore constructed a second model that reproduces the *ab initio* data with a similar accuracy as the model with the parameters listed in Appendix C. Although some parameters of the second model differ quite considerably (about up to a factor of 5), the dynamics based on these two models lead to similar electron energy-loss spectra which will be discussed in a follow-up to this paper. In what follows we discuss the properties of the first model. The behavior of the second model is qualitatively the same.

A. Adiabatic potentials

Cuts through the model adiabatic potential energy surfaces calculated from the S-matrix poles as described in Sec. III C are shown in Fig. 4. Potential energies V with a nonzero imaginary part $-\Gamma/2$ are plotted as shaded areas between $V \pm \Gamma/2$. There is no resonance width as-

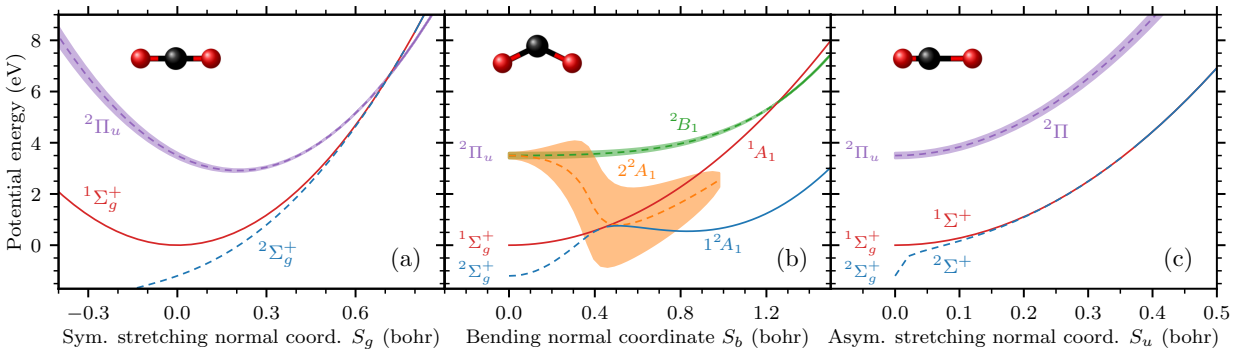

FIG. 4. Adiabatic potential energy curves of CO_2 and CO_2^- within our model; solid lines, geometries where states are bound; dashed lines, geometries where states are not bound. The shaded areas represent the resonance width of the Renner-Teller states. Panel (a): symmetric stretching geometries S_g, $S_b = 0$, $S_u = 0$. Panel (b): bending geometries S_b, $S_g = 0$, $S_u = 0$. Panel (c): asymmetric stretching geometries S_u, $S_g = 0$, $S_b = 0$.

sociated with the virtual state since the corresponding S-matrix poles are located on the negative real axis on the unphysical sheet in the energy complex plane [58]. In Fig. 4, we indicate geometries where the anionic states are not bound by dashed lines. The picture in linear geometries is rather simple since the degenerate $^2\Pi_u$ shape resonance and the Σ_g^+ virtual state do not interact with each other. The shape resonance becomes bound first at symmetric stretch $S_g = 0.7$ bohrs, which corresponds to the C–O distance $R_{CO} = 2.55$ bohrs, and the virtual state merges with the neutral potential at $S_g = 0.8$ bohrs ($R_{CO} = 2.6$ bohrs), see Fig 4a. In the case of the asymmetric stretching, the shape resonance is in the continuum for all relevant geometries, see Fig 4c. The R-matrix calculations do not show that the virtual state should become bound at any asymmetric stretch, however, it becomes very weakly bound for $S_u > 0.37$ bohrs ($R_{CO}^{(1)} < 1.83$ bohrs and $R_{CO}^{(2)} > 2.57$ bohrs) in our model. The disagreement is caused by the absence of the dipole moment induced by deformation of the molecule in our model as discussed in Sec. IV B.

The situation is very interesting upon bending of the molecule, see Fig. 4b. The upper Renner-Teller component $^2B_1$ is not much affected by the bending and it becomes bound at $S_b = 1.25$ bohrs ($R_{CO} = 2.53$ bohrs and the O–C–O angle $\angle OCO = 121°$). On the other hand, the lower component $2\,^2A_1$ quickly moves to the threshold and its width rapidly increases. The virtual state becomes bound at $S_b = 0.45$ bohrs ($R_{CO} = 2.24$ bohrs, $\angle OCO = 157°$) and posseses a minimum at $S_b = 0.83$ bohrs ($R_{CO} = 2.35$ bohrs, $\angle OCO = 139°$), which is in good agreement with Sommerfeld *et al.* [36]. The lower Renner-Teller component gets very close to the virtual state $1\,^2A_1$ and also crosses the neutral curve, however, it does not become bound. This behavior is more easily understandable in terms of the movement of the S-matrix poles shown in Fig. 5. The pole representing the virtual state is located at $k = -0.3i$ a.u. at the equilibrium geometry of CO_2, which quite differs

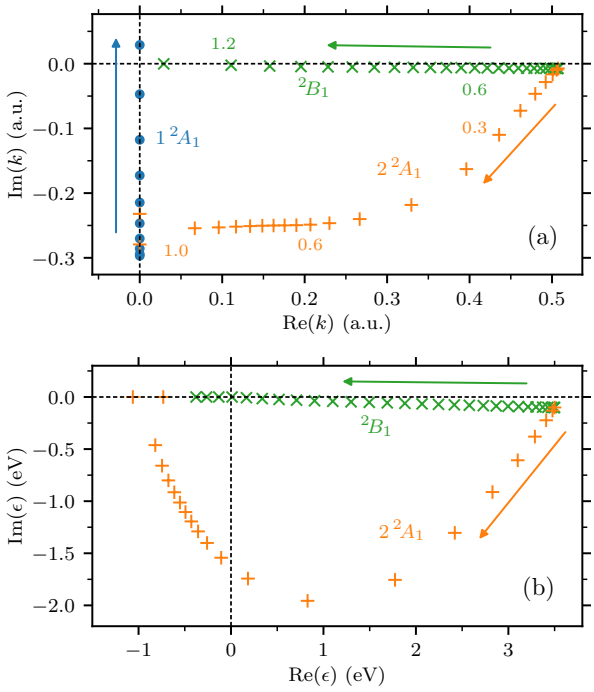

FIG. 5. Movement of S-matrix poles of the CO_2^- states in (a) momentum and (b) energy complex planes upon bending ($S_g = 0$, $S_u = 0$). The bending normal coordinate S_b increases from the equilibrium geometry in the direction of the arrows. Selected geometries S_b are labeled by the numbers. Pluses, $2\,^2A_1$ Renner-Teller state; crosses, $^2B_1$ Renner-Teller state; circles, $1\,^2A_1$ virtual state.

from values $k = -0.16i$ and $-0.2i$ reported by Morrison [19] and Morgan [21], respectively. The pole moves along the imaginary axis up as S_b increases and it becomes a bound state at $S_b = 0.45$ bohrs. The poles

representing the Renner-Teller components coincide at the equilibrium geometry at $k = (0.507 - 0.007i)$ a.u. The $^2B_1$ component moves closer to the origin and it becomes bound at $S_b = 0.7$ bohrs while the $2\,^2A_1$ component rapidly moves further away from the real axis. It gets on the imaginary axis for geometries $S_b > 1.0$ bohrs where two poles emerge. One of them moves down along the imaginary axis and the other up and becomes bound for $S_b > 1.5$ bohrs. However, the $2\,^2A_1$ state is not controlled well in the fitting procedure for $S_b \gtrsim 0.35$ bohrs because the state is so wide that it does not manifest itself in the eigenphase sums, see Fig. 3b. Therefore, we expect that the behavior for highly-bent configurations is the result of extrapolation of the model and probably is not physically relevant, see below.

When we plot the poles in the energy complex plane, see Fig. 5b, the $2\,^2A_1$ poles have a negative real part, which is measured relative to the threshold, for large values of S_b. Thus, the potential energy surface crosses the neutral surface V_0 but it does not become a true bound state. In fact, the state is so far away in the complex plane that it should not probably be called a resonance any more and its position is not well defined. For clarity, we do not show the $1\,^2A_1$ poles in Fig. 5b. They move on the negative real axis on the unphysical sheet towards the origin where they emerge on the physical sheet.

In reality, the $1\,^2A_1$ state is affected by the dipole moment acquired upon bending [59], which is not included in our model, and the corresponding pole moves along a parabolic trajectory as shown in the R-matrix calculations of Morgan [21]. Nevertheless, the avoided crossing of the $1\,^2A_1$ and $2\,^2A_1$ states within our model is in agreement with findings of Sommerfeld *et al.* [35, 36], see also our discussion in the introduction.

In Fig. 6, we compare our potentials (solid lines) with the *ab initio* model of McCurdy *et al.* [9] (dashed lines), who treated the nuclear dynamics of both the Renner-Teller components upon symmetric stretching and bending in the LCP approximation. In fact, their $2\,^2A_1$ surface was constructed in the earlier work by Rescigno *et al.* [8]. Unfortunately, they do not report their neutral potential and we suspect that there is an inconsistency in the definition of the bend angle throughout Refs. [8, 9], where potential plots state that the data are shown with respect to the bend angle $\theta = \pi - \angle\mathrm{OCO}$ but then the potential minimum corresponds to $\angle\mathrm{OCO} = 152°$ which is in a disagreement with other works [30, 31, 35, 36] which place the minimum at 135–140°. This notable difference is not discussed in Refs. [8, 9], and thus, we believe that their data are actually shown with respect to $\theta/2$ since then the minimum is at 134° and it is consistent with their definition of normal coordinates, see Sec. III in Ref. [8]. We took this into considerations when we plotted their potentials with respect to our bending normal coordinate S_b in Fig. 6. The width of the $^2B_1$ state in our model is somewhat smaller because of our imperfect fit, see Fig. 2b, but the position agrees very well. Since the model of McCurdy *et al.* [9] does not include the virtual state, the potential minimum connects to the $^2\Pi_u$ resonance but the $2\,^2A_1$ widths are in a qualitative agreement. The authors of Ref. [8] faced the same difficulties during the construction of the model from *ab initio* data as we did: the $2\,^2A_1$ state gets so wide as CO_2 bends that there are no longer any observable effects in the fixed-nuclei eigenphase sums or cross sections, see Sec. III A of Ref. [8]. They smoothly interpolated results of their fit and energies of the ground state of CO_2^-. In our case the decrease of the width is the result of extrapolation of the model beyond $S_b = 0.4$ bohrs. Although the topology of the anionic surfaces of CO_2^- is interesting, it does not seem to affect the vibrational excitation of CO_2 in the energy region of the $^2\Pi_u$ resonance (2–5 eV). Rescigno *et al.* [8] reported that the cross sections are insensitive to the interpolation of the width at highly-bent geometries since the molecular anion CO_2^- is formed by the vertical electron attachment at the equilibrium geometry of CO_2 and with high probability the anion decays before reaching highly-bent configurations. Our nonlocal calculations support this conclusion at these energies and we will discuss it more in a follow-up to this paper.

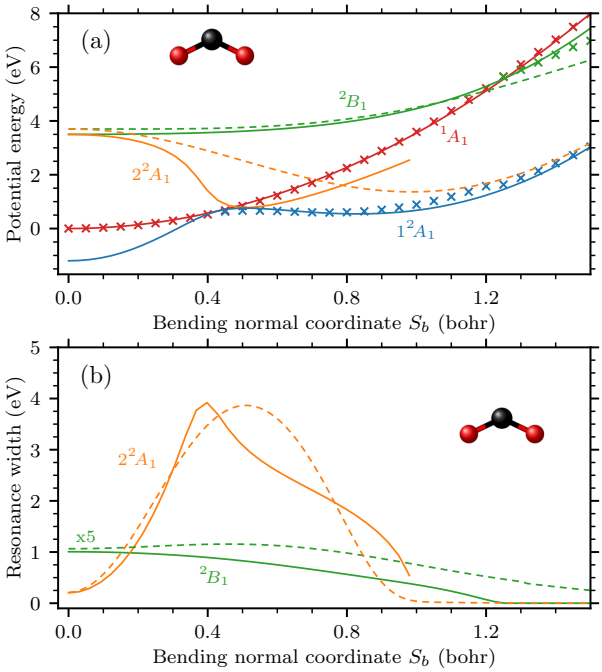

FIG. 6. (a) Real parts and (b) widths of the adiabatic potential energy curves upon bending ($S_g = 0$, $S_u = 0$) for the $1\,^2A_1$ virtual state and $2\,^2A_1$ and $^2B_1$ Renner-Teller components of the $^2\Pi_u$ resonance. Solid lines, our model; dashed lines, model of McCurdy *et al.* [9]; crosses, our R-matrix data for positions of bound states. The $^2B_1$ resonance width in Panel (b) is multiplied by factor 5.

The quantitative description of the potential energy surfaces is limited by the harmonic approximation of the neutral molecule used in order to keep the dynamics fea-

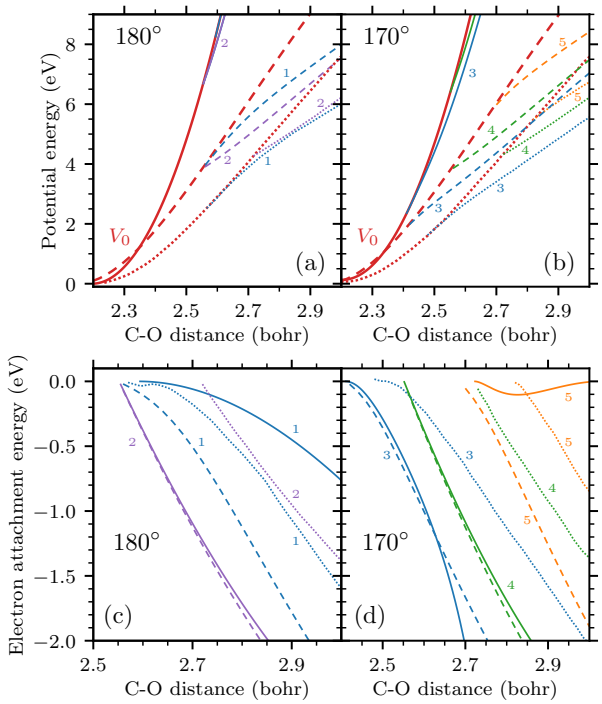

FIG. 7. Harmonic approximation to the neutral CO_2 potential and its influence on the adiabatic potential energy surfaces of CO_2^-; solid lines, our model; dashed lines, our R-matrix data; dotted lines, data of Sommerfeld *et al.* [36]. The neutral potentials are shown by thicker lines and anionic states are labeled by numbers: 1, $^2\Sigma_g^+$; 2, $^2\Pi_u$; 3, $1\,^2A_1$; 4, $^2B_1$; 5, $2\,^2A_1$. Panels (a) and (b) show cuts through the neutral and anionic surfaces for symmetric stretches with fixed O-C-O angles of 180° and 170°, respectively. Panels (c) and (d) show electron attachment energies of the anionic states for the same bond angles as above.

sible. The model reproduces the R-matrix neutral potential in the direction of pure bending very well, see Fig. 6, since we fitted the bending vibrational frequency to these data. There is a similarly good agreement for pure antisymmetric stretches. However, the agreement is rather poor in the symmetric stretching direction. The *ab initio* neutral potential is anharmonic in its shape, and futhermore, we did not use the frequency corresponding to the potential itself but we used the double of the bending frequency in this case, see Sec. IV C.

Figure 7 shows a comparison of the model potentials (solid lines) with our R-matrix data (dashed lines) and with calculations of Sommerfeld *et al.* [36] (dotted lines). When comparing these three data sets, we observe a similar behavior on the qualitative level but there are notable quantitative differences. The description of the neutral molecule at the Hartree-Fock level within our SEP scattering calculations does not fully describe the electron correlation energy and produces the bending vibrational frequency of CO_2 about 30 % larger than the experimental value, see Sec. IV C. We therefore expect that the equation-of-motion coupled-cluster potentials [36] are more accurate. For linear geometries the order of states in the R-matrix calculation is reversed ($^2\Pi_u$ state below $^2\Sigma_g$) compared to Ref. [36], but both the calculations are consistent in this respect when the molecule is bent, i.e. the anion states are bound in the order $1\,^2A_1$, $^2B_1$, $2\,^2A_1$. The harmonic approximation for V_0 causes the vertical discrepancy between the model and the R-matrix potentials but the electron attachment energy (energy difference between anionic and neutral states) agrees well for potential energies up to about 5 eV above the ground vibrational state of CO_2.

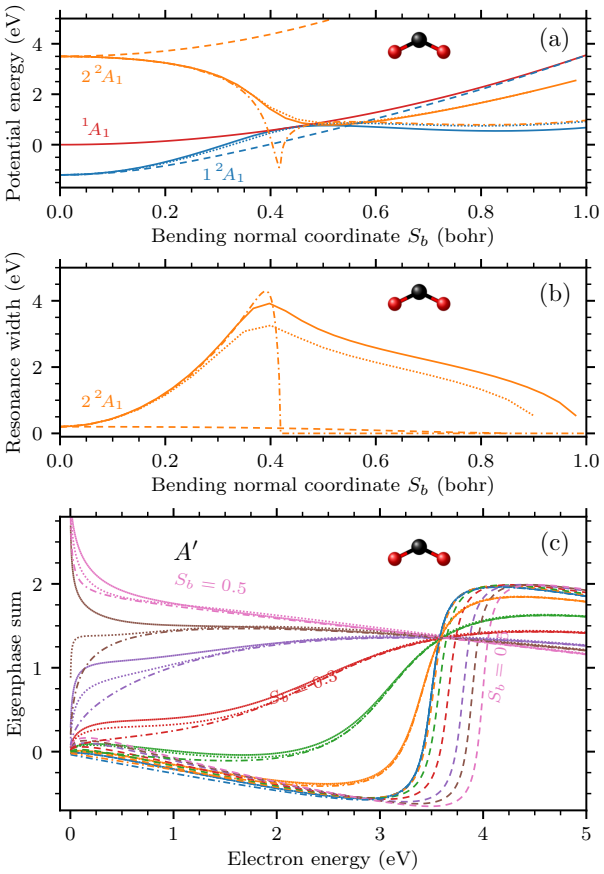

FIG. 8. Effect of model parameters describing the ΣΠ coupling on the $1\,^2A_1$ virtual state and $2\,^2A_1$ Renner-Teller component of the $^2\Pi_u$ resonance. Solid lines, full model; dotted lines, model with $\lambda = 0$; dashed lines, model with $v_{\Pi s} = 0$; dot-dashed lines, model without the Σ state (all relevant parameters are set to zero). Panels (a) and (b) show real part and width of the adiabatic potential energy surfaces upon bending ($S_g = 0$, $S_u = 0$). Panel (c) shows the A' model eigenphase sums for geometries $S_g = 0$, $S_u = 0$, $S_b = 0.0$, 0.1, 0.2, 0.3, 0.4, 0.45, and 0.5 bohrs.

B. Role of individual terms in the model

Let us now focus on examining the effect of model parameters on the behavior of the anionic states upon bending. The origin of the $1\,^2A_1$ state potential minimum at nonlinear, i.e. bent geometries (we will use the term *nonlinear minimum* below for short) is related to the square root that appears in the formula for the adiabatic surfaces in Eq. (33) since the discrete-state potentials $V_0 + E_\Sigma$ and $V_0 + E_\Pi$ do not possess any nonlinear minima. The first term in the square root depends on the Renner-Teller coupling through the ξ and $f_\Pi(\epsilon)$ functions and the second on the $\Sigma\Pi$ coupling through λ and $f_{\Sigma\Pi}(\epsilon)$. In principle both coupling mechanisms can lead to the formation of a nonlinear minimum, see also the discussion of Köppel *et al.* [37]. We found that the direct $\Sigma\Pi$ coupling given by λ has a minor effect, see Fig. 8 where dotted lines are calculated from our model but with $\lambda = 0$. The coupling of the $2\,^2A_1$ Renner-Teller state to the s wave represented by the $v_{\Pi s}$ function is responsible not only for the rapid broadening of the resonance width but also for the nonlinear minimum, see dashed lines in Fig. 8 which are calculated with $v_{\Pi s} = 0$. Finally, dot-dashed lines in Fig. 8 show results if we set all parameters related to the virtual state to zero. Even in this case the minimum does not disappear. The direct Renner-Teller term ξ affects the potential curves quite significantly, see Fig. 9, but the nonlinear minimum still exists. On the other hand, the indirect coupling through the $w_{\Pi p}$ functions is rather negligible.

To summarize, the twofold degenerate $^2\Pi_u$ resonance splits into the $2\,^2A_1$ and $^2B_1$ states upon bending of the CO_2 molecule partly due to the Renner-Teller effect but especially because of the coupling of the $2\,^2A_1$ component to the s wave. Because of this coupling the $2\,^2A_1$ state tends to become bound and connect to the nonlinear minimum but the presence of the $1\,^2A_1$ virtual state leads to the avoided crossing of the corresponding potential energy surfaces in the adiabatic representation. Nevertheless, we expect that the character of the adiabatic electronic wave functions changes along the bending coordinate. In other words, there is a diabatic electronic state that connects the $^2\Pi_u$ resonance with the nonlinear minimum.

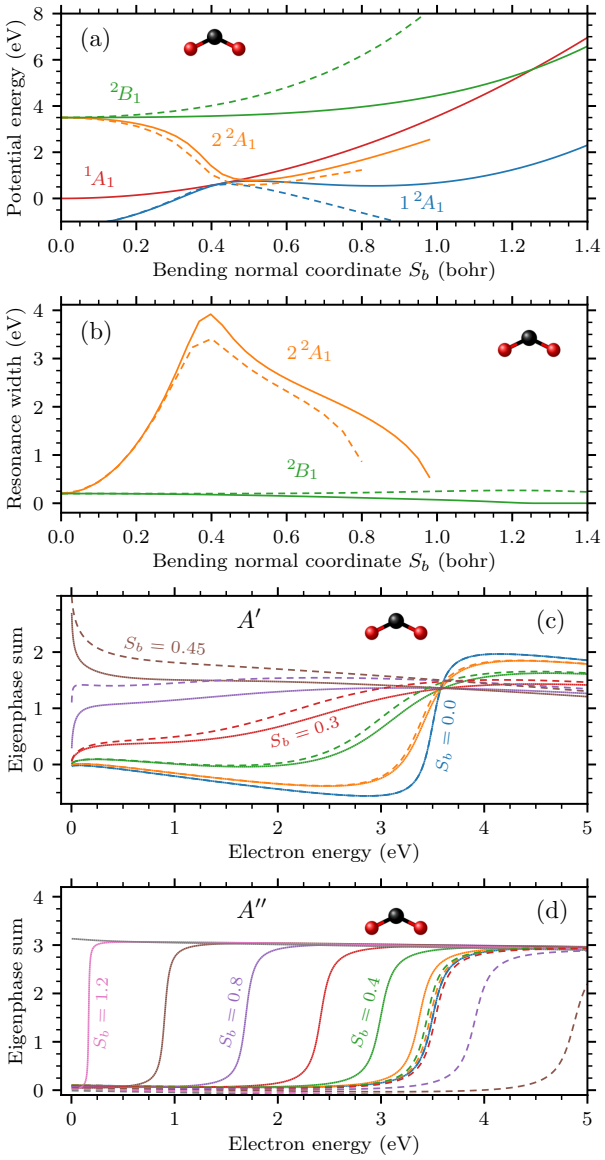

FIG. 9. Effect of the model parameter ξ describing the Renner-Teller coupling of the $^2\Pi_u$ shape resonance upon bending. Solid lines, full model; dashed lines, model with $\xi = 0$. Panels (a) and (b) show the real part and the width of the adiabatic potential energy surfaces upon bending ($S_g = 0$, $S_u = 0$). Panel (c) shows the A' model eigenphase sums for geometries $S_g = 0$, $S_u = 0$, $S_b = 0.0$, 0.1, 0.2, 0.3, 0.4, and 0.45 bohrs. Panel (d) shows the A'' model eigenphase sums for geometries $S_g = 0$, $S_u = 0$, $S_b = 0.0$, 0.2, 0.4, 0.6, 0.8, 1.0, 1.2, and 1.4 bohrs.

C. Contribution of individual partial waves

Our R-matrix calculations include electron partial waves up to $l = 4$ while the model for the dynamics takes into account only $l = 0, 1$. There are no principal obstacles to include all the partial waves into the model but it would immensely increase its complexity. By fitting the model to the full eigenphase sums we also included the information on higher partial waves into the model but the splitting of this information into partial waves is not captured correctly. We expect that this deficiency will have a small influence on the integral cross sections but it may harm the differential cross sections. To assess the possible effect of this approximation, we here discuss individual contributions of partial waves to *ab initio* K-matrices. In what follows we refer to $\arctan[K_{\mu\mu}(\epsilon)]$ where $K_{\mu\mu}$ is the diagonal K-matrix element for a partial

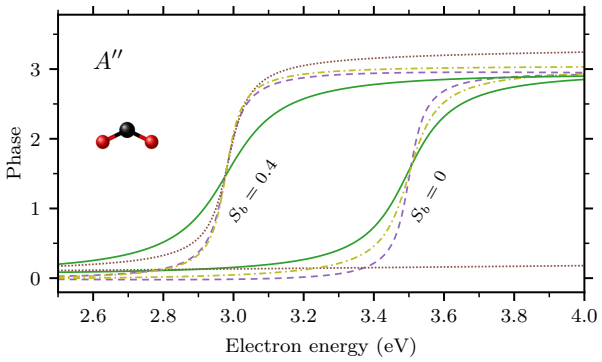

FIG. 10. Visualization of *ab initio* K-matrix elements for geometries $S_g = 0$, $S_u = 0$, $S_b = 0$ and 0.4 bohrs; solid lines, eigenphase sums; dashed lines, contribution of the $p_\perp$ partial wave; dotted lines, contribution of a d wave; dot-dashed lines, contribution of a f wave (see the text).

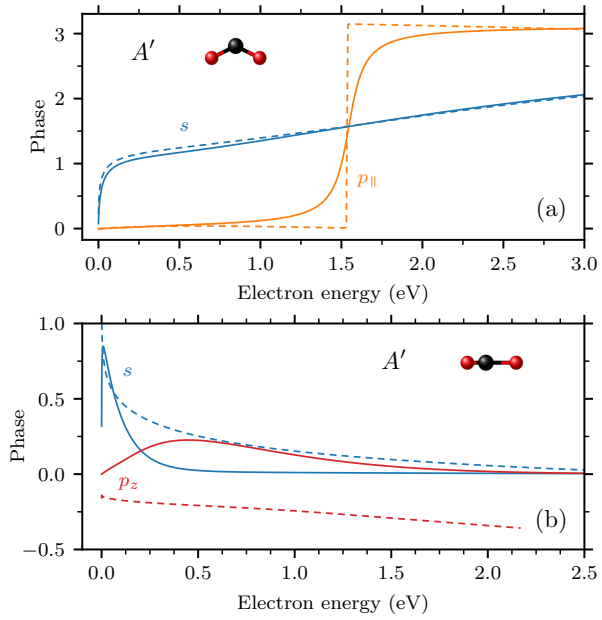

FIG. 11. Visualization of K-matrix elements; solid lines, our model; dashed lines, R-matrix data. Panel (a): s and $p_\parallel$-wave contributions for geometry $S_g = 0$, $S_u = 0$, $S_b = 0.4$ bohrs. Panel (b): s and p_z-wave contributions for geometry $S_g = 0$, $S_b = 0$, $S_u = 0.3$ bohrs.

wave μ as to partial-wave phase.

In the A'' contribution, the model K matrix has just one element $K_{p_\perp p_\perp}(\epsilon)$ since the model includes only the $\Pi_\perp$ state coupled to the $p_\perp$ electron partial wave. On the other hand, the *ab initio* K matrix contains ten contributions. The $p_\perp$ partial-wave phase dominantly contributes to the A'' *ab initio* eigenphase sums but there is also a considerable contribution of one f-wave component and for nonzero bending a d wave is involved too, see Fig. 10, which is consistent with Morgan [21].

In the A' problem, the discrete-state (resonant) K matrix within our nonlocal model is a 3×3 matrix labeled by the partial waves s, p_z, $p_\parallel$. It can be calculated using the Cayley transform [58] from the following T matrix

$$T_{A'}(\epsilon) = (V_\epsilon^{A'})^T(\epsilon - H_{A'})^{-1}V_\epsilon^{A'}, \qquad (47)$$

where $H_{A'}$ and $V_\epsilon^{A'}$ are given by Eqs. (26) and (27), respectively. Upon bending, the s wave dominates and the model partial-wave phase is in a very good agreement with the *ab initio* phase, see Fig. 11a. The discrepancy between the $p_\parallel$-wave contributions is again caused by the fact that the model effectively describes also the higher partial waves. Figure 11b shows that the s-wave again dominates the *ab initio* data in the asymmetric stretching while p_z rather contributes to the background. The model s wave is not able to describe the *ab initio* data because of the limitations in our parametrization of the model, see Sec. IV B and IV C. By fitting the model to the eigenphase sums, it is difficult to get the behavior of the p_z wave consistent with the R-matrix data because of the background-like contribution and the model p_z wave tries to compensate the s-wave behavior. Therefore, we can not expect a very good agreement of our cross sections with experimental data for asymmetric stretching.

VI. VIBRONIC DYNAMICS

The final purpose of the theoretical treatment is to obtain the cross sections that can be compared to experiments or used in simulations of the inelastic electron scattering. The differential cross section for vibrational excitation can be computed by averaging the T matrix over molecular orientations [9]

$$\frac{\mathrm{d}\sigma_{\nu_f\leftarrow\nu_i}}{\mathrm{d}\Omega}(\epsilon,\theta) = \frac{8\pi^4}{\epsilon^2}\overline{|T_{\nu_f\mathbf{k}_f\leftarrow\nu_i\mathbf{k}_i}|^2}, \qquad (48)$$

where the horizontal bar denotes the averaging and θ is a scattering angle. The T matrix $T_{\nu_f\mu_f\leftarrow\nu_i\mu_i}$ given by Eq. (7) and the T matrix $T_{\nu_f\mathbf{k}_f\leftarrow\nu_i\mathbf{k}_i}$ are related through partial-wave expansions

$$T_{\nu_f\mathbf{k}_f\leftarrow\nu_i\mathbf{k}_i} = \sum_{\mu_i,\mu_f} Y^*_{\mu_f}(\hat{\mathbf{k}}_f)T_{\nu_f\mu_f\leftarrow\nu_i\mu_i}Y_{\mu_i}(\hat{\mathbf{k}}_i), \qquad (49)$$

where $\hat{\mathbf{k}}_i$ and $\hat{\mathbf{k}}_f$ denote the directions of the incoming and outgoing electrons in the molecular frame, respectively. To calculate the cross sections we consider only the discrete-state (resonant) T matrix, that is we neglect the background contribution to all inelastic processes.

Since most experiments are conducted at room temperature where only the ground vibrational state of CO_2 is significantly populated, we consider only the ground state as the initial state ν_i in our calculations. Then, the initial state of the CO_2 molecule (including the electronic degrees of freedom) is totally symmetric which implies that the symmetry of the initial asymptotic state of

the e+CO_2 system is solely given by the symmetry of the incoming electron partial wave $\mu_i = (l_i, m_i)$. Consequently, the scattering wave function $|\Psi\rangle$, which satisfies the inhomogeneous Schrödinger equation

$$(E\mathbb{1} - H)|\Psi\rangle = V_{\epsilon_i}^{\mu_i}|\nu_i\rangle, \tag{50}$$

also has the symmetry of the incoming wave. The T matrix $T_{\nu_f\mu_f\leftarrow\nu_i\mu_i}$ given by Eq. (7), which can be written as the following integral

$$T_{\nu_f\mu_f\leftarrow\nu_i\mu_i} = \langle\nu_f|{V_{\epsilon_f}^{\mu_f}}^\dagger|\Psi\rangle, \tag{51}$$

is thus nonzero only when the product of representations of the final vibrational state ν_f and the final electron partial wave $\mu_f = (l_f, m_f)$ contains the irreducible representation of the initial partial wave, which restricts possible symmetries of the final vibrational states. Alternatively, we can determine the possible final states from conservation laws of angular momentum and parity. In our model, we take into account only rotations around the molecular axis associated with bending of the molecule. We denote the corresponding angular momentum quantum number by ℓ_b. Its values are then restricted by $m_i = m_f + \ell_b$ and we find out that vibrational states of the Σ_g^+, Σ_u^+, Π_g, Π_u, and Δ_g symmetries can be excited in our model. The resulting formulas for the differential cross sections are derived in Appendix D, where the averaging of the T matrix over molecular orientations is explicitly performed for each symmetry of the final vibrational states.

The integral cross section for vibrational excitation is obtained by integrating over the solid angle Ω

$$\sigma_{\nu_f\leftarrow\nu_i}(\epsilon) = \frac{2\pi^3}{\epsilon}\sum_{\mu_i,\mu_f}|T_{\nu_f\mu_f\leftarrow\nu_i\mu_i}|^2. \tag{52}$$

In our model, the vibrational states $|\nu_f\rangle$ are determined within the harmonic approximation (A8). However, anharmonic terms in the neutral potential of CO_2 cause a strong mixing between symmetric stretching and bending modes, the so-called Fermi resonance effect [45]. This effect is thus not included in our dynamics but can be incorporated to a good approximation by replacing the T matrix in the formulas for the cross sections by a proper linear combination of T-matrices obtained using harmonic states [8], see our Letter [18]. We will discuss this problem more in our follow-up paper.

A. Expansion of the dynamics in the oscillator basis

To obtain the T matrix given by Eq. (51) we solve the Schrödinger equation (50) for each μ_i independently with total energy E given by the conservation law (8). The vibronic wave function $|\Psi\rangle$ of the anion has three vibrational components $|\psi_d\rangle$, one for each discrete electronic states Σ and $\Pi_\pm$,

$$|\Psi\rangle = \begin{pmatrix} |\psi_{\Pi_+}\rangle \\ |\psi_\Sigma\rangle \\ |\psi_{\Pi_-}\rangle \end{pmatrix}. \tag{53}$$

Note that the dynamics reflects the full molecular symmetry group $D_{\infty h}$. The vibrational wave functions $|\psi_d\rangle$ compensate the symmetry of the discrete states so that $|\Psi\rangle$ has the total symmetry given by the incoming partial wave.

To solve the Schrödinger equation (50) we expand the components $|\psi_d\rangle$ into the four-dimensional oscillator basis that consists of eigenfunctions $|\nu_g, \nu_b, \ell_b, \nu_u\rangle$ of the neutral molecule Hamiltonian H_0 (the explicit form is given in Appendix A)

$$|\psi_d\rangle = \sum_{\nu_g,\nu_b,\ell_b,\nu_u}\psi_d(\nu_g,\nu_b,\ell_b,\nu_u)|\nu_g,\nu_b,\ell_b,\nu_u\rangle, \tag{54}$$

where $\psi_d(\nu_g, \nu_b, \ell_b, \nu_u)$ are the expansion coefficients. The basis expansion is truncated in the individual dimensions. We have $\nu_g = 0, \ldots, N_g - 1$, $\nu_u = 0, \ldots, N_u - 1$, and $\nu_b = 0, \ldots, N_b - 1$ for symmetric stretching, asymmetric stretching, and bending, respectively. The incoming electron brings utmost one quantum of the angular momentum but intermediate and final vibrational states can have up to $\ell_b = \pm 2$. For that reason, it is sufficient to consider $\ell_b = 0, \pm 1, \pm 2$.

By expressing the effective Hamiltonian H and the right-hand side $V_{\epsilon_i}^{\mu_i}|\nu_i\rangle$ in Eq. (50) in the same basis, we get a system of linear equations $Ax = b$ for x representing the unknown coefficients $\psi_d(\nu_g, \nu_b, \ell_b, \nu_u)$. Although the number $N \propto N_g N_u N_b$ of the unknowns is large (typically $\sim 10^6$, see below), the resulting matrix A is sparse due to the restriction of the model functions to low-order polynomials in the normal coordinates. Thus, the linear system is, at least in principle, solvable by iterative matrix methods. Algorithms of these methods depend only on matrix-vector multiplications, that is, the explicit knowledge of the coefficient matrix A is not necessary. Hence, we implemented only the action of the Hamiltonian (5) on the nuclear wave function $|\Psi\rangle$. The action of the first term H_0 is trivial since the basis functions are the eigenstates of H_0. The action of the second term U given by Eq. (17) can be expressed in a straightforward way if we can act with operators Q_g, Q_u, $Q_\pm$, ρ^2 on the components $|\psi_d\rangle$. The first two operators are represented by tridiagonal matrices acting only on one index ν_g or ν_u, respectively. Similarly, operators $Q_\pm$ and ρ^2 act in a simple manner only on indexes ν_b and ℓ_b. For details see Appendix A.

On the other hand, the third term $F(E - H_0)$ is an operator function of H_0 and its action via Eq. (6) deserves to be explained in more detail. The continuum coupling elements $V_{d\epsilon}^\mu$ were constructed to be separable in space and energy variables

$$V_{d\epsilon}^\mu(\vec{q}) = \mathcal{A}_d^\mu(\vec{q})\zeta_d^\mu(\epsilon), \tag{55}$$

where $\zeta_d^\mu(\epsilon) = (\beta\epsilon)^{(2l+1)/4}\exp(-\beta\epsilon)$ depends only on energy, see Eq. (44), $\mathcal{A}_d^\mu(\vec{q})$ includes the polynomial a from Eq. (44) and in some cases also $Q_\pm$ or Q_u, see Eq. (18). By substituting the separated form (55) into Eq. (19), we get

$$F_{dd'}(E-H_0) = \sum_\mu \mathcal{A}_d^\mu(\vec{q}) f_{dd'}^\mu(E-H_0)\mathcal{A}_{d'}^\mu(\vec{q}), \quad (56a)$$

where

$$f_{dd'}^\mu(E-H_0) = \text{v.p.}\int_0^\infty \mathrm{d}\epsilon \frac{\zeta_d^\mu(\epsilon)\zeta_{d'}^\mu(\epsilon)}{E-H_0-\epsilon} - i\pi\zeta_d^\mu(E-H_0)\zeta_{d'}^\mu(E-H_0). \quad (56b)$$

The order of the operators in the sum above is important since the normal coordinates do not commute with H_0. Some $V_{d\epsilon}^\mu$ terms are given by several separable terms, for example, see Eq. (40). The generalization of the formulas above for such cases is straightforward.

The $F_{dd'}(E-H_0)$ operators act on a vibrational wave function $|\psi\rangle$ in the oscillator basis in the following way

$$\langle\nu|F_{dd'}(E-H_0)|\psi\rangle = \sum_{\mu,\nu',\nu''} \langle\nu|\mathcal{A}_d^\mu|\nu''\rangle f_{dd'}^\mu(E-E_{\nu''})\langle\nu''|\mathcal{A}_{d'}^\mu|\nu'\rangle\psi(\nu'), \quad (57)$$

where ν, ν', and ν'' are multiindices $(\nu_g, \nu_b, \ell_b, \nu_u)$. The action of $F_{dd'}$ corresponds to a multiplication of a vector by three matrices. The energy matrix $f_{dd'}^\mu(E-E_{\nu''})$ is diagonal because of the harmonic approximation for the neutral molecule and the multiplication by matrices $\mathcal{A}_d^\mu$ can be decomposed to action of the coordinate operators Q_g, Q_u, $Q_\pm$ which significantly simplifies the evaluation.

In total, the action of the sparse matrix A that represents $E\mathbb{1}-H$ on a vector v requires cN operations rather then N^2 operations required for a general matrix of the same size, where c is a small number depending on the complexity of our model but independent of the basis size N.

B. Numerical solution

The matrix A representing the $E\mathbb{1}-H$ operator is complex symmetric but not Hermitian, and thus, the conjugate gradient method [60] can not be used. Instead, we used its generalization, the conjugate orthogonal conjugate gradient method (COCG), proposed by van der Vorst and Melissen [61].

The COCG method converges rather quickly for small electron energies but not even 10^5 iterations were sufficient for achieving the convergence above 2.5 eV. We found that the COCR [62], BiCG [63], and BiCGStab [64] methods exhibit a similar behavior. Finding a suitable preconditioner that improves the rate of convergence is thus necessary. Physically motivated preconditioners based on freezing some of the vibrational modes did not turn out to be viable. In the end, we came up with a rather standard preconditioner using the LU decomposition which significantly improves the rate of convergence. Let us write the matrix A in the following form

$$A = \sum_{d,d',\nu,\nu'} |\nu\rangle|d\rangle A_{d\nu,d'\nu'}\langle d'|\langle\nu'|, \quad (58)$$

where d, d' run over the discrete states, ν, ν' run over vibrational quantum numbers ν_g, ν_b, ℓ_b, and ν_u. Then, we consider only diagonal blocks in the stretching modes for the matrix P of the preconditioner

$$P = \sum_{d,d',\nu,\nu'} |\nu\rangle|d\rangle\delta_{\nu_g\nu_g'}\delta_{\nu_u\nu_u'}A_{d\nu,d'\nu'}\langle d'|\langle\nu'|. \quad (59)$$

In the other words, P is block diagonal with the blocks including the discrete-state space in combination with only the bending mode. Applying the preconditioner to a vector v corresponds to solving a linear system $Py = v$, which can be done for each block separately using the LU decomposition.

The construction of the matrix P is somewhat challenging since we have to explicitly evaluate the matrix A. The action of A on the i-th basis vector provides the i-th column of A. To act by A on all basis vectors is very time consuming, however, it can be greatly optimized when we realize the Hamiltonian spreads the nonzero basis component to only nearby components because of the polynomial structure of H. Therefore, we can act by A on a small section of basis vectors and speed up the calculation.

In total, we solved the vibrational dynamics for each incoming electron partial wave for 1500 electron energies from 0.001 eV up to 5 eV. The basis size has to be increased for larger energies since the anion can probe more of the potential energy surfaces, which is especially true in the bending dimension, see Fig. 4. The final basis sizes used are listed in Table I. The iterations were stopped when the ratio of norms of the residua and right-hand side b was smaller than a tolerance $\tau = 10^{-3}$. The convergence of the cross sections with respect to both the basis size and tolerance τ was tested. The calculations can be easily parallelized over electron energies. The calculation for 1 eV took approximately 600 seconds on one CPU core and the convergence without the precondition-

TABLE I. Basis sizes used in the dynamics for given ranges of electron energies; N_g, N_u, and N_b give the number of basis functions in symmetric stretching, asymmetric stretching, and bending, respectively; N_e is the number of calculated electron energies.

energies (eV)	N_g	N_b	N_u	N_e
$0.001-1.0$	30	60	20	500
$1.0-2.0$	30	80	20	400
$2.0-3.0$	30	100	20	300
$3.0-4.0$	35	120	25	200
$4.0-5.0$	40	140	30	100

ing was achieved after about 1000 iterations. The preconditioning was essential above 2.5 eV. For 3 eV we needed 200 iterations and an hour of computational time, and finally, 1800 iterations were necessary for 5 eV with around 9 hours of the elapsed time, from which the construction of the preconditioner took a half of the time.

VII. CONCLUSION

In this paper, we have presented our nonlocal model describing the nuclear dynamics of the vibrational excitation of the CO_2 molecule by low-energy electrons. The model includes the mutually interacting $^2\Sigma_g^+$ virtual state and the Renner-Teller coupled $^2\Pi_u$ shape resonance of the CO_2^- in combination with all four vibrational modes. The general form of the direct discrete-state coupling matrix and discrete-state-continuum coupling matrix resulting from the $D_{\infty h}$ symmetry group has been derived. The construction of the model from our R-matrix eigenphase sums and potential energies has been described in detail. Although the model contains a large number of parameters, the symmetry considerations significantly simplify the fitting process. We have shown that the explicit inclusion of the coupling of the lower Renner-Teller component to the electronic s-wave continuum explains the peculiar behavior of this state. Moreover, we have discussed the origin of the nonlinear potential minimum of the ground state of CO_2^-. We have proposed the numerical treatment of the dynamics based on preconditioned Krylov subspace methods suitable for a large class of nonlocal discrete-state-in-continuum models and we have demonstrated its feasibility for the four-dimensional dynamics within the present model.

In order to be able to solve the multidimensional dynamics, we have made several approximations. Most notably, we have used only the harmonic approximation for the neutral molecule (description of the molecular anion includes anharmonic terms) and constant threshold exponents, which prevent the description of a geometry-dependent dipole moment. Despite the fact that the harmonic approximation leads to a quantitative disagreement between the model and *ab initio* potentials in the symmetric stretching vibrational mode, the model captures primary features of the system and provides an interpretation of unexplained observations in the electron scattering off CO_2, see the outlined discussion in our Letter [18]. In our follow-up to this paper, we will extend the discussion of our results and their comparison with experimental data including also effects of model parameters described here.

The application of the present theoretical treatment to other polyatomic systems is rather straightforward. The model structure is the consequence of the symmetry of the involved discrete electronic states and vibrational modes, and the dynamics allows excitation of nontotally symmetric vibrations. Such vibrations have been known to be excited by resonant processes for a long time, at least since measurements of Wong and Schulz [65], who also formulated selection rules based on symmetry considerations. These rules were later thoroughly discussed by Gallup [66, 67] but actual dynamical calculations are scarce. Čurík *et al.* [68, 69] studied vibrational excitation of diacetylene and cyclopropane molecules using the *ab initio* discrete momentum representation method and they even reported breaking of the selection rules in the case of the cyclopropane. We thus hope that the presented approach can bring additional insight into the multimode vibronic dynamics and explain spectra of other polyatomic systems. However, the model construction from *ab initio* data and solution of the dynamics remain to be challenging.

Several improvements of the model are possible. First, the approximations we have made can be lifted at the cost of a more complicated evaluation of the nonlocal potential $F(E - H_0)$. In the case of a geometry-dependent dipole, the Bateman approximation [70] has been successfully used to simplify the nonlocal dynamics [55, 71]. Second, our model does not allow for the description of the dissociative electron attachment process. The form of discrete-state potentials based on polynomials in vibrational coordinates, which is essential for producing the sparse linear system for the dynamics, prevents straightforward implementation of a dissociative attachment channel. On the other hand, the incorporation of at least one dissociative channel is desirable for future development of the present approach.

ACKNOWLEDGMENTS

We gratefully acknowledge the financial support provided by the Czech Science Foundation under project No. 19-20524S and by the Charles University Grant Agency, Project No. 552120.

Appendix A: Vibrational coordinates and harmonic oscillator basis

Here, we define normal coordinates S_g, S_u, S_x, and S_y of symmetric stretching, antisymmetric stretching, and two-dimensional bending, respectively. We used Witteman's definition [42] with one minor modification. We changed the sign of S_g so that positive values correspond to the lengthening of the C-O bond and not to its shortening. The molecular axis at the equilibrium geometry coincides with the z axis with the carbon atom being at the origin. The Cartesian coordinates of the atoms expressed in terms of the normal coordinates are

$$\vec{R}_{\rm C} \equiv (x_{\rm C}, y_{\rm C}, z_{\rm C}) = -\frac{2m_{\rm O}}{M}\,(S_x, S_y, S_u)\,, \qquad \text{(A1)}$$

$$\vec{R}_{\rm O1} = \left[\frac{S_g}{2} + R_{\rm CO}\right](0, 0, -1) + \frac{m_{\rm C}}{M}\,(S_x, S_y, S_u)\,, \quad \text{(A2)}$$

$$\vec{R}_{O2} = \left[\frac{S_g}{2} + R_{CO}\right](0,0,1) + \frac{m_C}{M}(S_x, S_y, S_u), \quad \text{(A3)}$$

where $m_C = 21874.66$ m$_e$ is the mass of the carbon atom in the electron mass, $m_O = 29156.95$ m$_e$ is the oxygen mass, $M = m_C + 2m_O$ is the total mass of CO_2, and $R_{CO} = 2.1961$ bohr is the experimental equilibrium distance of the carbon-oxygen bond. The dimensionless normal coordinates are given by [42]

$$Q_g = \sqrt{\frac{\mu_1\omega_g}{\hbar}}S_g, \; Q_u = \sqrt{\frac{\mu_2\omega_u}{\hbar}}S_u, \quad \text{(A4)}$$

$$Q_x = \sqrt{\frac{\mu_2\omega_b}{\hbar}}S_x, \; Q_y = \sqrt{\frac{\mu_2\omega_b}{\hbar}}S_y, \quad \text{(A5)}$$

where ω_g, ω_u, and ω_b are the angular frequencies of the symmetric stretching, antisymmetric stretching and bending, respectively, $\mu_1 = m_O/2$, and $\mu_2 = 2m_Om_C/M$.

The neutral molecule Hamiltonian in the harmonic approximation is then written as $H_0 = T_N + V_0$ with

$$\begin{aligned} T_N &= -\frac{1}{2}\omega_g\frac{\partial^2}{\partial Q_g^2} - \frac{1}{2}\omega_u\frac{\partial^2}{\partial Q_u^2} \\ &\quad -\frac{1}{2}\omega_b\left(\frac{\partial^2}{\partial\rho^2} + \frac{1}{\rho}\frac{\partial}{\partial\rho} + \frac{1}{\rho^2}\frac{\partial^2}{\partial\varphi^2}\right), \quad \text{(A6a)} \\ V_0 &= \frac{1}{2}\omega_g Q_g^2 + \frac{1}{2}\omega_b\rho^2 + \frac{1}{2}\omega_u Q_u^2, \quad \text{(A6b)} \end{aligned}$$

where cylindrical coordinates ρ and φ are defined in Eq. (9).

To solve the vibronic dynamics we expand each discrete-state component $\psi_d(\vec{q}\,)$ in the basis of vibrational eigenfunctions of the neutral molecule, see Eq. (54), and implement the action of the Hamiltonian (5) on the expansion coefficients. The basis is thus defined by relation $H_0|\nu\rangle = E_\nu|\nu\rangle$ with

$$E_\nu = \omega_g(\nu_g + 1/2) + \omega_b(\nu_b + 1) + \omega_u(\nu_u + 1/2), \quad \text{(A7)}$$

where we use a shorthand notation $\nu \equiv (\nu_g, \nu_b, \ell_b, \nu_u)$. The basis wave functions $\langle\vec{q}\,|\nu\rangle$ are given by the product of wave functions of one-dimensional harmonic oscillators in the stretching modes and two-dimensional harmonic oscillator in the bending motion which read in x-representation [72]

$$\langle\vec{q}\,|\nu_g, \nu_b, \ell_b, \nu_u\rangle = \phi_{\nu_g}(Q_g)\Phi_{\nu_b\ell_b}(\rho,\varphi)\phi_{\nu_u}(Q_u) \quad \text{(A8a)}$$

with

$$\phi_n(q) = \left(\sqrt{2^n n!\sqrt{\pi}}\right)^{-1} H_n(q)e^{-q^2/2}, \quad \text{(A8b)}$$

$$\Phi_{n\ell}(\rho,\varphi) = \frac{1}{\sqrt{2\pi}}\sqrt{\frac{2n_r!}{(n_r+|\ell|)!}}\rho^{|\ell|}L_{n_r}^{|\ell|}(\rho^2)e^{i\ell\varphi}e^{-\rho^2/2}, \quad \text{(A8c)}$$

where $n = \nu_g$ or ν_u, $q = Q_g$ or Q_u, $H_n(q)$ are the Hermite polynomials, $L_{n_r}^{|\ell|}(\rho^2)$ are the generalized Laguerre polynomials, $n_r = \frac{1}{2}(n - |\ell|)$, and $\ell = -n, -n+2, \ldots, n$.

For evaluation of the action of operators U and F we need to act with operators of the normal coordinates Q_g, Q_u, and $Q_\pm$ on the wave functions. The coordinates Q_g and Q_u are represented in the one-dimensional oscillator basis by the well-known matrix

$$\langle n'|Q_{g,u}|n\rangle = \left(\sqrt{n}\,\delta_{n'n-1} + \sqrt{n+1}\,\delta_{n'n+1}\right)/\sqrt{2}, \quad \text{(A9)}$$

where $n = \nu_g$ and ν_u, respectively. For the coordinates $Q_\pm$ and $\rho^2 = Q_+Q_-$, we have in the two-dimensional basis [37]

$$\begin{aligned} \langle n', \ell'|Q_\pm|n, \ell\rangle &= \pm\frac{1}{\sqrt{2}}\delta_{\ell'\ell\pm1}s_\pm(\ell) \times \\ &\left[\sqrt{n\pm\ell+2}\,\delta_{n'n+1} - \sqrt{n\mp\ell}\,\delta_{n'n-1}\right], \quad \text{(A10)} \end{aligned}$$

where

$$s_+(\ell) = \begin{cases} +1 & \text{for } \ell \geq 0 \\ -1 & \text{for } \ell < 0 \end{cases}, \; s_-(\ell) = \begin{cases} +1 & \text{for } \ell > 0 \\ -1 & \text{for } \ell \leq 0 \end{cases}, \quad \text{(A11)}$$

$$\begin{aligned} \langle n', \ell'|\rho^2|n, \ell\rangle &= \delta_{\ell'\ell}(n+1)\,\delta_{n'n} - \tfrac{1}{2}\delta_{\ell'\ell} \times \\ &\left[\sqrt{n^2-\ell^2}\,\delta_{n'n-2} + \sqrt{(n+2)^2-\ell^2}\,\delta_{n'n+2}\right] \quad \text{(A12)} \end{aligned}$$

The formulas above can be derived using creation and annihilation operators for right and left circular quanta [72]. Higher powers of the coordinates are obtained in terms of matrix multiplication.

Appendix B: Eigenphase sum for two-state problem

Let us consider two discrete states that belong to the same irreducible representation of a molecular point group and are coupled to an arbitrary number of electron partial waves. In general, the fixed-nuclei Hamiltonian within the discrete-states-in-continuum model then reads

$$H = U + F(\epsilon) = \begin{pmatrix} U_{11} + F_{11}(\epsilon) & U_{12} + F_{12}(\epsilon) \\ U_{12} + F_{12}(\epsilon) & U_{22} + F_{22}(\epsilon) \end{pmatrix}, \quad \text{(B1)}$$

where $F_{dd'}(\epsilon)$ are calculated analogically to Eq. (6). Note that we shifted the Hamiltonian with respect to, for example, Eq. (26) by subtracting V_0 so that it corresponds to the electron energy $\epsilon = E - V_0$ relative to threshold at given geometry. The fixed-nuclei T-matrix element for incoming μ_i and outgoing μ_f partial waves is given by

$$T_{\mu_f\leftarrow\mu_i} = \sum_{d,d'=1}^{2} V_{d\epsilon_f}^{\mu_f *}\left(\epsilon\mathbb{1}_2 - H\right)^{-1}_{dd'} V_{d'\epsilon_i}^{\mu_i}. \quad \text{(B2)}$$

We observe that T matrix is a rank-two operator in the space of partial waves μ. By denoting the vector of $V_{d\epsilon}^{\mu}$

amplitudes in the partial wave index μ by $|v_d\rangle$, we can write the S matrix in the form

$$S = \mathcal{I} - 2\pi i \sum_{d,d'=1}^{2} |v_d\rangle \left(\epsilon \mathbb{1}_2 - H\right)^{-1}_{dd'} \langle v_{d'}|, \tag{B3}$$

which implies that the S matrix has only two nontrivial eigenvalues $s = e^{2i\delta} \neq 1$, that is, there are only two nontrivial eigenphases $\delta \neq 0$. Thus, we can write eigenvectors as a linear combination of vectors $|v_d\rangle$, $|s\rangle = \sum_d c_d |v_d\rangle$. By projecting $\langle v_d|$ on the eigenproblem

$$S|s\rangle = s|s\rangle, \tag{B4}$$

we get the following equation for the coefficients c_d

$$\sum_{d'=1}^{2} \left(\tilde{S}_{dd'} - s\Gamma_{dd'}\right) c_{d'} = 0, \tag{B5}$$

where $\Gamma_{dd'} = -2\,\mathrm{Im}\, F_{dd'} = 2\pi \sum_\mu V^\mu_{d\epsilon} V^\mu_{d'\epsilon} = 2\pi \langle v_d | v_{d'}\rangle$ and (after some algebraic manipulations and realization that $H_{dp} + i\Gamma_{dp} = H^*_{dp}$)

$$\tilde{S}_{dd'} = \sum_{p,q=1}^{2} \left(\epsilon\delta_{dp} - H^*_{dp}\right) \left(\epsilon \mathbb{1}_2 - H\right)^{-1}_{pq} \Gamma_{qd'}. \tag{B6}$$

The condition for the existence of a nontrivial solution of Eq. (B5) is

$$\det(\tilde{S} - s\Gamma) = 0, \tag{B7}$$

which leads to a quadratic equation for the eigenvalues s_1 and s_2 and we can obtain the eigenphase sum $\delta_1 + \delta_2$ from the constant coefficient of the quadratic equation

$$s_1 s_2 = e^{2i(\delta_1+\delta_2)} = \frac{(\epsilon - H^*_{11})(\epsilon - H^*_{22}) - (H^*_{12})^2}{(\epsilon - H_{11})(\epsilon - H_{22}) - H^2_{12}}, \tag{B8}$$

which is equivalent to Eq. (30).

Appendix C: Model parameters

Here, we list numerical values of the model parameters obtained from our fitting of the model to the R-matrix data. The parameter values of the matrix U, which is given by Eqs. (17), (37), (38), and (39), are listed in Table II.

The continuum-coupling matrix V_ϵ is given by Eqs. (18), (40), (41), and (42) and the parameters are of the form $v(\epsilon)$ (44). Actually, the parameter $v^{2b}_{\Pi p}$ that appears in Eq. (40) is given by the sum of two terms $v(\epsilon)$, $v^{2b}_{\Pi p} = v^{2b1}_{\Pi p} + v^{2b2}_{\Pi p}$, and similarly, $w_{\Pi p}$ in Eq. (18) is given by $w_{\Pi p} = w^1_{\Pi p} + w^2_{\Pi p}$. The reason is the following. The model was constructed in the A'' and A' symmetries which depend on $v^{2b}_{\Pi p} - w_{\Pi p}$ and $v^{2b}_{\Pi p} + w_{\Pi p}$, respectively. These terms were independently parametrized by functions of the form $v(\epsilon)$. Thus, when we express $v^{2b}_{\Pi p}$ and $w_{\Pi p}$, we get two $v(\epsilon)$ terms. The obtained parameter values of the V_ϵ matrix are listed in Table III.

Finally, the parameter values of the background eigenphase sums, which are given by Eqs. (45) and (46), are listed in Table IV.

Appendix D: Differential cross sections

The differential cross section for vibrational excitation of a molecule from the initial vibrational state ν_i to final state ν_f by an electron with the initial $\mathbf{k}_i$ and final $\mathbf{k}_f$ momenta is given by averaging the T matrix over molecular orientations [9]

$$\frac{\mathrm{d}\sigma_{\nu_f \leftarrow \nu_i}}{\mathrm{d}\Omega}(\epsilon, \theta) = \frac{8\pi^4}{\epsilon^2} \overline{|T_{\nu_f \mathbf{k}_f \leftarrow \nu_i \mathbf{k}_i}|^2}, \tag{D1}$$

where the discrete-state (resonant) contribution to the T matrix within the nonlocal model reads [15]

$$T_{\nu_f \mathbf{k}_f \leftarrow \nu_i \mathbf{k}_i} = \langle \nu_f | V^\dagger_{\mathbf{k}_f} (E\mathbb{1} - H)^{-1} V_{\mathbf{k}_i} | \nu_i \rangle. \tag{D2}$$

The discrete-state-continuum coupling $V_{\mathbf{k}}$ is a vector in the discrete-state index d. By expanding its elements into partial waves $\mu = (l, m)$

$$V_{d\mathbf{k}} = \sum_\mu V^\mu_{d\epsilon} Y_\mu(\hat{\mathbf{k}}), \tag{D3}$$

we get

$$T_{\nu_f \mathbf{k_f} \leftarrow \nu_i \mathbf{k_i}} = \sum_{\mu_i, \mu_f} Y^*_{\mu_f}(\hat{\mathbf{k}}_f) T_{\nu_f \mu_f \leftarrow \nu_i \mu_i} Y_{\mu_i}(\hat{\mathbf{k}}_i) \tag{D4}$$

TABLE II. Obtained values of the parameters of the matrix U. The parameters are polynomials $\sum_{i=0}^{4} c_i Q_g^i$ in the symmetric stretching normal coordinate Q_g. The notation $x(y)$ means $x \times 10^y$ and values are in the hartree unit of energy E_h.

	c_0 (E_h)	c_1 (E_h)	c_2 (E_h)	c_3 (E_h)	c_4 (E_h)
E_Π^0	0.13229(0)	−0.20130(−1)	0.40310(−3)	0	0
E_Π^{2b}	−0.37108(−3)	0.39684(−3)	0.23170(−4)	0	0
E_Π^{2u}	0.12675(−2)	−0.31060(−5)	0.22870(−6)	0	0
E_Π^{4b}	0.17624(−4)	0.12929(−4)	0.42013(−5)	0	0
E_Σ^0	0.40000(0)	0	0	0	0
E_Σ^{2b}	0.88740(−2)	−0.22622(−2)	0.75278(−3)	−0.18248(−3)	0.14277(−4)
E_Σ^{2u}	0.46670(−1)	−0.66847(−2)	0.19314(−3)	−0.17239(−3)	0.15079(−4)
E_Σ^{4b}	−0.31629(−4)	0.11550(−4)	−0.86640(−6)	0	0
E_Σ^{4u}	0.19697(−2)	−0.67839(−3)	0.62488(−4)	0	0
E_Σ^{4bu}	0.39880(−2)	−0.44038(−5)	−0.42582(−4)	0	0
λ	−0.77277(−2)	−0.80054(−5)	−0.59084(−3)	0	0
g	0.14523(−2)	0.28492(−3)	0.23170(−4)	0	0
κ	0.12134(−4)	0.13003(−4)	0.42013(−5)	0	0

TABLE III. Obtained values of the parameters of the continuum-coupling matrix V_ϵ. The parameters has the form of Eq. (44) with the parameter a being a polynomial $\sum_{i=0}^{2} c_i Q_g^i$ in the symmetric stretching normal coordinate Q_g. The notation $x(y)$ means $x \times 10^y$ and E_h is the hartree unit of energy.

	c_0 ($E_h^{1/2}$)	c_1 ($E_h^{1/2}$)	c_2 ($E_h^{1/2}$)	l	β (E_h^{-1})
$v_{\Sigma s}^0$	0.15505(0)	0.40072(−1)	0.88177(−3)	0	0.14586(2)
$v_{\Sigma s}^{2b}$	0.86210(−2)	−0.25939(−2)	0.17858(−3)	0	0.28841(2)
$v_{\Sigma s}^{2u}$	0.50983(−1)	−0.85719(−2)	0.17197(−3)	0	0.20000(3)
$v_{\Pi s}^0$ [a]	0.62981(−1)	0.27292(−2)	−0.18793(−3)	0	0.88654(0)
$v_{\Pi s}^{2u}$	−0.24927(−3)	0.53192(−4)	0.12654(−4)	0	0.40101(2)
$v_{\Pi p}^0$	0.10265(0)	−0.11894(−1)	0.57839(−3)	1	0.29575(1)
$v_{\Pi p}^{2b1}$	−0.44586(−2)	−0.27871(−2)	−0.14301(−5)	1	0.21098(0)
$v_{\Pi p}^{2b2}$	0.91958(−4)	0.24018(−4)	0.11016(−5)	1	0.33418(2)
$v_{\Pi p}^{2u}$	0.16151(−2)	−0.32262(−4)	−0.86390(−6)	1	0.33815(1)
$w_{\Pi p}^1$	−0.44586(−2)	−0.27871(−2)	−0.14301(−5)	1	0.21098(0)
$w_{\Pi p}^2$	−0.91958(−4)	−0.24018(−4)	−0.11016(−5)	1	0.33418(2)
$v_{\Pi z}$	0.10947(−1)	0.14344(−2)	−0.24540(−3)	1	0.15189(2)
$v_{\Sigma p}$	0.29400(−1)	−0.11984(−2)	−0.24803(−2)	1	0.19498(2)
$v_{\Sigma z}$	0.22929(0)	−0.11758(−1)	−0.34163(−2)	1	0.41721(2)

[a] The $v_{\Pi s}^0$ parameter has also terms of the third and fourth order with coefficients $c_3 = -0.42421(-4)\ E_h^{1/2}$ and $c_4 = -0.51748(-5)\ E_h^{1/2}$.

with

$$T_{\nu_f \mu_f \leftarrow \nu_i \mu_i} = \langle \nu_f | {V_{\epsilon_f}^{\mu_f}}^\dagger (E\mathbb{1} - H)^{-1} V_{\epsilon_i}^{\mu_i} | \nu_i \rangle. \tag{D5}$$

Then, we can perform the averaging over the molecular orientations using Euler angles α, β, γ

$$\frac{d\sigma_{\nu_f \leftarrow \nu_i}}{d\Omega}(\epsilon, \theta) = \frac{f(\epsilon)}{8\pi^2} \int_0^{2\pi} d\alpha \int_0^{2\pi} d\gamma \int_0^{\pi} d\beta \sin\beta \left| \mathcal{R}(\alpha, \beta, \gamma) \sum_{l_i, m_i} \sum_{l_f, m_f} Y_{l_f m_f}^*(\hat{\mathbf{k}}_f) T_{\nu_f l_f m_f \leftarrow \nu_i l_i m_i} Y_{l_i m_i}(\hat{\mathbf{k}}_i) \right|^2, \tag{D6}$$

where $\mathcal{R}(\alpha, \beta, \gamma)$ is the corresponding rotational operator and $f(\epsilon) = \pi^2/(2\epsilon)$. The rotational operator $\mathcal{R}$ acts on the direction vectors $\hat{\mathbf{k}}_i$ and $\hat{\mathbf{k}}_f$ of the initial and final electron momenta via the rotational matrix R

$$R(\alpha, \beta, \gamma) = \begin{pmatrix} \cos\alpha & \sin\alpha & 0 \\ -\sin\alpha & \cos\alpha & 0 \\ 0 & 0 & 1 \end{pmatrix} \begin{pmatrix} \cos\beta & 0 & \sin\beta \\ 0 & 1 & 0 \\ -\sin\beta & 0 & \cos\beta \end{pmatrix} \begin{pmatrix} \cos\gamma & \sin\gamma & 0 \\ -\sin\gamma & \cos\gamma & 0 \\ 0 & 0 & 1 \end{pmatrix}, \tag{D7}$$

TABLE IV. Obtained values of the parameters of the background eigenphase sums. The parameters are polynomials $\sum_{i=0}^{4} c_i Q_g^i$ in the symmetric stretching normal coordinate Q_g. The coefficients of the $a_{\rm bg}$, $c_{\rm bg}$, $c_{\rm bg}^{1b}$, and $c_{\rm bg}^{2u}$ parameters are in units of E_h^{-1}, where E_h is the hartree unit of energy, the rest of the parameters are dimensionless. The notation $x(y)$ means $x \times 10^y$.

	c_0	c_1	c_2	c_3	c_4
$a_{\rm bg}$	−0.11585(1)	0.20994(−1)	0.36453(−3)	0	0
$b_{\rm bg}$	0.10443(0)	−0.10081(−2)	−0.11098(−3)	0	0
$b_{\rm bg}^{2b}$	−0.90841(−3)	0.12924(−6)	0.19154(−7)	0	0
$b_{\rm bg}^{2u}$	0.15270(−2)	−0.16398(−3)	0	0	0
$c_{\rm bg}$	−0.63794(1)	0.61145(0)	0.83917(−1)	0	
$c_{\rm bg}^{1b}$	−0.11542(−1)	−0.62076(−1)	−0.16750(−1)	0.46431(−3)	0.49201(−3)
$c_{\rm bg}^{2u}$	0.72745(−1)	0.50706(−2)	−0.78337(−3)	0	0
$d_{\rm bg}$	−0.35235(−1)	0.77574(−2)	0.91983(−3)	0	0
$d_{\rm bg}^{1b}$	0.16629(−1)	−0.51348(−2)	0.11835(−2)	0.27039(−3)	−0.567215(−6)
$d_{\rm bg}^{2u}$	−0.16497(−2)	0.61585(−3)	0.17584(−3)	0	0
$d_{\rm bg}^{3bu}$	0.90811(−3)	0.73771(−6)	0.49481(−6)	−0.12696(−7)	0

that is, we have

$$\frac{d\sigma_{\nu_f\leftarrow\nu_i}}{d\Omega}(\epsilon,\theta) = \frac{f(\epsilon)}{8\pi^2}\int_0^{2\pi} d\alpha \int_0^{2\pi} d\gamma \int_0^{\pi} d\beta \sin\beta \sum_{l_i,m_i}\sum_{l_f,m_f} Y^*_{l_f m_f}(R\hat{\mathbf{k}}_f) T_{\nu_f l_f m_f \leftarrow \nu_i l_i m_i} Y_{l_i m_i}(R\hat{\mathbf{k}}_i) \times \sum_{l'_i,m'_i}\sum_{l'_f,m'_f} Y_{l'_f m'_f}(R\hat{\mathbf{k}}_f) T^*_{\nu_f l'_f m'_f \leftarrow \nu_i l'_i m'_i} Y^*_{l'_i m'_i}(R\hat{\mathbf{k}}_i). \tag{D8}$$

In our model of the e+CO_2 system, we consider electron partial waves $\mu = (l,m) = (0,0)$, $(1,0)$, and $(1,\pm1)$ for the s, p_z, and $p_\pm$ partial waves in the expansion (D3). The corresponding spherical harmonic functions Y_μ are

$$Y_{00} = 1/\sqrt{4\pi},\ Y_{10} = \sqrt{3/(4\pi)}k_z,\ Y_{1\pm1} = \mp\sqrt{3/(8\pi)}(k_x \pm ik_y), \tag{D9}$$

where k_x, k_y, k_z are the Cartesian components of the electron momentum direction vector. In addition, we consider only the initial vibrational state ν_i to be the ground vibrational state of CO_2, and thus, the symmetry of the final vibrational state ν_f restricts possible combinations of the incoming and outgoing partial waves, see Sec. VI. Without loss of generality, we set $\hat{\mathbf{k}}_i = (0,0,1)^T$ and $\hat{\mathbf{k}}_f = (\sin\theta, 0, \cos\theta)^T$, where θ is a scattering angle. The integration over the Euler angles results in the following formulas for Σ_g^+, Σ_u^+, Π_g, Π_u, and Δ_g final vibrational states

$$\frac{d\sigma}{d\Omega}(\epsilon,\theta)\Big|_{\Sigma_g^+} = f(\epsilon)\Big\{|T_{ss}|^2 + \frac{3}{5}\left(1+2\cos^2\theta\right)|T_{zz}|^2 + \frac{3}{10}\left(3+\cos^2\theta\right)\left(|T_{++}|^2 + |T_{--}|^2\right) + 2\cos\theta\,\mathrm{Re}\left[T_{ss}\left(T^*_{++}+T^*_{--}+T^*_{zz}\right)\right] - \frac{3}{5}(1-3\cos^2\theta)\left[2\,\mathrm{Re}\left(T_{++}T^*_{--}\right) + \mathrm{Re}\left(T_{zz}[T^*_{++}+T^*_{--}]\right)\right]\Big\}, \tag{D10}$$

$$\frac{d\sigma}{d\Omega}(\epsilon,\theta)\Big|_{\Sigma_u^+} = f(\epsilon)\left[|T_{sz}|^2 + |T_{zs}|^2 + 2\cos\theta\,\mathrm{Re}\left(T_{sz}T^*_{zs}\right)\right], \tag{D11}$$

$$\frac{d\sigma}{d\Omega}(\epsilon,\theta)\Big|_{\Pi_g} = f(\epsilon)\frac{3}{5}\left[\left(2-\cos^2\theta\right)\left(|T_{z+}|^2 + |T_{-z}|^2 + |T_{z-}|^2 + |T_{+z}|^2\right) + \left(1-3\cos^2\theta\right)\mathrm{Re}\left(T_{z+}T^*_{-z} + T_{z-}T^*_{+z}\right)\right], \tag{D12}$$

$$\frac{d\sigma}{d\Omega}(\epsilon,\theta)\Big|_{\Pi_u} = f(\epsilon)\left[|T_{s+}|^2 + |T_{-s}|^2 + |T_{s-}|^2 + |T_{+s}|^2 - 2\cos\theta\,\mathrm{Re}\left(T_{s+}T^*_{-s} + T_{s-}T^*_{+s}\right)\right], \tag{D13}$$

$$\frac{d\sigma}{d\Omega}(\epsilon,\theta)\Big|_{\Delta_g} = f(\epsilon)\frac{3}{10}(3+\cos\theta)\left(|T_{-+}|^2 + |T_{+-}|^2\right), \tag{D14}$$

where we suppressed the ν_i and ν_f indices and used a shorthand notation for partial waves (l, m): s corresponds to $(0, 0)$, z to $(1, 0)$, and $\pm$ to $(1, \pm 1)$.

Alternatively, we can calculate the differential cross sections by extending the derivation of McCurdy *et al.* [9] which leads to the following formula

$$\frac{d\sigma_{\nu_f \leftarrow \nu_i}}{d\Omega}(\epsilon, \theta) = \frac{8\pi^4}{\epsilon} \sum_{l_i, m_i} \sum_{l_i', m_i'} \sum_{l_f, m_f} \sum_{l_f', m_f'} \frac{\sqrt{(2l_i+1)(2l_i'+1)}}{4\pi} T_{\nu_f l_f m_f \leftarrow \nu_i l_i m_i} T^*_{\nu_f l_f' m_f' \leftarrow \nu_i l_i' m_i'}$$

$$\times \sum_{M=-l_f}^{l_f} Y^*_{l_f M}(\hat{\mathbf{k}}_f) Y_{l_f' M}(\hat{\mathbf{k}}_f) \sum_{j=|l_f - l_i'|}^{l_f + l_i'} \sum_{m=-j}^{j} (2j+1) \begin{pmatrix} l_f & l_i' & j \\ M & 0 & -M \end{pmatrix} \begin{pmatrix} l_f' & l_i & j \\ M & 0 & -M \end{pmatrix} \begin{pmatrix} l_f & l_i' & j \\ m_f & m_i' & m \end{pmatrix} \begin{pmatrix} l_f' & l_i & j \\ m_f' & m_i & m \end{pmatrix}, \quad \text{(D15)}$$

where the matrices are the Wigner 3-j symbols. We tested that both the approaches provide the same results.

[1] T. F. O'Malley, Theory of Dissociative Attachment, Phys. Rev. **150**, 14 (1966).

[2] J. N. Bardsley and F. Mandl, Resonant scattering of electrons by molecules, Rep. Prog. Phys. **31**, 471 (1968).

[3] A. Herzenberg, Oscillatory energy dependence of resonant electron-molecule scattering, J. Phys. B **1**, 548 (1968).

[4] W. Domcke and L. S. Cederbaum, On the interpretation of low-energy electron-HCl scattering phenomena, J. Phys. B: At. Mol. Phys. **14**, 149 (1981).

[5] L. S. Cederbaum and W. Domcke, Local against non-local complex potential in resonant electron-molecule scattering, J. Phys. B: At. Mol. Phys. **14**, 4665 (1981).

[6] W. Domcke and L. S. Cederbaum, Vibration-induced narrowing of electron scattering resonances near threshold, J. Phys. B: At. Mol. Phys. **13**, 2829 (1980).

[7] M. Čížek, J. Horáček, M. Allan, and W. Domcke, Resonances and threshold phenomena in low-energy electron collisions with hydrogen halides: new experimental and theoretical results, Czech. J. Phys. **52**, 1057 (2002).

[8] T. N. Rescigno, W. A. Isaacs, A. E. Orel, H.-D. Meyer, and C. W. McCurdy, Theoretical study of resonant vibrational excitation of CO_2 by electron impact, Phys. Rev. A **65**, 032716 (2002).

[9] C. W. McCurdy, W. A. Isaacs, H.-D. Meyer, and T. N. Rescigno, Resonant vibrational excitation of CO_2 by electron impact: Nuclear dynamics on the coupled components of the $^2\Pi_u$ resonance, Phys. Rev. A **67**, 042708 (2003).

[10] D. J. Haxton, Z. Zhang, H.-D. Meyer, T. N. Rescigno, and C. W. McCurdy, Dynamics of dissociative attachment of electrons to water through the $^2B_1$ metastable state of the anion, Phys. Rev. A **69**, 062714 (2004).

[11] D. J. Haxton, T. N. Rescigno, and C. W. McCurdy, Dissociative electron attachment to the H_2O molecule. II. Nuclear dynamics on coupled electronic surfaces within the local complex potential model, Phys. Rev. A **75**, 012711 (2007).

[12] S. T. Chourou and A. E. Orel, Dissociative electron attachment to HCN and HNC, Phys. Rev. A **80**, 032709 (2009).

[13] S. T. Chourou and A. E. Orel, Isotope effect in dissociative electron attachment to HCN, Phys. Rev. A **83**, 032709 (2011).

[14] H. B. Ambalampitiya and I. I. Fabrikant, Nonlocal complex potential theory of dissociative electron attachment: Inclusion of two vibrational modes, Phys. Rev. A **102**, 022802 (2020).

[15] H. Estrada, L. S. Cederbaum, and W. Domcke, Vibronic coupling of short-lived electronic states, J. Chem. Phys. **84**, 152 (1986).

[16] S. Feuerbacher, T. Sommerfeld, and L. S. Cederbaum, Intersections of potential energy surfaces of short-lived states: The complex analogue of conical intersections, J. Chem. Phys. **120**, 3201 (2004).

[17] S. Feuerbacher and L. S. Cederbaum, Jahn-Teller effect for short-lived states: Study of the complex potential energy surfaces, J. Chem. Phys. **121**, 5 (2004).

[18] J. Dvořák, M. Ranković, K. Houfek, P. Nag, R. vCurík, J. Fedor, and M. Čížek, Vibronic coupling through the continuum in the $e + co_2$ system, Phys. Rev. Lett. **129**, 013401 (2022).

[19] M. A. Morrison, Interpretation of the near-threshold behavior of cross sections for $e - CO_2$ scattering, Phys. Rev. A **25**, 1445 (1982).

[20] K. H. Kochem, W. Sohn, N. Hebel, K. Jung, and H. Ehrhardt, Elastic electron scattering and vibrational excitation of CO_2 in the threshold energy region, J. Phys. B: At. Mol. Phys. **18**, 4455 (1985).

[21] L. A. Morgan, Virtual States and Resonances in Electron Scattering by CO_2, Phys. Rev. Lett. **80**, 1873 (1998).

[22] M. J. W. Boness and G. J. Schulz, Vibrational excitation in CO_2 via the 3.8-eV resonance, Phys. Rev. A **9**, 1969 (1974).

[23] B. L. Whitten and N. F. Lane, Near-threshold vibrational excitation in electron-CO_2 collisions: A simple model, Phys. Rev. A **26**, 3170 (1982).

[24] S. Mazevet, M. A. Morrison, L. A. Morgan, and R. K. Nesbet, Virtual-state effects on elastic scattering and vibrational excitation of CO_2 by electron impact, Phys. Rev. A **64**, 040701 (2001).

[25] H. Estrada and W. Domcke, On the virtual-state effect in low-energy electron-CO_2 scattering, J. Phys. B **18**, 4469 (1985).

[26] W. Vanroose, Z. Zhang, C. W. McCurdy, and T. N. Rescigno, Threshold vibrational excitation of CO_2 by

slow electrons, Phys. Rev. Lett. **92**, 053201 (2004).
[27] I. Čadež, F. Gresteau, M. Tronc, and R. I. Hall, Resonant electron impact excitation of CO_2 in the 4 eV region, J. Phys. B: At. Mol. Phys. **10**, 3821 (1977).
[28] A. K. Kazansky and L. Y. Sergeeva, On the local theory of resonant inelastic collisions of slow electrons with carbon dioxide, J. Phys. B: At., Mol. Opt. Phys. **27**, 3217 (1994).
[29] A. Kazansky and L. Y. Sergeeva, A model study of vibrational excitation of carbon dioxide molecule by slow electrons: the role of wave packet sliding from the ridge, Z. Phys. D **37**, 305 (1996).
[30] D. G. Hopper, Analytic representation of the ground state potential surfaces for CO_2^- and CO_2. implications for the $O^- + CO \rightarrow CO_2^* + e$ chemiluminescent reaction and other related processes, Chem. Phys. **53**, 85 (1980).
[31] G. L. Gutsev, R. J. Bartlett, and R. N. Compton, Electron affinities of CO_2, OCS, and CS_2, J. Chem. Phys. **108**, 6756 (1998).
[32] T. N. Rescigno, D. A. Byrum, W. A. Isaacs, and C. W. McCurdy, Theoretical studies of low-energy electron-CO_2 scattering: Total, elastic, and differential cross sections, Phys. Rev. A **60**, 2186 (1999).
[33] J. Tennyson and L. A. Morgan, Electron collisions with polyatomic molecules using the R–matrix method, Phil. Trans. R. Soc. A. **357**, 1161–1173 (1999).
[34] W. Vanroose, C. W. McCurdy, and T. N. Rescigno, Interpretation of low-energy electron-CO_2 scattering, Phys. Rev. A **66**, 032720 (2002).
[35] T. Sommerfeld, A fresh look at the $^2A_1$ $CO_2{}^-$ potential energy surface, J. Phys. B: At., Mol. Opt. Phys. **36**, L127 (2003).
[36] T. Sommerfeld, H.-D. Meyer, and L. S. Cederbaum, Potential energy surface of the $CO_2{}^-$ anion, Phys. Chem. Chem. Phys. **6**, 42 (2004).
[37] H. Köppel, W. Domcke, and L. S. Cederbaum, Theory of vibronic coupling in linear molecules, The Journal of Chemical Physics **74**, 2945 (1981).
[38] H. Köppel, W. Domcke, and L. S. Cederbaum, Multimode Molecular Dynamics Beyond the Born-Oppenheimer Approximation, in *Advances in Chemical Physics* (John Wiley & Sons, Ltd, 1984) pp. 59–246.
[39] H. Feshbach, A unified theory of nuclear reactions. II, Ann. Phys. **19**, 287 (1962).
[40] M. Čížek and K. Houfek, Nonlocal Theory of Resonance Electron-Molecule Scattering, in *Low-energy Electron Scattering from Molecules, Biomolecules and Surfaces*, edited by P. Čársky and R. Čurík (CRC Press, 2012) Chap. 4, pp. 91–125.
[41] W. Domcke, Theory of resonance and threshold effects in electron-molecule collisions: The projection-operator approach, Phys. Rep. **208**, 97 (1991).
[42] W. J. Witteman, *The CO_2 Laser* (Springer, 1987).
[43] A. Moradmand, D. S. Slaughter, D. J. Haxton, T. N. Rescigno, C. W. McCurdy, T. Weber, S. Matsika, A. L. Landers, A. Belkacem, and M. Fogle, Dissociative electron attachment to carbon dioxide via the $^2\Pi_u$ shape resonance, Phys. Rev. A **88**, 032703 (2013).
[44] D. Spence and G. J. Schulz, Temperature dependence of dissociative attachment in O_2 and CO_2, Phys. Rev. **188**, 280 (1969).
[45] G. Herzberg, *Molecular spectra and molecular structure. Vol.2, Infrared and Raman spectra of polyatomic molecules* (Van Nostrand, New York, 1945).
[46] E. P. Wigner, On the Behavior of Cross Sections Near Thresholds, Phys. Rev. **73**, 1002 (1948).
[47] R. J. Bieniek, Complex potential and electron spectrum in atomic collisions involving fast electronic transitions: Penning and associative ionization, Phys. Rev. A **18**, 392 (1978).
[48] M. Berman, H. Estrada, L. S. Cederbaum, and W. Domcke, Nuclear dynamics in resonant electron-molecule scattering beyond the local approximation: The 2.3-ev shape resonance in N_2, Phys. Rev. A **28**, 1363 (1983).
[49] R. Parini, cxroots: A Python module to find all the roots of a complex analytic function within a given contour (2018–).
[50] P. Kravanja and M. V. Barel, *Computing the Zeros of Analytic Functions* (Springer-Verlag Berlin Heidelberg, 2000).
[51] T. H. Dunning, Gaussian basis sets for use in correlated molecular calculations. I. The atoms boron through neon and hydrogen, J. Chem. Phys. **90**, 1007 (1989).
[52] J. Tennyson, Electron–molecule collision calculations using the R-matrix method, Phys. Rep. **491**, 29 (2010).
[53] Z. Mašín, J. Benda, J. D. Gorfinkiel, A. G. Harvey, and J. Tennyson, Ukrmol+: A suite for modelling electronic processes in molecules interacting with electrons, positrons and photons using the R-matrix method, Comput. Phys. Commun. **249**, 107092 (2020).
[54] W. Domcke and C. Mündel, Calculation of cross sections for vibrational excitation and dissociative attachment in HCl and DCl beyond the local-complex-potential approximation, J. Phys. B: At. Mol. Phys. **18**, 4491 (1985).
[55] J. Horáček, M. Čížek, and W. Domcke, Generalization of the nonlocal resonance model for low-energy electron collisions with hydrogen halides: the variable threshold exponent, Theor. Chem. Acc. **100**, 31 (1998).
[56] D. M. Dennison, The Infra-Red Spectra of Polyatomic Molecules. Part II, Rev. Mod. Phys. **12**, 175 (1940).
[57] H. Friedrich, *Scattering Theory* (Springer, 2013).
[58] J. R. Taylor, *Scattering Theory: The Quantum Theory on Nonrelativistic Collisions* (Wiley, New York, 1972).
[59] H. Estrada and W. Domcke, Analytic properties of the S matrix for a simple model of fixed-nuclei electron-polar-molecule scattering, J. Phys. B: At. Mol. Phys. **17**, 279 (1984).
[60] M. Hestenes and E. Stiefel, Methods of conjugate gradients for solving linear systems, J. Res. Nat. Bur. Stand. **49**, 409 (1952).
[61] H. van der Vorst and J. Melissen, A Petrov-Galerkin type method for solving Axk=b, where A is symmetric complex, IEEE Transactions on Magnetics **26**, 706 (1990).
[62] T. Sogabe and S.-L. Zhang, A COCR method for solving complex symmetric linear systems, Journal of Computational and Applied Mathematics **199**, 297 (2007), special Issue on Scientific Computing, Computer Arithmetic, and Validated Numerics (SCAN 2004).
[63] R. Fletcher, Conjugate gradient methods for indefinite systems, in *Numerical Analysis*, edited by G. A. Watson (Springer Berlin Heidelberg, Berlin, Heidelberg, 1976) pp. 73–89.
[64] H. A. van der Vorst, Bi-CGSTAB: A Fast and Smoothly Converging Variant of Bi-CG for the Solution of Nonsymmetric Linear Systems, SIAM J. Sci. and Stat. Comput. **13**, 631 (1992).
[65] S. F. Wong and G. J. Schulz, Vibrational excitation in benzene by electron impact via resonances: Selection

rules, Phys. Rev. Lett. **35**, 1429 (1975).
[66] G. A. Gallup, Selection rules for vibrational energy loss by resonant electron impact in polyatomic molecules, Phys. Rev. A **34**, 2746 (1986).
[67] G. A. Gallup, Symmetry selection rules for vibrational excitation by resonant electron impact and a unified treatment of vibronic coupling between resonances and to the continuum: A complete symmetry analysis of vibrational excitation in benzene, J. Chem. Phys. **99**, 827 (1993).
[68] R. Čurík, I. Paidarová, M. Allan, and P. Čársky, Joint experimental and theoretical study on vibrational excitation cross sections for electron collisions with diacetylene, J. Phys. Chem. A **118**, 9734 (2014).
[69] R. Čurík, P. Čársky, and M. Allan, Electron-impact vibrational excitation of cyclopropane, J. Chem. Phys. **142**, 144312 (2015).
[70] H. Bateman, On the numerical solution of linear integral equations, Proc. R. Soc. London A **100**, 441 (1922).
[71] K. Houfek, M. Čížek, and J. Horáček, Dissociative attachment of low-energy electrons to vibrationally excited hydrogen molecules, Czech. J. Phys. **52**, 29 (2002).
[72] C. Cohen-Tannoudji, B. Diu, and F. Laloë, *Quantum Mechanics, Volume 1: Basic Concepts, Tools, and Applications* (New York: Wiley, 2005).

Vibrational excitation in the e + CO_2 system: Analysis of two-dimensional energy-loss spectrum

Jan Dvořák,[1,*] Miloš Ranković,[2] Karel Houfek,[1] Pamir Nag,[2] Roman Čurík,[2] Juraj Fedor,[2] and Martin Čížek[1,†]

[1] *Charles University, Faculty of Mathematics and Physics, Institute of Theoretical Physics, V Holešovičkách 2, 180 00 Prague 8, Czech Republic*

[2] *J. Heyrovský Institute of Physical Chemistry, Czech Academy of Sciences, Dolejškova 2155/3, 182 23 Prague 8, Czech Republic*

(Dated: October 8, 2022)

We present a detailed analysis of two-dimensional electron energy-loss spectrum of CO_2, which extends our recent Letter [Phys. Rev. Lett. 129, 013401 (2022)]. We show that our vibronic coupling model [Phys. Rev. A 105, 062821 (2022)] captures primary features of the multidimensional dynamics of the temporary molecular anion and the calculations qualitatively reproduce the spectrum. The shape of the spectrum is given by two overlapping contributions that originate in excitation of vibrational states within Σ_g^+ and Π_u Fermi polyads. Propensity rules in terms of scattered and vibrational wave functions are also discussed to clarify the selectivity of states from the vibrational pseudocontinuum that is responsible for the observed fine structure.

I. INTRODUCTION

The low-energy (< 5 eV) inelastic electron scattering from the CO_2 molecule

$$e + CO_2 \rightarrow {CO_2}^- \rightarrow e + CO_2^* \tag{1}$$

is full of interesting phenomena. The experimental effort to probe this system goes back as early as the 1920s by Ramsauer [1]. In the 1960s and 1970s, Boness and Schulz [2–4] and Čadež *et al.* [5, 6] thoroughly studied the 3–5 eV region dominated by a $^2\Pi_u$ resonance. Observed peaks in the energy-loss spectra were attributed to $(n, 0^0, 0)$ and $(n, 1^1, 0)$ vibrational progressions. The energy dependence of the vibrational cross sections revealed an oscillatory structure, which they correctly recognized as the boomerang oscillations and even reproduced [6] by one-dimensional (1D) calculations for the symmetric stretching using the local complex potential (LCP) model developed by Herzenberg [7]. They also studied the shift of the boomerang peaks towards higher incident energies with energy loss, which explains the diagonal rays later observed in the 2D energy-loss spectrum, see below. The LCP nuclear dynamics was further studied by Kazansky and Sergeeva [8, 9], who also included the bending motion.

By improving the signal-to-noise ratio, Allan [10] divided the energy-loss spectra into three regions. Region I was dominated by the $(n, 0^0, 0)$ progression (for a small scattering angle). Region II showed a complex structure. Well distinguishable broad peaks reappeared at high energy losses (region III) with positions that did not correspond to the $(n, 0^0, 0)$ progression. Using the 2D scanning technique developed by Reddish *et al.* [11], Currell and Comer [12–14] recorded the first 2D energy-loss spectrum of CO_2. They fully realized the importance of the Fermi resonance effect on neutral vibrational states [15, 16] and argued that the excitation of fairly linear states and highly bent states within Σ_g^+ polyads was responsible for the two newly observed structures (labeled by A and B).

Itikawa *et al.* [17, 18] and Kochem *et al.* [19] probed the increase of the cross sections near the threshold, see also references therein for earlier works. They showed that the direct dipole scattering explains well the threshold peaks of the $(0, 1^1, 0)$ bending and $(0, 0^0, 1)$ asymmetric stretching modes whereas the s-wave scattering effected by a $^2\Sigma_g^+$ virtual state is largely responsible for the $(1, 0^0, 0)$ symmetric stretching excitation. The effect of the virtual state was studied by many theoretical methods, such as coupled-channel calculations of Morrison *et al.* [20, 21], two-state model by Whitten and Lane [22], discrete-state-in-continuum model by Estrada and Domcke [23] or the energy-modified adiabatic phase matrix method by Mazevet *et al.* [24].

From a plethora of *ab initio* fixed-nuclei calculations, we emphasize the work of Morgan [25], who located the S-matrix poles in the complex plane corresponding to the $^2\Sigma_g^+$ virtual state and both Renner-Teller components of the $^2\Pi_u$ shape resonance. Other works include Morrison *et al.* [20], Lee *et al.* [26], and Rescigno *et al.* [27]. The angular dependence of the differential cross sections was also studied by many groups: Register *et al.* [28], Kochem *et al.* [19], Antoni *et al.* [29], Cartwright *et al.* [30, 31], and Kitajima *et al.* [32, 33].

Thanks to the improvement of the energy resolution down to 7 meV, Allan [34, 35] revealed a strong selectivity in excitation of individual members of the Fermi polyads. Such a behavior in the $^2\Pi_u$ region was reproduced by McCurdy *et al.* [36, 37], who performed time-dependent 2D LCP calculations [38] with both Renner-Teller states. Shortly after, Vanroose *et al.* [39] explained the selectivity at the threshold using a 2D effective-range potential model [40, 41]. Recently, Laporta *et al.* [42] have reported

* jan.dvorak@utf.mff.cuni.cz
† martin.cizek@mff.cuni.cz

1D LCP calculations considering each vibrational mode independently.

Despite the theoretical effort that the $e + CO_2$ system have received, the shape of the spectrum for moderate and high energy losses is still not explained. Furthermore, we are not aware of any dynamical calculations of this system that predict the excitation of non-totally symmetric vibrational states such as states with odd quanta of bending or asymmetric stretching. Such states can be excited due to the vibronic coupling in the resonant electron-molecule scattering as was investigated by Gallup [43]. He showed that the first order terms in the electron-molecule potential give the selection rules formulated by Wong and Schulz [44] to explain the spectrum of benzene. The symmetries of expected excited vibrational states are those that belong (i) to the symmetrized square of the irreducible representation of the resonance, or (ii) to the irreducible representation of the resonance, which leads to the outgoing s-wave electron.

The two-state discrete momentum representation method developed by Čurík and Čársky [45] have been used to study the inelastic electron scattering from polyatomic molecules, such as methane [46], diacetylene [47] and cyclopropane [48]. In the case of cyclopropane, Čurík *et al.* [48] showed that excitation of the ν_4 twist mode does not follow the selection rules because the incoming f wave is transformed to a p wave. Gallup [43] concluded his paper that higher orders cause excitation of additional symmetries but the relations become too complicated to be useful.

The present paper concludes our study of vibrational excitation of the CO_2 molecule by slow electrons. Our joint experimental and theoretical work is summarized in a recent letter [49], which will be referred to as Letter throughout this paper. The detailed description of our work is then divided in two parts. The paper [50] (referred to as Paper I in the following text) discusses the derivation of the theoretical model dictated by the symmetry of the system, together with the determination of the model parameters by fitting the results of our fixed-nuclei electron-molecule scattering calculations for a large set of geometries. Paper I also describes the computational procedure based on Krylov subspace iteration methods to find the wave function of the anion and the formulae for calculation of the vibrational excitation cross sections. Here, we focus on a detailed presentation of the results of our calculations including the comparison with our and previous experimental data.

The paper is organized as follows. Section II describes the experimental setup used to measure the energy-loss spectra, which are also shown there. Section III discusses the grouping of neutral vibrational states into polyads. In Sec. IV, we summarize and emphasize the key theoretical points that are important for the subsequent discussion. The calculated spectra are presented in a similar way as the experimental data in Sec. V. Then, we analyze the energy-loss spectra based on various aspects (symmetry of final states, electron partial waves, angular dependence, etc.) and examine the underlying mechanisms in terms of wave functions in Sec. VI, where the cross sections for low-lying states are also shown. In Sec. VII, we study the sensitivity of the calculations to parameters of the model and finally our work is concluded in Sec. VIII by summarizing the results and discussing possible improvements and applications of the approach to another systems.

II. EXPERIMENTAL SPECTRA

The electron energy-loss spectra were recorded on the electrostatic spectrometer [51, 52]. The electrons were emitted from a heated iridium filament and energy-selected by a double-hemispherical electron monochromator. The incident electron energy ϵ_i was controlled by floating the monochromator with respect to the potential of the collision region. The electrons were scattered on the effusive beam of the CO_2 gas and their residual energy ϵ_f was analyzed with a double-hemispherical electron analyzer. The analyzer can be rotated in order to probe various scattering angles. The energy of the incident beam was calibrated on the 2^2S resonance in helium at 19.365 eV. Electron-energy resolution was 18 meV, as determined from the width of the elastic peak.

All the spectra presented here were recorded in a *constant* ϵ_i mode where the incident energy was fixed, the residual energy was scanned, and the signal was plotted as a function of the energy loss $\Delta\epsilon = \epsilon_i - \epsilon_f$. Figure 1 shows a two-dimensional (2D) energy-loss spectrum recorded at the 135° scattering angle. It is constructed from individual 1D energy-loss spectra recorded at 220 incident electron energies with 10 meV increments. Such color-coded map can reveal complex dynamics of nuclear motion induced by the electron scattering [53–56]. The individual features of our 2D spectrum for CO_2 are outlined in the Letter and further discussed in the following sections.

To better understand the detailed structure of the spectrum, Fig. 2 shows the individual electron energy-loss spectra at four selected incident energies (horizontal sections of 2D spectrum) but separately recorded for a better signal-to-noise ratio. The spectra in both figures were recorded at high scattering angle to enhance the resonance processes with respect to direct-dipole excitations. It is well known that direct excitation processes related to direct-dipole excitation have cross sections peaking at small scattering angles [10, 57], the resonant processes are thus most pronounced in the backscattering direction. The 135° angle is the highest mechanical angle achievable with the present setup.

Before proceeding to the calculated spectra, we discuss the vibrational states of the neutral CO_2 molecule and their energies since they are directly related to the energy-loss axis of the spectra.

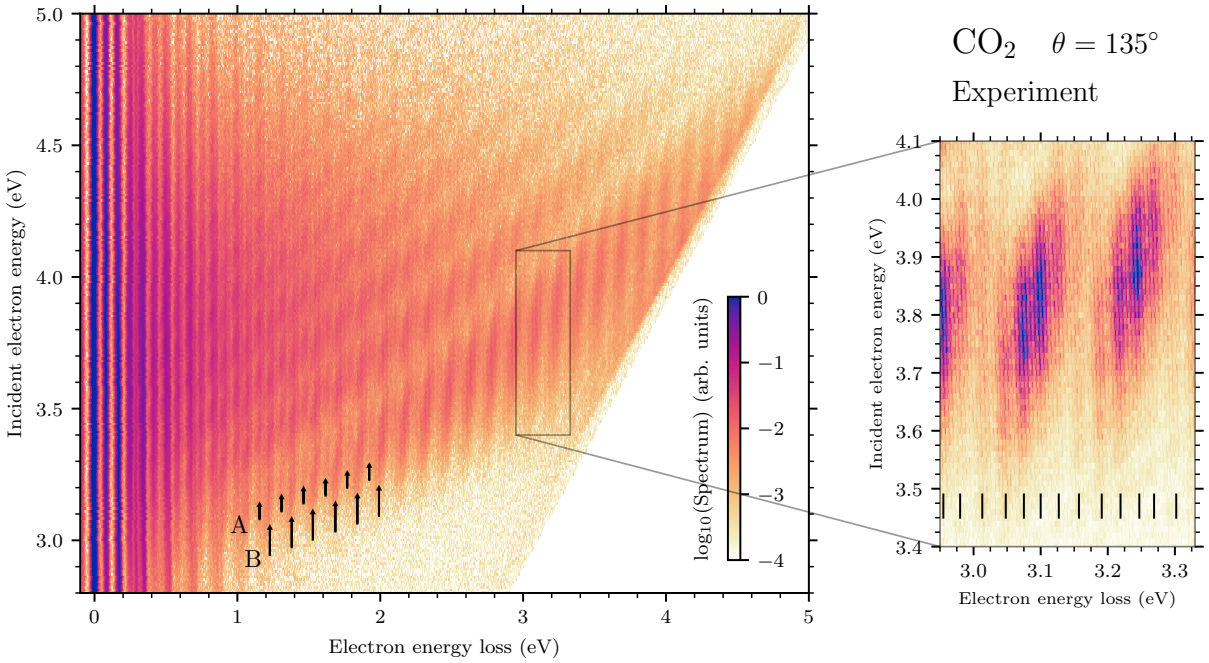

FIG. 1. Experimental 2D electron energy-loss spectrum of CO_2 for a scattering angle of 135°. A detail of the spectrum is shown in a linear scale from 0 to 1 and the fine structure is indicated (average spacing ∼29 meV). Structures A and B observed by Currell and Comer [12–14] are labeled in the main plot.

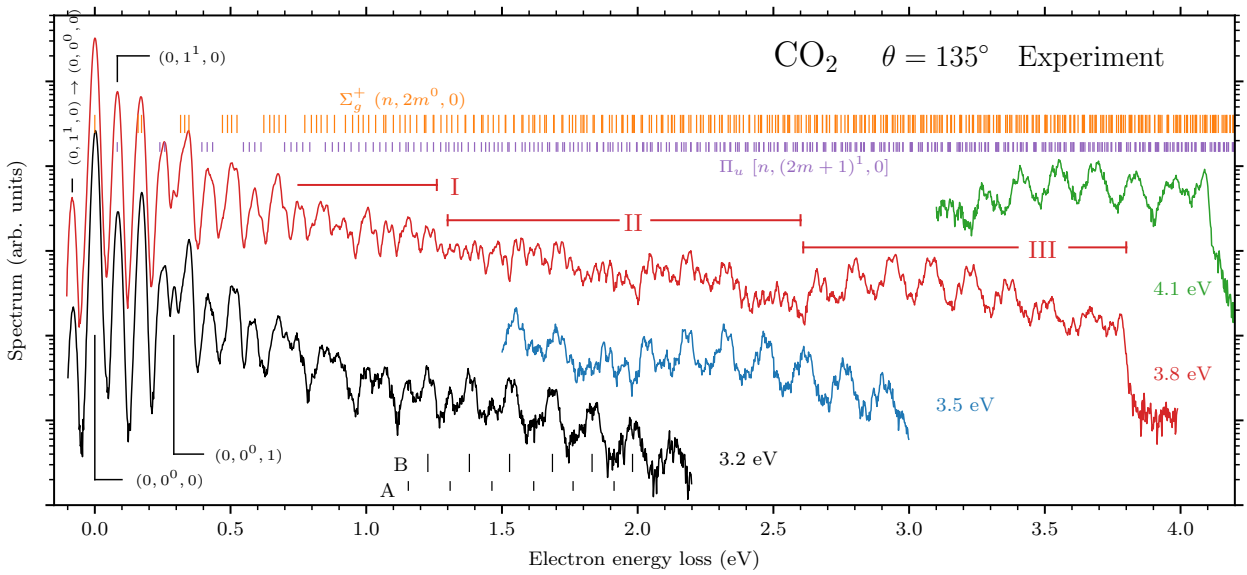

FIG. 2. Experimental 1D energy-loss spectra for a scattering angle of 135° and incident electron energies 3.2, 3.5, 3.8, and 4.1 eV. The spectra are shown in the logarithmic scale but lines for different incident energies are arbitrarily shifted with respect to each other. Calculated energies of Fermi-coupled vibrational states that belong to Σ_g^+ $(n, 2m^0, 0)$ and Π_u $[n, (2m+1)^1, 0]$ polyads $(n + m = 0, 1, \ldots)$ are shown. Regions of order, chaos, and order observed by Allan [10] are labeled by I, II, and III for the 3.8 eV spectrum. Positions of A and B structures observed by Currell and Comer [12–14] are indicated for the 3.2 eV spectrum.

III. VIBRATIONAL STATES OF NEUTRAL CO_2

The vibrational states of the CO_2 molecule within the harmonic approximation are identified by four numbers [16]

$$\nu \equiv (\nu_g, \nu_b^{\ell_b}, \nu_u), \tag{2}$$

where ν_g, ν_b, and ν_u denote numbers of quanta in symmetric stretching, bending, and asymmetric stretching, respectively, and ℓ_b is the angular momentum of the bending motion with respect to the molecular axis. The corresponding experimental vibrational frequencies are $\omega_g = 167.5$ meV, $\omega_u = 297.1$ meV, and $\omega_b = 83.3$ meV [58].

Although the anharmonic corrections are important for the understanding of the spectrum of the neutral CO_2, we start with the harmonic basis because it is used in our numerical treatment of the dynamics as discussed in Paper I and here below.

For the later discussion it is important to remind the classification of the states according to the irreducible representations of the molecular symmetry group $D_{\infty h}$ [16]. The angular momentum is determined by ℓ_b and the parity is given by the product $\nu_u\nu_b$. Thus, the states $|\nu\rangle$ correspond to the Σ_g^+ and Σ_u^+ representations for $\ell_b = 0$ with ν_u even and ν_u odd, respectively, to Π_u or Π_g for $\ell_b = 1$ with ν_u even or odd, to Δ_g or Δ_u for $\ell_b = 2$ with ν_u even or odd, and so on.

A. Harmonic polyads

The energies of one quantum of symmetric stretching and two bending quanta are almost degenerate ($\omega_g - 2\omega_b = 0.9$ meV). Therefore, the harmonic states are naturally organized into groups (polyads) with nearly the same energy. The harmonic energy of the state $|\nu\rangle$ reads

$$E_\nu = E_0 + \nu_g\omega_g + \nu_b\omega_b + \nu_u\omega_u, \tag{3}$$

where E_0 is the ground state energy, ν_g and ν_u attain values $0, 1, 2, \ldots$ and $\nu_b = \ell_b, \ell_b + 2, \ell_b + 4, \ldots$. As a result, all harmonic states $|\nu\rangle$ for

$$\nu = (\nu_g, \nu_b^{\ell_b}, \nu_u) = [n, (2m + \ell_b)^{\ell_b}, \nu_u], \tag{4}$$

where $n + m = N = \text{const}$, have the energy close to the value

$$E_\nu \simeq E_0 + N\omega_g + \ell_b\omega_b + \nu_u\omega_u \tag{5}$$

with a spread of $0.9N$ meV. For example, the Σ_g^+ dyad ($N = 1$) with $\nu_u = 0$ contains two harmonic states $(1, 0^0, 0)$ and $(0, 2^0, 0)$ while the harmonic Π_u polyad with $N = 10$ consists of eleven states $(10, 1^1, 0)$, $(9, 3^1, 0), \ldots$, $(0, 21^1, 0)$.

Considering the energy-loss range of the experimental data (Fig. 1), the maximum N that we need to take into account is $N = 30$. The energy spread of the states within individual harmonic polyads is thus less then $0.9N \simeq 30$ meV. The 2D spectrum in Fig. 1 below energy loss $\Delta\epsilon < 1$ eV is clearly organized into polyads but the quasi-continuous character of the spectrum at higher electron energy losses is inconsistent with this estimate for the energy spread.

B. Fermi-coupled states

The inconsistency is not surprising since it is well known that the vibrational states of neutral CO_2 are significantly influenced by the Fermi resonance effect [15, 16]. Anharmonic corrections to the potential energy surface split the nearly degenerate harmonic states of the same symmetry and also correlate the vibrational motion in the symmetric stretching and bending directions mixing the different states within the polyads.

To calculate these proper final vibrational states, we employ the Hamiltonian of Chedin [59], which includes the anharmonic corrections. The Fermi-coupled states $|\nu_{\rm FR}\rangle$, for the symmetry given by fixed values of ℓ_b and ν_u, are expanded into linear combinations of harmonic states:

$$|\nu_{\rm FR}\rangle = \sum_\nu c_\nu |\nu\rangle, \tag{6}$$

where the coefficients c_ν are obtained by diagonalizing the anharmonic vibrational Hamiltonian [59]. In principle, the sum runs over all allowed ν_g, ν_b but the results show that the coupling among polyads with different values of N is negligible for the range of vibrational energies considered in this study. We can thus identify the Fermi-coupled states by specifying numbers ℓ_b, ν_u and N to determine the specific polyad $[n, (2m + \ell_b)^{\ell_b}, \nu_u]$ of harmonic states. After the diagonalization, the Fermi-coupled states are sorted by their energy. The individual state can be referred to by a symbol $N(i)$, which denotes the i-th state in the polyad $N = n + m$. Note that the ground state $\nu_i = (0, 0^0, 0)$, i. e. the initial vibrational state ν_i, is subject to no anharmonic corrections and thus belongs to both, the harmonic and the Fermi-coupled sets of states.

The anharmonic energies $\epsilon_{\rm FR}$ emerging from the Σ_g^+ $(n, 2m^0, 0)$ and Π_u $[n, (2m + 1)^1, 0]$ polyads are shown in Fig. 2 by a grid of small vertical lines displayed in the upper part of the figure. The positions of the low energy-loss peaks correspond approximately to the middle of the polyads, but above $\Delta\epsilon \approx 0.9$ eV the energy ranges of the individual polyads start to overlap. At high energy losses, the spectrum of the Fermi-coupled states is dense and rather erratic and so there is no obvious connection between individual experimental peaks and the vibrational energies. We conclude that either polyads with nonzero ν_u have to be involved or there is some selective mechanism that allows excitation of only certain states from the pseudocontinuum.

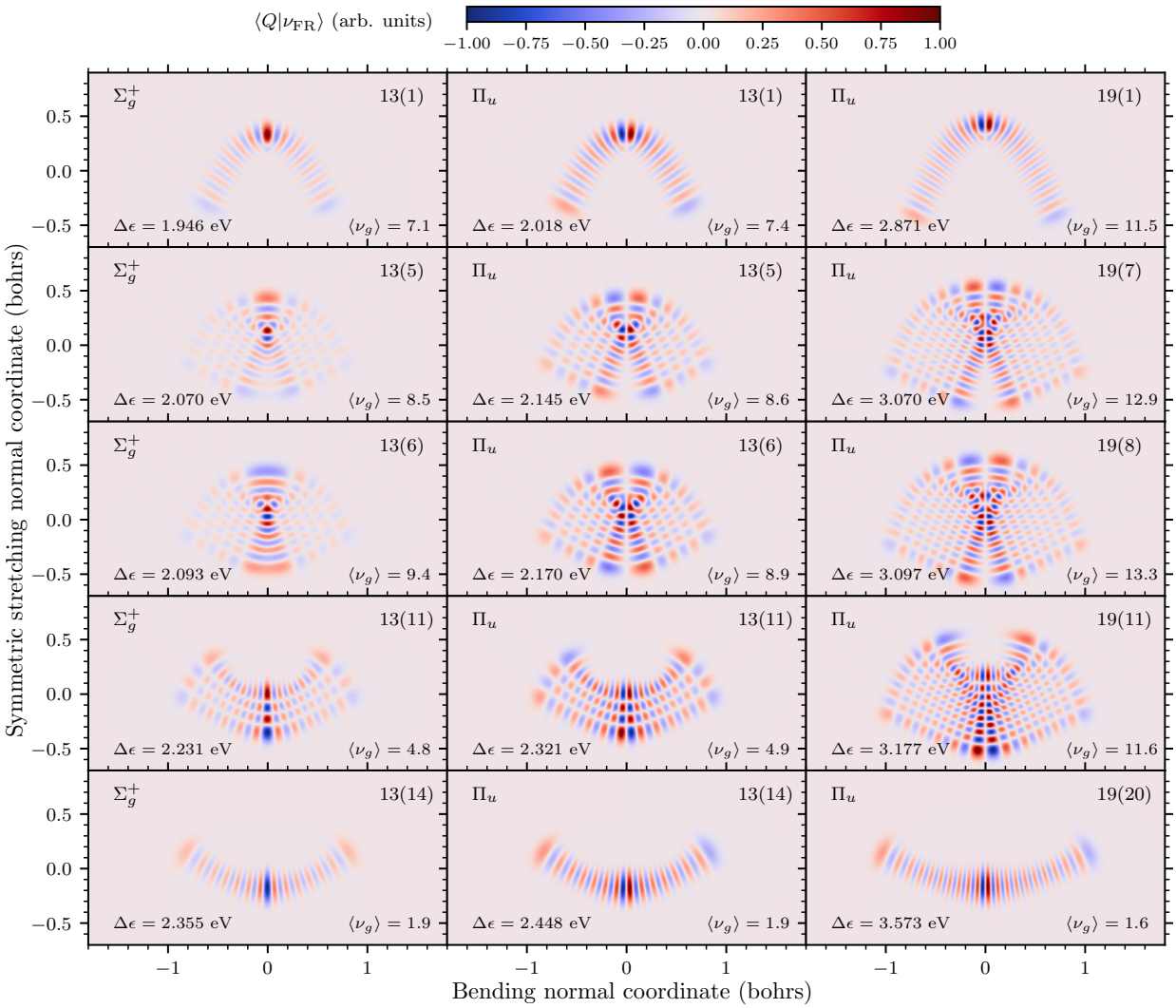

FIG. 3. Fermi-coupled vibrational wave functions upon symmetric stretching and bending (asymmetric stretching coordinate is set to zero). The first two columns show states $N(i)$ for $i = 1, 5, 6, 11, 14$ (from top), belonging to the Σ_g^+ $(n, 2m^0, 0)$ and Π_u $[n, (2m+1)^1, 0]$ Fermi polyads with $N = n + m = 13$, respectively. The third column shows states $N(i)$ for $i = 1, 7, 8, 11, 20$ (from top), within the Π_u polyad with $N = n + m = 19$. The energy loss $\Delta\epsilon$ and the mean value of number of symmetric stretching quanta $\langle\nu_g\rangle$ are also shown for each state. The wave functions are independently normalized.

To gain more insight into the Fermi coupling and the correlation of the bending and stretching motion within the polyads, we plot the wave functions of selected states in Fig. 3. The first column shows the shape of the lowest ($i = 1$) and highest ($i = 14$) states together with some states from the middle ($i = 5$, 6, 11) for the Σ_g^+ polyad with $N = 13$, and similarly, other two columns contain the wave functions from Π_u polyads with $N = 13$ and 19. The wave functions are plotted with respect to the normal coordinates used in the dynamics, see Sec. IV and Note 1.

Small bending correlates to positive symmetric stretching (prolongation of the C-O bonds) for the lowest states within each polyad (first row in Fig. 3) while the highest states are more spread in the bending direction (highly bent states) with negative stretching values at small bending. The middle states have rather intriguing shapes but overall the probability density is localized in the vicinity of the stretching axis (linear states). Note that the harmonic states would have nodal planes parallel with the coordinate axes since there is no correlation between stretching and bending, in contrast to the behavior seen here for the coupled states.

To somehow quantify the shape of the wave functions, we characterize each Fermi-coupled state by a simple quantity, the mean value of the number of symmetric

stretching quanta

$$\langle \nu_g \rangle = \sum_\nu \nu_g |c_\nu|^2, \tag{7}$$

where the sum runs over all harmonic states within the particular polyad, c_ν are the expansion coefficients in the harmonic basis [Eq. (6)], and ν_g is the symmetric stretching coordinate of the ν vector [Eq. (2)]. The mean value $\langle \nu_g \rangle$ therefore describes the amount of symmetric stretching.

Similarly, we can define the mean value for bending quanta

$$\langle \nu_b \rangle = \sum_\nu \nu_b |c_\nu|^2, \tag{8}$$

but the two values are not independent due to the relation $n + m = N$. Larger values of $\langle \nu_b \rangle$ thus corresponds to smaller $\langle \nu_g \rangle$ and vice versa. The quantity $\langle \nu_g \rangle$ is also shown in Fig. 3 together with the energy loss $\Delta\epsilon_{\rm FR}$ for each state (when excited by an electron from the ground vibrational state).

IV. THEORY

Our theoretical model is discussed in detail in Paper I. For convenience, we summarize the basic aspects of the theory used in the discussion of the results in this paper.

A. Nonlocal model of vibronic dynamics

The model is designed to treat the vibronic dynamics of vibrational excitation of the CO_2 molecule in its ground electronic $^1\Sigma_g^+$ state by low-energy electrons, see Eq. (1). The process is mediated by three states of the temporary molecular anion CO_2^-: the $^2\Sigma_g^+$ virtual state and the double-degenerate $^2\Pi_u$ shape resonance.

These anionic states are assumed to be diabatic with respect to the vibrational motion described by normal coordinates Q_g, Q_u, and $Q_\pm = Q_x \pm iQ_y$. We refer to these states as discrete electronic states $|d\rangle$, $d \in \{\Pi_+, \Sigma, \Pi_-\}$.

The vibronic dynamics of the CO_2^- is described by a three-component wave function

$$|\Psi\rangle = \begin{pmatrix} |\psi_{\Pi_+}\rangle \\ |\psi_{\Sigma}\rangle \\ |\psi_{\Pi_-}\rangle \end{pmatrix} = \sum_d |\psi_d\rangle |d\rangle, \tag{9}$$

where the components $|\psi_d\rangle$ are functions of the vibrational coordinates expanded in the basis of neutral harmonic vibrational states, see Appendix A of Paper I. The wave function $|\Psi\rangle$ is found by solving the inhomogenous Schrödinger equation

$$[(E - H_0)\mathbb{1} - U - F(E - H_0)]|\Psi\rangle = |\Phi\rangle, \tag{10}$$

where E is total energy conserved during the collision [Eq. (8) in Paper I], H_0 is the vibrational Hamiltonian of the neutral molecule in the harmonic approximation, $U = \{U_{dd'}\}$ is the 3×3 matrix describing the diabatic potential energy surfaces and the direct vibronic coupling of the discrete states, and $F(E - H_0)$ is the nonlocal operator matrix giving the indirect vibronic coupling through the electron continuum [Eq. (6) in Paper I].

The right-hand side of the Schrödinger equation

$$|\Phi\rangle = \begin{pmatrix} V^{\mu_i}_{\Pi_+\epsilon_i}|\nu_i\rangle \\ V^{\mu_i}_{\Sigma\epsilon_i}|\nu_i\rangle \\ V^{\mu_i}_{\Pi_-\epsilon_i}|\nu_i\rangle \end{pmatrix}. \tag{11}$$

describes the vertical attachment of the incoming electron with energy ϵ_i to CO_2 in its ground vibrational state $|\nu_i\rangle$, where the energy-dependent amplitudes $V^{\mu_i}_{d\epsilon}$ control the coupling between the discrete states $|d\rangle$ and the partial-wave components $\mu_i \equiv (l, m)$ of the incoming electron.

To obtain the energy-loss spectra discussed below we solved the Schrödinger equation Eq. (10) for 1500 incident energies $\epsilon_i \in [0.001, 5.0]$ eV and for each included incoming electron partial wave μ_i. An example of these wave functions for $\epsilon_i = 3.8$ eV and $\mu_i = s$ and p_+ is shown in Fig. 4, where the absolute value of $|\psi_d\rangle$ is plotted as a function of symmetric stretching and bending coordinates.[1]

The electron autodetachment from CO_2^- into neutral CO_2 in the vibrational state $|\nu_f\rangle$ is controlled by the amplitude (an element of T matrix)

$$T_{\nu_f\mu_f \leftarrow \nu_i\mu_i} = \sum_d \langle \nu_f | V^{\mu_f *}_{d\epsilon_f} | \psi_d \rangle. \tag{12}$$

The exact relation of this quantity to the cross sections and spectra was derived in Paper I and will be discussed in the text below. We calculated the T matrix for all 1500 values of the incident energy ϵ_i, all partial waves and all accessible harmonic final states $|\nu_f\rangle$ (about 8000 states). These values are stored and both integral and differential cross sections for all final states and angles, as well as 2D electron energy-loss spectra for any scattering angle can be obtained from these matrices in a fast post-processing procedure, see below.

---

[1] The two-dimensional bending can be described by the Cartesian normal coordinates Q_x and Q_y, their complex combinations $Q_\pm = Q_x \pm iQ_y$, or by polar coordinates (ρ, φ), where ρ represents the magnitude of the bending and φ the orientation of the molecular plane, see Sec. II B 1 in Paper I. We plot the wave functions (anionic or vibrational shown above) with respect to the magnitude of the bending measured in bohrs and we set $\varphi = 0$. The dependence on φ gives only an overall phase factor $\exp(i\ell_b\varphi)$ because ℓ_b is fixed for any given vibrational state of CO_2 or one vibrational component $|\psi_d\rangle$ of the anionic wave function.

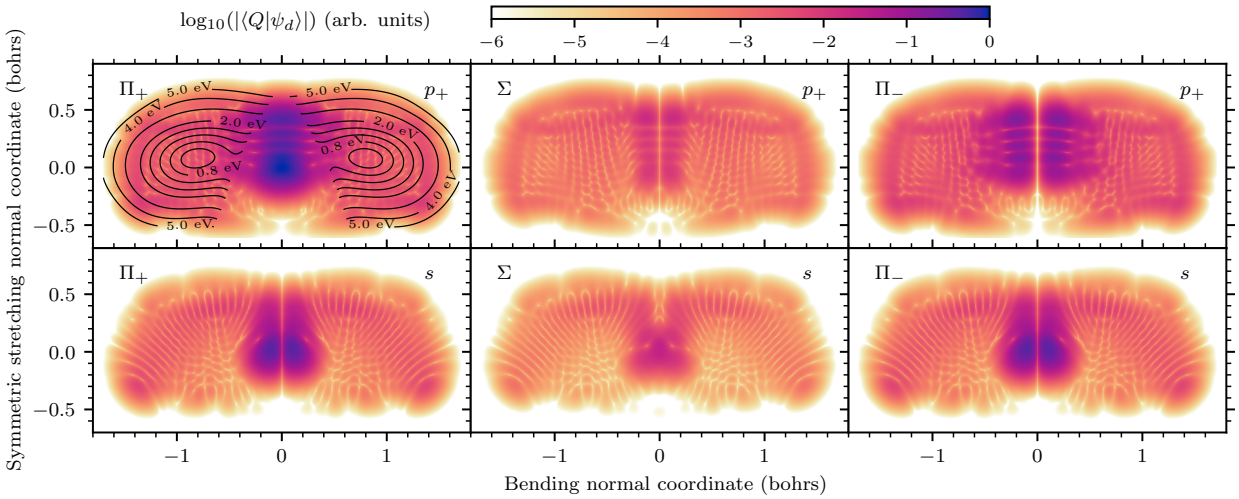

FIG. 4. Vibrational components $\langle Q|\psi_d\rangle$ of the scattering wave function $|\Psi\rangle$ that belongs to the discrete states $|d\rangle$, $d = \Pi_+$, Σ, and Π_- upon symmetric stretching and bending (asymmetric stretching coordinate is set to zero). The shown wave function $|\Psi\rangle$ is the solution of Eq. (10) for incident electron energy of 3.8 eV and for incoming electron partial waves p_+ (first row) and s (second row). The components are all normalized with respect to the global maximum. The contours in the top-left panel represent the lowest adiabatic potential energy surface of CO_2^- for geometries where it is bound and the energies are given with respect to the minimum of the neutral potential.

B. Symmetry considerations for the dynamics and final states

Before proceeding to the actual discussion of the calculated spectra, we would like to comment on the symmetry in the process of vibrational excitation of CO_2, which is closely related to conservation of angular momentum and parity. These principles have already been discussed in Paper I since they are important in the construction of the model, but we need to add a few remarks important for the following discussion of the results.

The total electron and nuclear symmetry of the e+CO_2 system is conserved during the collision. Since the neutral molecule is initially in the ground electronic and ground vibrational states, which are both totally symmetric, the total symmetry is exclusively given by the incoming electron. Its wave function can be decomposed into partial waves $\mu \equiv (l, m)$. As explained in Paper I, there are four electron partial waves, $\mu = s$, p_z, and $p_\pm = p_x \pm i p_y$ considered in our model, which are coupled to the discrete states $|d\rangle$ through the energy-dependent amplitudes $V^\mu_{d\epsilon}$ organized into the following 3×4 matrix [Eq. (18) in Paper I]

$$V_\epsilon = \begin{array}{c} \\ \Pi_+ \\ \Sigma \\ \Pi_- \end{array} \begin{array}{c} \begin{array}{cccc} s & p_z & p_+ & p_- \end{array} \\ \begin{pmatrix} v_{\Pi s} Q_- & v_{\Pi z} Q_- Q_\mathrm{u} & v_{\Pi p} & w_{\Pi p} Q_-^2 \\ v_{\Sigma s} & v_{\Sigma z} Q_\mathrm{u} & v_{\Sigma p} Q_+ & v_{\Sigma p} Q_- \\ v_{\Pi s} Q_+ & v_{\Pi z} Q_+ Q_\mathrm{u} & w_{\Pi p} Q_+^2 & v_{\Pi p} \end{pmatrix} \end{array} \quad (13)$$

with row index d and column index μ. In this matrix we explicitly show the dependence on the vibrational coordinates Q_i that are not totally symmetric. Symmetric combinations of coordinates are still hidden in the coefficients $v_{d\mu}$ and $w_{d\mu}$ (Sec. IV B of Paper I).

For example, the first column of the matrix V_ϵ describes the attachment of an s-wave electron to the molecule given by the right-hand side $|\Phi\rangle$ Eq. (11) of the Schrödinger equation. Its vibrational parts $|\phi_d\rangle$ have the same symmetry as the coordinates in the first column of the matrix V_ϵ, i. e. Π_u, Σ_g^+, and Π_u, in order for the product of $|\phi_d\rangle$ and electronic part $|d\rangle$ to have the same symmetry as the incoming electron s wave, i. e. Σ_g^+. Since the symmetry is respected by the model quantities H_0, U, and $F(E)$, the same discussion applies for the components of the solution $|\Psi\rangle$ Eq. (9). The resulting symmetries of $|\psi_d\rangle$, $|\phi_d\rangle$ are listed in the first block of Table I. These symmetries can be observed in Fig. 4. The wave functions in the top row of the figure have symmetries Σ_g^+, Π_u and Δ_g as apparent from their shape since the probability close to the zero axis of the bending coordinate is being pushed to higher bending values for a larger angular momentum projection.

Due to the vibronic coupling built in the Q-dependence of the matrix V_ϵ, the symmetry of the outgoing electron can differ from the symmetry of the incoming electron. This change has to be compensated by the final vibrational state of CO_2, that is, the product of the vibrational and electronic parts of the final e+CO_2 wave function has to have the same symmetry as the incoming electron. In our model, the final states of the Σ_g^+, Σ_u^+, Π_g, Π_u, and Δ_g symmetries can be excited, see the second block of Table I.

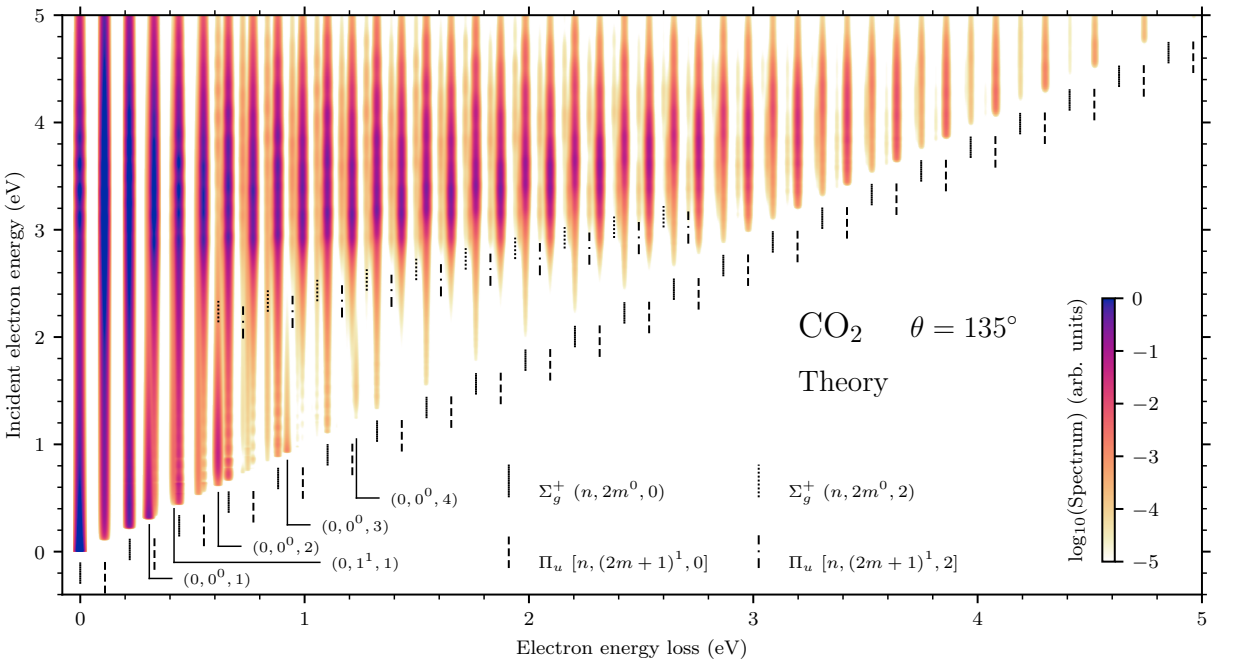

FIG. 5. Calculated 2D electron energy-loss spectrum of CO_2 for harmonic final vibrational states and for a scattering angle of 135°. Positions of some harmonic vibrational levels of CO_2 within our model are shown, see the legend ($n + m = 0, 1, \ldots$).

V. CALCULATED SPECTRA

Finally, we present the results of our calculations. We start with the spectrum calculated directly using harmonic basis as final states and then we describe the results of the transformation of the final states into Fermi-coupled basis, which could be more directly compared to experiments.

A. Spectrum with harmonic final states

The differential cross section $d\sigma_{\nu_f \leftarrow \nu_i}/d\Omega(\epsilon_i)$ for the vibrational excitation of the CO_2 molecule from the initial state $|\nu_i\rangle$ to the final state $|\nu_f\rangle$ is calculated from the T-matrix elements Eq. (12) by summing over initial μ_i and final μ_f partial waves including the proper angular factors for each symmetry of the final state. The formulae are given in Appendix D of Paper I and they also include the averaging over the orientation of the molecule.

The final 2D spectrum intensity $S(\epsilon_i, \Delta\epsilon)$ is obtained by identifying the energy loss $\Delta\epsilon = \epsilon_i - \epsilon_f = E_{\nu_f} - E_{\nu_i}$ for each final state and adding a Gaussian profile $f(x)$ with the full width at half maximum of 18 meV to the electron-loss lines to simulate the finite experimental resolution

$$S(\epsilon_i, \Delta\epsilon) = \sum_{\nu_f} \frac{d\sigma_{\nu_f \leftarrow \nu_i}}{d\Omega}(\epsilon_i) f(\Delta\epsilon - \Delta\epsilon_{\nu_f}). \qquad (14)$$

Note that we also convolve the spectra with the incident electron energy resolution function but it does not effect significantly the results since the cross sections are rather smooth in ϵ_i.

TABLE I. Correlation of the symmetry of the electronic and vibrational parts of the wave function resulting from the conservation of angular momentum and parity. Rows correspond to partial waves of the incident electron. The first block (columns 2–4) gives the symmetry of the vibrational parts $|\psi_d\rangle$ for the three discrete states $|d\rangle$. The second block shows the vibrational symmetry of the resulting CO_2 when the electron leaves as partial wave μ_f.

	$\|\psi_d\rangle$ for d:			$\|\nu_f\rangle$ for μ_f:			
μ_i	Π_+	Σ	Π_-	s	p_z	p_+	p_-
s	Π_u	Σ_g^+	Π_u	Σ_g^+	Σ_u	Π_u	Π_u
p_z	Π_g	Σ_u^+	Π_g	Σ_u^+	Σ_g^+	Π_g	Π_g
p_+	Σ_g^+	Π_u	Δ_g	Π_u	Π_g	Σ_g^+	Δ_g
p_-	Δ_g	Π_u	Σ_g^+	Π_u	Π_g	Δ_g	Σ_g^+

Figure 5 shows the 2D energy-loss spectrum for harmonic final vibrational states of CO_2 and a scattering angle of 135°, where the Fermi resonance effect is not included. The harmonic spectrum is dominated by energy-loss peaks at positions of Σ_g^+ and Π_u harmonic states that belong to polyads $(n, 2m^0, 0)$ and $[n, (2m+1)^1, 0]$, respectively. Their energy losses are given by $\Delta\epsilon = N\omega_g$ and $N\omega_g + \omega_b$, $N = n + m = 0, 1, \ldots$, respectively. In the case of asymmetric stretching mode, only $(0, 0^0, 1)$ and $(0, 0^0, 2)$ states are significantly populated, especially

near the threshold. The higher Σ_g^+ and Π_u polyads derived from the $(0, 0^0, 2)$ state are also clearly seen in the spectrum although the magnitude of the signal is about three orders of magnitude smaller. Higher values of ν_u are not populated significantly but are included in the presented data.

The harmonic spectrum of Fig. 5 reproduces qualitatively the general shape of the spectrum seen in the current and previous experiments [13, 14]. At low energy losses the signal starts directly at the threshold. In the $^2\Pi_u$ resonance region (incident energies 3–4 eV), the signal extends to the complete energy loss. The hint of the boomerang oscillations [4, 60], which creates the diagonal rays in the spectrum, is also visible but their positions do not correspond to the experimental positions because of the substantial difference of our potentials along the symmetric stretching direction due to the harmonic approximation of the neutral molecule, see the discussion in Sec. V A of Paper I.

The most obvious difference between the experimental (Fig. 1) and theoretical (Fig. 5) spectra is the contrast between continuous character of the experimental spectrum and the discrete lines at specific energy losses dominating the theoretical spectrum. This is the effect of using the harmonic polyads (and their energies) as the final states in our calculations instead of the Fermi-coupled states. Let us also remind that the model vibrational frequencies are $\omega_b = 110$ meV, $\omega_g = 2\omega_b$, and $\omega_u = 308$ meV, which originate from the *ab initio* R-matrix data (Sec. IV C in Paper I). The frequencies in the case of bending and symmetric stretching are about 30% larger than the experimental values and one symmetric stretching quantum is exactly degenerate with two quanta of bending. The difference of the frequencies $\omega_s - 2\omega_b = 0.9$ meV does not explain the continuous character of the experimental spectrum since the highest polyads $N = 30$ fitting in the energy window still have energy spread comparable to the experimental resolution (Sec. III A). The Fermi coupling that mixes the states and splits their energies (Sec. III B) is responsible for the quasi-continuous character of the spectra. Note that in the energy range of interest the spectrum comprises of about 8000 states.

B. Spectrum with Fermi-coupled final states

As discussed in Sec. IV and VI of Paper I, we restricted the model only to harmonic vibrations of the neutral molecule. The anharmonic terms are included in the dynamics of the temporary molecular anion through the dependence of the vibronic coupling matrices U and V_ϵ on the polynomials of the vibrational coordinates. However, the harmonic states of the neutral CO_2 enter the nonlocal term $F(E - H_0)$ and the calculation of the T matrix Eq. (12) through the projection on the final harmonic vibrational state $|v_f\rangle$.

The first of these two approximations is important in order for the four-dimensional nonlocal dynamics to be manageable but the latter one is rather easily corrected by projecting the anionic wave function on the Fermi-coupled states $|\nu_{\rm FR}\rangle$, which are given by the expansion into the harmonic basis with the coefficients c_ν [Eq. (6)]. In practice, such a projection to the Fermi-coupled state leads to the linear combinations of the harmonic T matrices

$$T_{\nu_{\rm FR}\mu_f \leftarrow \nu_i\mu_i} = \sum_\nu c_\nu \, T_{\nu\mu_f \leftarrow \nu_i\mu_i}. \qquad (15)$$

The differential cross sections $d\sigma_{\nu_{\rm FR}\leftarrow\nu_i}/d\Omega(\epsilon_i)$, given in Appendix D of Paper I for the harmonic final states, are then obtained by the same procedure in which the T matrices Eq. (15) replace the harmonic T matrices Eq. (12). Note that Rescigno *et al.* [37] used a similar procedure with mixing coefficients derived by Dennison [58] to compute the excitation of the members of the Σ_g^+ Fermi dyad from their population of harmonic states.

The 2D spectrum with the corrected final states is calculated in a straightforward manner using Eq. (14) with the cross sections $d\sigma_{\nu_{\rm FR}\leftarrow\nu_i}/d\Omega(\epsilon_i)$, the anharmonic energy losses $\Delta\epsilon_{\rm FR}$, and summed over all $\nu_{\rm FR}$. The remaining harmonic approximation inside $F(E - H_0)$ should have a smaller effect since the action of the nonlocal potential contains an average over many states in the harmonic approximation of H_0. The exception will be the threshold region as discussed below.

Figure 6 shows the calculated 2D spectrum at 135° for the Fermi-coupled final vibrational states. As expected, the most obvious effect compared to the harmonic spectrum (Fig. 5) is the disappearance of the vertical bands associated with polyads in the deeply inelastic region. The spectrum also considerably shrinks in the energy-loss direction because of the 30 % difference of the model and experimental vibrational frequencies. The vibrational Hamiltonian of Chedin [59] produces energies of the Fermi-coupled states that are in a very good agreement with spectroscopic data. The employed procedure corrects only the energy of the final electron. The dependence on the incoming electron is not effected. Therefore, the corrected 2D spectrum does not respect the threshold diagonal line, which is approximately 30% more steep and also broken. Also the Wigner cusps seen in some channels [35] do not have the correct position in our calculation, see the discussion below.

Despite these distortions, the spectrum in Fig. 6 qualitatively reproduces the measured spectrum in Fig. 1. We observe the boomerang rays although their exact positions are influenced by the distorted shape of the potentials. Both structures of type A and B discovered by Currell and Comer [13, 14] are present and the fine structure at high energy losses has the correct shape, see also the comparison in Fig. 1 in Letter.

The qualitative agreement is even more apparent when 1D spectra are compared, see Fig. 7, where the spectra for incident energies 3.2, 3.5, 3.8, and 4.1 eV are plotted in the similar way as the experimental ones in Fig. 2. The spectra clearly follow the same pattern. At small

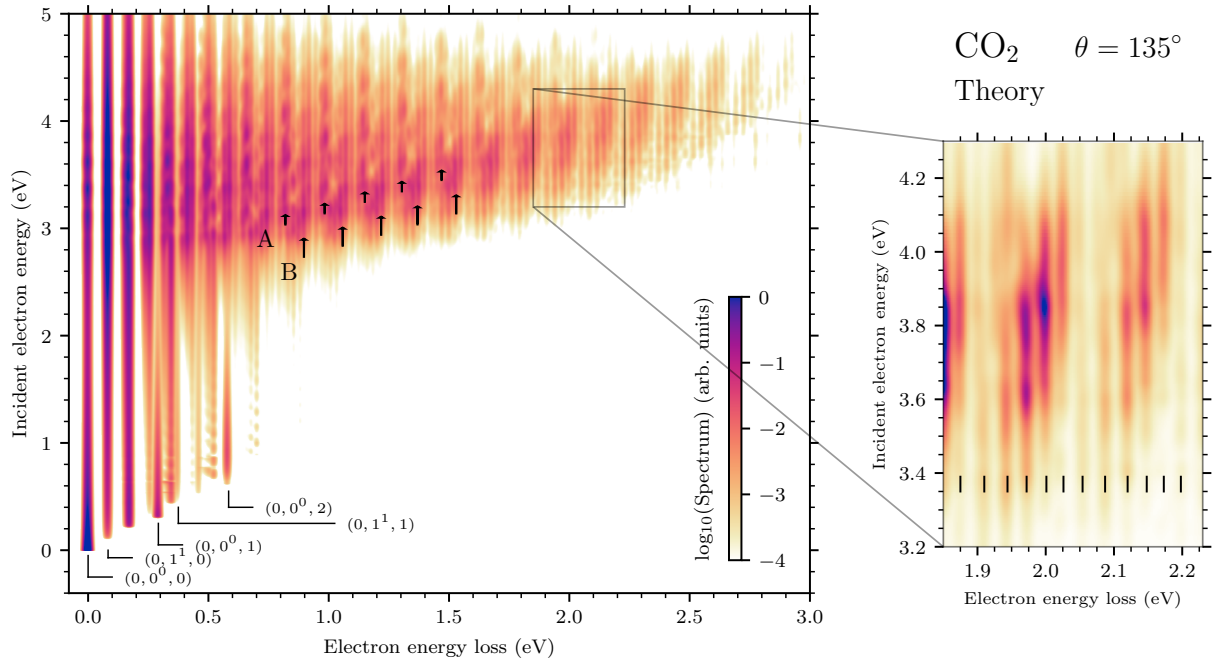

FIG. 6. Calculated 2D electron energy-loss spectrum of CO_2 for Fermi-coupled final vibrational states and a scattering angle of 135°. The magnified section of the signal (right – shown in linear scale from 0 to 1) focuses on a detail of the high energy loss features where the fine structure with spacing 25–33 meV is indicated. Structures *A* and *B* observed by Currell and Comer [12–14] are labeled in the main plot.

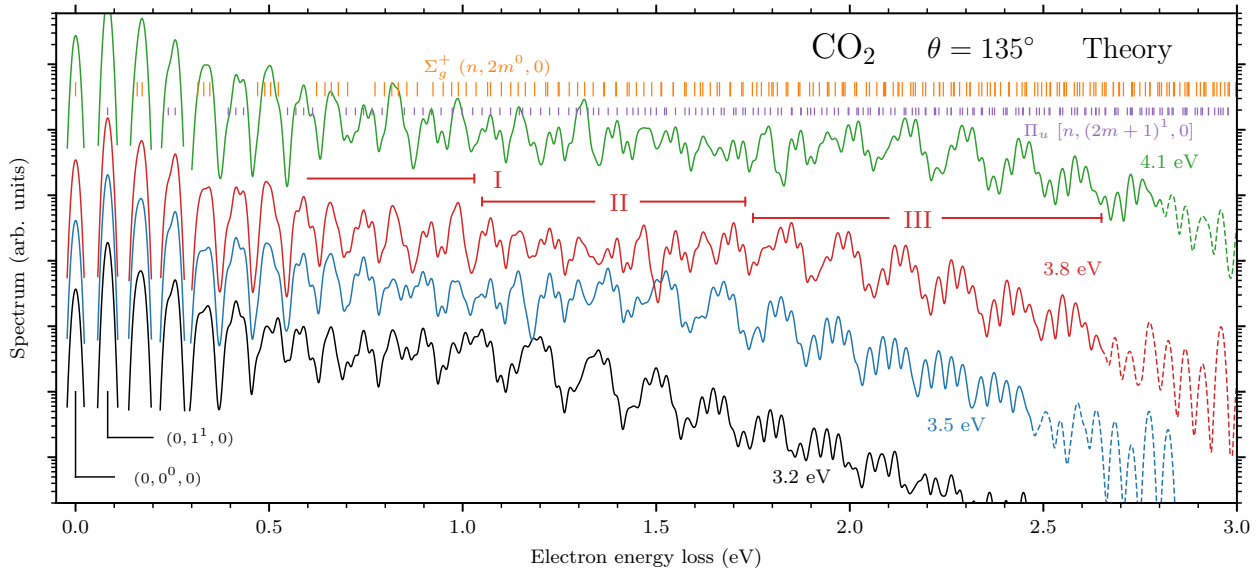

FIG. 7. Calculated 1D electron energy-loss spectra for Fermi-coupled final vibrational states and for a scattering angle of 135° and incident electron energies 3.2, 3.5, 3.8, and 4.1 eV. The spectra are shown in the logarithmic scale but lines for different incident energies are arbitrarily shifted with respect to each other. Calculated energies of states within Σ_g^+ $(n, 2m^0, 0)$ and Π_u $[n, (2m+1)^1, 0]$ Fermi polyads $(n + m = 0, 1, \ldots)$ are shown. Regions of order, chaos, and order observed by Allan [10] are labeled by I, II, and III for the 3.8 eV spectrum. The very end of the spectra near the threshold line (dashed parts) is an artifact of the anharmonic correction of final state energies, see the text.

energy losses we observe well distinguishable peaks of the Σ_g^+ and Π_u symmetries, then, a seemingly chaotic region (region II) occurs at intermediate energy losses, which is not as pronounced in the theory as it is in the experiment, and finally, there are broad peaks modulated by the fine structure with spacing of 25–33 meV at the end of the spectra. The analysis that reveals the origin of these features is deferred to the next section. The very end of the spectra (dashed parts in Fig. 7) is an artifact caused by the above mentioned inconsistency of the energies in the dynamics and the corrected energies of the Fermi-coupled levels. It only affects the near threshold region, i. e. high energy losses for incident energies in the region of the $^2\Pi_u$ resonance.

Although the fundamental asymmetric stretching mode $(0, 0^0, 1)$ is excited in our model (Figs. 5 and 6), it is excited by about one order of magnitude less in the region of the $^2\Pi_u$ resonance than experimental observations show [35] and is barely not visible in the 1D spectra. Our calculations only include the resonant (discrete-state) contribution to the vibrational excitation T matrix but we expect a considerable contribution of the background scattering to the elastic peak. It would also explain why the elastic cross section for a high scattering angle is less excited than the $(0, 1^1, 0)$ peak.

Before going to the detailed analysis of the spectra, we also look closer to the region of small initial electron energies ($\epsilon_i < 2.8$ eV), which is not covered by the current experimental data. The threshold region dominantly influenced by the $^2\Sigma_g^+$ virtual state of CO_2^- is visible in both calculated 2D spectra (Figs. 5 and 6). We would also like to remind a deficiency of our model that influences this region. The CO_2 molecule acquires a dipole moment upon bending or asymmetric stretching, which is not included in our model because the geometry dependence of the threshold exponent of the coupling amplitudes $V_{d\epsilon}^{\mu}$ would substantially increase the computational cost of the dynamics. As a result, threshold peaks are not as sharp and pronounced as in the experiments [34, 35]. The cross sections will be discussed in Sec. VI D.

In Fig. 8, we show 1D spectra for fixed final electron energy (residual energy) of 0.12 and 3.8 eV (diagonal cuts through the 2D spectrum). The intensity of the excited peaks does not match perfectly with the experimental observations of Allan [34, 35] but the calculations qualitatively reproduce the selectivity of the low-lying Fermi-coupled states near the threshold and in the region of the $^2\Pi_u$ resonance. Compare our Fig. 8 with Fig. 1 in Ref. [34] and Fig. 2 in Ref. [35]. Allan in Refs. [34, 35] reached an astonishing resolution of 7 meV. Therefore, we used the same value in Eq. (14) to produce Fig. 8. To avoid the above mentioned artifacts near the main diagonal in the spectrum, we chose slightly higher final energy (0.12 eV) in Fig. 8 in comparison to 0.05 eV of Allan [34, 35]. The top members of the polyads are dominantly excited at the threshold because the vibrational wave function of these members reaches the closest to the region where the anionic and neutral potentials cross, see

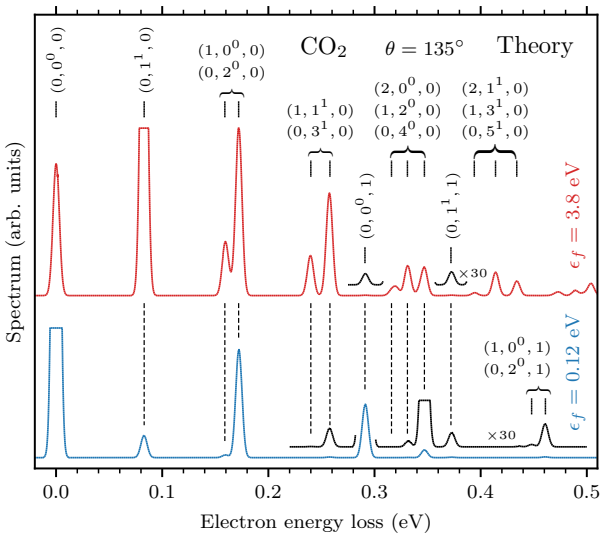

FIG. 8. Calculated 1D electron energy-loss spectra for fixed final electron energy of 0.12 eV (lower line) and 3.8 eV (upper line) and for a scattering angle of 135°. Some peaks are, for clarity, cut off. Compare it with experimental results of Allan shown in Fig. 1 of Ref. [34] and Fig. 2 of Ref. [35].

Vanroose *et al.* [39], who reproduced such a behavior for the Σ_g^+ polyads. The Π_u polyads follow the same mechanism. At small incident energies, our $(0, 1^1, 0)$ peak is suppressed in comparison to the experiment due to the missing dipole in our model.

VI. ANALYSIS OF THE RESULTS

In Secs. II and V, we have presented the obtained experimental and theoretical results. Here, we focus on a further analysis of the calculations to understand the underlying mechanisms. We start by decomposing the spectra based on vibrational state symmetries and electron partial waves. Then, we examine which states within the vibrational pseudocontinua are dominantly excited and we describe propensity rules in terms of wave functions. We use the obtained insight to interpret the experimental data and also discuss the angle dependence. We conclude this part by discussing the energy dependence of cross sections for low-lying final vibrational states.

A. Dominant vibrational state symmetries

We can decompose the 1D energy-loss spectrum based on final state symmetries included in our model (Σ_g^+, Σ_u^+, Π_g, Π_u, and Δ_g), see Fig. 9. The spectrum is almost completely described by excitation of Σ_g^+ and Π_u vibrational states, from which the Fermi polyads $(n, 2m^0, 0)$ and $[n, (2m+1)^1, 0]$ dominate. States within Σ_g^+ $(n, 2m^0, 2)$

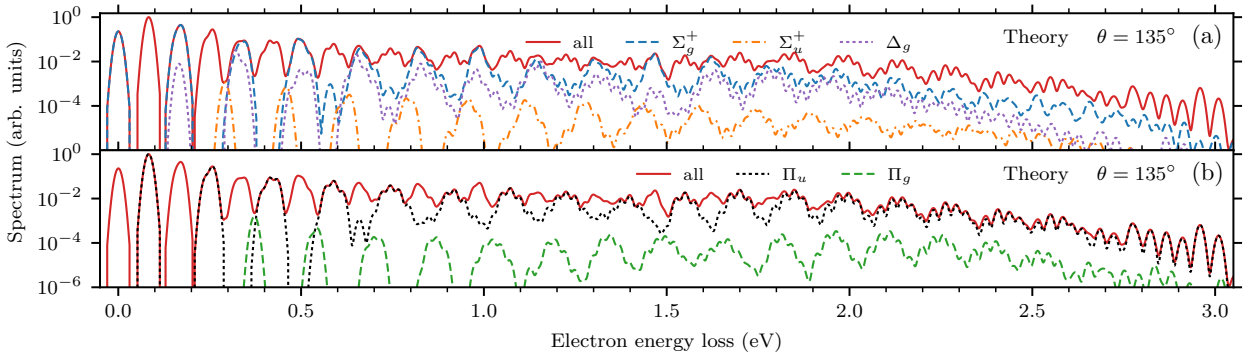

FIG. 9. Decomposition of the calculated 1D electron energy-loss spectrum for a scattering angle of 135° and incident electron energy of 3.8 eV to contributions of individual symmetries of final vibrational states. Panel (a): contributions of Σ_g^+, Σ_u^+, and Δ_g symmetries. Panel (b): contributions of Π_u and Π_g symmetries.

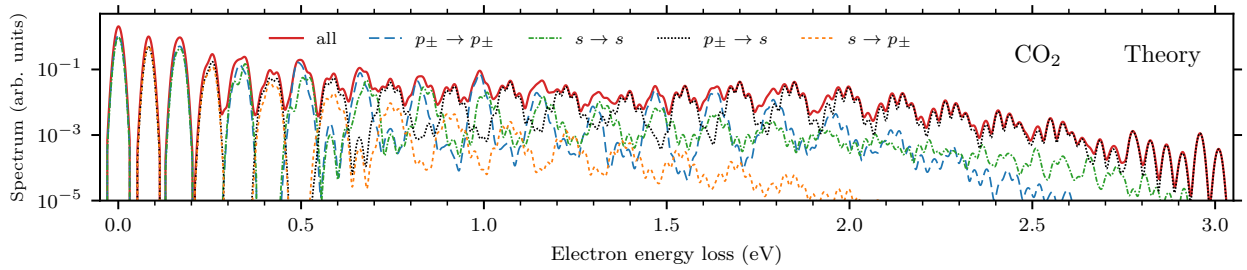

FIG. 10. Decomposition of the calculated integral 1D electron energy-loss spectrum for incident electron energy of 3.8 eV to contributions of individual incoming and outgoing partial waves. Processes $p_\pm \to p_\pm$ and $s \to s$ leads to excitation of Σ_g^+ vibrational states while Π_u states are excited when $p_\pm \to s$ and $s \to p_\pm$.

and Π_u $[n, (2m+1)^1, 2]$ polyads are included in the contributions shown in Fig. 9 but they are negligible as is apparent from the harmonic 2D spectrum in Fig. 5. States of the Δ_g symmetry are moderately excited throughout most of the spectrum but they are masked by similar energy dependence of the Σ_g^+ states. The Σ_u^+ and Π_g states, containing at least one excitation of the asymmetric stretching, do not contribute substantially.

The selection rules [43, 44, 61] predict strong excitation of Σ_g^+ and Δ_g vibrational states since they belong to the symmetrized square of the Π_u representation of the $^2\Pi_u$ resonance[2] and the excitation of the Π_u symmetry because the electron leaves as an s wave, see Sec. I. Overall, the results in Fig. 9 are in accordance with the selection rules. The mutual ratio of the Σ_g^+ and Δ_g is the result of the dynamics.

The decomposition of the spectrum to symmetries of the final states is straightforward since it is just a separation of different symmetries in the sum over all states in Eq. (14). The contributions of the individual electron partial waves are more easily identified in the spectrum integrated over all scattering angles, which we can calculate also from Eq. (14) by replacing the differential cross sections $d\sigma_{\nu_{\rm FR}\leftarrow\nu_i}/d\Omega(\epsilon_i)$ with the integrated ones $\sigma_{\nu_{\rm FR}\leftarrow\nu_i}(\epsilon_i)$. This quantity is simply a sum over all combinations of the initial and final partial waves μ_i, μ_f [see Eq. (52) in Paper I] while the differential cross sections also contain interference terms.

Figure 10 shows the dominant contributions to the integral energy-loss spectrum in terms of incoming and outgoing partial waves. As shown in Table I, to excite the totally symmetric Σ_g^+ states, the electron symmetry does not change during the process and we have four contributions: $s \to s$, $p_z \to p_z$, $p_+ \to p_+$, and $p_- \to p_-$. The $p_z \to p_z$ process is negligible and $p_+ \to p_+$ and $p_- \to p_-$ give the same contribution. In the case of Π_u states, there has to be a change of the angular momentum, thus, they can be excited via $p_\pm \to s$ or $s \to p_\pm$ processes.

The attaching s wave contributes almost equally to the elastic peak and the $(0, 1^1, 0)$ peak as the $p_\pm$ waves. The $p_\pm$ attachment is expected to be dominant since $p_\pm$ are the principal partial waves of the $^2\Pi_u$ shape resonance. As we will see below, the Σ_g^+ virtual state does not significantly affect the dynamics at incident energies around 3.8 eV, therefore, the s wave also substantially populates

[2] Characters of the symmetrized square of a representation are given by $[\chi^2](R) = [\chi(R)^2 + \chi(R^2)]/2$, where R denotes the symmetry operation [43].

the $^2\Pi_u$ resonance. The s wave cannot populate the resonance at the equilibrium linear geometry but due to the delocalized nature of the initial vibrational state $|\nu_i\rangle$, it attaches through the exponential tails to the $\Pi_\pm$ discrete states. Such a weaker attachment is compensated by the prefactor function $v_{\Pi s}$ [Eq. (13)], which is also responsible for the rapid broadening of the resonance width of the lower Renner-Teller component upon bending, see potentials in Fig. 4(b) and Sec. V B in Paper I.

In Fig. 10, we can also observe a selectivity of the outgoing electron. Independently of the incoming partial wave, the outgoing s electron dominates over $p_\pm$ electrons at high energy losses, which is the consequence of Wigner threshold law [62]. The partial resonance widths $2\pi|V^\mu_{d\epsilon}|^2$ behave near the threshold as $\epsilon^{(2l+1)/2}$ with $l = 0, 1$ for s, p electrons. Thus, the electron preferentially detaches from the molecular anion as the s wave at small final energies.

B. Excitation of individual states and fine structure

We have seen that the Σ_g^+ $(n, 2m^0, 0)$ and Π_u $[n, (2m+1)^1, 0]$ Fermi polyads dominate the spectrum. Now, we pinpoint the states responsible for the observed structures emerging from the vibrational pseudocontinua.

We can analyze the contribution of individual final states to the theoretical spectrum in terms of the quantity $\langle\nu_g\rangle$, see Eq. (7). Figure 11 shows the calculated cross sections $d\sigma_{\nu_{\rm FR}\leftarrow\nu_i}/d\Omega(\epsilon_i)$ entering the sum in Eq. (14) for the spectrum with the Fermi-coupled states $|\nu_{\rm FR}\rangle$ grouped into the polyads (full symbols) in combination with the $\langle\nu_g\rangle$ values (open symbols). In the case of the Σ_g^+ $(n, 2m^0, 0)$ polyads [Fig 11(a)], the states from the end of the polyads are dominantly excited for the lowest polyads but as the energy loss increases we observe a shift to excitation of the most linear states (largest $\langle\nu_g\rangle$). Typically only two to three states from one polyad are excited enough to visibly affect the spectrum. The trend is similar but to some degree different for the Π_u symmetry [Fig. 11(b)]. The significance of peaks shifts from the end of the polyads to states at fixed positions (fifth and sixth states) somewhat in front of the maximum of $\langle\nu_g\rangle$.

The individual polyads within one symmetry dominate at different energy-loss ranges and the excitation of the several consecutive fairly linear states gives rise to the fine structure, whose energy spacing is not constant but varies around 25–33 meV. A detail of the fine structure is also shown in Fig. 4 in Letter.

To understand why only fairly linear states are significantly excited, we have to look at the wave functions. In Fig. 4, we have presented the scattered wave function $|\Psi\rangle$, which illustrates the dynamics even though we work in the time-independent picture. The initial vibrational state of CO_2^- is given by the wave function $|\Phi\rangle$ [Eq. (11)], that is, we have Gaussian packets modified by the coupling amplitude $V^{\mu_i}_{d\epsilon_i}$ on each potential energy surface. Then, the wave packets move predominantly along the symmetric stretching coordinate since only in this direction there is a nonzero gradient at the equilibrium geometry, see the potentials in Fig. 4 in Paper I. As the anion symmetrically stretches, the wave packets probe bent geometries too but the anion decays with a high probability by the electron autodetachment because of the large resonance width of the lower Renner-Teller component of the $^2\Pi_u$ resonance. This results in the significant suppression of the scattered wave functions at highly bent configurations in comparison to the vicinity of the symmetric stretching axis (Fig. 4). But note that the wave function still fills the energy-allowed region, see the contours of the lowest adiabatic potential in the top left panel of Fig. 4 and the potentials in Fig. 4 of Paper I.

The dynamics is also confined in the asymmetric stretching because the potentials are repulsive in addition to the missing gradient at the equilibrium geometry. The excitation of vibrational states is controlled by the T-matrix element Eq. (12), and thus, the states that have the probability density localized along positive symmetric stretches are dominantly populated, see the vibrational wave functions in Fig. 3. Moreover, the $^2\Sigma_g^+$ virtual state has a negligible effect on the spectra for incident energies above $\sim$3 eV since the magnitude of the Σ component $|\psi_\Sigma\rangle$ of the anionic wave function is substantially smaller than the magnitude of the $\Pi_\pm$ components (Fig. 4). This was directly confirmed by calculations where the Σ discrete state was absent, see also Secs. VI D and VII B.

Now, we can confront these findings with the experiment, see Fig. 12 where the full and open symbols represent the $\langle\nu_g\rangle$ quantity for states within the Σ_g^+ and Π_u polyads, respectively. We observe the same trend of shifting the significance of the states within the polyads. It is not as clear for the Σ_g^+ symmetry because the shift towards the most linear states is somewhat slower and they soon disappear in the middle "chaotic" region, but the Π_u states distinctly follow the pattern. This time, the high energy-loss region (around 3 eV) is dominated by excitation of states at around the seventh and eighth positions within the Π_u polyads, see the last column in Fig. 3.

To summarize, the competition of the Σ_g^+ $(n, 2m^0, 0)$ and Π_u $[n, (2m+1)^1, 0]$ Fermi polyads explains the shape of the energy-loss spectra. The peaks are well separated in region I since the polyads do not overlap (Figs. 2 and 7). The complex region II is given by the overlapping Σ_g^+ and Π_u contributions, which have similar magnitudes. As the energy loss increases the selectivity of the outgoing s-wave electrons starts to favor the Π_u states, which dominate in region III and are responsible for the broad peaks. The A and B structures of Currell and Comer [13, 14] originate from the Σ_g^+ and Π_u contributions, respectively.

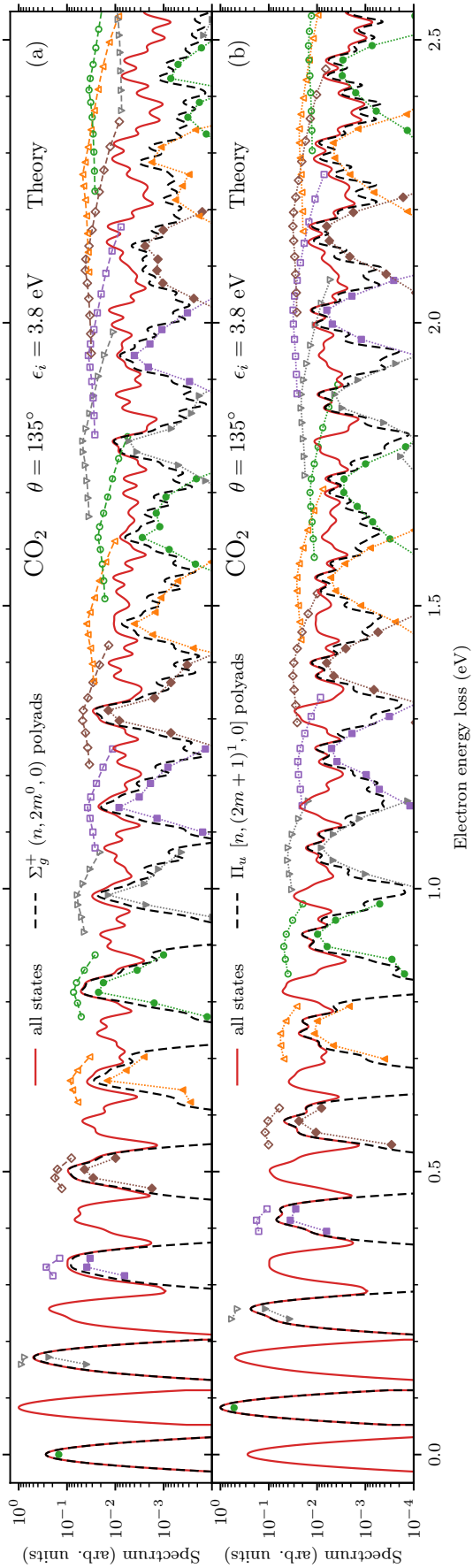

FIG. 11. Analysis of calculated 1D electron energy-loss spectrum for a scattering angle of 135° and incident electron energy of 3.8 eV. Full symbols represent the calculated cross sections (scaled down with respect to the spectrum for clarity) for exciting individual Fermi final vibrational states grouped into polyads. For each final state, the value of number of symmetric stretching quanta $\langle \nu_g \rangle$ (arbitrarily scaled) is shown by the open symbol above the spectra to indicate the character of the state, see the text. Panel (a) shows final states that belong to $\Sigma_g^+ \, (n, 2m^0, 0)$ Fermi polyads and Panel (b) shows $\Pi_u \, [n, (2m+1)^1, 0]$ Fermi polyads $(n + m = 1, 2, \ldots)$.

FIG. 12. Analysis of experimental 1D electron energy-loss spectrum for a scattering angle of 135° and incident electron energy of 3.8 eV. Symbols represent the theoretical energy and the value of number of symmetric stretching quanta $\langle \nu_g \rangle$ (arbitrarily scaled) for vibrational states grouped into Fermi polyads. Full symbols show $\Sigma_g^+ \, (n, 2m^0, 0)$ polyads with $n + m = 1, 2, \ldots, 7$. Open symbols show $\Pi_u \, [n, (2m+1)^1, 0]$ polyads with $n + m = 1, 2, \ldots, 7, 9, 10, 13, 14, 17, \ldots, 21$. Note that there are $N + 1$ states for a polyad with $n + m = N = \text{const}$.

C. Angular dependence

We also investigated the angular dependence of the calculated energy-loss spectrum for incident electron energy of 3.8 eV, see Fig. 13(a). The deeply inelastic region (above 1.8 eV) is almost independent of the angle, which is consistent with our interpretation in terms of final Π_u states dominated by the $p_\pm \to s$ change of the electron partial waves, where the outgoing s wave leads to the isotropic character. To further experimentally verify this mechanism, we measured the spectrum for the scattering angles $\theta = 10^\circ$ and 45°, see Fig. 13(b). First, we should explain an experimental artifact with respect to the data in Fig. 13(b). The analyzer sensitivity for the recording of slow electrons is very low for small scattering angles. This is manifested as an artificial cutoff of the spectrum at near complete energy losses (for $\theta = 10^\circ$ the electrons with residual energies below 300 meV are not recorded, electrons slower than 100 meV are missing for 45°). The most probable reason for this cutoff is charging of the analyzer entrance slit by the primary electron beam. Also note that we normalized the experimental spectra to coincide at the peak of the Σ_g^+ Fermi dyad $\{(1,0^0,0),\ (0,2^0,0)\}$, which is assumed to be relatively weakly dependent on the angle. The theoretical spectra are calculated with the same mutual normalization.

Truly, the shape of the experimental broad peaks at high energy losses ($\sim$3 eV) depends weakly on the scattering angle. For smaller energy losses, the Π_u peaks are suppressed at small angles because the $s \to p_\pm$ transition contributes while the Σ_g^+ peaks depend weakly on the angle, which is also consistent with previous measurements [10, 17–19, 28–33]. The analysis of the experimental spectrum for $\theta = 10^\circ$ in terms of the $\langle \nu_g \rangle$ quantity, see the previous section, confirms that the broader peaks at moderate energy losses are of the Σ_g^+ symmetry centered at the most linear states.

Overall, we can not expect a good agreement between our calculations and the experiments for the angular dependence. First, the direct scattering due to the dipole acquired at distorted geometries, which is not included in our model, significantly affects the elastic peak $(0,0^0,0)$ and principal excitation $(0,1^1,0)$ and $(0,0^0,1)$ [17–19]. Second, the R-matrix calculations show (Sec. V C in Paper I) that d- and f-waves strongly contribute to the $^2\Pi_u$ resonance but we limited the model to the lowest partial waves needed to excite all fundamental modes. As mentioned in Paper I, our s- and p-wave model includes higher partial waves in an averaged sense since we fitted the scattering eigenphase sums and so we expect that the results will be more accurate for the integral cross sections rather then the differential ones.

In the experimental spectrum, the fundamental asymmetric stretching peak $(0,0^0,1)$ is strongly peaked in the forward direction and we also observe excitation of the Σ_u^+ Fermi dyad given by a mixture of harmonic states $(1,0^0,1)$ and $(0,2^0,1)$. Two quanta of asymmetric stretching $(0,0^0,2)$ seems to be visible at $\theta = 10^\circ$ but for higher angles the $(0,0^0,2)$ peak is hidden under the Π_u triad. On the other hand, we do not observe the $(0,1^1,1)$ peak of the Π_g symmetry for any angle at the incident energy of 3.8 eV.

D. Cross sections

Hitherto, we have analyzed the 2D spectrum from the point of view of the electron energy loss. In this section, we focus on the vibrational excitation cross sections, that is, 1D profiles along the incident electron energy axis for fixed energy loss corresponding to energies of individual final vibrational states of CO_2.

Figure 14 shows the differential cross sections for a scattering angle of 135° for excitation of various low-lying vibrational states of CO_2. As expected from the simplifications used in the model, we find only a qualitative agreement with experimental observations [35]. The resonance broad peak at 3–4 eV is modulated by the boomerang oscillations [4, 60]. As was shown by Rescigno *et al.* [37] and we will see it here in Sec. VII, these oscillations originate from the symmetric stretching and are dampen by the bending motion. In our calculations, the oscillations are more pronounced because they are sensitive to the shape of the potential, which substantially differs from the *ab initio* potential in our model due to the employed harmonic approximation for the neutral molecule, see Fig. 7 in Paper I. The elastic cross section is about order of magnitude less excited due to the missing direct background scattering in our calculations.

The excitation and selectivity of the members of the low-lying Σ_g^+ Fermi polyads (dyad, triad, ...) observed by Allan [34, 35] and discussed here in Sec. V is already well reproduced by the theory thanks to the work of McCurdy *et al.* [36] and Vanroose *et al.* [39], who treated the threshold and resonance regions separately. We can provide a further insight, see Fig. 15, where the cross sections for the lower (I, $\Delta\epsilon = 0.159$ eV) and upper (II, $\Delta\epsilon = 0.172$ eV) members of the Σ_g^+ dyad are shown [Fig. 15(a)], in combination with the harmonic states $(1,0^0,0)$ and $(0,2^0,0)$ that these members comprise of [Fig. 15(b)]. Except for the missing sharp threshold peak of the upper member, the general shape is well reproduced. The process $s \to s$ (dashed lines) overall dominates over $p_\pm \to p_\pm$ (the difference between full and dashed lines) and it contributes to the cross sections to both harmonic states, which results in the observed cancellation of the cross section for the lower member in the low to middle region [34] in comparison to Refs. [36, 37].

Despite the interesting topology of the $1\,^2A_1$ and $2\,^2A_1$ potentials upon bending (Sec. V in Paper I), we do not observe any related effects in the region of the $^2\Pi_u$ resonance, see dotted lines in Fig. 15, which were calculated without the Σ discrete state (all relevant parameters were set to zero). Without the Σ state, the lower Renner-Teller component is connected with the nonlinear minimum and the surfaces behave similarly to the model of McCurdy

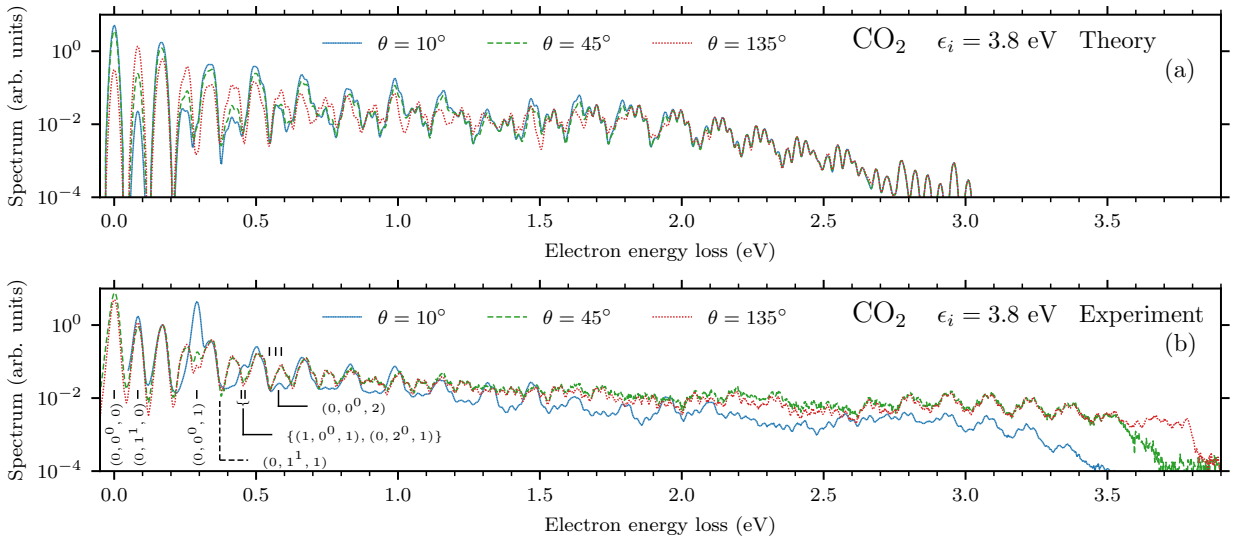

FIG. 13. Dependence of the electron energy-loss spectra at incident electron energy of 3.8 eV on the scattering angle θ for the calculations (Panel a) and the experiment (Panel b).

et al. [36] (Figs. 6 and 8 in Paper I). The region where the $1\,^2A_1$ potential crosses (or rather merges with) the neutral potential is important at very low incident energies (Fig. 15). For higher polyads $n + m \geq 2$, oscillatory structures appear in the cross sections [35, 39]. In our calculations, we also observe such structures (visible in the 2D spectra in Figs. 5 and 6) but again their precise position is not reproduced due to the missing dipole and too large vibrational frequencies in the dynamics.

VII. SENSITIVITY OF THE RESULTS TO MODEL PARAMETERS

A. Sensitivity to values of parameters and fitting

Here, we conclude the discussion from Paper I (Sec. V) about the model construction and sensitivity of the calculations to the model parameters.

The construction of a discretes-state-in-continuum model is inherently ambiguous because the discrete states are not uniquely defined. The ambiguity remains even though we have not constructed the model directly using the projection-operator approach [63], but we obtained the model parameters from *ab initio* eigenphase sums and potential energies. To validate the calculations, we constructed three models (Models 1, 2, 3) with the same parameter form but with different values. All presented results were calculated using Model 1, whose parameter values are given in Appendix C of Paper I. Model 2 behaves in the same way as Model 1, that is, the role of individual model parameters is analogous to Model 1, for which we discussed it in Sec. V of Paper I.

In these two models, the direct coupling λ of the Σ and

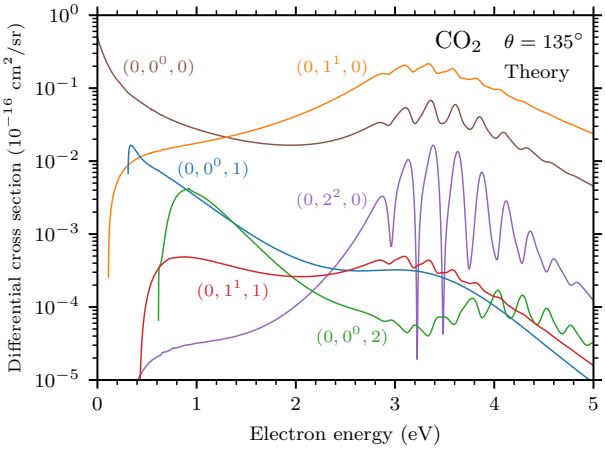

FIG. 14. Differential cross sections for vibrational excitation of CO_2 from initial state $(0, 0^0, 0)$ to final states: $(0, 0^0, 0)$, $(0, 1^1, 0)$, $(0, 0^0, 1)$, $(0, 2^2, 0)$, $(0, 1^1, 1)$, and $(0, 0^0, 2)$.

$\Pi_\pm$ states have a small effect on the potential energy surfaces (Fig. 8 in Paper I). The primary effects upon bending (broadening of the lower Renner-Teller state, formation of the nonlinear minimum) are related to the indirect coupling through the s-wave continuum described by the parameter $v_{\Pi s}$. Since we can not distinguish between these two types of the coupling, we managed to construct Model 3 where the role of the parameters λ and $v_{\Pi s}$ is to a large degree interchanged. Model 3 does not reproduce the *ab initio* eigenphase sums as well as Models 1 and 2 but still it reproduces them to a satisfactory level. However, we found that Model 3 is not consistent with the *ab initio* K matrix because the role of partial waves

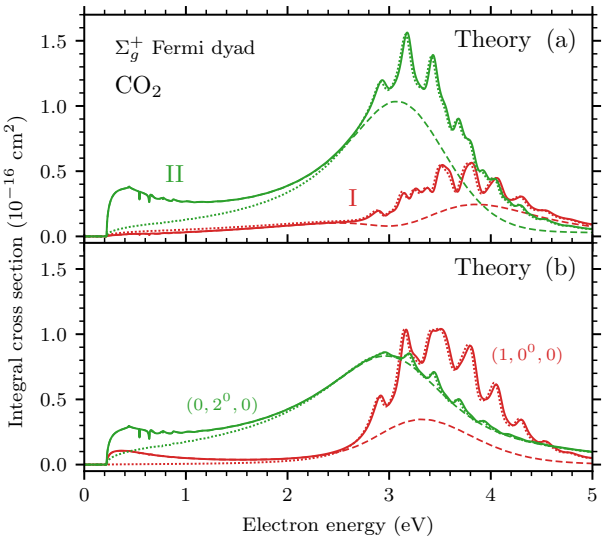

FIG. 15. Integral cross sections for vibrational excitation of CO_2 from initial state $(0, 0^0, 0)$ to members of the Σ_g^+ Fermi dyad in Panel (a) and to harmonic states $(1, 0^0, 0)$ and $(0, 2^0, 0)$ in Panel (b). Solid lines, full 4D calculations; dashed lines, contribution of incoming s wave for 4D dynamics; dotted lines, calculations without the Σ_g^+ virtual state and without asymmetric stretching motion.

s and $p_\parallel$ is interchanged, see Sec. V C in Paper I for the case of Model 1.

Models 1 and 2 produce very similar spectra at the region of the $^2\Pi_u$ resonance, see Fig. 16. There is some quantitative difference for smaller incident energies but qualitatively both models behave the same. In the case of Model 3, the spectra for all final states do not look too different but contributions of individual final state symmetries differ more substantially. Because of the inconsistency with the R-matrix data, we do not consider Model 3 to be physically relevant.

B. Dimensionality and electronic states

It is interesting to investigate the effect of freezing some of vibrational modes, which can be easily achieved in our model by reducing the basis in the corresponding dimension only to one state and setting appropriate parameters to zero. Such a reduction of the dimensionality is demonstrated for the elastic scattering in Fig. 17 and for the excitation of $(1, 0^0, 0)$, $(0, 2^0, 0)$, $(0, 1^1, 0)$, and $(0, 2^2, 0)$ harmonic states in Fig. 18, where also contributions of the individual incoming partial waves are shown when nonzero. The excitation of $(0, 2^2, 0)$ can only proceed via $p_\pm \to p_\mp$. We cannot perform 1D dynamics for pure asymmetric stretching motion, see below.

Upon pure symmetric stretching the threshold and resonance regions are well separated because the s wave cannot interact with the resonance. The boomerang oscillations originate in the symmetric stretching motion and are dampen by the broad resonance as the anion bends [36, 37]. Moreover, the oscillations only occur if the electron comes in as p_+ or p_-. When the incoming electron is of the s-wave character, the formation of the $^2\Pi_u$ state forces the molecule to bend and the wave packet traveling along the symmetric stretch axis is a subject of the broader decay width. As a consequence, the oscillations of the anionic wave function along this axis are significantly suppressed (Fig. 4).

The whole dynamics is driven by the symmetric stretching vibrations because of the nonzero gradient. The pure bending motion leads to the cross sections with a structureless $^2\Pi_u$ peak, which is typically narrower and higher than the one in the case where the symmetric stretching is present. These results are similar to results of Laporta *et al.* [42] who performed 1D LCP calculations in each vibrational mode separately. In our model, we cannot perform 1D dynamics of the $^2\Pi_u$ doublet for pure asymmetric stretching motion because the p_z wave couples to the $\Pi_\pm$ discrete states only at combined asymmetrically stretched and bent geometries, see Eq. (13). Such 1D calculations are possible for an incoming d-wave electron, which is not included in our model.

Nevertheless, we do not expect 1D calculations of the vibrational motion in nontotally symmetric modes of polyatomic molecules to be appropriate in general. For such modes, potentials are even functions of the corresponding vibrational coordinates, that is, they possess no gradients at the equilibrium. They can play a key role as the bending does in the case of CO_2 but the dynamics in these modes alone is probably not sufficient. Moreover, if neutral and anionic potentials are close to being parallel and there is no symmetry breaking mechanism, the cross sections are strongly influenced by the fact that the neutral and anionic vibrational states for different quanta are almost orthogonal to each other. We are convinced that this is the origin (not the boomerang effect) of structures in the cross sections upon asymmetric stretching presented in Ref. [42].

VIII. CONCLUSION

In conclusion, we summarize our join experimental and theoretical work on the vibrational excitation of CO_2 by slow electrons and we also discuss possible future improvements. The study comprises of our Letter [49] that outlines the primary results, the description of the theoretical model Ref. [50], and the detailed analysis of the results presented in this paper.

The theoretical work was motivated by three open challenges in the low-energy electron-molecule scattering. The first of them was the unexplained shape of the energy-loss spectra and the discovery of the fine structure with ∼30 meV spacing in our high-resolution 2D spectrum. The second challenge was the absence of the theoretical treatment of the interaction of the near thresh-

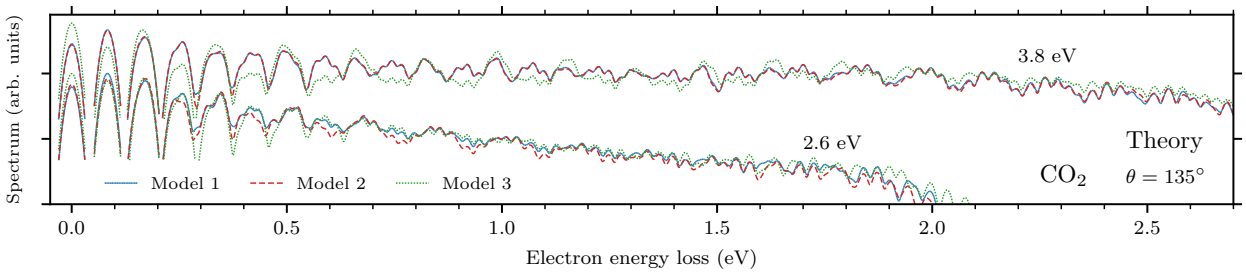

FIG. 16. Comparison of three constructed models in terms of calculated energy-loss spectra for a scattering angle of 135° and incident electron energy of 2.6 and 3.8 eV. The spectra are shown in the logarithmic scale but the two sets of data are arbitrarily shifted with respect to each other. Model 3 is not consistent with the *ab initio* data, see the text.

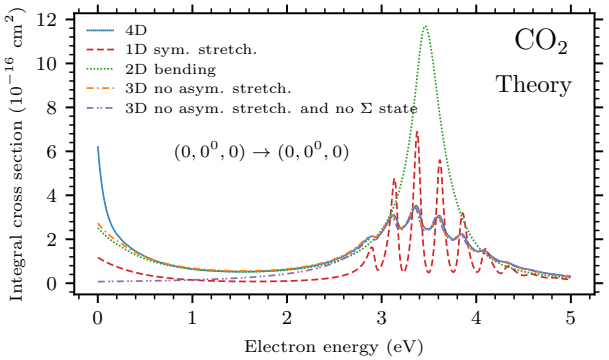

FIG. 17. Effect of the dimensionality of the dynamics on the integral elastic cross sections of CO_2. Both 3D calculations did not include the asymmetric stretching motion and in one case the Σ discrete state was excluded.

old $^2\Sigma_g^+$ virtual state with the $^2\Pi_u$ resonance pointed out by Sommerfeld *et al.* [64] and hinted in experiments by Allan [34, 35]. The last challenge was posed by the lack of development in the treatment of electron-molecule scattering by the nonlocal discrete-state-in-continuum model for polyatomic molecules including the vibronic coupling. The importance of the direct and indirect (through electron continuum) vibronic coupling was analyzed by Gallup [43]. However, only the direct vibronic coupling was previously included in the model study of 2D nonlocal dynamics by Estrada *et al.* [65] and in LCP calculations, e.g., by McCurdy *et al.* [36] for the $e + CO_2$ system (see also the introduction of Ref. [50]).

On the experimental side, we have presented the 2D energy-loss spectrum measured at the scattering angle of 135° with the energy resolution of 18 meV and to almost complete energy loss, in combination with additional 1D cuts for fixed incident energies at 10°, 45°, and 135°. The nuclear dynamics of the CO_2^- anion was modeled in the full vibrational dimensionality and in the presence of the $^2\Sigma_g^+$ virtual state and the $^2\Pi_u$ shape resonance coupled upon bending. We also included the vibronic coupling of these states to four electron partial waves s, p_z, $p_\pm$, which is the minimum set needed to explain the symmetries of all observed energy-loss peaks in the region up to 5 eV.

The inclusion of the vibronic coupling of the $^2\Pi_u$ resonance to the s-wave electron continuum is the most important aspect of the current model in comparison with previous calculations. It allows excitation of $^2\Pi_u$ vibrational states of CO_2, which have been found to dominate the highly inelastic region of the spectrum and their competition with $^2\Sigma_g^+$ states explains the shape of the spectrum. Only vibrational states that are localized in the vicinity of the symmetric stretching axis are significantly excited because the s-wave coupling causes an effective decay of the molecular anion at highly bent geometries. This selective mechanism gives rise to the observed fine structure with ∼30 meV spacing.

The interpretation of the fine structure by identification of the specific states from the quasi-continuum of energetically available final states is one of the primary successes of our model. Another achievement is the vibrationally complete description of the dynamics, which allows the prediction of all vibrational transitions experimentally observed. Moreover, the anionic wave functions (apart from giving aesthetic pictures) provide a further insight and interpretation for the results. The calculation also gives access to splitting of the dynamics based on irreducible representations of the molecular symmetry group and electron partial waves. Moreover, the possibilities of simplifying the dynamics were tested. This aspect may be important for treatment of larger molecules. In the case of CO_2, we have seen that the dynamics is driven by the symmetric stretching but the bending is important as well since it couples the states and partial waves. On the other side, the asymmetric stretching motion can be left out unless we are specifically looking into excitation of the energy-loss peaks associated with excitation of this motion. We have also discussed energy regions where the $^2\Sigma_g^+$ state or the $^2\Pi_u$ doublet can be omitted.

To achieve not only a qualitative but also quantitative agreement with the experimental data, several improvements of the model should be considered in the future. The most straightforward step is improving the quality of the potential energy surfaces. However, it is difficult to reach a better correlation in the fixed-nuclei electron scattering to have a consistent set of data for the con-

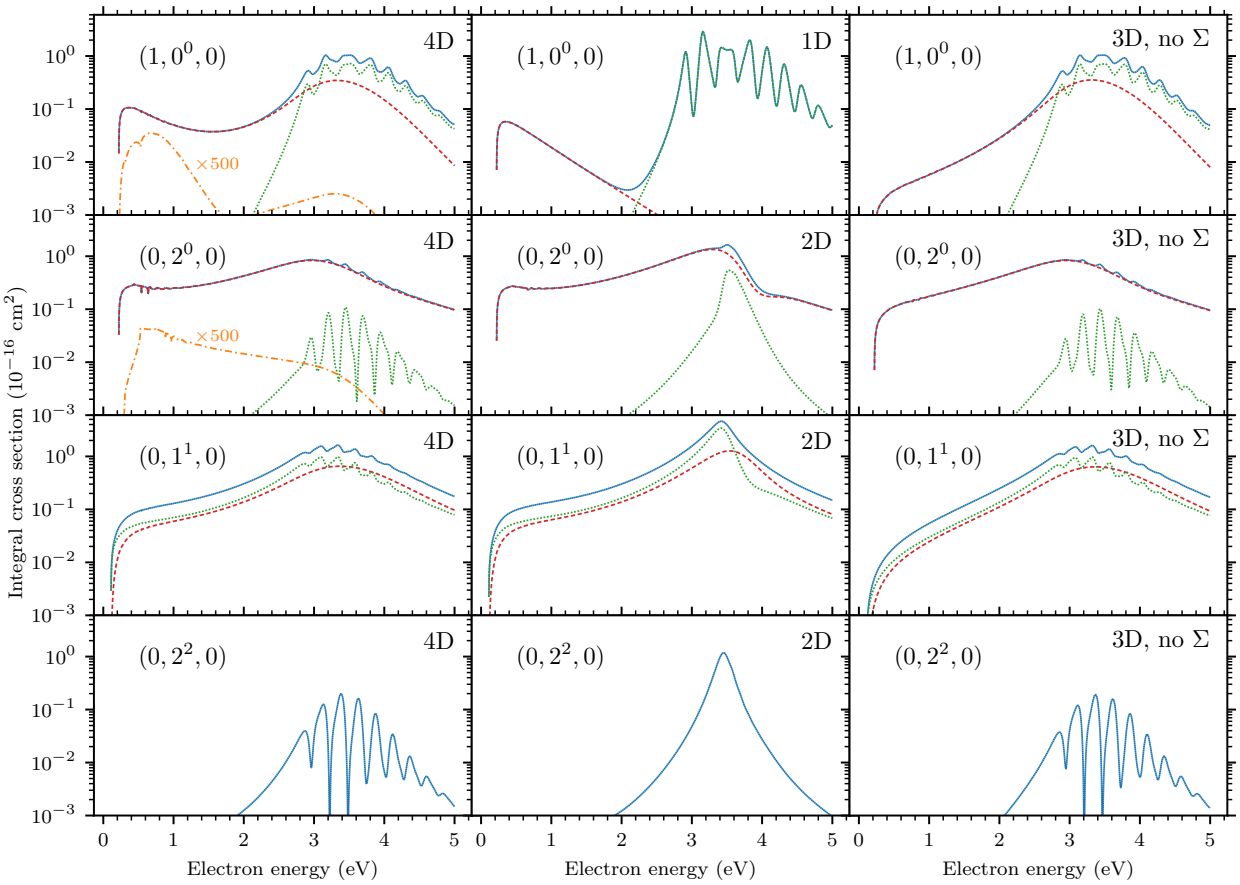

FIG. 18. Effect of the dimensionality of the dynamics on the integral cross sections for vibrational excitation of CO_2 from $(0,0^0,0)$ to four final harmonic states: $(1,0^0,0)$, $(0,2^0,0)$, $(0,1^1,0)$, and $(0,2^2,0)$ (in rows). First column, full 4D dynamics; second column, 1D dynamics in pure symmetric stretching for $(1,0^0,0)$ and 2D dynamics in pure bending for $(0,2^0,0)$, $(0,1^1,0)$, and $(0,2^2,0)$; third column, 3D dynamics without asymmetric stretching and without the Σ discrete state. Solid lines, contribution of all incoming electron partial waves; dashed lines, contribution of incoming s wave; dotted lines, contribution of incoming $p_\pm$ waves; dot-dashed lines, contribution of incoming p_z wave.

struction of the model. The harmonic approximation for the neutral vibrations should also be lifted to include the Fermi resonance directly into the dynamics. Furthermore, the inclusion of the dipole moment emerging upon bending and asymmetric stretching is necessary to precisely reproduce the threshold region and probably d- and f-waves are needed to improve the dependence on the scattering angle. The incorporation of the $O^- + CO$ dissociation channel that opens around 4 eV into the nuclear dynamics is the ultimate but computationally challenging goal since the dissociation proceeds via a conical intersection of the $^2\Pi_u$ resonance with another state of the $^2\Pi_g$ symmetry that is connected to the dissociation asymptote [66].

In the future the present approach can also be applied to other linear molecules, for example CS_2, N_2O or to larger molecules with fixing some degrees of freedom.

ACKNOWLEDGMENTS

We gratefully acknowledge the financial support provided by the Czech Science Foundation Projects No. 19-20524S (M. Č., K. H., J. D.), No. 20-11460S (J. F.), and No. 21-12598S (R. Č.) and by the Charles University Grant Agency, Project No. 552120 (J. D., M. Č.).

[1] C. Ramsauer, Über den wirkungsquerschnitt der kohlensäuremoleküle gegenüber langsamen elektronen, Ann. Phys. **388**, 1129 (1927).
[2] M. Boness and J. Hasted, Resonances in electron scat-

tering by molecules, Phys. Lett. **21**, 526 (1966).
[3] M. J. W. Boness and G. J. Schulz, Vibrational Excitation of CO_2 by Electron Impact, Phys. Rev. Lett. **21**, 1031 (1968).
[4] M. J. W. Boness and G. J. Schulz, Vibrational excitation in CO_2 via the 3.8-eV resonance, Phys. Rev. A **9**, 1969 (1974).
[5] I. Cadez, M. Tronc, and R. I. Hall, Oscillations in electron impact cross sections of CO_2 between 3 and 5 eV, J. Phys. B: At. Mol. Phys. **7**, L132 (1974).
[6] I. Cadez, F. Gresteau, M. Tronc, and R. I. Hall, Resonant electron impact excitation of CO_2 in the 4 eV region, J. Phys. B: At. Mol. Phys. **10**, 3821 (1977).
[7] A. Herzenberg, Oscillatory energy dependence of resonant electron-molecule scattering, J. Phys. B **1**, 548 (1968).
[8] A. K. Kazansky and L. Y. Sergeeva, On the local theory of resonant inelastic collisions of slow electrons with carbon dioxide, J. Phys. B: At., Mol. Opt. Phys. **27**, 3217 (1994).
[9] A. Kazansky and L. Y. Sergeeva, A model study of vibrational excitation of carbon dioxide molecule by slow electrons: the role of wave packet sliding from the ridge, Z. Phys. D **37**, 305 (1996).
[10] M. Allan, Study of triplet states and short-lived negative ions by means of electron impact spectroscopy, J. Electron Spectrosc. Relat. Phenom. **48**, 219 (1989).
[11] T. Reddish, F. Currell, and J. Comer, Studies of the 2 eV shape resonance in N_2 using a two-dimensional scanning technique, J. Phys. E: Sci. Instrum. **21**, 203 (1988).
[12] F. Currell and J. Comer, Polyatomic excitation effects observed in an electron impact study of the 4 eV shape resonance of carbon dioxide, J. Phys. B: At., Mol. Opt. Phys. **26**, 2463 (1993).
[13] F. Currell and J. Comer, Observation of friction in the nuclear dynamics of CO_2^- near the equilibrium geometry of the negative ion, Phys. Rev. Lett. **74**, 1319 (1995).
[14] F. Currell, Friction effects in excitation to high vibrational states of the electronic ground state of carbon dioxide via the 4 eV shape resonance, J. Phys. B: At., Mol. Opt. Phys. **29**, 3855 (1996).
[15] E. Fermi, Über den Ramaneffekt des Kohlendioxyds, Z. Phys. **71**, 250 (1931).
[16] G. Herzberg, *Molecular spectra and molecular structure. Vol.2, Infrared and Raman spectra of polyatomic molecules* (Van Nostrand, New York, 1945).
[17] Y. Itikawa, Differential cross section for vibrational excitation of co by slow-electron collision, J. Phys. Soc. Jpn. **28**, 1062 (1970).
[18] Y. Itikawa, Nonresonant vibrational excitation of co_2 by electron collision, Phys. Rev. A **3**, 831 (1971).
[19] K. H. Kochem, W. Sohn, N. Hebel, K. Jung, and H. Ehrhardt, Elastic electron scattering and vibrational excitation of CO_2 in the threshold energy region, J. Phys. B: At. Mol. Phys. **18**, 4455 (1985).
[20] M. A. Morrison, N. F. Lane, and L. A. Collins, Low-energy electron-molecule scattering: Application of coupled-channel theory to e-CO_2 collisions, Phys. Rev. A **15**, 2186 (1977).
[21] M. A. Morrison, Interpretation of the near-threshold behavior of cross sections for $e-CO_2$ scattering, Phys. Rev. A **25**, 1445 (1982).
[22] B. L. Whitten and N. F. Lane, Near-threshold vibrational excitation in electron-CO_2 collisions: A simple model, Phys. Rev. A **26**, 3170 (1982).
[23] H. Estrada and W. Domcke, On the virtual-state effect in low-energy electron-CO_2 scattering, J. Phys. B **18**, 4469 (1985).
[24] S. Mazevet, M. A. Morrison, L. A. Morgan, and R. K. Nesbet, Virtual-state effects on elastic scattering and vibrational excitation of CO_2 by electron impact, Phys. Rev. A **64**, 040701 (2001).
[25] L. A. Morgan, Virtual States and Resonances in Electron Scattering by CO_2, Phys. Rev. Lett. **80**, 1873 (1998).
[26] C.-H. Lee, C. Winstead, and V. McKoy, Collisions of low-energy electrons with CO_2, J. Chem. Phys. **111**, 5056 (1999).
[27] T. N. Rescigno, D. A. Byrum, W. A. Isaacs, and C. W. McCurdy, Theoretical studies of low-energy electron-CO_2 scattering: Total, elastic, and differential cross sections, Phys. Rev. A **60**, 2186 (1999).
[28] D. F. Register, H. Nishimura, and S. Trajmar, Elastic scattering and vibrational excitation of CO_2 by 4, 10, 20 and 50 eV electrons, J. Phys. B: At. Mol. Phys. **13**, 1651 (1980).
[29] T. Antoni, K. Jung, H. Ehrhardt, and E. S. Chang, Rotational branch analysis of the excitation of the fundamental vibrational modes of CO_2 by slow electron collisions, J. Phys. B: At. Mol. Phys. **19**, 1377 (1986).
[30] D. C. Cartwright and S. Trajmar, Resonant electron-impact excitation of vibrational modes in polyatomic molecules, J. Phys. B: At., Mol. Opt. Phys. **29**, 1549 (1996).
[31] D. C. Cartwright and S. Trajmar, Resonant electron-impact excitation of vibrational modes in polyatomic molecules, J. Phys. B: At., Mol. Opt. Phys. **29**, 1549 (1996).
[32] M. Kitajima, S. Watanabe, H. Tanaka, M. Takekawa, M. Kimura, and Y. Itikawa, Strong mode dependence of the 3.8-eV resonance in CO_2 vibrational excitation by electron impact, Phys. Rev. A **61**, 060701 (2000).
[33] M. Kitajima, S. Watanabe, H. Tanaka, M. Takekawa, M. Kimura, and Y. Itikawa, Differential cross sections for vibrational excitation of CO_2 by 1.5-30 eV electrons, J. Phys. B: At., Mol. Opt. Phys. **34**, 1929 (2001).
[34] M. Allan, Selectivity in the Excitation of Fermi-Coupled Vibrations in CO_2 by Impact of Slow Electrons, Phys. Rev. Lett. **87**, 033201 (2001).
[35] M. Allan, Vibrational structures in electron CO_2 scattering below the $^2\Pi_u$ shape resonance, J. Phys. B: At., Mol. Opt. Phys. **35**, L387 (2002).
[36] C. W. McCurdy, W. A. Isaacs, H.-D. Meyer, and T. N. Rescigno, Resonant vibrational excitation of CO_2 by electron impact: Nuclear dynamics on the coupled components of the $^2\Pi_u$ resonance, Phys. Rev. A **67**, 042708 (2003).
[37] T. N. Rescigno, W. A. Isaacs, A. E. Orel, H.-D. Meyer, and C. W. McCurdy, Theoretical study of resonant vibrational excitation of CO_2 by electron impact, Phys. Rev. A **65**, 032716 (2002).
[38] C. W. McCurdy and J. L. Turner, Wave packet formulation of the boomerang model for resonant electron–molecule scattering, J. Chem. Phys. **78**, 6773 (1983).
[39] W. Vanroose, Z. Zhang, C. W. McCurdy, and T. N. Rescigno, Threshold vibrational excitation of CO_2 by slow electrons, Phys. Rev. Lett. **92**, 053201 (2004).

[40] J. P. Gauyacq and A. Herzenberg, Nuclear-excited feshbach resonances in $e + \mathrm{HCl}$ scattering, Phys. Rev. A **25**, 2959 (1982).

[41] W. Vanroose, C. W. McCurdy, and T. N. Rescigno, Scattering of slow electrons by polar molecules: Application of effective-range potential theory to HCl, Phys. Rev. A **68**, 052713 (2003).

[42] V. Laporta, J. Tennyson, and R. Celiberto, Calculated low-energy electron-impact vibrational excitation cross sections for CO_2 molecule, Plasma Sources Sci. Technol. **25**, 06LT02 (2016).

[43] G. A. Gallup, Symmetry selection rules for vibrational excitation by resonant electron impact and a unified treatment of vibronic coupling between resonances and to the continuum: A complete symmetry analysis of vibrational excitation in benzene, J. Chem. Phys. **99**, 827 (1993).

[44] S. F. Wong and G. J. Schulz, Vibrational excitation in benzene by electron impact via resonances: Selection rules, Phys. Rev. Lett. **35**, 1429 (1975).

[45] R. Čurík and P. Čársky, Vibrationally inelastic electron scattering on polyatomic molecules by the discrete momentum representation (DMR) method, J. Phys. B: At., Mol. Opt. Phys. **36**, 2165 (2003).

[46] R. Čurík, P. Čársky, and M. Allan, Vibrational excitation of methane by slow electrons revisited: theoretical and experimental study, J. Phys. B: At., Mol. Opt. Phys. **41**, 115203 (2008).

[47] R. Čurík, I. Paidarová, M. Allan, and P. Čársky, Joint experimental and theoretical study on vibrational excitation cross sections for electron collisions with diacetylene, J. Phys. Chem. A **118**, 9734 (2014).

[48] R. Čurík, P. Čársky, and M. Allan, Electron-impact vibrational excitation of cyclopropane, J. Chem. Phys. **142**, 144312 (2015).

[49] J. Dvořák, M. Ranković, K. Houfek, P. Nag, R. Čurík, J. Fedor, and M. Čížek, Vibronic coupling through the continuum in the $e + \mathrm{CO_2}$ system, Phys. Rev. Lett. **129**, 013401 (2022).

[50] J. Dvořák, K. Houfek, and M. Čížek, Vibrational excitation in the $e + \mathrm{CO_2}$ system: Nonlocal model of $\Sigma\Pi$ vibronic coupling through the continuum, Phys. Rev. A **105**, 062821 (2022).

[51] M. Allan, Measurement of differential cross sections for excitation of helium by electron impact within the first 4 eV above threshold, J. Phys. B: At. Mol. Opt. Phys. **25**, 1559 (1992).

[52] M. Allan, Measurement of the elastic and $\nu = 0 \rightarrow 1$ differential electron–N_2 cross sections over a wide angular range, J. Phys. B: At. Mol. Opt. Phys. **38**, 3655 (2005).

[53] K. Regeta and M. Allan, Autodetachment Dynamics of Acrylonitrile Anion Revealed by Two-Dimensional Electron Impact Spectra, Phys. Rev. Lett. **110**, 203201 (2013).

[54] C. S. Anstöter, G. Mensa-Bonsu, P. Nag, M. Ranković, T. P. Ragesh Kumar, A. N. Boichenko, A. V. Bochenkova, J. Fedor, and J. R. R. Verlet, Mode-Specific Vibrational Autodetachment Following Excitation of Electronic Resonances by Electrons and Photons, Phys. Rev. Lett. **124**, 203401 (2020).

[55] M. Allan, M. Lacko, P. Papp, Š. Matejčík, M. Zlatar, I. I. Fabrikant, J. Kočišek, and J. Fedor, Dissociative electron attachment and electronic excitation in $Fe(CO)_5$, Phys. Chem. Chem. Phys. **20**, 11692 (2018).

[56] M. Ranković, P. Nag, M. Zawadzki, L. Ballauf, J. Žabka, M. Polášek, J. Kočišek, and J. Fedor, Electron Collisions With Cyanoacetylene HC_3N: Vibrational Excitation and Dissociative Electron Attachment, Phys. Rev. A **98**, 052708 (2018).

[57] Y. Itikawa, Electron-impact vibrational excitation of polyatomic molecules, Int. Rev. Phys. Chem. **16**, 155 (1997).

[58] D. M. Dennison, The Infra-Red Spectra of Polyatomic Molecules. Part II, Rev. Mod. Phys. **12**, 175 (1940).

[59] A. Chedin, The carbon dioxide molecule: Potential, spectroscopic, and molecular constants from its infrared spectrum, J. Mol. Spectrosc. **76**, 430 (1979).

[60] K. Houfek, M. Čížek, and J. Horáček, On irregular oscillatory structures in resonant vibrational excitation cross-sections in diatomic molecules, Chem. Phys. **347**, 250 (2008), ultrafast Photoinduced Processes in Polyatomic Molecules.

[61] G. A. Gallup, Selection rules for vibrational energy loss by resonant electron impact in polyatomic molecules, Phys. Rev. A **34**, 2746 (1986).

[62] E. P. Wigner, On the Behavior of Cross Sections Near Thresholds, Phys. Rev. **73**, 1002 (1948).

[63] W. Domcke, Theory of resonance and threshold effects in electron-molecule collisions: The projection-operator approach, Phys. Rep. **208**, 97 (1991).

[64] T. Sommerfeld, H.-D. Meyer, and L. S. Cederbaum, Potential energy surface of the CO_2^- anion, Phys. Chem. Chem. Phys. **6**, 42 (2004).

[65] H. Estrada, L. S. Cederbaum, and W. Domcke, Vibronic coupling of short-lived electronic states, J. Chem. Phys. **84**, 152 (1986).

[66] A. Moradmand, D. S. Slaughter, D. J. Haxton, T. N. Rescigno, C. W. McCurdy, T. Weber, S. Matsika, A. L. Landers, A. Belkacem, and M. Fogle, Dissociative electron attachment to carbon dioxide via the $^2\Pi_u$ shape resonance, Phys. Rev. A **88**, 032703 (2013).

Chapter 3

Vibronic dynamics with dissociative channel

In the previous chapter, we presented the feasibility of the vibronic dynamics for three discrete states and all vibrational modes of a triatomic linear molecule. However, as we mentioned in Sec. 1.3.2, even 2D vibronic dynamics can produce some features observed in 2D energy-loss spectra of larger polyatomic molecules, where we cannot hope for the inclusion of all vibrations at least in the near future. The geometry-dependent coupling of the discrete states to electron partial waves showed to be a crucial aspect of the model for the $e + CO_2$ system, but its general importance is not clear. Similarly, the interaction of multiple electronic states contributing to the DEA process is worth investigating because it seems to affect biological systems in a significant way [2, 3].

We present a model for 2D vibronic dynamics with an arbitrary number of discrete states and electron partial waves. The implementation of the $e + CO_2$ dynamics is tailored to the constructed model and is not easily modifiable for other cases. Our goal is to have a rather simple model that can qualitatively describe a broad class of systems, therefore, we consider only two vibrational modes but lift some approximations made for CO_2. Potentials tend to be anharmonic or even dissociative along coordinates of totally symmetric modes. On the other hand, the potentials are even functions of nontotally symmetric vibrational coordinates and often times they can be well approximated by the harmonic potential. We thus consider one general mode, in which the anion will be allowed to dissociate, and one harmonic mode. Further, we do not *a priori* assume any particular symmetry of the vibrations nor the discrete states. The implementation is general and the symmetry is introduced for specific applications of the model by the dependence of the Hamiltonian elements on the vibrational coordinates. In this chapter we describe the general model, which is applied to the pyrrole molecule in Chapter 4, but a systematic study of the 2D vibronic dynamics goes beyond the scope of this thesis.

The description of the dynamics still follows the general discrete-states-in-continuum model outlined in Sec. 1.2. Here, we define the parametrization of the model functions, that is, we define the neutral vibrational Hamiltonian H_0, the matrix U of the direct coupling of the discrete states and their energies with respect to the threshold V_0, and the matrix V_ϵ describing the coupling between the discrete states and electron partial waves.

3.1 Hamiltonian H_0 and basis for the anion

We consider a two-dimensional motion of nuclei described by coordinates Q_1 and Q_2. The shape of the neutral potential in Q_1 [$V_0^{(1)}(Q_1)$ below] can be arbitrary (anharmonic, dissociative) but we limit the Q_2 coordinate to describe only a harmonic mode. In order to reduce computational demands, we further assume that the neutral 2D Hamiltonian H_0 is a sum of 1D Hamiltonians:

$$H_0 = H_0^{(1)} + H_0^{(2)} = -\frac{1}{2\mu_1}\frac{\partial^2}{\partial Q_1^2} + V_0^{(1)}(Q_1) - \frac{1}{2}\omega_2\frac{\partial^2}{\partial Q_2^2} + \frac{1}{2}\omega_2 Q_2^2, \tag{3.1}$$

where μ_1 is the reduced mass of mode 1, and ω_2 is the vibrational angular frequency of the harmonic mode (mode 2).

Consequently, neutral vibrational wave functions $|\chi_n\rangle$ [$n \equiv (n_1, n_2)$] given as solutions of Eq. (1.5) are separable:

$$|\chi_n\rangle = |\chi_{n_1}^{(1)}\rangle|\chi_{n_2}^{(2)}\rangle \tag{3.2}$$

with energies

$$E_n = E_{n_1}^{(1)} + E_{n_2}^{(2)} = E_{n_1}^{(1)} + \omega_2\left(n_2 + \frac{1}{2}\right), \tag{3.3}$$

where $|\chi_{n_2}^{(2)}\rangle$ are the familiar oscillator functions [86] and we can find the $|\chi_{n_1}^{(1)}\rangle$ states using the discrete variable representation (DVR) method with a Fourier sine basis [87].

In the case of CO_2, we restricted the molecule only to harmonic vibrations and expressed the anionic Hamiltonian and wave functions in the oscillator basis. However, the oscillator basis is not convenient for the description of the dissociation. We could use the $|\chi_{n_1}^{(1)}\rangle$ states, which include the discretized continuum [87], as a basis for mode 1 and rewrite the Schrödinger equation Eq. (1.3) to the corresponding Lippmann-Schwinger equation as in the case of 1D dynamics, see Ref. [18, ch. 4]. Then, the Green's function for the local problem enforces the outgoing boundary condition. We decided for another approach. We employ the grid method developed by Rescigno and McCurdy [88] that is based on the finite element method (FEM) and the DVR method in combination with the exterior complex scaling (ECS) to deal with the boundary condition.

In the FEM DVR method [88], the interval where the wave function is to be found is divided into elements (subintervals). In each element we have a basis of linearly independent local functions, Lobatto shape functions, which are associated with DVR grid points generated by the Gauss-Lobatto quadrature. Adjacent elements are connected by so-called bridge functions. In total, we have a set of orthonormal functions $|\phi_{n_1}^{(1)}\rangle$ that correspond to grid points x_{n_1}. Thanks to the finite elements, such a grid is very flexible since various density of points can be easily achieved for different parts of the grid. In addition, we also have the property of the DVR methods that local potentials are represented by diagonal matrices:

$$\langle\phi_{n_1}^{(1)}|g(Q_1)|\phi_{m_1}^{(1)}\rangle \cong g(x_{n_1})\delta_{n_1 m_1}. \tag{3.4}$$

The matrix of the kinetic energy operator expressed in this basis is almost block diagonal (i.e. sparse) because blocks for two adjacent elements overlap only at one point thanks to the bridge functions.

Dissociative channels in the DEA process are described by asymptotes of the discrete-state potentials V_0+U_{dd}. Then, the corresponding vibrational components $|\psi_d\rangle$ of the scattered wave function $|\Psi\rangle$, which satisfies the Schrödinger equation Eq. (1.3), are purely outgoing waves

$$\psi_d(Q_1,Q_2) \underset{Q_1\to\infty}{\sim} e^{ikQ_1}, \tag{3.5}$$

where k is the channel momentum. We discuss the boundary condition more precisely in Sec. 3.4. In the ECS approach, a part of the FEM DVR grid for large distances is rotated to the upper half of the complex plane, which results in an exponential decrease of the wave function and we do not have to explicitly enforce the boundary condition. Note that anionic potentials that dissociate either as $Q_1 \to -\infty$ or even $Q_1 \to \pm\infty$ can also be used. For $Q_1 \to -\infty$, we rotate the beginning of the grid to the lower half of the complex plane. The implementation of the FEM DVR ECS method was provided by Karel Houfek [89] and further details can be found in Ref. [88].

To summarize, we expand the vibrational components $|\psi_d\rangle$ of $|\Psi\rangle$ in the basis of the FEM DVR ECS functions $|\phi^{(1)}_{n_1}\rangle$ for mode 1 and in the basis of the harmonic oscillator functions $|\chi^{(2)}_{n_2}\rangle$ for mode 2:

$$|\psi_d\rangle = \sum_{n_1,n_2} \psi^d_{n_1n_2}|\phi^{(1)}_{n_1}\rangle|\chi^{(2)}_{n_2}\rangle, \quad d=1,\ldots,N_\mathrm{d}, \tag{3.6}$$

where $\psi^d_{n_1n_2}$ are the expansion coefficients.

The Hamiltonian H_0 given by Eq. (3.1) acts in a simple way on the vibrational components $|\psi_d\rangle$:

$$\begin{aligned}(H_0\psi_d)_{m_1m_2} &\equiv \langle\phi^{(1)}_{m_1}|\langle\chi^{(2)}_{m_2}|H_0|\psi_d\rangle = \sum_{n_1n_2}\langle\phi^{(1)}_{m_1}|\langle\chi^{(2)}_{m_2}|H_0|\phi^{(1)}_{n_1}\rangle|\chi^{(2)}_{n_2}\rangle\psi^d_{n_1n_2}\\ &= \sum_{n_1n_2}\left(\langle\phi^{(1)}_{m_1}|H^{(1)}_0|\phi^{(1)}_{n_1}\rangle\delta_{m_2n_2} + \delta_{m_1n_1}\langle\chi^{(2)}_{m_2}|H^{(2)}_0|\chi^{(2)}_{n_2}\rangle\right)\psi^d_{n_1n_2}\\ &= \sum_{n_1} T^{(1)}_{m_1n_1}\psi^d_{n_1m_2} + V^{(1)}_0(x_{m_1})\psi^d_{m_1m_2} + \omega_2\left(m_2+\frac{1}{2}\right)\psi^d_{m_1m_2},\end{aligned} \tag{3.7}$$

where $T^{(1)}_{m_1n_1}$ is the matrix of the kinetic energy operator for mode 1 in the FEM DVR ECS basis [88] and we used the DVR property Eq. (3.4) for the $V^{(1)}_0(Q_1)$ potential.

3.2 Matrices U and V_ϵ

In the model for CO_2, we restricted all elements of the Hamiltonian to low-order polynomials in the vibrational coordinates. Here, we lift this restriction for mode 1. We parametrize the elements of the matrix U in the following way

$$U_{dd'}(Q_1,Q_2) = \sum_j u^j_{dd'}(Q_1)Q_2^{p^j_{dd'}}, \quad d,d'=1,\ldots,N_\mathrm{d}, \tag{3.8}$$

where $u^j_{dd'}$ can be arbitrary functions of the Q_1 coordinate and $p^j_{dd'}$ are integers. In other words, the elements are polynomials in Q_2 with arbitrary Q_1-dependent

coefficients. If Q_2 does not describe a totally symmetric mode, the molecular symmetry typically restricts the polynomials to be even or odd.

The elements of the discrete-state-continuum coupling V_ϵ are also functions of electron energy ϵ. The coordinate dependence is parametrized in the same way as above:

$$V^\mu_{d\epsilon}(Q_1, Q_2) = \sum_j g^\mu_{dj}(Q_1) Q_2^{p^\mu_{dj}} \xi^\mu_{dj}(\epsilon), \tag{3.9}$$

and we assume the Wigner threshold behavior [90] with an exponential cutoff for the energy parts [8]:

$$\xi^\mu_{dj}(\epsilon) = (\beta^\mu_{dj}\epsilon)^{\alpha^\mu_{dj}} \exp(-\beta^\mu_{dj}\epsilon). \tag{3.10}$$

Threshold exponents α^μ_{dj} and exponential parameters β^μ_{dj} are still kept constant to simplify the evaluation of $F(E - H_0)$.

When the molecule has a dipole moment, the threshold exponent α becomes coordinate dependent [85]. Thus, the current parametrization does not allow the inclusion of the dipole moment unless the corresponding term in $V^\mu_{d\epsilon}$ is in advance approximated by a sum of separable terms in coordinates and energy. For the critical dipole moment, the threshold exponent becomes zero resulting in a finite resonance width at the threshold [8]. Moreover, the width oscillates with increasing frequency as $\epsilon \to 0$ for supercritical dipoles reflecting the fact that there is an infinite number of dipolar bound states of the electron-molecule system with energies exponentially converging to the threshold [8, 91]. However, $\alpha = 0$ can be a good approximation even for supercritical dipoles because the oscillatory character primarily affects a very close vicinity of the threshold comparable to the energy of the rotational splitting [91], see also Refs. [36, 37] where the authors considered $\alpha = 0$ for HNCO. Without a dipole we have $\alpha = (2l + 1)/4$ for the electron partial wave $\mu = (l, m)$ [90].[1]

Considering the U term as an operator, it acts on the full wave functions $|\Psi\rangle$ as follows

$$\begin{aligned}(U\Psi)^d_{m_1m_2} &\equiv \langle d|\langle\phi^{(1)}_{m_1}|\langle\chi^{(2)}_{m_2}|U|\Psi\rangle = \sum_{d'}\sum_{n_1n_2}\langle\phi^{(1)}_{m_1}|\langle\chi^{(2)}_{m_2}|U_{dd'}|\phi^{(1)}_{n_1}\rangle|\chi^{(2)}_{n_2}\rangle\psi^d_{n_1n_2} \\ &= \sum_{d'}\sum_{n_2}\sum_j u^j_{dd'}(x_{m_1})\langle\chi^{(2)}_{m_2}|Q_2^{p^j_{dd'}}|\chi^{(2)}_{n_2}\rangle\psi^{d'}_{m_1n_2},\end{aligned} \tag{3.11}$$

where the DVR property Eq. (3.4) was used again. The Q_2 coordinate is given in the oscillator basis by the tridiagonal matrix [86]

$$\langle\chi^{(2)}_{m_2}|Q_2|\chi^{(2)}_{n_2}\rangle = \frac{1}{\sqrt{2}}\left(\sqrt{n_2}\,\delta_{m_2n_2-1} + \sqrt{n_2+1}\,\delta_{m_2n_2+1}\right), \tag{3.12}$$

which are multiplied to get higher powers of Q_2.

To calculate the right-hand part of the Schrödinger equation Eq. (1.3) and the VE T matrix Eq. (1.9), we need to act by the elements of V_ϵ on the vibrational components $|\psi_d\rangle$. Similarly to U we get

$$\begin{aligned}(V^\mu_{d\epsilon}\psi_d)_{m_1m_2} &\equiv \langle\phi^{(1)}_{m_1}|\langle\chi^{(2)}_{m_2}|V^\mu_{d\epsilon}|\psi_d\rangle = \sum_{n_1n_2}\langle\phi^{(1)}_{m_1}|\langle\chi^{(2)}_{m_2}|V^\mu_{d\epsilon}|\phi^{(1)}_{n_1}\rangle|\chi^{(2)}_{n_2}\rangle\psi^d_{n_1n_2} \\ &= \sum_{n_2}\sum_j g^\mu_{dj}(x_{m_1})\langle\chi^{(2)}_{m_2}|Q_2^{p^\mu_{dj}}|\chi^{(2)}_{n_2}\rangle\xi^\mu_{dj}(\epsilon)\psi^d_{m_1n_2}.\end{aligned} \tag{3.13}$$

[1] Note that resonance widths depend on $V^\mu_{d\epsilon}V^\mu_{d'\epsilon}$, see Eq. (19b) in Sec. 2 II C, resulting in the threshold behavior $\epsilon^{(2l+1)/2}$.

3.3 Nonlocal operator $F(E - H_0)$

The evaluation of the action of the nonlocal operator $F(E - H_0)$ on the full wave function $|\Psi\rangle$

$$\begin{aligned}(F\Psi)^d_{m_1m_2} &\equiv \langle d|\langle\phi^{(1)}_{m_1}|\langle\chi^{(2)}_{m_2}|F(E-H_0)|\Psi\rangle \\ &= \sum_{d'}\sum_{n_1,n_2}\langle\phi^{(1)}_{m_1}|\langle\chi^{(2)}_{m_2}|F_{dd'}(E-H_0)|\phi^{(1)}_{n_1}\rangle|\chi^{(2)}_{n_2}\rangle\psi^{d'}_{n_1n_2}\end{aligned} \tag{3.14}$$

is the most complicated step. The discrete-state elements of $F(E - H_0)$ are given by Eq. (1.7). By substituting the spectral decomposition [see Eqs. (3.2) and (3.3)]

$$H_0 = \sum_{k_1k_2}|\chi^{(1)}_{k_1}\rangle|\chi^{(2)}_{k_2}\rangle E_{k_1k_2}\langle\chi^{(1)}_{k_1}|\langle\chi^{(2)}_{k_2}| \tag{3.15}$$

into Eq. (1.7), we obtain

$$F_{dd'}(E-H_0) = \sum_{\mu}\sum_{k_1,k_2}\int \mathrm{d}\epsilon\, V^{\mu}_{d\epsilon}|\chi^{(1)}_{k_1}\rangle|\chi^{(2)}_{k_2}\rangle\,(E-E_{k_1k_2}-\epsilon+i\eta)^{-1}\,\langle\chi^{(1)}_{k_1}|\langle\chi^{(2)}_{k_2}|V^{\mu*}_{d'\epsilon}. \tag{3.16}$$

When Eq. (3.16) is substituted into Eq. (3.14), the resulting formula contains matrix elements of $V^{\mu}_{d\epsilon}$ and $V^{\mu}_{d'\epsilon}$, which can be written using the general form of the $V^{\mu}_{d\epsilon}$ functions [see Eq. (3.9)] as

$$\langle\phi^{(1)}_{m_1}|\langle\chi^{(2)}_{m_2}|V^{\mu}_{d\epsilon}|\chi^{(1)}_{k_1}\rangle|\chi^{(2)}_{k_2}\rangle = \sum_j g^{\mu}_{dj}(x_{m_1})\langle\phi^{(1)}_{m_1}|\chi^{(1)}_{k_1}\rangle\langle\chi^{(2)}_{m_2}|Q_2^{p^{\mu}_{dj}}|\chi^{(2)}_{k_2}\rangle\xi^{\mu}_{dj}(\epsilon), \tag{3.17}$$

$$\langle\chi^{(1)}_{k_1}|\langle\chi^{(2)}_{k_2}|V^{\mu}_{d'\epsilon}|\phi^{(1)}_{n_1}\rangle|\chi^{(2)}_{n_2}\rangle = \sum_{j'} g^{\mu}_{d'j'}(x_{n_1})\langle\chi^{(1)}_{k_1}|\phi^{(1)}_{n_1}\rangle\langle\chi^{(2)}_{k_2}|Q_2^{p^{\mu}_{d'j'}}|\phi^{(2)}_{n_2}\rangle\xi^{\mu}_{d'j'}(\epsilon), \tag{3.18}$$

where we also assumed that $V^{\mu}_{d\epsilon}$ are real.

In total, we get

$$\begin{aligned}(F\Psi)^d_{m_1m_2} = &\sum_{\mu}\sum_j g^{\mu}_{dj}(x_{m_1})\sum_{k_1}\langle\phi^{(1)}_{m_1}|\chi^{(1)}_{k_1}\rangle\sum_{k_2}\langle\chi^{(2)}_{m_2}|Q_2^{p^{\mu}_{dj}}|\chi^{(2)}_{k_2}\rangle \\ &\times\sum_{d'}\sum_{j'} f^{\mu}_{dd'jj'}(E-E_{k_1k_2}) \\ &\times\sum_{n_1}\langle\chi^{(1)}_{k_1}|\phi^{(1)}_{n_1}\rangle g^{\mu}_{d'j'}(x_{n_1})\sum_{n_2}\langle\chi^{(2)}_{k_2}|Q_2^{p^{\mu}_{d'j'}}|\chi^{(2)}_{n_2}\rangle\psi^{d'}_{n_1n_2},\end{aligned} \tag{3.19}$$

where the energy-dependent term $f^{\mu}_{dd'jj'}(E - E_{k_1k_2})$ is given by

$$\begin{aligned}f^{\mu}_{dd'jj'}(E-E_{k_1k_2}) &= \int \mathrm{d}\epsilon\,\xi^{\mu}_{dj}(\epsilon)(E-E_{k_1k_2}-\epsilon+i\eta)^{-1}\xi^{\mu}_{d'j'}(\epsilon) \\ &= \left(\beta^{\mu}_{dj}\right)^{\alpha^{\mu}_{dj}}\left(\beta^{\mu}_{d'j'}\right)^{\alpha^{\mu}_{d'j'}}\left[\text{v.p.}\int_0^{\infty}\mathrm{d}\epsilon\frac{\epsilon^{\alpha}e^{-\beta\epsilon}}{t-\epsilon} - i\pi e^{-\beta t}\right]\end{aligned} \tag{3.20}$$

with $\alpha \equiv \alpha^{\mu}_{dj} + \alpha^{\mu}_{d'j'}$, $\beta \equiv \beta^{\mu}_{dj} + \beta^{\mu}_{d'j'}$, $t \equiv E - E_{k_1k_2}$, and η is positive infinitesimal. In the formula above, we split the integrand into the real and imaginary parts using the relation $(x+i\eta)^{-1} = \text{v.p.}\, x^{-1} - i\pi\delta(x)$, where v.p. is the Cauchy principal value and $\delta(x)$ is the Dirac δ distribution.

The integral

$$I(t,\alpha,\beta) \equiv \text{v.p.} \int_0^\infty \mathrm{d}\epsilon \frac{\epsilon^\alpha e^{-\beta\epsilon}}{t-\epsilon} \tag{3.21}$$

can be calculated [18, 92] in terms of the exponential integral $\mathrm{E_i}(x)$, the gamma function $\Gamma(x)$, the upper incomplete gamma function $\Gamma(s,x)$, and the confluent hypergeometric function ${}_1F_1(a,b,x)$, see Abramowitz and Stegun [93, p. 227, 255, 260, 504] and also Ref. [18, p. 149]:

$$I = \begin{cases} e^{-\beta t}\,\mathrm{E_i}(\beta t) & \text{for } \alpha = 0, \\ -\Gamma(1+\alpha)(-t)^\alpha \Gamma(-\alpha,-\beta t)e^{-\beta t} & \text{for } \alpha > 0, t < 0, \\ t^\alpha e^{-\beta t}\left[\pi \cot \alpha\pi - \Gamma(\alpha)(\beta t)^{-\alpha}\,{}_1\mathrm{F}_1(-\alpha, 1-\alpha, \beta t)\right] & \text{for } \alpha > 0, t > 0. \end{cases} \tag{3.22}$$

The action of $F(E-H_0)$ on $|\Psi\rangle$ via Formula (3.19) can be viewed as a multiplication of the coefficient vector $\psi^{d'}_{n_1 n_2}$ by three sparse matrices (and summed over the partial waves μ). The first and third matrices [first and third lines in Eq. (3.19)] originate in coordinate-dependent parts of the coupling terms $V^\mu_{d\epsilon}$ and the transformation between the FEM DVR basis and the basis of the $H_0^{(1)}$ states for mode 1. This transformation matrix $\langle \phi^{(1)}_{m_1} | \chi^{(1)}_{k_1} \rangle$ can be easily obtained using

$$\langle \phi^{(1)}_{m_1} | \chi^{(1)}_{k_1} \rangle = \int \phi^{(1)}_{m_1}(x) \chi^{(1)}_{k_1}(x) \mathrm{d}x \cong \sum_j \phi^{(1)}_{m_1}(x_j) \chi^{(1)}_{k_1}(x_j) w_j = \chi^{(1)}_{k_1}(x_{m_1}) \sqrt{w_{m_1}}, \tag{3.23}$$

where we approximate the integral by the Gauss-Lobatto quadrature with weights w_j and use the property of the basis functions evaluated at the grid points $\phi^{(1)}_{m_1}(x_j) = \delta_{m_1 j}/\sqrt{w_j}$ [88]. Note that this matrix is in general full within the one-dimensional subspace for mode 1.

The middle matrix [second line in Eq. (3.19)] is energy dependent and it can be calculated once for each incident electron energy and stored for all iterations. Also note that the third matrix is independent of indices d, j, and especially, m_1 and m_2. As a result, the asymptotic complexity of the action of $F(E-H_0)$ and also of the full Hamiltonian H is $O(N_\mathrm{d}^2 N_\mathrm{p} N_1 N_2 N_1^0)$, where N_d, N_p, N_1, N_2, and N_1^0 are numbers of the discrete states, electron partial waves, basis functions for modes 1 and 2, and vibrational states of $H_0^{(1)}$, respectively. The size of the coefficient vector is $N = N_\mathrm{d} N_1 N_2$. In comparison with CO_2, where we achieved the complexity $O(N)$, we have here $O(N_0^1 N)$ because the basis functions for mode 1 are not eigenfunctions of $H_0^{(1)}$. Possible improvements for the evaluation of the Hamiltonian are discussed in Sec. 3.7.

To numerically check the implementation of $F(E-H_0)$, we also implemented its action in the x-representation (arbitrary grids for both modes). Analogically to the derivation above, we find

$$\begin{aligned} (F\Psi)^d(Q_1,Q_2) = &\sum_\mu \sum_j g^\mu_{dj}(Q_1) Q_2^{p^\mu_{dj}} \sum_{k_1} \chi^{(1)}_{k_1}(Q_1) \sum_{k_2} \chi^{(2)}_{k_2}(Q_2) \\ &\times \sum_{d'} \sum_{j'} f^\mu_{dd'jj'}(E - E_{k_1 k_2}) \\ &\times \int \mathrm{d}Q_1' \int \mathrm{d}Q_2'\, g^\mu_{d'j'}(Q_1') Q_2^{p^\mu_{d'j'}} \chi^{(1)}_{k_1}(Q_1') \chi^{(2)}_{k_2}(Q_2') \psi_{d'}(Q_1', Q_2'), \end{aligned} \tag{3.24}$$

which can be compared with the result of Eq. (3.19) evaluated at some point (Q_1, Q_2). The integrals above can be calculated by the trapezoidal rule.

3.4 Cross section for dissociative electron attachment

The integral cross sections for the VE process are given by Formula (1.8). The differential cross sections could be calculated analogically to the CO_2 case, see Sec. 2 VI. Here, a formula for the integral DEA cross section is derived. We proceed similarly to Houfek *et al.* [94, 95] by considering the flux projected on final channels.

The discrete-state potentials $V_0 + U_{dd}$ $(d = 1, \ldots, N_d)$ that are bound as $Q_1 \to \infty$ describe different electronic states of the DEA fragments $A^- + B$. Thus, we can have up to N_d open electronic channels. Furthermore, we have to still consider vibrations within the Q_2 mode, which is nondissociative. As a result, the boundary condition for the scattered wave function ψ_d of each open electronic channel reads

$$\psi_d(Q_1, Q_2) \underset{Q_1\to\infty}{\longrightarrow} \sum_{\tilde{\nu}_f} f^{\mathrm{DEA}}_{d\tilde{\nu}_f \leftarrow \nu_i} \tilde{\chi}_{d\tilde{\nu}_f}(Q_2) \sqrt{\frac{2\mu_1 K_{d\tilde{\nu}_f}}{\pi}}\, Q_1 h_0^{(1)}(K_{d\tilde{\nu}_f} Q_1), \tag{3.25}$$

where the energy normalization is used, $h_0^{(1)}(x)$ is a spherical Hankel function of the first kind [93], $K_{d\tilde{\nu}_f}$ is the relative momentum of the fragments, $f^{\mathrm{DEA}}_{d\tilde{\nu}_f \leftarrow \nu_i}$ is the scattering amplitude (ν_i describes the initial vibrational state of the molecule), and $\tilde{\chi}_{d\tilde{\nu}_f}(Q_2)$ are vibrational states within the asymptotic anionic potential, that is, they satisfy

$$\left\{T_N^{(2)} + \lim_{Q_1\to\infty}\left[V_0(Q_1, Q_2) + U_{dd}(Q_1, Q_2)\right]\right\}\tilde{\chi}_{d\tilde{\nu}_f}(Q_2) = E_{d\tilde{\nu}_f}\tilde{\chi}_{d\tilde{\nu}_f}(Q_2), \tag{3.26}$$

where the kinetic energy operator for mode 2 $T_N^{(2)}$ is defined in Eq. (3.1). The momentum $K_{d\tilde{\nu}_f}$ is given by the conservation of the total energy E

$$E = \epsilon_i + E_{\nu_i} = E_{d\tilde{\nu}_f} + \frac{K^2_{d\tilde{\nu}_f}}{2\mu_1}. \tag{3.27}$$

Depending on the angular momenta of the incoming electron partial wave and the electronic states of the molecule and fragments, we should also consider higher partial waves $h_l^{(1)}$ in Eq. (3.25) to conserve the total angular momentum. For simplicity, we here neglect the rotational motion of the fragments and we consider only the s wave $h_0^{(1)}$ in the boundary condition.

The integral DEA cross section can be calculated by integrating the outgoing flux [94]

$$\sigma^{\mathrm{DEA}}_{d\tilde{\nu}_f \leftarrow \nu_i}(\epsilon_i) = \frac{\pi^2}{\epsilon_i} \lim_{Q_1\to\infty} \int_{-\infty}^{\infty} \vec{F}_{d\tilde{\nu}_f}(Q_1, Q_2) \cdot \vec{n}_{Q_1} \mathrm{d}Q_2, \tag{3.28}$$

where $\vec{n}_{Q_1}$ is a unit vector in the direction of the Q_1 coordinate and $\vec{F}_f$ is the flux projected on a final state f:

$$\vec{F}_f = \frac{1}{2i}\left[(P_f\Psi)^*\nabla(P_f\Psi) - (P_f\Psi)\nabla(P_f\Psi)^*\right] \tag{3.29}$$

with the gradient operator

$$\nabla = \begin{pmatrix} \frac{1}{\mu_1}\frac{\partial}{\partial Q_1} \\ \frac{1}{\mu_2}\frac{\partial}{\partial Q_2} \end{pmatrix}. \tag{3.30}$$

In our case, P_f projects on electronic channel d and final vibrational state $\tilde{\nu}_f$

$$P_{d\tilde{\nu}_f}\Psi = \tilde{\chi}_{d\tilde{\nu}_f}(Q_2)\int_{-\infty}^{\infty}\tilde{\chi}_{d\tilde{\nu}_f}(Q_2)^*\psi_d(Q_1,Q_2)\mathrm{d}Q_2 \equiv \tilde{\chi}_{d\tilde{\nu}_f}(Q_2)\psi_{d\tilde{\nu}_f}(Q_1), \tag{3.31}$$

where the integral was denoted by $\psi_{d\tilde{\nu}_f}(Q_1)$, and we get

$$\vec{F}_{d\tilde{\nu}_f}\cdot\vec{n}_{Q_1} = \frac{1}{2i\mu_1}\Big[(P_{d\tilde{\nu}_f}\Psi)^*\frac{\partial}{\partial Q_1}(P_{d\tilde{\nu}_f}\Psi) - (P_{d\tilde{\nu}_f}\Psi)\frac{\partial}{\partial Q_1}(P_{d\tilde{\nu}_f}\Psi)^*\Big]. \tag{3.32}$$

Using the asymptotic behavior Eq. (3.25) we can easily evaluate the derivative of $P_{d\tilde{\nu}_f}\Psi$ since $xh_0^{(1)}(x) = -i\exp(ix)$ [93]:

$$\lim_{Q_1\to\infty}\frac{\partial}{\partial Q_1}\psi_{d\tilde{\nu}_f}(Q_1) = \lim_{Q_1\to\infty} iK_{d\tilde{\nu}_f}\,\psi_{d\tilde{\nu}_f}(Q_1) \tag{3.33}$$

and we obtain

$$\lim_{Q_1\to\infty}\vec{F}_{d\tilde{\nu}_f}\cdot\vec{n}_{Q_1} = \frac{K_{d\tilde{\nu}_f}}{\mu_1}|\tilde{\chi}_{d\tilde{\nu}_f}(Q_2)|^2\lim_{Q_1\to\infty}|\psi_{d\tilde{\nu}_f}(Q_1)|^2. \tag{3.34}$$

Finally, the vibrational states $\tilde{\chi}_{d\tilde{\nu}_f}$ are normalized, and thus, the integral cross section reads

$$\sigma^{\mathrm{DEA}}_{d\tilde{\nu}_f\leftarrow\nu_i}(\epsilon_i) = \frac{\pi^2}{\epsilon_i}\frac{K_{d\tilde{\nu}_f}}{\mu_1}\lim_{Q_1\to\infty}|\psi_{d\tilde{\nu}_f}(Q_1)|^2. \tag{3.35}$$

In practice, the limit above is calculated by evaluating the wave function at the end of the real part of the FEM DVR ECS grid.

3.5 Implementation and numerical solution

The implementation for mode 2 is straightforward since we deal only with the oscillator basis and it follows the treatment of CO_2. The case of mode 1 is more complicated because we have the FEM DVR ECS grid, whose part is complex (when the anion can dissociate), and furthermore, we have another DVR grid used to find the eigenstates of $H_0^{(1)}$. When the molecular anion can dissociate via one or more discrete states, the potentials $V_d \equiv V_0 + U_{dd}$ should tend to constants in Q_1 as $Q_1 \to \infty$ and the corresponding coupling elements $U_{dd'}$ and $V^{\mu}_{d\epsilon}$ should vanish in order to satisfy the assumptions of the scattering theory [96].

It is not necessary to evaluate every term of the effective Hamiltonian H Eq. (1.6) on the full complex grid. The kinetic energy operator has to be evaluated on the full grid to enforce the outgoing boundary condition. We evaluate the neutral potential V_0 and elements of U on the full grid as well because they may contain long-range terms. On the other side, it is convenient to restrict the $H_0^{(1)}$ grid to geometries where $V^{\mu}_{d\epsilon}$ are nonzero and choose the FEM DVR ECS grid in such a way that the $H_0^{(1)}$ grid either coincides with the real part of the complex grid or is its subinterval. Then, $F(E-H_0)|\Psi\rangle$ is nonzero only in grid points that are in the interval of geometries defined by the $H_0^{(1)}$ grid.

To solve the Schrödinger equation Eq. (1.3) rewritten to a system of linear equations, we again use the Conjugate Orthogonal Conjugate Gradient (COCG) method [97] as in the case of CO_2, see Sec. 2 VI B. We found that the rate of

convergence is slow when the dissociation channel is open. Thus, we, analogically to CO_2, implemented a preconditioner based on the inversion of blocks comprised of the discrete states and one of the vibrational modes (Sec. 2 VI B). Details about the iterative solution are also given by Šarmanová *et al.* [65–67].

We verified the implementation of this dynamics by calculating the VE cross sections for the model of Estrada *et al.* [9] (Sec. 1.3.2) and its generalization studied by Šarmanová *et al.* [67]. The results are in agreement with the cross sections obtained using the harmonic bases for both vibrational modes. Furthermore, the dissociative dynamics was tested on a 1D model for the e + pyrrole system (Chapter 4), which we are also able to solve by the Schwinger-Lanczos approach used before for 1D nonlocal calculations [18, ch. 4].

3.6 Structure of Hamiltonian matrix

In this section, we focus on the structure of the effective Hamiltonian H Eq. (1.6) expressed in the $|\phi^{(1)}_{n_1}\rangle|\chi^{(2)}_{n_2}\rangle|d\rangle$ basis. We consider two cases: the original system of Estrada *et al.* [9] (Sec. 1.3.2) and the e + pyrrole system that will be investigated in Chapter 4.

Figure 3.1 shows the Hamiltonian for the model of Estrada *et al.* [9]. The order of the basis indices is as follows. The inner index n_1 (changes the fastest) runs over the FEM DVR functions describing the Q_g mode. Then, the Q_u mode is expressed in the harmonic basis indexed by n_2 while the outer index d runs over the two discrete states. For the illustration purposes, we used two elements with seven DVR points in each element and three oscillator functions. Since there is no dissociation in this model, all FEM DVR grid points are real.

The structure of the neutral Hamiltonian H_0 given by Eq. (3.1) is mostly affected by the matrix of the kinetic energy operator expressed in the FEM DVR basis. This matrix is full within individual elements, which overlap at outer points [88]. Other terms of H_0 are diagonal, see Eq. (3.7).

In the case of the U matrix given by Eq. (1.16), the blocks that are diagonal in the discrete states (U_{11} and U_{22}) depend only on the Q_g coordinate, and thus, are diagonal due to the DVR basis. The U_{12} and U_{21} blocks are proportional to the Q_u coordinate that is represented by the tridiagonal matrix (with empty diagonal) in the harmonic basis, see Eq. (3.12). The $F(E - H_0)$ operator is independent of the nuclear coordinates, which results in a block-diagonal structure. The blocks within the FEM DVR basis are full because of the full transformation matrices between the $H_0^{(1)}$ eigenstates and the FEM DVR functions, see Eq. (3.19).

The model of the e + pyrrole system constructed in Sec. 4.2 is more elaborate, which results in a more complicated structure of the Hamiltonian, see Fig. 3.2. The dissociation is allowed in this case, which leads to complex grid points. For the illustration, we considered three elements for the Q_1 mode, where the third element is rotated to the complex plane, and eight harmonic functions for the Q_2 mode. The imaginary part of the $(E - H_0)I$ matrix is nonzero for complex grid points but the real part is analogous to the case in Fig. 3.1. The U_{12} and U_{21} blocks are again tridiagonal but U_{11} is pentadiagonal with empty first off-diagonals due to a term proportional to Q_2^2 while U_{22} is enneadiagonal[2] (first and third

[2] *Ennea-* is a Greek prefix for number nine.

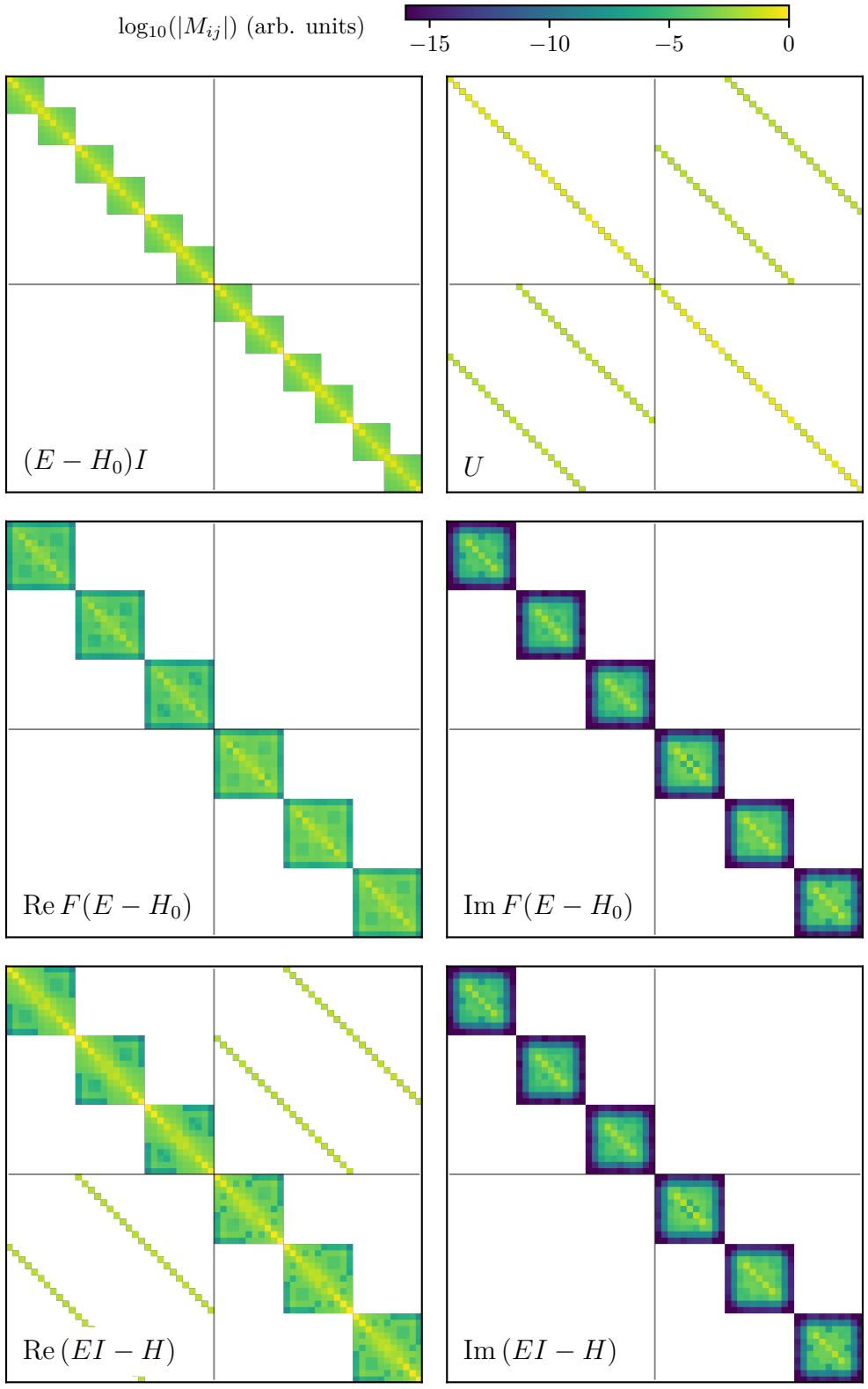

Figure 3.1: Structure of matrices $(E - H_0)I$, U, $F(E - H_0)$, and $EI - H$ for the model of Estrada *et al.* [9] and incoming electron energy of 3 eV. Matrix elements M_{ij} are normalized with respect to the maximum of $EI - H$ and the elements that are strictly zero are shown by white color for clarity. The order of indices from inner to outer is n_1 (FEM DVR basis for q_1 mode), n_2 (harmonic basis for q_2 mode), and d (discrete states). The 2×2 discrete-state blocks are indicated.

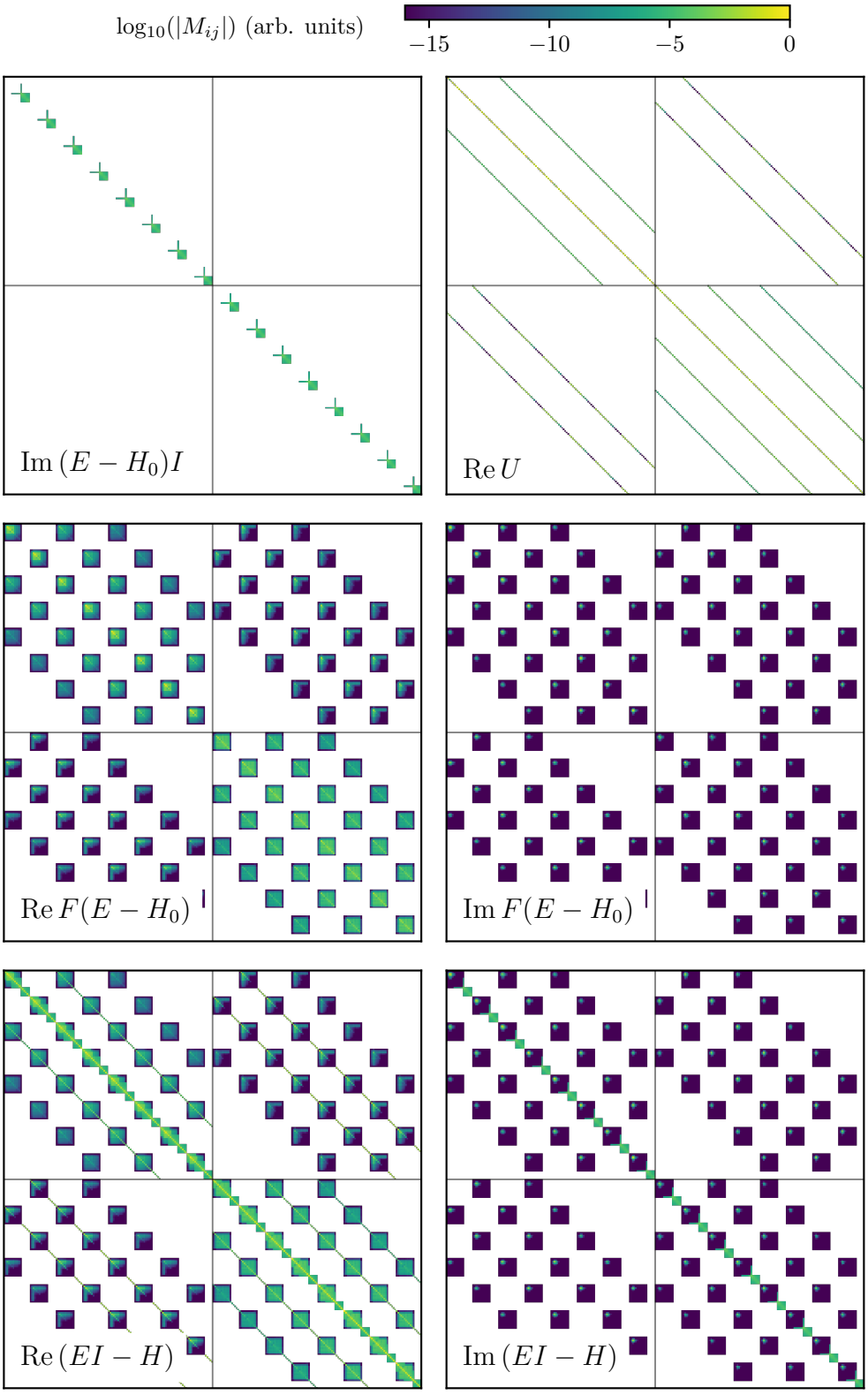

Figure 3.2: Structure of matrices $(E - H_0)I$, U, $F(E - H_0)$, and $EI - H$ for the e + pyrrole system and incoming electron energy of 2.5 eV. Matrix elements M_{ij} are normalized with respect to the maximum of $EI - H$ and the elements that are strictly zero are shown by white color for clarity. The order of indices from inner to outer is n_1 (FEM DVR basis for q_1 mode), n_2 (harmonic basis for q_2 mode), and d (discrete states). The 2×2 discrete-state blocks are indicated.

off-diagonals are empty) because of a Q_2^4 term.

This time, the $F(E - H_0)$ is also coordinate dependent and is no longer block diagonal. The F_{11} and F_{22} elements are again enneadiagonal since they depend on Q_2^4 whereas we have a heptadiagonal structure for F_{12} and F_{21} because of Q_2^3. We remind that the $F(E - H_0)$ operator is evaluated only at those FEM DVR grid points that are also in the interval where the $H_0^{(1)}$ eigenstates are constructed (Sec. 3.5). For this reason, the $F(E - H_0)$ blocks for the Q_1 mode are full matrices only within this subpart of the complex grid. Here, the $H_0^{(1)}$ grid coincides with the real part of the FEM DVR grid, that is, with the first two elements.

3.7 Possible improvements for the implementation of the dynamics

We implemented only the action of the $EI - H$ operator on the anionic wave function in all dynamical calculations presented in this thesis. Such an approach allows a rather straightforward implementation even of the 4D Hamiltonian of the $e + CO_2$ system. On the other hand, the explicit knowledge of the matrix elements is needed to construct the preconditioner. In our calculations we acted on all basis vectors to evaluate the Hamiltonian, which can be optimized in the case of the harmonic basis by acting only on a small part of the basis vector (Sec. 2 VI B). However, this trick cannot be used for the FEM DVR grid because, as shown above, the Hamiltonian within this dimension is a full matrix (or considerably full if the dissociation is allowed), which harms the performance. Solving the dynamics took about 110 seconds on one CPU core and for one electron energy (with open dissociative channel) in the case of pyrrole, where about 100 seconds is spent on the evaluation of the Hamiltonian. The 2D calculations are thus manageable but the calculation of the preconditioner could become quickly problematic if more vibrational dimensions described by the FEM DVR grids are taken into account.

This limitation could be overcome if we explicitly construct the Hamiltonian matrix. We could follow the same formulae used to evaluate the action on a vector but instead the action itself, we could gradually multiply the matrices to build H_0, U, and $F(E - H_0)$. The calculation should be efficient if all involved matrices are represented in suitable sparse formats. The $F(E - H_0)$ potential has the form of three multiplied matrices [see Eq. (3.14)], where the outer ones are energy independent. Thus, the H_0, U, and the coordinate-dependent parts of $F(E - H_0)$ could be built only once for all electron energies.

The explicit construction of the Hamiltonian would somewhat increase demands on computer memory. On the other hand, we could speed up the iterations (and lower memory demands) by neglecting very small elements of the Hamiltonian (Figs. 3.1 and 3.2), which would be especially significant when the FEM DVR grid is employed for more vibrational modes. Some of the negligible elements originate from the transformation matrices between the grid and the H_0 eigenstates, whose elements are proportional to the eigenstates evaluated on the grid, see Eq. (3.23). It did not turn out to be beneficial in the current implementation to represent only the transformation matrices in the compressed sparse row format because the related overhead outweighs the speed up gained by neglecting some of the elements.

Chapter 4

Dissociative electron attachment to pyrrole

Recently, Kumar *et al.* [14] have observed that the out-of-plane movement of carbon-bonded hydrogens significantly influences the breaking of the N-H bond in the dissociative electron attachment (DEA) to the pyrrole molecule

$$e + \mathrm{C_4H_4NH} \rightarrow \mathrm{H} + \mathrm{C_4H_4N^-}. \tag{4.1}$$

Pyrrole is a ring molecule belonging to the C_{2v} point group with the ring consisting of four carbon atoms and one nitrogen atom. When only the hydrogens attached to the carbons were deuterated, they observed the DEA signal to drop to about a half of the original signal with five undeuterated hydrogens. When all five hydrogens were deuterated, the signal decreased more than ten times, as expected from the increase of the reduced mass for the N-H motion. The deuteration of the four carbon-bonded hydrogens has a negligible effect on the N-H reduced mass and it does not explain the decrease of the signal. Based on *ab initio* fixed-nuclei R-matrix calculations, they reasoned that the dissociation is significantly mediated by a nondissociative π^* resonance, which couples to the dissociative σ^* state upon the out-of-plane movement of the carbon-attached hydrogens. In what follows, we study this system within the two-dimensional model that was introduced in the previous chapter.

4.1 *Ab initio* fixed-nuclei data

We start by discussing *ab initio* fixed-nuclei calculations of the e+pyrrole scattering. All *ab initio* data presented here were calculated by Zdeněk Mašín [14, 98] using the UKRmol+ implementation [99] of the R-matrix method [19]. Similarly to CO_2 (Sec. 2 IV A), the target was described by the Hartree-Fock approximation with the cc-pVDZ basis [100] and a static-exchange plus polarization model was employed as a scattering model within the R-matrix method. In particular, five lowest orbitals were kept frozen resulting in 13 active orbitals from which one electron could be additionally excited to one of 40 virtual orbitals. The R-matrix sphere with a radius of 20 bohrs was used and all calculations considered here were performed in the C_1 group, that is, without any symmetry.

The calculations reveal two low-lying π^* resonances, $^2B_1$ at 2.3 eV and $^2A_2$ at 3.7 eV, which do not dissociate as the N-H bond stretches in the energy window of interest (0–4 eV), see also the calculations of de Oliveira *et al.* [101]. The $^2A_2$ resonance does not contribute to the DEA [14] (no peak in the experimental

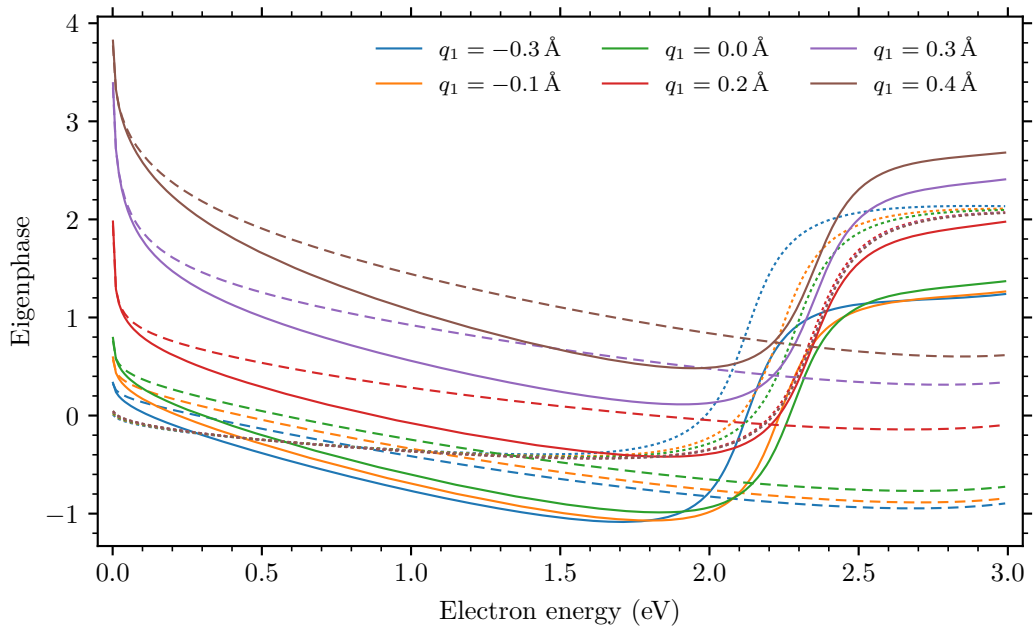

Figure 4.1: *Ab initio* R-matrix eigenphase sums of e + pyrrole scattering for stretched N–H geometries (ν_1 mode): sums over all irreducible representations (solid), only B_1 representation of C_{2v} (dotted), $A_1 + A_2 + B_2$ representation (dashed), where A_2 and B_2 contribute only to the background.

cross section) and is not considered further for the nuclear dynamics. In addition, a $^2A_1$ valence bound state, which is connected with the H+$C_4H_4N^-$ dissociation asymptote, appears for stretched N-H geometries. For smaller bond lengths the $^2A_1$ state does not become a σ^* resonance. It behaves like a virtual state but the corresponding S-matrix pole quickly disappears in the complex plane due to the supercritical dipole moment of pyrrole [14, 102].

Since the $^2A_1$ state and the $^2B_1$ resonance have different symmetries, they can not be coupled to each other upon pure N-H stretching, which respects the C_{2v} molecular symmetry. They can interact if the planar symmetry is distorted by displacements of the nuclei that follows the B_1 symmetry. The pyrrole molecule has ten atoms resulting in $3N-6 = 24$ vibrational modes, out of which four modes belong to the B_1 irreducible representation. For an illustration of the normal modes, see Fig. 2 of Mellouki *et al.* [103] or Davies *et al.* [104]. Based on the shape of the potentials from the R-matrix calculations, Kumar *et al.* [14] argued that the ν_{13} mode (predominantly out-of-plane movement of carbon-attached hydrogens) should play a prominent role in the dynamics. Therefore, our model includes the $^2A_1$ and $^2B_1$ electronic states of the pyrrole anion, together with the ν_1 (N-H stretching) and ν_{13} modes described by coordinates q_1 and q_2 (measured in ångström) or by dimensionless coordinates Q_1 and Q_2, see below.

By examining the vibrational modes (Fig. 2 of Refs. [103, 104]), it is not surprising that the higher-lying $^2A_2$ resonance does not contribute to the DEA cross section. It can couple to the $^2A_1$ state via vibrational modes of the A_2 symmetry but neither of these modes affects the N-H bond.

Figure 4.1 shows *ab initio* eigenphase sums for purely N-H stretched geometries calculated in the C_1 group (solid lines). Because the C_{2v} symmetry is still

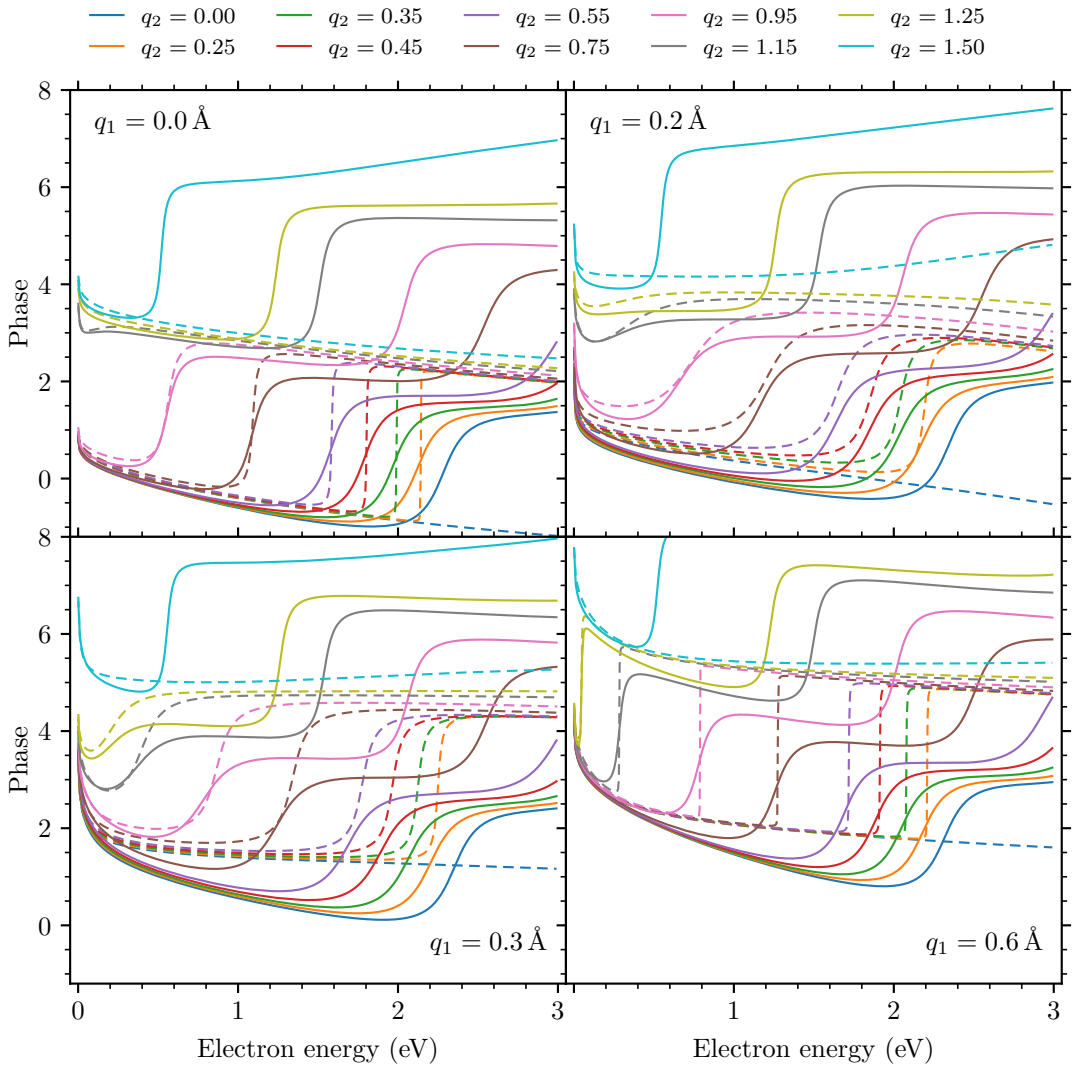

Figure 4.2: *Ab initio* R-matrix phases of e+pyrrole scattering for geometries distorted in ν_1 and ν_{13} modes (coordinates q_1 and q_2 in ångström, respectively): total eigenphase sums (solid) and s-wave K-matrix phases $\arctan K_{ss}$ (dashed).

preserved, we can manually separate the contributions of individual irreducible representations, which helps us to understand the rather peculiar behavior of the eigenphase sums. The $^2B_1$ resonance slowly moves further away from the threshold as the N-H bond length increases (dotted lines). As mentioned above, no resonant behavior is observed for the $^2A_1$ state (dashed lines). Note that we use these data below to construct the model, where it is convenient to have a consistent background for all geometries. Therefore, we included the contributions of A_2 and B_2 representations in the dashed lines in Fig. 4.1 since they contribute only to the background in this energy interval. For $q_1 > -0.2$ Å, the dipole moment of pyrrole is supercritical, which results in the logarithmic divergence of the eigenphase sums at the threshold [102, 105]. Furthermore, the $^2A_1$ state becomes bound around $q_1 = 0.3$ Å (potentials are shown in the next section) that is reflected by the vertical shift of π radians in the eigenphases in accordance with Levinson's theorem [102].

The behavior of the eigenphase sums upon distortion of the geometry along

the ν_{13} mode (q_2 coordinate) is shown in Fig. 4.2 for four N-H stretches $q_1 = 0.0$, 0.2, 0.3, and 0.6 Å. The higher-lying $^2A_2$ resonance is visible for larger values of q_2. Both resonances move closer to the threshold as q_2 increases and eventually become bound. The symmetry of the molecule is lowered to the C_s group for $q_2 \neq 0$ and both the $^2A_1$ and $^2B_1$ states transform according to the A' representation of C_s, that is, they can mix. The $^2A_2$ resonance transforms as A'' and could be separated off the data in Fig. 4.2. The mixing of the $^2A_1$ and $^2B_1$ states is much more subtle than what we observed upon bending in the case of CO_2. Here, the resonance is still well recognizable. It gets somewhat wider for N-H stretches where the $^2A_1$ state is about to become bound or is weakly bound ($q_1 = 0.2$–0.4 Å).

To investigate the mixing further, we examined the energy dependence of the s-wave element K_{ss} of the fixed-nuclei K matrix (dashed lines in Fig. 4.2), see also Sec. 2 V C. Because of the symmetry lowering, the $^2B_1$ resonance can interact with the s wave for $q_2 \neq 0$ resulting in the resonance step by π radians that also appears in $\arctan K_{ss}$. The width of this resonance step reflects the amount of mixing between the states, which primarily occurs at geometries where the states get close to each other, that is, most dominantly at geometries where the $^2A_1$ becomes bound.

4.2 Model

In this section, the two-dimensional approach described in Chapter 3 is applied to the e + pyrrole system and model parameters are obtained by fitting the fixed-nuclei data. As explained above, our simplified dynamics takes into account only the N-H stretching (ν_1 normal mode) and the out-of-plane movement of carbon-attached hydrogens (ν_{13} model) described by coordinates q_1 and q_2, respectively. The molecular anion can dissociate in the ν_1 mode, therefore, we describe it within the FEM DVR ECS basis. The ν_{13} mode is restricted to be harmonic.

4.2.1 Form of Hamiltonian elements

The neutral potential along the q_1 coordinate can be well approximated by a Morse potential and we have a harmonic potential along q_2:

$$V_0^{(1)}(q_1) = D(e^{-aq_1} - 1)^2, \tag{4.2}$$

$$V_0^{(2)}(q_2) = \frac{1}{2}kq_2^2. \tag{4.3}$$

We obtained $D = 0.29511$ hartree, $a = 1.0381$ bohr^{-1}, and $k = 0.065265$ a.u. from the fit to *ab initio* potential energies of the $^1A_1$ ground electronic state of pyrrole.

We define dimensionless coordinates Q_1 and Q_2 by

$$Q_1 = \frac{q_1}{x_0^{(1)}}, \quad x_0^{(1)} = \frac{1}{a}, \tag{4.4}$$

$$Q_2 = \frac{q_2}{x_0^{(2)}}, \quad x_0^{(2)} = \sqrt{\frac{1}{\mu_2\omega_2}}, \quad \omega_2 = \sqrt{\frac{k}{\mu_2}}, \tag{4.5}$$

where the reduced masses $\mu_1 = 1.0811$ Da (see below) and $\mu_2 = 1.2586$ Da were obtained by Kumar *et al.* [14, 98] from calculations of the vibrational structure

using the GAUSSIAN software [106]. The neutral vibrational Hamiltonian H_0 has the following form in the dimensionless coordinates

$$H_0 = -\frac{1}{2}\frac{D}{\lambda_0}\frac{\partial^2}{\partial Q_1^2} - \frac{1}{2}\omega_2\frac{\partial^2}{\partial Q_2^2} + D(e^{-Q_1} - 1)^2 + \frac{1}{2}\omega_2 Q_2^2, \tag{4.6}$$

where $\lambda_0 = \mu_1 D/a^2$.

For the vibrational frequencies, we get $\omega_1 = a\sqrt{2D/\mu_1} = 489$ meV and $\omega_2 = 145$ meV. In comparison, the experimental values are [107][1] $\omega_1^{\text{exp}} = 438$ meV and $\omega_2^{\text{exp}} = 102$ meV, that is, the disagreement is quite substantial for the ν_{13} mode. More elaborate quantum chemical calculations could be affordable for the target and geometries where anionic states are bound, however, it is difficult to ensure consistency (positions where potentials cross each other) between these data and data for the scattering in the case of multiple nuclear dimensions. Therefore, we prefer to use all data from the same electron-molecule scattering calculations even thought the agreement for the vibrational frequencies is not ideal.

For the electron in the continuum, we consider the lowest partial waves that couples to the $^2A_1$ and $^2B_1$ states in the equilibrium symmetry, that is, s and p_x waves (molecular plane is the yz plane), respectively. The dependence of the U and V_ϵ matrices on the vibrational coordinates can be derived analogically to the CO_2 case, see Sec. 2 II C. This time the derivation is simpler since the C_{2v} point group is a smaller and also Abelian group and we obtain

$$U = \begin{array}{c} \\ A_1 \\ B_1 \end{array} \begin{array}{c} \begin{array}{cc} A_1 & B_1 \end{array} \\ \begin{pmatrix} E_A & \lambda Q_2 \\ \lambda Q_2 & E_B \end{pmatrix} \end{array}, \tag{4.7}$$

$$V_\epsilon = \begin{array}{c} \\ A_1 \\ B_1 \end{array} \begin{array}{c} \begin{array}{cc} s & p_x \end{array} \\ \begin{pmatrix} v_{As} & v_{Ap}Q_2 \\ v_{Bs}Q_2 & v_{Bp} \end{pmatrix} \end{array}, \tag{4.8}$$

where E_A, E_B, λ, v_{As}, v_{Bp}, v_{Bs}, and v_{Ap} are in general arbitrary functions of totally symmetric combinations of the coordinates, that is, they can depend on Q_1 and Q_2^2. To reiterate, $V_0 + E_A$ and $V_0 + E_B$ give the diabatic potentials that are directly coupled via λ and both partial waves can attach or detach from or to both discrete states for $Q_2 \neq 0$.

We expand the parameter functions to low-order polynomials in Q_2:

$$E_A = E_A^0 + E_A^2 Q_2^2, \tag{4.9}$$

$$E_B = E_B^0 + E_B^2 Q_2^2 + E_B^4 Q_2^4, \tag{4.10}$$

$$v_{As} = v_{As}^0 + \tilde{v}_{As}^0 + v_{As}^2 Q_2^2, \tag{4.11}$$

$$v_{Bp} = v_{Bp}^0 + v_{Bp}^2 Q_2^2, \tag{4.12}$$

$$v_{Bs} = v_{Bs}^1 + \tilde{v}_{Bs}^1, \tag{4.13}$$

$$v_{Ap} = v_{Ap}^1, \tag{4.14}$$

[1] Note that Ref. [107] uses a different numbering of the vibrational modes. Modes ν_1 and ν_{13} used here correspond to modes ν_{24} and ν_6 in Ref. [107], respectively.

where the energy-dependent terms $v^i_{d\mu}$ of the continuum coupling are of the form

$$v^i_{d\mu} = a(Q_1)(\beta\epsilon)^\alpha e^{-\beta\epsilon}. \tag{4.15}$$

The coefficients E^i_d and prefactors a are so far unspecified functions of Q_1 and αs with βs are constant. The parameter λ is considered to depend only on Q_1 without other terms in Q_2.

The pyrrole molecule possesses a supercritical dipole moment along the ν_1 and ν_{13} modes. Thus, we set the threshold exponent $\alpha = 0$ for the terms $\tilde{v}^0_{As}$ and $\tilde{v}^0_{Bs}$, see also the discussion about α in Sec. 3.2. However, we found that such a parametrization is not flexible enough to describe the widths further away from the threshold, therefore, we added purely s-wave terms v^0_{As} and v^0_{Bs}, which have $\alpha = (2l+1)/4 = 1/4$. For completeness, v^2_{As} behaves as an s wave as well and the remaining terms v^0_{Bp}, v^2_{Bp}, and v^1_{Ap}, have a p-wave character, that is, $\alpha = 3/4$.

4.2.2 Obtaining model parameters from *ab initio* data

We utilized the molecular symmetry to obtain the parameter functions by fitting the model to the *ab initio* fixed-nuclei data. The fitting strategy was similar to the CO_2 case discussed in Sec. 2 IV C. In the first step, we considered only C_{2v} geometries ($q_2 = 0$), where the $^2A_1$ and $^2B_1$ states can be treated separately as shown above in Fig. 4.1. Once again, we compared the corresponding *ab initio* eigenphase sums with model eigenphase sums of the form

$$\delta(\epsilon) = \delta_{\text{disc}}(\epsilon) + \delta_{\text{bg}}(\epsilon), \tag{4.16}$$

where the formula for the discrete-state contribution $\delta_{\text{disc}}(\epsilon)$ is given by Eq. (29a) in Sec. 2 III B. The background for the $^2A_1$ and $^2B_1$ states is considered as follows

$$\delta^A_{\text{bg}}(\epsilon) = a^A_{\log} \log\epsilon + a^A\epsilon + b^A, \tag{4.17}$$

$$\delta^B_{\text{bg}}(\epsilon) = a^B_{\log} \log\epsilon + a^B\epsilon + b^B. \tag{4.18}$$

The $\log\epsilon$ terms related to the supercriticality of the dipole have to be included even in the background, see below.

We fitted the model to the data for $q_1 \in \{-0.3, -0.2, -0.1, 0.0, 0.2, 0.3, 0.4, 0.6, \text{and } 0.8\}$ Å, and then, we approximated the obtained data points for Q_1-dependent coefficients by suitable functions. We also included $^2A_1$ bound energies into the fit. This way we fixed E^0_A, E^0_B, v^0_{As}, $\tilde{v}^0_{As}$, and v^0_{Bp}. The resulting comparison of the model and R-matrix eigenphase sums at the equilibrium configuration is shown in the left part of Fig. 4.3.

The $\log\epsilon$ term is necessary in the A_1 background [see Eq. (4.17)] because the discrete-state-continuum coupling should vanish as $q_1 \to \infty$ since the $^2A_1$ state is bound for large N-H stretches. However, the separation of the eigenphases into the discrete-state contribution and the background becomes ambiguous. We regarded the eigenphases for $q_1 = -0.3$ and 0.8 Å as a pure background but the increase by π radians was subtracted from $q_1 = 0.8$ Å. The coefficients $a^A_{\log}$, a^A, and b^A for other geometries were obtained by linear interpolation. This way the discrete-state part contains the change by π radians as the $^2A_1$ state becomes bound and the coupling vanishes as $q_1 \to \infty$, see the right panel of Fig. 4.3.

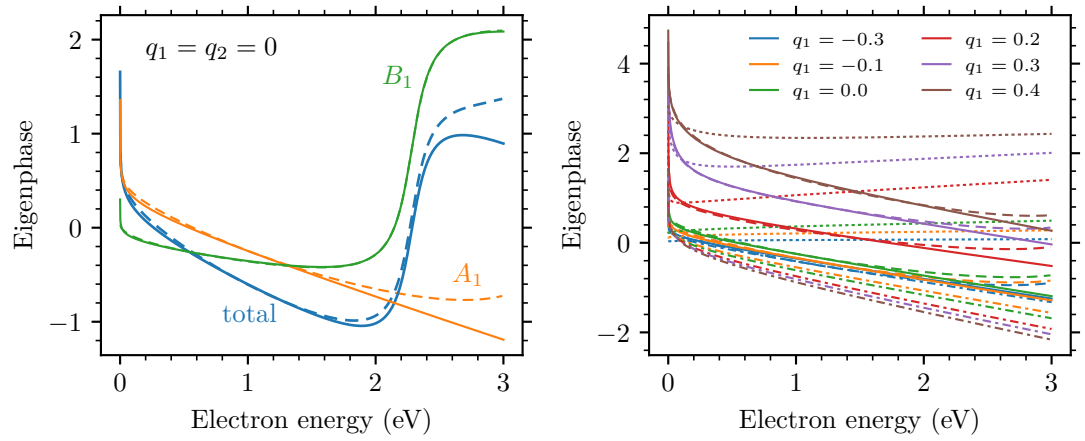

Figure 4.3: **Left panel**: Comparison of model eigenphase sums (solid) with R-matrix data (dashed) for the equilibrium geometry ($q_1 = q_2 = 0$). The total sum is the sum of the B_1 and A_1 contributions, which were fitted separately. **Right panel**: A_1 eigenphase sums for N-H stretches in ångström ($q_2 = 0$): model (solid), *ab initio* data (dashed), model discrete-state part (dotted), and model background part (dot-dashed).

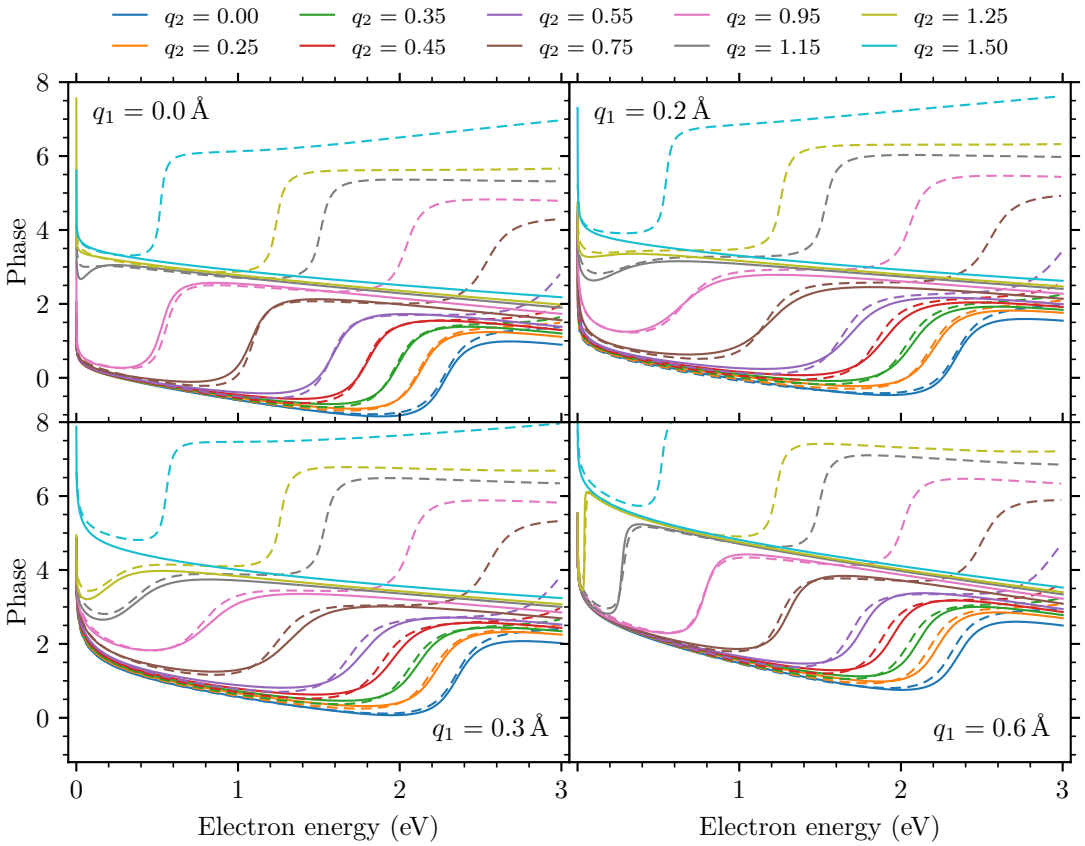

Figure 4.4: Comparison of model (solid) and *ab initio* (dashed) eigenphase sums of e + pyrrole for geometries along the q_2 coordinate (in ånström, legend on the top) and for $q_1 = 0.0$, 0.2, 0.3, 0.6 Å (different panels).

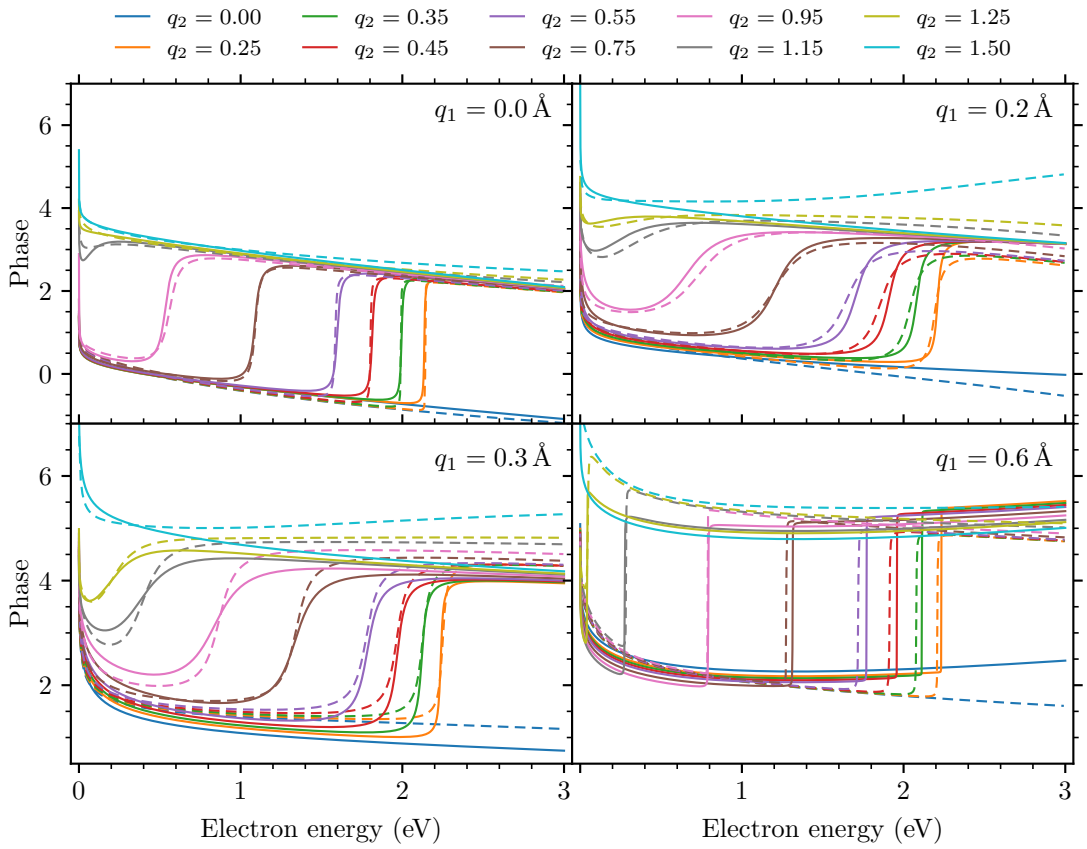

Figure 4.5: Comparison of model (solid) and *ab initio* (dashed) s-wave K-matrix phases $\arctan K_{ss}$ of e + pyrrole for geometries along the q_2 coordinate (in ångström, legend on the top) and for $q_1 = 0.0$, 0.2, 0.3, 0.6 Å (different panels).

Since the resonance behavior is well separated from the threshold, we can easily determine the background $a^B_{\log}$ term for the $^2B_1$ state [Eq. (4.18)].

At this point, the model was constructed along the N-H stretching. In the second step of the fitting procedure, we considered the ν_{13} mode. First, we preformed fits with a fixed q_1 and for $q_2 \in \{0.00, 0.15, 0.25, 0.35, 0.45, 0.50, 0.55, 0.65, 0.75, 0.85, 0.95, 1.00, 1.05, 1.15, 1.25, \text{and } 1.50\}$ Å. Since the mixing between the $^2A_1$ and $^2B_1$ states is rather subtle, we fitted not only the eigenphase sums but also the s-wave K-matrix phases $\arctan K_{ss}(\epsilon)$. The background parts for the eigenphase sums and the s-wave K-matrix elements were assumed in the following forms

$$\delta_{\text{bg}}(\epsilon) = \delta^A_{\text{bg}}(\epsilon) + \delta^B_{\text{bg}}(\epsilon) + (a_1\epsilon + b_1)Q_2, \tag{4.19}$$

$$\delta^K_{\text{bg}}(\epsilon) = \delta^A_{\text{bg}}(\epsilon) + a^K\epsilon + a^K_{\text{sqrt}}\sqrt{\epsilon} + b^K Q_2. \tag{4.20}$$

Moreover, we took into consideration R-matrix potential energies of the $^2A_1$ and $^2B_1$ states for geometries where they are bound. We again obtained a series of points for each Q_1-dependent parameter. We typically approximated one or two parameters by suitable functions and we refitted the model to get a smoother series of points for the remaining parameters. This process was repeated until all parameters were fixed. Then, a final global fit was performed for all used geometries to vary parameters of the Q_1-dependent functions and the exponential parameters β. The resulting model parameters are listed in Appendix A. The

agreement between the *ab initio* data and the model is satisfactory, see Figs. 4.4 and 4.5, with a notable disagreement in the background of the s-wave phase for larger N-H stretches.

4.2.3 Potential energy surfaces

One-dimensional cuts through the constructed 2D bound PESs are shown in Fig. 4.6 including the comparison with the *ab initio* energies from the R-matrix calculations. Note that the neutral potential is the sum of 1D potentials along q_1 and q_2 [see Eq. (3.1)] and we fitted the difference between bound neutral and anionic energies instead of absolute positions. The anionic states are very weakly bound for many geometries due to the supercritical dipole.

Figure 4.7 shows the full 2D bound PESs as contours calculated within the model. The resonance becomes bound as q_2 increases for all q_1 but the virtual-like state remains in the continuum for N-H stretches around the equilibrium. As a result, we observe an avoided crossing between the anionic potentials, see cut along q_1 for $q_2 = 1.5$ Å in Fig. 4.6. However, it occurs at high energies. The discrete-state potentials $V_d \equiv V_0 + U_{dd}$ are shown in Fig. 4.8 for pure N-H stretches, together with the $^2B_1$ LCP potential defined by K-matrix poles (Sec. 2 III C). Since the $^2A_1$ virtual-like state is very broad, S-matrix poles should be used to define the local potential for this state and for both states when $q_2 \neq 0$ because of their mutual mixing. The complex adiabatic potentials are worth investigating but we will not focus on it here. It requires an analytic continuation of the exponential integral to the complex plane, see Eq. (3.22).

4.3 Results

Before discussing the results for the VE and DEA processes with pyrrole, let us briefly comment on the numerical solution. We considered a FEM DVR ECS grid from -0.7 Å to 20.0 Å with 293 points for the N-H stretching. The part of the grid for $q_1 > 5.0$ Å was rotated to the complex plane under an angle of 30°. For the calculation of the nonlocal potential, we took into account 50 lowest neutral vibrational states within the N-H mode (including states of the discretized continuum), which were calculated on a DVR grid from -0.7 Å to 3.0 Å with 300 sine basis functions [index k_1 in Eq. (3.19)]. In the case of the ν_{13} mode, the harmonic basis contained 60 lowest states. The iterations were stopped when the ratio of the norms of the residuum and the right-hand side was below 10^{-10}. We tested that the results are converged with respect to the numerical parameters.

4.3.1 Vibrational excitation

The calculated integral 2D energy-loss spectrum reproduces the basic shape of the experimental spectrum measured at a scattering angle of 135° [14], see Fig. 4.9, but we should keep in mind that we include only 2 out of 24 vibrational modes in the model and the $^2A_2$ resonance at 3.5 eV is not considered. The threshold peaks for excitation of the N-H stretching are not as pronounced and they are completely missing for excitation of ν_{13} quanta, see also Fig. 4.10, where the VE cross sections are shown for several low-lying final vibrational states.

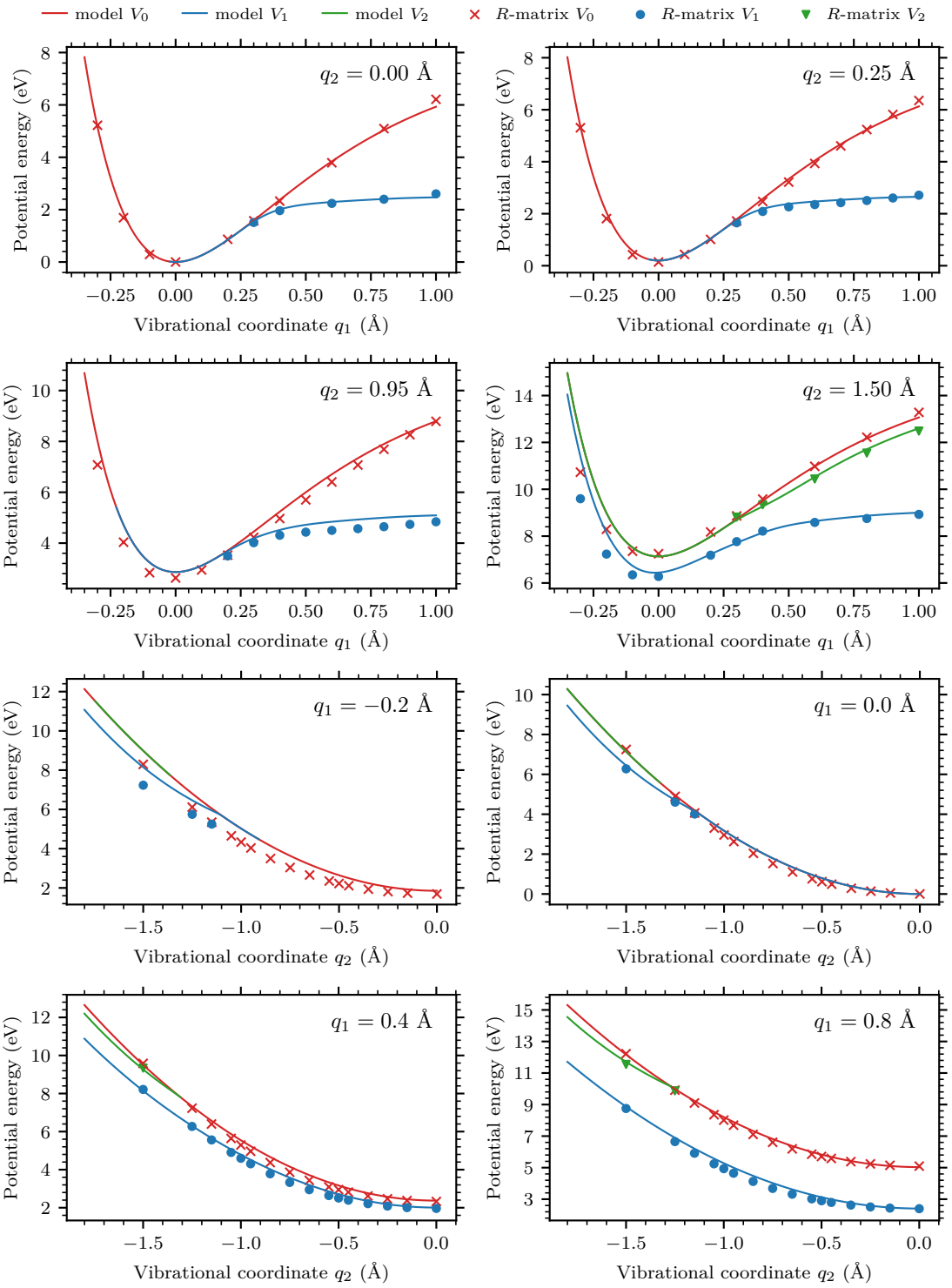

Figure 4.6: Cuts through the two-dimensional bound potential energy surfaces of the ground state of pyrrole (V_0) and two lowest states of pyrrole$^-$ (V_1, V_2): model (lines), *ab initio* data (symbols), see the legend on the top.

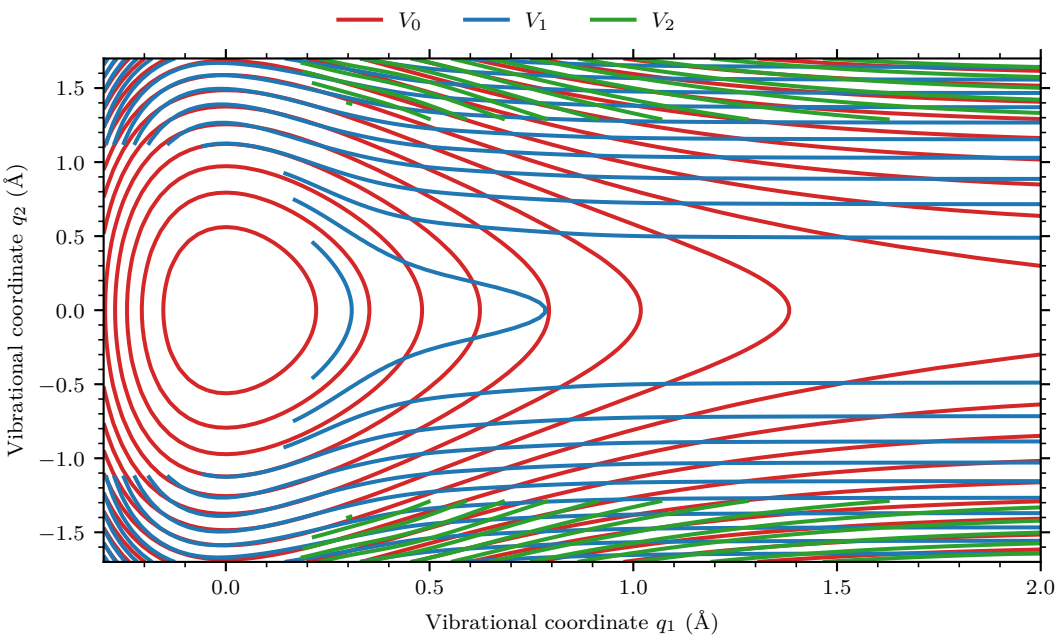

Figure 4.7: Bound potential energy surfaces of the ground state of pyrrole (V_0) and two lowest states of pyrrole$^-$ (V_1, V_2) obtained from the model. Anionic potentials are shown if their binding energy is at least 1 meV.

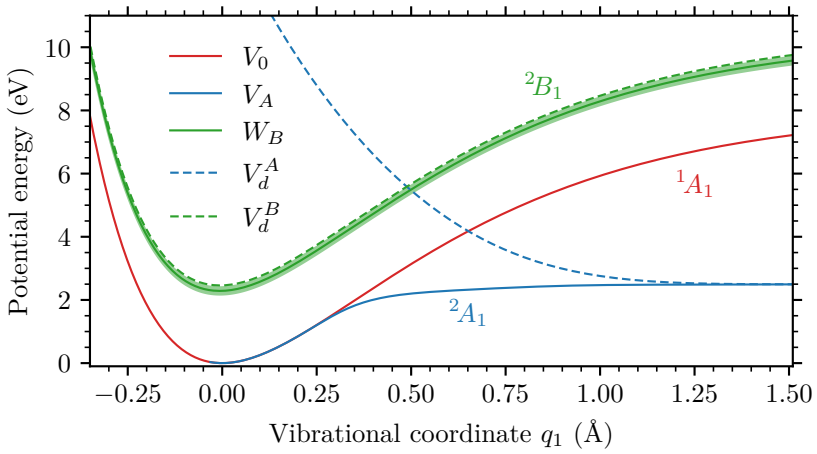

Figure 4.8: Model potentials of e + pyrrole along q_1 coordinate ($q_2 = 0$): the diabatic discrete-state potentials (dashed), W_B is the $^2B_1$ LCP potential with the resonance width represented by the shaded area.

To understand the behavior of the cross sections, we can decompose them into contributions of processes of individual incoming and outgoing electron partial waves. These contributions are given by the square of the corresponding T-matrix element, see Eq. (1.8). Moreover, a particular combination of the incoming and outgoing partial waves determines the symmetry of the final vibrational state since the total symmetry is conserved during the VE process, see Table 4.1. We should also realize that the partial-wave contributions still contain effects of both electronic states since they are the sum of processes that the electron attaches to a discrete state d and detaches from d', see Eqs. (1.8) and (1.9). For the interpretation purposes, it is helpful to consider the situation when the electron

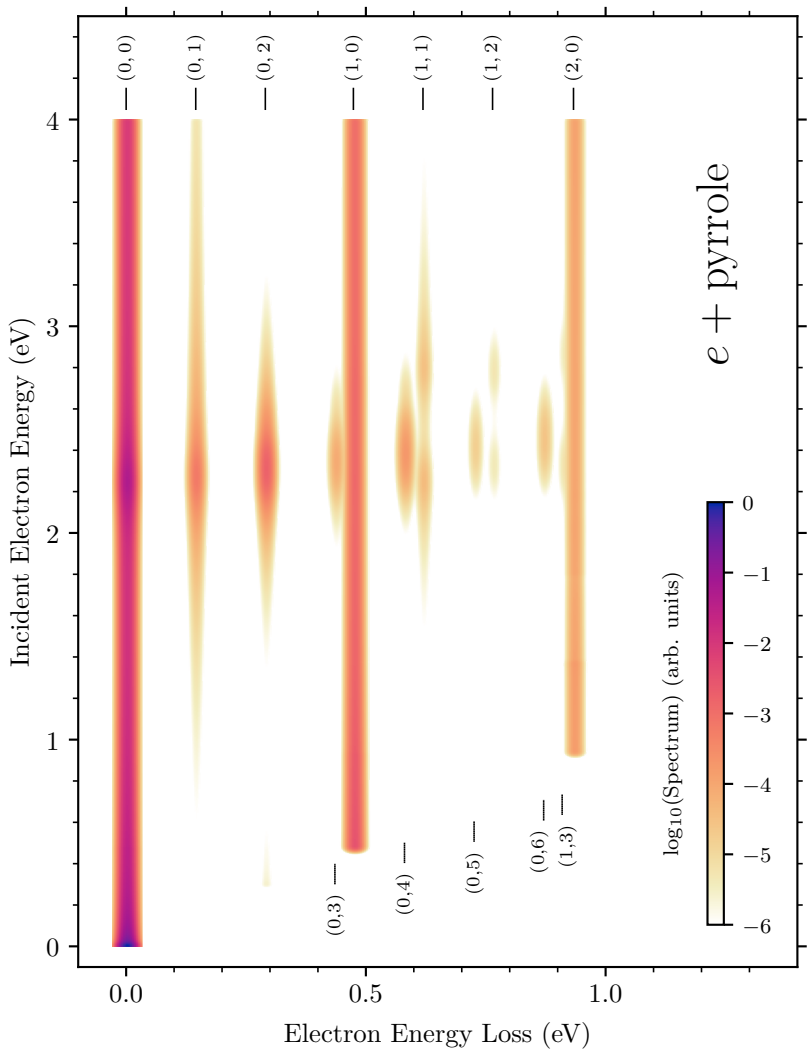

Figure 4.9: Integral two-dimensional electron energy-loss spectrum of pyrrole within the 2D model. Positions of final vibrational states (ν_1, ν_{13}) are indicated.

attaches only either to the $^2A_1$ or $^2B_1$ state, that is, to exchange the order of the sum over d and the square in Eqs. (1.8) and (1.9). The sum of such quantities does not give the total cross section but provides an insight into the dynamics.[2] Furthermore, we can learn about the multidimensional effects and the interaction of the electronic states by reducing the complexity of the model. Figure 4.11 shows the VE cross sections when we omit the ν_{13} mode and/or one of the electronic states.

First, we discuss the excitation of pure N-H stretching, that is, $\nu_f = (\nu_1, 0)$. In this case the cross sections are almost entirely described by the sum of the cross sections from 1D calculations of the N-H stretching with the $^2A_1$ and $^2B_1$ states considered separately (Fig. 4.11). In other words, the $(\nu_1, 0)$ excitation is almost unaffected by the ν_{13} mode. The threshold region influenced by the $^2A_1$

[2] The contributions of the individual initial discrete states cannot be obtained from the solution of the Schrödinger equation Eq. (1.3) with the initial state given by Eq. (1.4) that contains the electron attached to all the discrete states. Thus, we have to solve the Schrödinger equation separately for each right-hand side with the population of a single discrete state if we are interested in these quantities.

Table 4.1: Symmetry considerations for VE of pyrrole. The electron partial wave s, vibrational mode ν_1, and initial state of the molecule are totally symmetric (A_1 symmetry). The p_x wave and mode ν_{13} are of the B_1 symmetry.

in electron μ_i	out electron μ_f	final vibrational state (ν_1, ν_{13})
s	s	ν_{13} even
s	p_x	ν_{13} odd
p_x	s	ν_{13} odd
p_x	p_x	ν_{13} even

virtual-like state is similar to the cross sections for hydrogen halides, see Refs. [17, 18] and references therein. We observe abrupt changes known as Wigner cusps at the openings of higher vibrational channels $(\nu_1, 0)$. Their shape is given by the energy dependence of the resonance width near the threshold, which is heavily influenced by the large dipole moment of pyrrole (width is finite at the threshold). The $(2, 0)$ cusp in the excitation of the $(1, 0)$ state (top right panel in Figs. 4.10 and 4.11) reproduces well the experimental data [14].

The shape of the $^2B_1$ contributions to the cross sections is the result of the fact that the neutral and anionic potentials along Q_1 are to a large extent parallel (Fig. 4.8). We can rewrite Eq. (1.9) for the T matrix using the spectral decomposition for the Green's function

$$\langle \nu_f | V_{d\epsilon_f}^{\mu_f} (E - H)_{dd}^{-1} V_{d\epsilon_i}^{\mu_i} | \nu_i \rangle = \sum_{\nu'} \frac{1}{E - E_{\nu'}} \langle \nu_f | V_{d\epsilon_f}^{\mu_f} | \nu' \rangle \langle \nu' | V_{d\epsilon_i}^{\mu_i} | \nu_i \rangle, \tag{4.21}$$

where $|\nu'\rangle$ are vibrational states of the anion with energies $E_{\nu'}$. The shape of the potentials implies that the neutral and anionic states are almost orthogonal. The coordinate dependence of the coupling amplitudes $V_{d\epsilon}^{\mu}$ does not influence the overlaps as much, therefore, depending on the initial and final neutral states, only few anionic states contribute, which explains the observed peaks. However, the experimental data for the $\nu_1 = 1$ excitation reveal only one resonance peak in contrast to two peaks in the calculations. It may indicate that other modes not included in our dynamics affect the N-H stretching.

The multidimensionality of the dynamics and the interaction of the electronic states play an important role for the excitation of odd quanta of the ν_{13} mode (last rows Figs. 4.10 and 4.11). The cross sections are given by the $s \to p_x$ and $p_x \to s$ contributions, which correlates well with the situation when only the $^2A_1$ state or the $^2B_1$ resonance is populated by the incoming wave. Thus, in the $s \to p_x$ case, the s wave dominantly attaches to the $^2A_1$ state but there are still two pathways to the excitation: either the p_x wave detaches ($s \to {}^2A_1 \to p_x$) or the resonance is involved ($s \to {}^2A_1 \to {}^2B_1 \to p_x$). We found that the coupling of the $^2A_1$ state to the p_x-wave continuum (v_{Ap} term) has a negligible effect in our model, that is, the latter pathway is responsible for the $s \to p_x$ process. Figure 4.11 confirms this conclusion because the $s \to p_x$ contribution is basically zero when the $^2B_1$ resonance is excluded from the dynamics. Similarly, there are also two pathways for $p_x \to s$: $p_x \to {}^2B_1 \to s$ and $p_x \to {}^2B_1 \to {}^2A_1 \to s$, which are both operational. The $p_x \to {}^2B_1 \to s$ process dominates for the $(0, 1)$ excitation but the $^2A_1$ state significantly enhances the excitation in the case of $(1, 1)$.

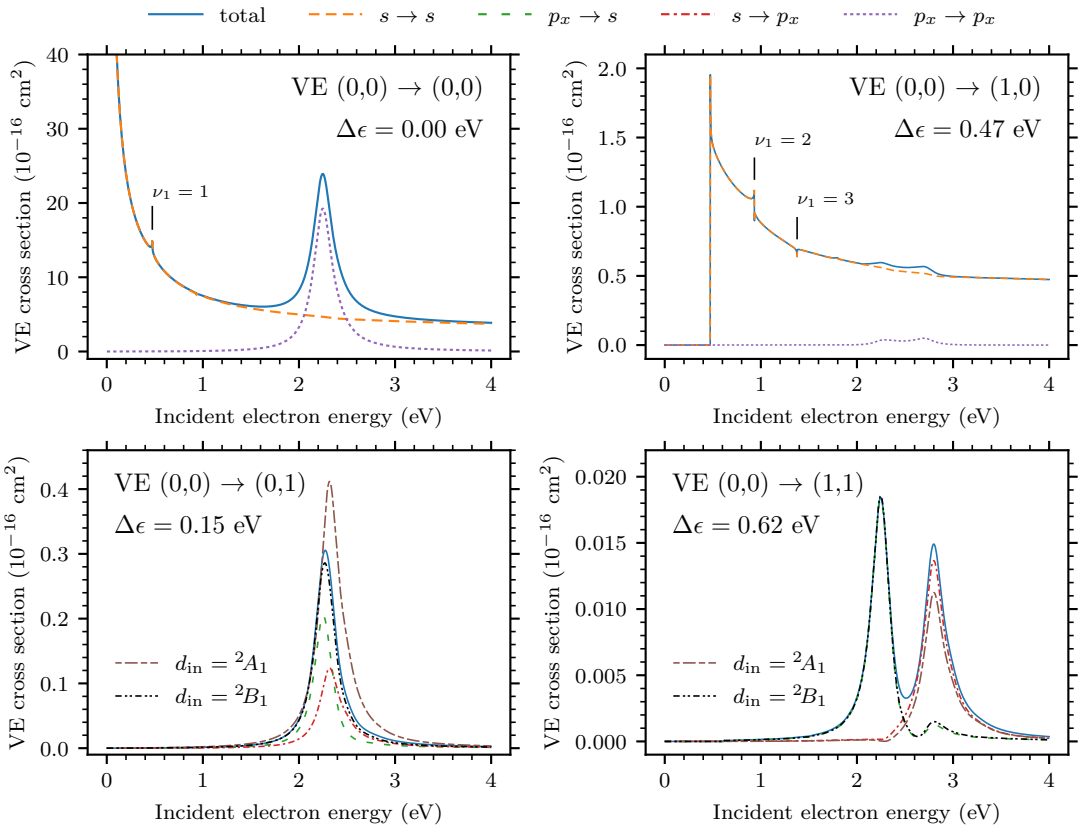

Figure 4.10: Integral cross sections for vibrational excitation $(0,0) \to (\nu_1, \nu_{13})$ of pyrrole within the 2D model. The electron energy loss $\Delta\epsilon$ and contributions of individual in → out partial-wave processes are also shown (legend on the top). For $\nu_{13} = 1$ (second row), we also show the contribution when the electron attaches only to the $^2A_1$ or $^2B_1$ discrete state (d_{in}). Their sum does not give the total cross section, see the text.

The peak in the $s \to p_x$ contribution is shifted towards higher energies by the number of excited quanta in comparison to the peak in $p_x \to s$, which appears at the energy of the $^2B_1$ ground vibrational state (Fig. 4.10. Our interpretation is as follows. During the $s \to {}^2A_1 \to {}^2B_1$ transition, the $^2B_1$ anion is formed vibrationally excited while the $p_x \to {}^2B_1$ process predominantly populates the ground state because of the similarity of the potentials discussed above.

Sharp threshold peaks are observed in the experimental cross sections for the fundamental excitation of the ν_{11}–ν_{15} modes (out-of-plane bending motions of the hydrogen atoms) [14]. Such peaks are completely missing in our calculations for the ν_{13} mode. We would expect them in the $s \to {}^2A_1 \to p_x$ process in our model. When the v_{Ap} coupling is substantially increased, we observe rather broad peaks at the threshold but such values of v_{Ap} are not compatible with the fixed-nuclei data. It is possible that these peaks originate in the direct-dipole scattering not included in our model, similarly to the excitation of the fundamental bending $(0, 1^1, 0)$ and asymmetric stretching $(0, 0^0, 1)$ peaks in the case of CO_2.

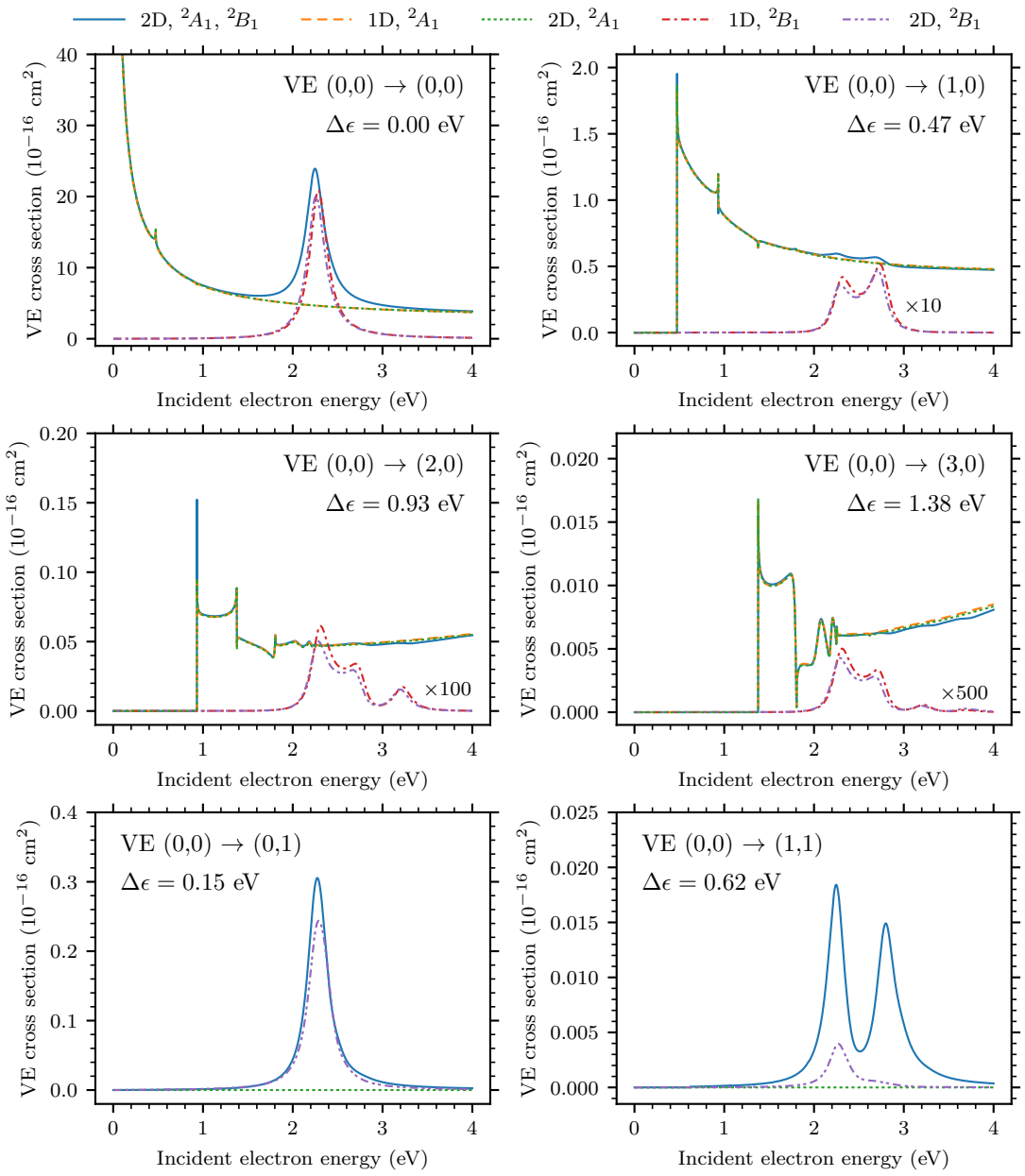

Figure 4.11: Integral cross sections for vibrational excitation $(0,0) \to (\nu_1, \nu_{13})$ of pyrrole within reduced models where we consider both modes (2D) or only the N-H stretching (1D), in combination with one or both electronic states, see the legend on the top (2D, $^2A_1$, $^2B_1$ denotes the full model).

4.3.2 Dissociative electron attachment

Let us now focus on the dissociation of the N-H bond of pyrrole. Within our 2D model the produced ring fragment still has one vibrational degree of freedom described by the asymptotic form of the $^2A_1$ potential along the Q_2 coordinate given by [see Eqs. (3.26) and (4.7)]

$$\lim_{Q_1 \to \infty} [V_0(Q_1, Q_2) + E_A(Q_1, Q_2)]. \tag{4.22}$$

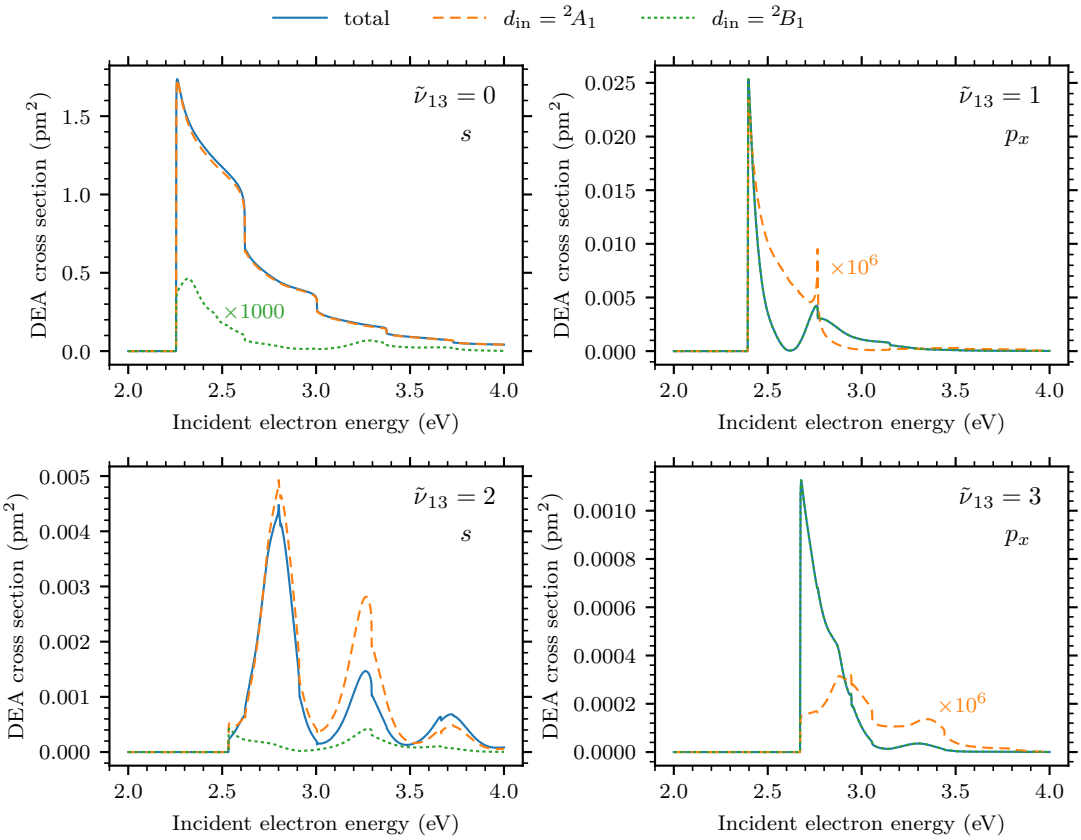

Figure 4.12: Integral cross sections for the dissociation of the N-H bond of pyrrole within our 2D model for the ring fragment left in vibrational states with $\tilde{\nu}_{13} = 0, 1, 2,$ and 3. Contributions of the electron attaching only to the $^2A_1$ or $^2B_1$ discrete state (d_{in}) are also shown. Their sum does not give the total cross section, see the text.

We denote the corresponding vibrational quantum number by $\tilde{\nu}_{13}$. The total symmetry is conserved during the DEA process, and therefore, the parity of the final vibrational state $\tilde{\nu}_{13}$ restricts the symmetry of the incoming electron. When the electron comes in as the s wave, only states with even $\tilde{\nu}_{13}$ can be excited while $\tilde{\nu}_{13}$ has to be odd for the incoming p_x wave. The resulting integral cross sections calculated using Eq. (3.35) for $\tilde{\nu}_{13} = 0, \ldots, 3$ are shown in Fig. 4.12. The total DEA cross section is then given by the sum over $\tilde{\nu}_{13}$. To gain more insight into the processes, we also plot the contributions when the incoming electron either populates only the $^2A_1$ or $^2B_1$ discrete state (d_{in}), but note that the sum of these quantities does not give the total cross section since we exchange the order of the sum and square in Eq. (3.35).[3]

The direct dissociation via the $^2A_1$ state after the s-wave attachment is almost entirely responsible for the cross section to the lowest channel $\tilde{\nu}_{13} = 0$ (top left panel of Fig 4.12) and closely resembles the DEA to hydrogen halides [17, 18] or formic acid [58]. The 1D dynamics gives practically the same result for the direct mechanism as the 2D calculations. We also observe a negligible contribution from the process when the s wave attaches to the $^2B_1$ resonance and then dissociate

[3]The wave function ψ_d in Sec. 3.4, where d denotes the outgoing DEA channel, implicitly contains the sum over initial discrete states, see also Note 2.

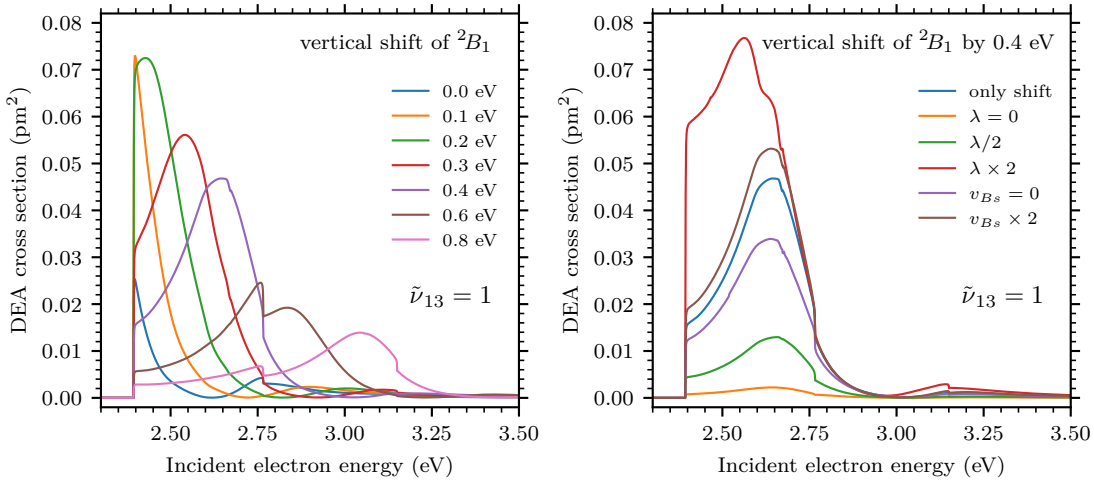

Figure 4.13: Effect of model parameters on the integral cross section for the dissociation of the N-H bond of pyrrole when the ring fragment is left in vibrational state $\tilde{\nu}_{13} = 1$. **Left panel**: the $^2B_1$ resonance is vertically shifted upwards with respect to the original model. **Right panel**: dependence on the strength of the direct coupling λ and indirect coupling through the s-wave continuum v_{Bs} between the $^2A_1$ and $^2B_1$ electronic states, the $^2B_1$ resonance is vertically shifted by 0.4 eV.

via the $^2A_1$ state ($s \to {}^2B_1 \to {}^2A_1$).

The primary indirect contribution of the dissociation is given by the process where the $^2B_1$ resonance is populated by the incoming p_x wave and the resulting ring fragment is left with $\tilde{\nu}_{13} = 1$ ($p_x \to {}^2B_1 \to {}^2A_1$). The calculated cross section rather differs from the expected Gaussian-like profile that would reflect the ground vibrational state (top right panel of Fig. 4.12). However, the explanation of the shape is simple. The energy of the ground vibrational state of the $^2B_1$ resonance is 2.24 eV (based on the position of the resonance peak in the elastic VE cross section), which is below the DEA thresholds at 2.26 eV for $\tilde{\nu}_{13} = 0$ and 2.39 eV for $\tilde{\nu}_{13} = 1$. In comparison, the experimental DEA threshold is at ∼1.9 eV [14]. The discrepancy is probably caused by the use of the N-H normal coordinate for the fixed-nuclei calculations even for large displacements out of the equilibrium geometry. In the normal mode, the nitrogen atom moves closer to the neighboring carbons and their mutual repulsion increases the potential energy. The proper but computationally demanding approach would be fixing the N-H bond length and letting the ring relax to a new equilibrium geometry.

We examined the effect of the mutual position of the $^2B_1$ ground vibrational state and the DEA threshold by shifting the $^2B_1$ resonance upwards, see the left panel of Fig. 4.13. The calculations with a suitable shift produce a shape similar to a Gaussian profile, which is in an agreement with the experiment [14], however, the calculated magnitude is too small. The peak maximum of the experimental absolute DEA cross section is 2 pm^2 [14], which is around 40 times larger than our indirect contribution via the $^2B_1$ resonance. In contrast, our direct contribution has the maximum at 1.7 pm^2, which appears to be too large. The experimental signal drops to about a half after the deuteration of the four carbon-bonded hydrogens, which does not affect the direct mechanism, and the cross section retains a Gaussian profile, that is, a pronounced threshold behavior is not apparent

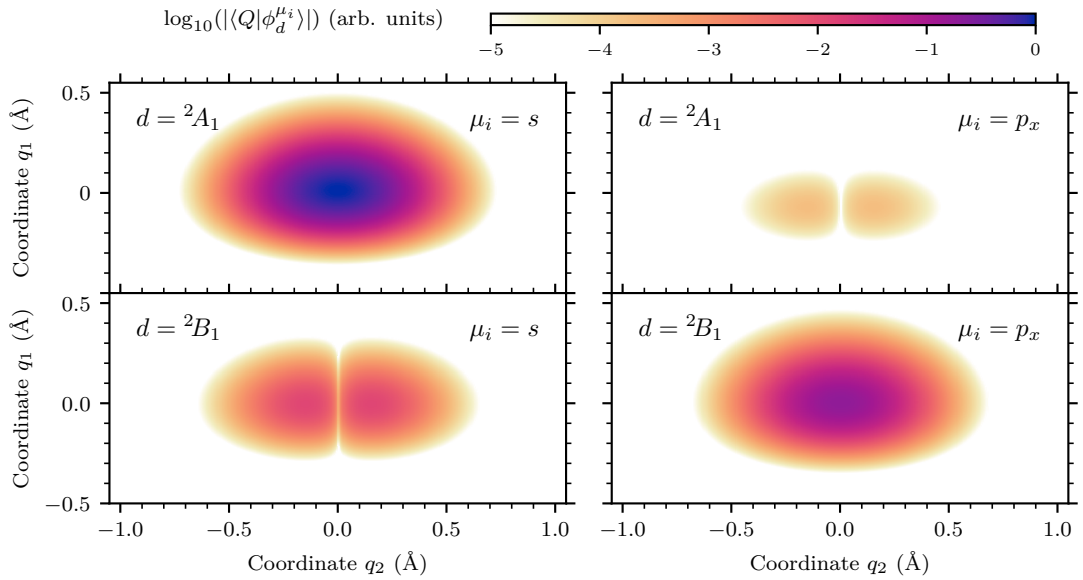

Figure 4.14: Initial wave function $|\Phi^{\mu_i}\rangle$ of the e + pyrrole system given by the attachment of the incoming electron with energy 2.5 eV and partial wave $\mu_i = s$ or p_x (columns). The wave function has two vibrational components $|\phi_d^{\mu_i}\rangle$ that belong to the discrete states ${}^2A_1$ and ${}^2B_1$ (rows). The ${}^2B_1$ resonance was vertically shifted by 0.4 eV. The components are normalized with respect to the overall maximum.

in the experiment but note that the energy resolution was 70 meV [14].

The ${}^2B_1$ resonance considerably influences the DEA cross section to $\tilde{\nu}_{13} = 2$. When the s wave populates the ${}^2A_1$ state (dashed line in Fig. 4.12), the anion does not immediately dissociate. From the reduced models we found that the dissociation occurs via a pathway like $s \to {}^2A_1 \to {}^2B_1 \to {}^2A_1$ and the peaks appear at the positions of vibrational states within the ${}^2B_1$ potential. The second contribution (dotted line) is given by $s \to {}^2B_1 \to {}^2A_1$. The cross section for $\tilde{\nu}_{13} = 3$ is again cut off by the too high dissociation limit.

Furthermore, we investigated the influence of the coupling strength between the electronic states on the indirect mechanism of the dissociation, see the right panel of Fig. 4.13. After forming the ${}^2B_1$ resonance by the p_x-wave attachment, the system can transit to the ${}^2A_1$ state either directly thanks to the λ term or indirectly through the s-wave continuum, which is controlled by the v_{Bs} term, see Eqs. (4.7) and (4.8). Both these paths are operational but the direct coupling dominates, compare $\lambda = 0$ with $v_{Bs} = 0$ in Fig. 4.13. Doubling the coupling strength enhances the DEA but not nearly enough to be comparable with the experiment ($\lambda \times 2$ and $v_{Bs} \times 2$ in Fig. 4.13). On the other hand, the VE process competes with the dissociation and the excitation of the $(0, 1)$ state increases six times when λ is doubled. As for the VE process, the effect of the p_x-wave coupling to the ${}^2A_1$ state is negligible.

For illustration, Figs. 4.14 and 4.15 show the vibrational components of the initial wave function given by the attachment of the electron to the neutral ground vibrational state [see Eq. (1.4)] and the scattered wave function that satisfies the Schrödinger equation Eq. (1.3). The ${}^2B_1$ diabatic component of the scattered wave for the incoming p_x wave dominates but the coupling to the ${}^2A_1$ state is too

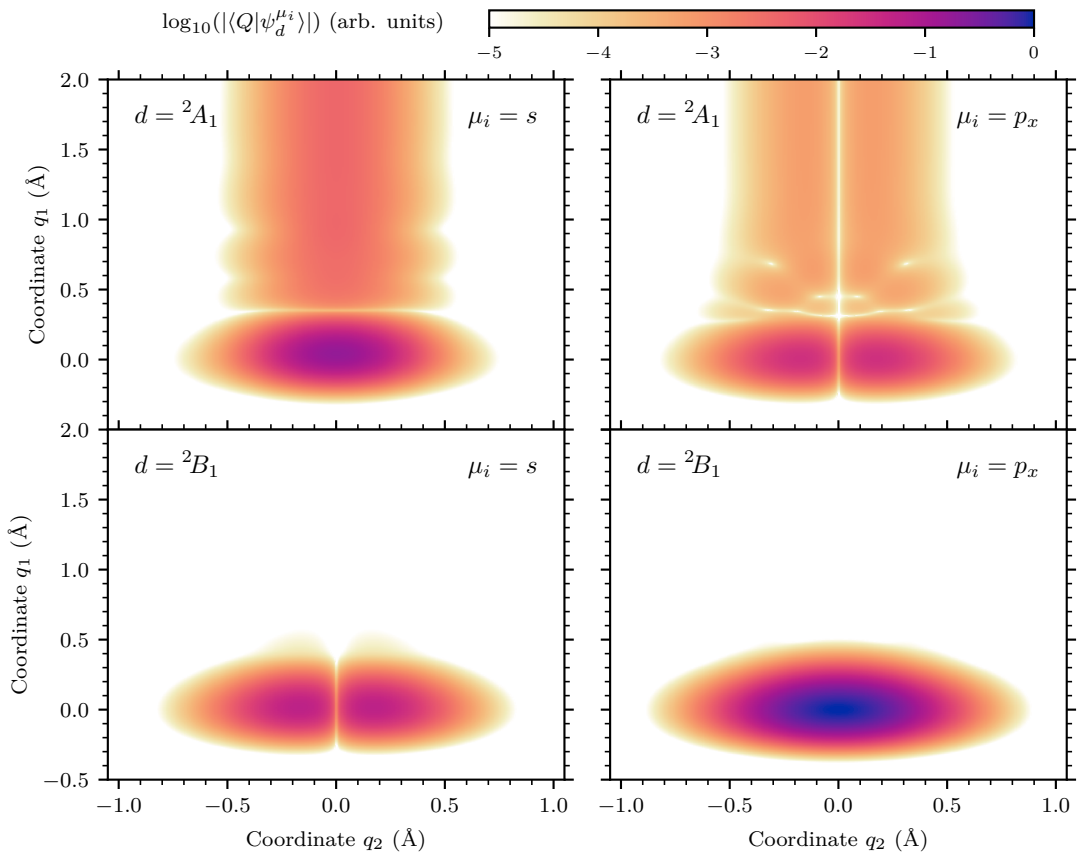

Figure 4.15: Scattered wave function $|\Psi^{\mu_i}\rangle$ of the e + pyrrole system for incoming electron with energy 2.5 eV and partial wave $\mu_i = s$ and p_x (columns). The wave function has two vibrational components $|\psi_d^{\mu_i}\rangle$ that belong to the discrete states $^2A_1$ and $^2B_1$ (rows). The $^2B_1$ resonance was vertically shifted by 0.4 eV. The components are normalized with respect to the overall maximum.

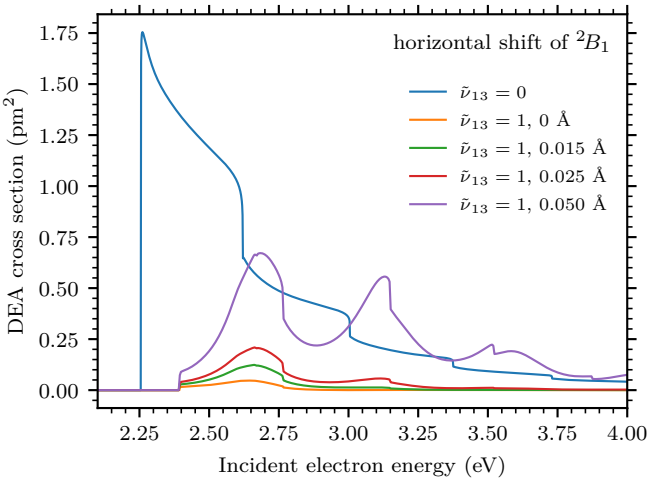

Figure 4.16: Effect of horizontal shift of the $^2B_1$ resonance on the integral cross section for the dissociation of the N-H bond of pyrrole. The potential minimum is shifted by the value indicated in the legend towards larger N-H bond lengths. The $^2B_1$ resonance is also vertically shifted by 0.4 eV for all cases.

weak resulting in an order of magnitude smaller tail of the wave function, which determines the DEA, in comparison with the direct mechanism.

The fixed-nuclei data (Fig. 4.5) show that the electronic states mix the most for N-H bond lengths where the $^2A_1$ state becomes bound ($q_1 = 0.2$–0.4 Å). However, the anion in the $^2B_1$ state does not efficiently probe these geometries (Fig. 4.15). Therefore, we horizontally shifted the $^2B_1$ potential towards larger N-H separations to examine if it increases the DEA, see Fig. 4.16. The DEA cross section to the $\tilde{\nu}_{13} = 1$ state is quite sensitive to this modification. There is an increase by a factor of two for the shift by 0.015 Å. But as the shift increases, the anionic and neutral potentials start to be less parallel. As a result, multiple anionic vibrational states are populated by the incoming p_x-wave, which leads to the additional peaks in the cross section that are not observed in the experiment [14].

4.4 Discussion

Before discussing the results further, let us summarize the e+pyrrole problem. The dissociation of the N-H bond is predicted to occur via two mechanisms [14]. The additional electron can occupy the antibonding σ^* orbital ($^2A_1$ state of the anion) localized along the N-H bond that leads to the dissociation without being affected by a movement of distant parts of the molecule (direct σ^* mechanism). On the other side, the electron can be captured to the π^* orbital ($^2B_1$ resonance) predominantly localized on the nitrogen and two neighboring carbons [14]. Distorting the C_{2v} geometry allows the transition of the system from the $^2B_1$ resonance to the $^2A_1$ state and towards the dissociation (indirect π^*/σ^* mechanism). Both pathways are included in our calculations, which, to the best of our knowledge, are the first nonlocal calculations of this kind, but the indirect contribution is at least by an order of magnitude smaller than is needed to explain the experimental DEA cross section [14].

Since pyrrole has 24 vibrational degrees of freedom, we employed a simplistic approach and considered only the N-H stretching in combination with the out-of-plane movement of carbon-attached hydrogens described by the normal mode ν_{13}. However, the hydrogen produced during the DEA process can leave along a trajectory with a nonzero angle with respect to the molecular plane, which is not captured in our model. The anionic potential does not become asymptotically flat as the N-H bond length increases (Fig. 4.7) because of the use of the normal coordinate, which properly describes the molecular geometry only near the equilibrium. We expect that the incorporation of this out-of-plane movement strengthens the coupling between the electronic states because it increases the overlap between the π^* and σ^* orbitals. The fixed-nuclei calculations reported by Kumar *et al.* [14] show that the $^2B_1$ resonance significantly broadens along the ν_{16} mode, which predominantly describes the out-of-plane movement of the nitrogen-bonded hydrogen. The authors argued that the broadening would increase the electron autodetachment, and thus, they favored the ν_{13} mode as the dominant coupling mode. In the view of the present calculations, the broadening may indicate a strong mixing of the resonance with the broad virtual-like state that also enhances the dissociation. On the other hand, the deuteration of the carbon-bonded hydrogen, which significantly influences the experiment, is not expected to affect the out-of-plane motion of the nitrogen-bonded hydrogen, that

is, a three-dimensional model that includes the N-H stretching in combination with the out-of-plane motions of the nitrogen-bonded hydrogen and the carbon-bonded hydrogens seems to be necessary to understand the N-H dissociation in pyrrole.

The suggested extension of the model is nontrivial and it goes beyond this thesis. We leave the DEA in pyrrole and the study of the isotopic effect, which we have not investigated at all here, as an open problem for future research.

Conclusion

In conclusion, we summarize the results and address open problems and possible directions for future research.

Our primary result is the calculation and interpretation of the two-dimensional electron energy-loss spectrum of CO_2 presented in Chapter 2 based on two papers in *Physical Review Letters* [11] and *Physical Review A* [12] and one submitted manuscript [13]. To explain the experimental observations, we constructed a rather elaborate discrete-states-in-continuum model of the vibrational excitation of CO_2 by slow electrons. Considering all four vibrational modes, we modeled the nuclear motion of the molecular anion with its electronic structure represented by three low-lying states: the $^2\Sigma_g^+$ virtual state and twofold degenerate $^2\Pi_u$ shape resonance. All these states interact through the vibronic coupling as the anion bends because the Renner-Teller effect splits the $^2\Pi_u$ doublet into $^2A_1$ and $^2B_1$ components, from which the $^2A_1$ component mixes with the virtual state. Furthermore, the electron in the continuum was described by s and p partial waves that allows excitation of nontotally symmetric vibrational states of CO_2, which was not included in previous models.

The vibronic coupling of the resonance to the s-wave continuum turned out to be the key for understanding the behavior of the $e + CO_2$ system. Its inclusion clarifies not only the topology of the anionic potentials but especially the puzzling shape of the experimental energy-loss spectrum. We interpret the spectrum in terms of two overlapping contributions that result from excitation of Σ_g^+ and Π_u vibrational states of CO_2. The Π_u states prevail at high energy losses because the electron captured to the $^2\Pi_u$ resonance preferentially leaves as the s wave due to the energy dependence of the interaction. While the bending is important, the whole dynamics is driven by the symmetric stretching because the anion effectively decays by the autodetachment at highly bent geometries. Consequently, only fairly linear vibrational states are significantly excited, which gives rise to the fine structure superimposed to the spectrum.

The calculations reproduce the behavior of the system on a qualitative level and so there is a room for future improvements of the model. To achieve a quantitative agreement, the harmonic approximation for the neutral molecule has to be lifted in order to properly describe the potentials in the symmetric stretching and to include the Fermi resonance effect directly into the dynamics. It will complicate the evaluation of the nonlocal potential but it could be easier than we had originally anticipated since we found that the coupling between different Fermi polyads can be neglected. In addition, CO_2^- can dissociate to the $O^- + CO$ fragments for electron energy around 4 eV, which we have not considered in the presented model. The dissociation proceeds through $^2\Pi_u$ and $^2\Pi_g$ states that are connected via a conical intersection [108], that is, the inclusion of the dissociation into the 4D nonlocal dynamics poses a significant challenge.

We made a step in this direction by incorporating one-dimensional dissociation into two-dimensional nuclear dynamics with an arbitrary number of discrete states

in Chapter 3. Our primary motivation was to study the e + pyrrole system because the experimental observations of Kumar *et al.* [14] suggest that the vibronic interaction of $^2A_1$ and $^2B_1$ electronic states plays an important role in the dissociation of the pyrrole anion into the $C_4H_4N^-$ and H fragments. In our nuclear calculations of this system, we took into account only two out of twenty-four vibrational modes: the N-H stretching and out-of-plane movement of carbon-bonded hydrogens. We found that the coupling between the electronic states is too weak in the current model and it does not fully reproduce the observations. We expect that the out-of-plane movement of the detached hydrogen will increase the coupling between the states, that is, 3D dynamics with 2D dissociation is probably needed to explain the experiment, which is unfortunately beyond the scope of this thesis.

The dissociation of the pyrrole anion is thus left as an open problem that is worth investigating further. Similarly, it would be interesting to extend the 1D calculations of Gallup *et al.* [58, 62] by including the π^* resonance to study the π^*/σ^* coupling in the cases of formic acid and uracil.

We face two challenges in studies of the nuclear dynamics of inelastic electron-molecule collisions: the construction of the model from *ab initio* data and solving the multidimensional and nonlocal dynamics with multiple anionic states. We showed that finding the solution by the iterative methods based on Krylov subspaces works well and more than two nuclear dimensions should be reachable even in the case of the dissociation. To construct the models, we fitted model parameters to *ab initio* eigenphase sums and potential energies. However, it is not easy to properly extract the information about the model partial waves from the eigenphase sums. Therefore, we also included the s-wave phase from the *ab initio* K matrix in the case of pyrrole. A question remains how to use the information about the full K matrix in the construction of the models since the fixed-nuclei calculations consider many partial waves (typically up to $l = 4$) while the model for the dynamics is limited to a few lowest waves. It is also problematic to fully automatize the fitting process, which makes the construction of multidimensional models laborious.

To conclude, the approach to the nuclear dynamics of the vibrational excitation and dissociative electron attachment extended throughout this thesis is very convenient especially for qualitative studies of multidimensional effects in the presence of coupled short-lived anionic states. These effects include the change of the symmetry of the incoming and outgoing electrons that leads to excitation of nontotally symmetric vibrational states or the π^*/σ^* coupling that is expected to substantially influence bond cleavage upon electron impact in biologically relevant molecules. We thus hope that the presented progress will be utilized in further studies of such phenomena.

Appendix A

Model parameters for the e + pyrrole system

Here, we list Q_1-dependent functions of the two-dimensional two-state model for the e + pyrrole system described in Sec. 4.2. The coefficients are in atomic units and the coordinate Q_1 of the N-H stretching is dimensionless.

A.1 Discrete-state potentials and direct coupling

The diabatic potentials of the discrete states and their direct coupling are given by Eqs. (4.7), (4.9), and (4.10) with the following parameter functions

$$E_A^0(Q_1) = V_A^0(Q_1) - V_0(Q_1, 0), \tag{A.1}$$

where

$$\begin{aligned} V_A^0(Q_1) = {} & 0.64928 \exp[-1.170(Q_1 + 0.15063)] \frac{1}{1 + \exp[2(Q_1 - 1.45)]} \\ & \times \frac{1}{1 + \exp[3(Q_1 - 2.4)]} \\ & - 0.093230 \exp(-1.972 Q_1) + 0.091873, \end{aligned} \tag{A.2}$$

$$E_A^2(Q_1) = 0.001494 \exp[-11.07(Q_1 - 0.18799)^2] - 0.00020468, \tag{A.3}$$

$$E_B^0(Q_1) = \begin{cases} -0.00584(0.642 - Q_1)^{1.697} + 0.09319, & Q_1 < 0.642, \\ 0.09319, & Q_1 \geq 0.642, \end{cases} \tag{A.4}$$

$$E_B^2(Q_1) = 0.00027411 \exp[-5.531(Q_1 + 0.295)^2] - 0.0014107, \tag{A.5}$$

$$E_B^4(Q_1) = 8.44 \times 10^{-6}, \tag{A.6}$$

$$\lambda(Q_1) = 0.019814 \exp[-1.341(Q_1 + 0.429)^2]. \tag{A.7}$$

A.2 Coupling to the continuum

The discrete-state-continuum coupling is given by Eqs. (4.8), (4.11)–(4.15) with

$$v_{As}^0(\epsilon, Q_1) = 0.10094 \exp[-1.519(Q_1 + 0.0626)^2] \exp(-0.339\epsilon), \tag{A.8}$$

$$\tilde{v}_{As}^0(\epsilon, Q_1) = 0.33903 \exp[-0.6438(Q_1 - 0.675)^2](0.3387\epsilon)^{1/4} \exp(-0.3387\epsilon), \tag{A.9}$$

$$v_{As}^2(\epsilon, Q_1) = 0.00083871 \exp(-0.6863 Q_1) \exp(-2.663\epsilon), \tag{A.10}$$

$$v^1_{Ap}(\epsilon, Q_1) = 0.00083732 \exp[-6.389(Q_1 + 0.554)^2](11.71\epsilon)^{3/4} \exp(-11.71\epsilon), \tag{A.11}$$

$$v^0_{Bp}(\epsilon, Q_1) = \{-0.00217 \exp[-1.309(Q_1 + 0.0453)^2] + 0.12968\} \times (3.241\epsilon)^{3/4} \exp(-3.241\epsilon), \tag{A.12}$$

$$v^2_{Bp}(\epsilon, Q_1) = f(Q_1)(0.9526\epsilon)^{3/4} \exp(-0.9526\epsilon), \tag{A.13}$$

where

$$f(Q_1) = \begin{cases} -0.00058125(1.16 - Q_1)^{1.763} + 0.0032510, & Q_1 < 1.16, \\ 0.0032510, & Q_1 \geq 1.16, \end{cases} \tag{A.14}$$

$$v^1_{Bs}(\epsilon, Q_1) = 0.0031880 \exp[-1.509(Q_1 + 0.683)^2] \exp(-12.73\epsilon), \tag{A.15}$$

$$\tilde{v}^1_{Bs}(\epsilon, Q_1) = 0.0093164 \exp[-3.851(Q_1 + 0.0625)^2](0.3989\epsilon)^{1/4} \exp(-0.3989\epsilon). \tag{A.16}$$

A.3 Background phases

Finally, the coefficients of the background phases (in radians) given by Eqs. (4.17)–(4.20) are

$$a^A_{\log}(Q_1) = -0.10797 - 0.083738Q_1, \tag{A.17}$$

$$a^A(Q_1) = -12.961 - 2.4351Q_1, \tag{A.18}$$

$$b^A(Q_1) = -0.49381 - 0.52605Q_1, \tag{A.19}$$

$$a^B_{\log}(Q_1) = -0.041916 - 0.0070866Q_1 - 0.0019281Q_1^2, \tag{A.20}$$

$$a^B(Q_1) = -5.6354 + 0.026100Q_1 + 0.12297Q_1^2, \tag{A.21}$$

$$b^B(Q_1) = -0.32103 - 0.026983Q_1 - 0.017198Q_1^2, \tag{A.22}$$

$$a_1(Q_1) = -1.1603 - 0.51672Q_1 + 0.63540Q_1^2, \tag{A.23}$$

$$b_1(Q_1) = 0.014376 - 0.019647Q_1, \tag{A.24}$$

$$a^K(Q_1) = 4.7929 + 1.75019Q_1 + 14.850Q_1^2, \tag{A.25}$$

$$a^K_{\text{sqrt}}(Q_1) = -1.28072 + 1.4822Q_1 - 2.5141Q_1^2, \tag{A.26}$$

$$b^K(Q_1) = 0.0044722 - 0.084373Q_1 - 0.10791Q_1^2 + 0.18265Q_1^3. \tag{A.27}$$

Bibliography

[1] S. C. Glover, J. Chluba, S. R. Furlanetto, J. R. Pritchard, and D. W. Savin. Chapter Three - Atomic, Molecular, and Optical Physics in the Early Universe: From Recombination to Reionization, ed. by E. Arimondo et al. Vol. 63. Advances In Atomic, Molecular, and Optical Physics. Academic Press, 2014, 135–270.

[2] I. I. Fabrikant, S. Eden, N. J. Mason, and J. Fedor. Chapter Nine - Recent Progress in Dissociative Electron Attachment: From Diatomics to Biomolecules, ed. by E. Arimondo et al. Vol. 66. Advances In Atomic, Molecular, and Optical Physics. Academic Press, 2017, 545–657.

[3] I. Bald, R. Čurík, J. Kopyra, and M. Tarana. Dissociative Electron Attachment to Biomolecules. *Nanoscale Insights into Ion-Beam Cancer Therapy*, ed. by A. V. Solov'yov. Cham: Springer International Publishing, 2017, 159–207.

[4] G. J. Schulz. Resonances in Electron Impact on Diatomic Molecules. *Rev. Mod. Phys.* 45, 423–486, 1973.

[5] G. J. Schulz. Resonance in the Elastic Scattering of Electrons in Helium. *Phys. Rev. Lett.* 10, 104–105, 1963.

[6] T. Reddish, F. Currell, and J. Comer. Studies of the 2 eV shape resonance in N_2 using a two-dimensional scanning technique. *J. Phys. E: Sci. Instrum.* 21(2), 203–207, 1988.

[7] M. Allan, K. Regeta, J. D. Gorfinkiel, Z. Mašín, S. Grimme, and C. Bannwarth. Recent research directions in Fribourg: nuclear dynamics in resonances revealed by 2-dimensional EEL spectra, electron collisions with ionic liquids and electronic excitation of pyrimidine. *Eur. Phys. J. D* 70(5), 123, 2016.

[8] W. Domcke. Theory of resonance and threshold effects in electron-molecule collisions: The projection-operator approach. *Phys. Rep.* 208(2), 97–188, 1991.

[9] H. Estrada, L. S. Cederbaum, and W. Domcke. Vibronic coupling of short-lived electronic states. *J. Chem. Phys.* 84(1), 152–169, 1986.

[10] H. Köppel, W. Domcke, and L. S. Cederbaum. Multimode Molecular Dynamics Beyond the Born-Oppenheimer Approximation. *Advances in Chemical Physics*. John Wiley & Sons, 1984, 59–246.

[11] J. Dvořák, M. Ranković, K. Houfek, P. Nag, R. Čurík, J. Fedor, and M. Čížek. Vibronic Coupling through the Continuum in the $e + CO_2$ System. *Phys. Rev. Lett.* 129, 013401, 2022.

[12] J. Dvořák, K. Houfek, and M. Čížek. Vibrational excitation in the $e + CO_2$ system: Nonlocal model of $\Sigma\Pi$ vibronic coupling through the continuum. *Phys. Rev. A* 105, 062821, 2022.

[13] J. Dvořák, M. Ranković, K. Houfek, P. Nag, R. Čurík, J. Fedor, and M. Čížek. *Vibrational excitation in the $e + CO_2$ system: Analysis of two-dimensional energy-loss spectrum*. Submitted to Phys. Rev. A. 2022.

[14] R. Kumar T. P., P. Nag, M. Ranković, T. F. M. Luxford, J. Kočišek, Z. Mašín, and J. Fedor. *Distant Symmetry Control in Electron-Induced Bond Cleavage*. To be published.

[15] B. Boudaïffa, P. Cloutier, D. Hunting, M. A. Huels, and L. Sanche. Resonant Formation of DNA Strand Breaks by Low-Energy (3 to 20 eV) Electrons. *Science* 287(5458), 1658–1660, 2000.

[16] J. Kopyra, A. Keller, and I. Bald. On the role of fluoro-substituted nucleosides in DNA radiosensitization for tumor radiation therapy. *RSC Adv.* 4, 6825–6829, 2014.

[17] H. Hotop, M.-W. Ruf, M. Allan, and I. Fabrikant. Resonance and Threshold Phenomena in Low-Energy Electron Collisions with Molecules and Clusters, ed. by B. Bederson et al. Vol. 49. Advances In Atomic, Molecular, and Optical Physics. Academic Press, 2003, 85–216.

[18] P. Čársky and R. Čurík, eds. *Low-energy Electron Scattering from Molecules, Biomolecules and Surfaces*. CRC Press, 2012.

[19] J. Tennyson. Electron–molecule collision calculations using the R-matrix method. *Phys. Rep.* 491(2), 29–76, 2010.

[20] D. R. Yarkony. *Modern Electronic Structure Theory*. World Scientific Publishing Company, 1995.

[21] T. N. Rescigno, C. W. McCurdy, A. E. Orel, and B. H. Lengsfield. The Complex Kohn Variational Method. *Computational Methods for Electron–Molecule Collisions*, ed. by W. M. Huo et al. Boston, MA: Springer US, 1995, 1–44.

[22] D. K. Watson. Schwinger Variational Methods, ed. by D. Bates et al. Vol. 25. Advances in Atomic and Molecular Physics. Academic Press, 1989, 221–250.

[23] L. Dubé and A. Herzenberg. Absolute cross sections from the "boomerang model" for resonant electron-molecule scattering. *Phys. Rev. A* 20, 194–213, 1979.

[24] L. S. Cederbaum and W. Domcke. Local against non-local complex potential in resonant electron-molecule scattering. *J. Phys. B: At. Mol. Phys.* 14(23), 4665–4690, 1981.

[25] W. Domcke and L. S. Cederbaum. On the interpretation of low-energy electron-HCl scattering phenomena. *J. Phys. B: At. Mol. Phys.* 14(1), 149–173, 1981.

[26] J. P. Gauyacq and A. Herzenberg. Nuclear-excited Feshbach resonances in $e + HCl$ scattering. *Phys. Rev. A* 25, 2959–2967, 1982.

[27] W. Vanroose, C. W. McCurdy, and T. N. Rescigno. Scattering of slow electrons by polar molecules: Application of effective-range potential theory to HCl. *Phys. Rev. A* 68, 052713, 2003.

[28] I. I. Fabrikant. R-matrix theory of vibrational excitation of the HCl molecule by slow electrons in the adiabatic approximation. *J. Phys. B: At. Mol. Phys.* 18(9), 1873–1879, 1985.

[29] I. I. Fabrikant. R-matrix theory of inelastic processes in low-energy electron collisions with HCl molecule. *Z. Phys. D* 3(4), 401–410, 1986.

[30] I. I. Fabrikant. Quasiclassical R-matrix theory of inelastic processes in collisions of electrons with HCl molecules. *Phys. Rev. A* 43, 3478–3486, 1991.

[31] J. C. Y. Chen. Dissociative Attachment in Rearrangement Electron Collision with Molecules. *Phys. Rev.* 148, 66–73, 1966.

[32] T. F. O'Malley. Theory of Dissociative Attachment. *Phys. Rev.* 150, 14–29, 1966. Erratum: *Phys. Rev.* 156, 230–230, 1967.

[33] J. N. Bardsley. The theory of dissociative recombination. *J. Phys. B: At. Mol. Phys.* 1(3), 365–380, 1968.

[34] H. Nakamura. Associative Ionization in Slow Collisions between Atoms. I. *J. Phys. Soc. Jpn.* 31(2), 574–583, 1971.

[35] S. Marienfeld, T. Sunagawa, I. I. Fabrikant, M. Braun, M.-W. Ruf, and H. Hotop. The dependence of low-energy electron attachment to CF3Br on electron and vibrational energy. *J. Chem. Phys.* 124(15), 154316, 2006.

[36] M. Zawadzki, M. Čížek, K. Houfek, R. Čurík, M. Ferus, S. Civiš, J. Kočišek, and J. Fedor. Resonances and Dissociative Electron Attachment in HNCO. *Phys. Rev. Lett.* 121, 143402, 2018.

[37] R. Kumar T. P., P. Nag, M. Ranković, R. Čurík, A. Knížek, S. Civiš, M. Ferus, J. Trnka, K. Houfek, M. Čížek, and J. Fedor. Electron-impact vibrational excitation of isocyanic acid HNCO. *Phys. Rev. A* 102, 062822, 2020.

[38] M. Tarana, P. Wielgus, S. Roszak, and I. I. Fabrikant. Effects of two vibrational modes in the dissociative electron attachment to CF_3Cl. *Phys. Rev. A* 79, 052712, 2009.

[39] M. Tarana, K. Houfek, J. Horáček, and I. I. Fabrikant. Dissociative electron attachment and vibrational excitation of CF_3Cl: Effect of two vibrational modes revisited. *Phys. Rev. A* 84, 052717, 2011.

[40] H. B. Ambalampitiya and I. I. Fabrikant. Nonlocal complex potential theory of dissociative electron attachment: Inclusion of two vibrational modes. *Phys. Rev. A* 102, 022802, 2020.

[41] W. Vanroose, Z. Zhang, C. W. McCurdy, and T. N. Rescigno. Threshold Vibrational Excitation of CO_2 by Slow Electrons. *Phys. Rev. Lett.* 92, 053201, 2004.

[42] C. W. McCurdy and J. L. Turner. Wave packet formulation of the boomerang model for resonant electron–molecule scattering. *J. Chem. Phys.* 78(11), 6773–6779, 1983.

[43] H.-D. Meyer, U. Manthe, and L. Cederbaum. The multi-configurational time-dependent Hartree approach. *Chem. Phys. Lett.* 165(1), 73–78, 1990.

[44] M. Beck, A. Jäckle, G. Worth, and H.-D. Meyer. The multiconfiguration time-dependent Hartree (MCTDH) method: a highly efficient algorithm for propagating wavepackets. *Phys. Rep.* 324(1), 1–105, 2000.

[45] C. W. McCurdy, W. A. Isaacs, H.-D. Meyer, and T. N. Rescigno. Resonant vibrational excitation of CO_2 by electron impact: Nuclear dynamics on the coupled components of the $^2\Pi_u$ resonance. *Phys. Rev. A* 67, 042708, 2003.

[46] D. J. Haxton, Z. Zhang, C. W. McCurdy, and T. N. Rescigno. Complex potential surface for the $^2B_1$ metastable state of the water anion. *Phys. Rev. A* 69, 062713, 2004.

[47] D. J. Haxton, Z. Zhang, H.-D. Meyer, T. N. Rescigno, and C. W. McCurdy. Dynamics of dissociative attachment of electrons to water through the $^2B_1$ metastable state of the anion. *Phys. Rev. A* 69, 062714, 2004.

[48] D. J. Haxton, T. N. Rescigno, and C. W. McCurdy. Topology of the adiabatic potential energy surfaces for the resonance states of the water anion. *Phys. Rev. A* 72, 022705, 2005.

[49] D. J. Haxton, C. W. McCurdy, and T. N. Rescigno. Dissociative electron attachment to the H_2O molecule I. Complex-valued potential-energy surfaces for the $^2B_1$, $^2A_1$, and $^2B_2$ metastable states of the water anion. *Phys. Rev. A* 75, 012710, 2007. Erratum: *Phys. Rev. A* 76, 049906, 2007.

[50] D. J. Haxton, T. N. Rescigno, and C. W. McCurdy. Dissociative electron attachment to the H_2O molecule. II. Nuclear dynamics on coupled electronic surfaces within the local complex potential model. *Phys. Rev. A* 75, 012711, 2007. Erratum: *Phys. Rev. A* 76, 049907, 2007.

[51] D. J. Haxton, T. N. Rescigno, and C. W. McCurdy. Three-body breakup in dissociative electron attachment to the water molecule. *Phys. Rev. A* 78, 040702, 2008.

[52] D. J. Haxton, H. Adaniya, D. S. Slaughter, B. Rudek, T. Osipov, T. Weber, T. N. Rescigno, C. W. McCurdy, and A. Belkacem. Observation of the dynamics leading to a conical intersection in dissociative electron attachment to water. *Phys. Rev. A* 84, 030701, 2011.

[53] S. T. Chourou and A. E. Orel. Dissociative electron attachment to acetylene. *Phys. Rev. A* 77, 042709, 2008.

[54] S. T. Chourou and A. E. Orel. Improved calculation on the isotope effect in dissociative electron attachment to acetylene. *Phys. Rev. A* 80, 034701, 2009.

[55] S. T. Chourou and A. E. Orel. Dissociative electron attachment to HCN and HNC. *Phys. Rev. A* 80, 032709, 2009.

[56] S. T. Chourou and A. E. Orel. Isotope effect in dissociative electron attachment to HCN. *Phys. Rev. A* 83, 032709, 2011.

[57] T. N. Rescigno, C. S. Trevisan, and A. E. Orel. Dynamics of Low-Energy Electron Attachment to Formic Acid. *Phys. Rev. Lett.* 96, 213201, 2006.

[58] G. A. Gallup, P. D. Burrow, and I. I. Fabrikant. Electron-induced bond breaking at low energies in HCOOH and glycine: The role of very short-lived σ^* anion states. *Phys. Rev. A* 79, 042701, 2009.

[59] T. N. Rescigno, C. S. Trevisan, and A. E. Orel. Comment on "Electron-induced bond breaking at low energies in HCOOH and glycine: The role of very short-lived σ^* anion states". *Phys. Rev. A* 80, 046701, 2009.

[60] G. A. Gallup, P. D. Burrow, and I. I. Fabrikant. Reply to "Comment on 'Electron-induced bond breaking at low energies in HCOOH and glycine: The role of very short-lived σ^* anion states' ". *Phys. Rev. A* 80, 046702, 2009.

[61] R. Janečková, D. Kubala, O. May, J. Fedor, and M. Allan. Experimental Evidence on the Mechanism of Dissociative Electron Attachment to Formic Acid. *Phys. Rev. Lett.* 111, 213201, 2013.

[62] G. A. Gallup and I. I. Fabrikant. Vibrational Feshbach resonances in dissociative electron attachment to uracil. *Phys. Rev. A* 83, 012706, 2011.

[63] S. Feuerbacher, T. Sommerfeld, and L. S. Cederbaum. Intersections of potential energy surfaces of short-lived states: The complex analogue of conical intersections. *J. Chem. Phys.* 120(7), 3201–3214, 2004.

[64] S. Feuerbacher and L. S. Cederbaum. Jahn-Teller effect for short-lived states: Study of the complex potential energy surfaces. *J. Chem. Phys.* 121(1), 5–15, 2004.

[65] M. Šarmanová. Iterative calculation of vibrational dynamics in electron scattering from molecule. Bachelor Thesis. Charles University, Faculty of Mathematics and Physics. Prague, 2020.

[66] M. Šarmanová. Mathematical modeling of vibrational dynamics in electron scattering from molecule. Master Thesis. Charles University, Faculty of Mathematics and Physics. Prague, 2022.

[67] M. Šarmanová, J. Dvořák, and M. Čížek. *Vibronic dynamics in electron continuum - iterative solvers.* In preparation.

[68] H. Feshbach. A unified theory of nuclear reactions. II. *Ann. Phys.* 19(2), 287–313, 1962.

[69] H. Köppel, W. Domcke, and L. S. Cederbaum. Theory of vibronic coupling in linear molecules. *J. Chem. Phys.* 74(5), 2945–2968, 1981.

[70] F. Currell and J. Comer. Polyatomic excitation effects observed in an electron impact study of the 4 eV shape resonance of carbon dioxide. *J. Phys. B: At., Mol. Opt. Phys.* 26(15), 2463–2474, 1993.

[71] F. Currell and J. Comer. Observation of Friction in the Nuclear Dynamics of CO_2^- near the Equilibrium Geometry of the Negative Ion. *Phys. Rev. Lett.* 74, 1319–1322, 1995.

[72] M. Allan. Threshold Phenomena in Electron-Molecule Scattering. *Phys. Scr.* 110, 161, 2004.

[73] K. Regeta and M. Allan. Autodetachment Dynamics of Acrylonitrile Anion Revealed by Two-Dimensional Electron Impact Spectra. *Phys. Rev. Lett.* 110, 203201, 2013.

[74] K. Regeta and M. Allan. Two-dimensional spectra of electron collisions with acrylonitrile and methacrylonitrile reveal nuclear dynamics. *J. Chem. Phys.* 142(18), 184307, 2015.

[75] M. Allan, M. Lacko, P. Papp, Š. Matejčík, M. Zlatar, I. I. Fabrikant, J. Kočišek, and J. Fedor. Dissociative electron attachment and electronic excitation in Fe(CO)5. *Phys. Chem. Chem. Phys.* 20, 11692–11701, 2018.

[76] R. Kumar T. P., J. Kočišek, K. Bravaya, and J. Fedor. Electron-induced vibrational excitation and dissociative electron attachment in methyl formate. *Phys. Chem. Chem. Phys.* 22, 518–524, 2020.

[77] J. Med, Š. Sršeň, P. Slavíček, A. Domaracka, S. Indrajith, P. Rousseau, M. Fárník, J. Fedor, and J. Kočišek. Vibrationally Mediated Stabilization of Electrons in Nonpolar Matter. *J. Phys. Chem. Lett.* 11(7), 2482–2489, 2020.

[78] C. S. Anstöter, G. Mensa-Bonsu, P. Nag, M. Ranković, R. Kumar T. P., A. N. Boichenko, A. V. Bochenkova, J. Fedor, and J. R. R. Verlet. Mode-Specific Vibrational Autodetachment Following Excitation of Electronic Resonances by Electrons and Photons. *Phys. Rev. Lett.* 124, 203401, 2020.

[79] M. Ranković, R. Kumar T. P., P. Nag, J. Kočišek, and J. Fedor. Temporary anions of the dielectric gas C3F7CN and their decay channels. *J. Chem. Phys.* 152(24), 244304, 2020.

[80] J. Horáček, M. Čížek, K. Houfek, P. Kolorenč, and W. Domcke. Dissociative electron attachment and vibrational excitation of H_2 by low-energy electrons: Calculations based on an improved nonlocal resonance model. *Phys. Rev. A* 70, 052712, 2004.

[81] J. Horáček, M. Čížek, K. Houfek, P. Kolorenč, and W. Domcke. Dissociative electron attachment and vibrational excitation of H_2 by low-energy electrons: Calculations based on an improved nonlocal resonance model. II. Vibrational excitation. *Phys. Rev. A* 73, 022701, 2006.

[82] M. Berman, H. Estrada, L. S. Cederbaum, and W. Domcke. Nuclear dynamics in resonant electron-molecule scattering beyond the local approximation: The 2.3-eV shape resonance in N_2. *Phys. Rev. A* 28, 1363–1381, 1983.

[83] V. Alt and K. Houfek. Resonant collisions of electrons with O_2 via the lowest-lying $^2\Pi_g$ state of O_2^-. *Phys. Rev. A* 103, 032829, 2021.

[84] M. Čížek, J. Horáček, M. Allan, I. I. Fabrikant, and W. Domcke. Vibrational excitation of hydrogen fluoride by low-energy electrons: theory and experiment. *J. Phys. B: At., Mol. Opt. Phys.* 36(13), 2837–2849, 2003.

[85] J. Horáček, M. Čížek, and W. Domcke. Generalization of the nonlocal resonance model for low-energy electron collisions with hydrogen halides: the variable threshold exponent. *Theor. Chem. Acc.* 100(1), 31–35, 1998.

[86] C. Cohen-Tannoudji, B. Diu, and F. Laloë. *Quantum Mechanics, Volume 1: Basic Concepts, Tools, and Applications*. New York: Wiley, 2005.

[87] J. Horáček, F. Gemperle, and H.-D. Meyer. Calculation of dissociative attachment of electrons to diatomic molecules by the Schwinger–Lanczos approach. *J. Chem. Phys.* 104(21), 8433–8441, 1996.

[88] T. N. Rescigno and C. W. McCurdy. Numerical grid methods for quantum-mechanical scattering problems. *Phys. Rev. A* 62, 032706, 2000.

[89] K. Houfek. Private communication. Implementation of FEM DVR ECS method. 2022.

[90] E. P. Wigner. On the Behavior of Cross Sections Near Thresholds. *Phys. Rev.* 73, 1002–1009, 1948.

[91] I. I. Fabrikant. Long-range effects in electron scattering by polar molecules. *J. Phys. B: At., Mol. Opt. Phys.* 49(22), 222005, 2016.

[92] W. Domcke and C. Mündel. Calculation of cross sections for vibrational excitation and dissociative attachment in HCl and DCl beyond the local-complex-potential approximation. *J. Phys. B: At. Mol. Phys.* 18(22), 4491–4509, 1985.

[93] M. Abramowitz and I. A. Stegun. *Handbook of Mathematical Functions with Formulas, Graphs, and Mathematical Tables*. ninth Dover printing, tenth GPO printing. New York: Dover, 1964.

[94] K. Houfek, T. N. Rescigno, and C. W. McCurdy. Numerically solvable model for resonant collisions of electrons with diatomic molecules. *Phys. Rev. A* 73, 032721, 2006.

[95] K. Houfek, T. N. Rescigno, and C. W. McCurdy. Probing the nonlocal approximation to resonant collisions of electrons with diatomic molecules. *Phys. Rev. A* 77, 012710, 2008.

[96] J. R. Taylor. *Scattering Theory: The Quantum Theory on Nonrelativistic Collisions*. John Wiley & Sons, Inc., 1972.

[97] H. van der Vorst and J. Melissen. A Petrov-Galerkin type method for solving Axk=b, where A is symmetric complex. *IEEE Trans. Magn.* 26(2), 706–708, 1990.

[98] Z. Mašín. Private communication. R-matrix fixed-nuclei data of e+pyrrole scattering. 2021.

[99] Z. Mašín, J. Benda, J. D. Gorfinkiel, A. G. Harvey, and J. Tennyson. UKRmol+: A suite for modelling electronic processes in molecules interacting with electrons, positrons and photons using the R-matrix method. *Comput. Phys. Commun.* 249, 107092, 2020.

[100] T. H. Dunning. Gaussian basis sets for use in correlated molecular calculations. I. The atoms boron through neon and hydrogen. *J. Chem. Phys.* 90(2), 1007–1023, 1989.

[101] E. M. de Oliveira, M. A. P. Lima, M. H. F. Bettega, S. d. Sanchez, R. F. da Costa, and M. T. d. N. Varella. Low-energy electron collisions with pyrrole. *J. Chem. Phys.* 132(20), 204301, 2010.

[102] H. Estrada and W. Domcke. Analytic properties of the S matrix for a simple model of fixed-nuclei electron-polar-molecule scattering. *J. Phys. B: At. Mol. Phys.* 17(2), 279–297, 1984.

[103] A. Mellouki, J. Liévin, and M. Herman. The vibrational spectrum of pyrrole (C4H5N) and furan (C4H4O) in the gas phase. *Chem. Phys.* 271(3), 239–266, 2001.

[104] A. R. Davies, D. J. Kemp, and T. G. Wright. Vibrations of pyrrole, N-substituted pyrroles, and their cations. *J. Mol. Spectrosc.* 376, 111410, 2021.

[105] H. Friedrich. *Scattering Theory*. Springer, 2013.

[106] M. J. Frisch, G. W. Trucks, H. B. Schlegel, G. E. Scuseria, M. A. Robb, J. R. Cheeseman, G. Scalmani, V. Barone, G. A. Petersson, H. Nakatsuji, X. Li, M. Caricato, A. V. Marenich, J. Bloino, B. G. Janesko, R. Gomperts, B. Mennucci, H. P. Hratchian, J. V. Ortiz, A. F. Izmaylov, J. L. Sonnenberg, D. Williams-Young, F. Ding, F. Lipparini, F. Egidi, J. Goings, B. Peng, A. Petrone, T. Henderson, D. Ranasinghe, V. G. Zakrzewski, J. Gao, N. Rega, G. Zheng, W. Liang, M. Hada, M. Ehara, K. Toyota, R. Fukuda, J. Hasegawa, M. Ishida, T. Nakajima, Y. Honda, O. Kitao, H. Nakai, T. Vreven, K. Throssell, J. A. Montgomery Jr., J. E. Peralta, F. Ogliaro, M. J. Bearpark, J. J. Heyd, E. N. Brothers, K. N. Kudin, V. N. Staroverov, T. A. Keith, R. Kobayashi, J. Normand, K. Raghavachari, A. P. Rendell, J. C. Burant, S. S. Iyengar, J. Tomasi, M. Cossi, J. M. Millam, M. Klene, C. Adamo, R. Cammi, J. W. Ochterski, R. L. Martin, K. Morokuma, O. Farkas, J. B. Foresman, and D. J. Fox. *Gaussian 16 Revision C.01*. Gaussian Inc. Wallingford CT. 2016.

[107] S. Y. Lee and B. H. Boo. Molecular Structures and Vibrational Spectra of Pyrrole and Carbazole by Density Functional Theory and Conventional ab Initio Calculations. *J. Phys. Chem.* 100(37), 15073–15078, 1996.

[108] A. Moradmand, D. S. Slaughter, D. J. Haxton, T. N. Rescigno, C. W. McCurdy, T. Weber, S. Matsika, A. L. Landers, A. Belkacem, and M. Fogle. Dissociative electron attachment to carbon dioxide via the $^2\Pi_u$ shape resonance. *Phys. Rev. A* 88, 032703, 2013.

List of publications

M. Čížek, J. Dvořák, and K. Houfek. Associative detachment in Li+H^- collisions. *Eur. Phys. J. D* 72(4), 66, 2018.

J. Dvořák, M. Ranković, K. Houfek, P. Nag, R. Čurík, J. Fedor, and M. Čížek. Vibronic Coupling through the Continuum in the $e + CO_2$ System. *Phys. Rev. Lett.* 129, 013401, 2022. (selected as Editors' Suggestion)

J. Dvořák, K. Houfek, and M. Čížek. Vibrational excitation in the $e + CO_2$ system: Nonlocal model of $\Sigma\Pi$ vibronic coupling through the continuum. *Phys. Rev. A* 105, 062821, 2022. (selected as Editors' Suggestion)

J. Dvořák, M. Ranković, K. Houfek, P. Nag, R. Čurík, J. Fedor, and M. Čížek. Vibrational excitation in the $e + CO_2$ system: Analysis of two-dimensional energy-loss spectrum. *Submitted to Phys. Rev. A*, 2022.